Cationic Rhodium Complexes with *Ortho*-Aryl Substituted DPEphos Ligands and Rhodium-Diphosphine Catalysed Phosphine-Borane Dehydropolymerisation

Submitted by

James Jonathan Race

A thesis submitted in partial fulfilment of the requirements for the degree of Doctor of Philosophy at the University of Oxford.

Linacre College

July 2022

Declaration

The work presented in this thesis was carried out between October 2018 and June 2012 under the supervision of Professor Andrew S. Weller. All of the work is my own unless otherwise stated and has not been submitted previously for any other degree at this, or any other, university.

James J. Race

July 2022

Acknowledgements

What a journey that was! I must start by thanking Professor Andrew Weller for being such a supportive, encouraging and influential supervisor. Thank you for your unrelenting guidance. You have taught me a great deal about scientific rigour (a.k.a. 'doing it properly') and the importance of effective communication. You have also provided us all with hours of entertainment, with your 'Wellerisms', inappropriate stories and dragging us out to the Yorkshire countryside. I have truly enjoyed my DPhil, from the unique science that we never really knew where it was going, to the incredible people and the life-long memories and friendships, and I owe a lot of it to you. Thank you, Andy.

Before I go on to thank the wonderful people I have had the privilege to share a research group with, I would like to say thank you to the service staff at the University of Oxford and the University of York. Without their help and welcoming support before and after the move, I would not have been able to produce most of the work in this thesis.

At the beginning, a highly capable and welcoming group of scientists took me into their lab, and under their wing. For this, I must thank the original postdocs: Alice Johnson and the legend himself, Antonio 'Big Tone' Martinez-Martinez.

Now, there are seven people who I will always have a special bond with; the group who moved from Oxford to York (or met us up there from the start). We turned something unexpected, and at the time quite annoying, into something really positive. I must start by thanking Sam Furfari, who has become a cherished friend of mine. You orchestrated the moving of entire research lab whilst also putting up with us delinquents. Sam, right from your interview, and the first column you helped me with, I knew you were great. We have formed a really close bond, and I will always be grateful for your hospitality during the final stages of my DPhil. Next, on the other end of the postdoc scale, we have Laurence Doyle. Laurence, your undying calming influence was vital during the more annoying days in the lab. I will never listen to Prince without thinking about you and your Dad dancing, even before you became a Dad. Claire, you are a formidable force in the lab, achieving things in a day that I did not know was possible, yet you are also the first to help anyone. I admire your ambition in the lab but also your ambition to enjoy your life hiking the mountains of Scotland. You will smash it wherever you go. I must also thank Alex Bukvic, for guiding me as the senior DPhil student when I started in the group, and also getting me into the Weller Cycling Club! A special thank you also goes to the MChem student

Matt ‘Little Matt’ Webb, who was a pleasure to work with in my third year and conducted some of the results in this thesis under my supervision.

Next, there are three very special people that I have no doubt will stay life-long friends of mine: Cameron, David and Tim. We all moved in together in the winter of 2020, and everyone thought working together and living together was a recipe for disaster. How we proved them wrong. What a laugh we had. I will cherish the memories of watching Louis Theroux together whilst David cooked up some delight from the international supermarket. Cameron, you transformed before our eyes, and it was wonderful to observe. Your taste in music, however, left more to be desired. Your unique thought process will serve you very well in the future mate. David, I cannot thank you enough for your help in the lab. Your understanding of chemistry is brilliant, and you are one of the funniest people I have had the pleasure to meet (and live with). We had a great time playing football and bopping around to electronic music in the lab, much to the dismay of Tim and his mopey folk musical taste. Timmy, we have a relationship like no other. Who would have thought that after living, working, socialising, exercising and going on holiday together, we would still be great friends? You have the rare combination of elite intelligence and elite compassion, thank you for everything Timmy. I have no doubt we will all continue to meet up in the future to exchange stories of our success.

To the current members of the Weller group continuing after me: good luck and make the most of it! Joe and Helena, you fitted into the group right from the start and I thoroughly enjoyed showing you what not to do in the lab. Chloe and Mat, you are excellent additions to the group, and I feel we had a real laugh, even if we only worked together for a few short months. The group is in very safe hands with Big (Hairy) Matt, who I must also thank for tolerating me and allowing me to steal your super milk during my last visits to York.

I have also been fortunate enough to collaborate with Professor Ian Manners, to whom I am very grateful for hosting me in his lab in Autumn 2021, which reignited my passion for chemistry.

Lastly, a special thank you to my parents, Claire and Andy, and my grandmother, Barbara, who have unwaveringly supported me throughout my life and are the sole reason I got to this position in the first place. I am forever grateful. I must also thank the other people special to me in my personal life who have contributed to the last few years being some of the best in my life so far.

Abbreviations

3c-2e	3-centre-2-electron
Å	Angstrom
Ar	Aryl
-*b*-	block
BAr^F_4	$B\{3,5\text{-}(CF_3)_2C_6H_3\}_4$
calc.	calculated
COD	1,5-cyclooctadiene
COSY	correlation spectroscopy
Cp	cyclopentadienyl
δ	chemical shift in ppm
Đ	polydispersity index (M_w/M_n)
d	doublet
D(A–B) or D(A···B)	the distance between atoms A and B
DFT	density functional theory
DOSY	diffusion ordered spectroscopy
DLS	dynamic light scattering
DBFphos	4,6-bis(diphenylphosphino)dibenzofuran
DPEphos	bis[(2-diphenylphosphino)phenyl]ether
dppb	1,2-bis(diphenylphosphino)butane
dppe	1,2-bis(diphenylphosphino)ethane
dppf	1,1'-bis(diphenylphosphino)ferrocene
dppp	1,2-bis(diphenylphosphino)propane
dppm	1,2-bis(diphenylphosphino)methane
eq.	equivalents
ESI-MS	electrospray ionisation mass spectrometry
g	gram(s)
HSQC	heteronuclear single quantum coherance
fac	facial
fwhm	full width at half maximum
GPC	gel permeation chromatography
Hz	Hertz
^{i}Bu	isobutyl
^{i}Pr	isopropyl
IR	infrared
J	coupling constant in Hz
K	Kelvin
KIE	kinetic isotope effect
M	mol dm^{-3}
m	milli or metre
m	*meta*
Me	methyl
mer	meridional
ml	millilitre
mmol	millimole
µmol	micromole
mol%	mole percentage

M_n	number average molecular weight
M_w	weight average molecular weight
m/z	mass to charge ratio
NBA	norbornane
NBD	norbornadiene
^{n}Bu	normal butyl
^{n}Hex	normal hexyl
NMR	nuclear magnetic resonance
NOESY	nuclear Overhauser effect spectroscopy
o	*ortho*
$[OTf]^-$	triflate
Ph	phenyl
PDI	polydispersity index
ppm	parts per million
σ-CAM	sigma complex assisted metathesis
TBE	3,3-dimethylbut-1-ene
^{t}Bu	tertiary butyl
R	generic group
t	triplet
THF	tetrahydrofuran
TEM	transmission electron microscopy
TOF	time-of-flight
Xantphos	4,5-bis(diphenylphosphino)-9,9-dimethylxanthene
°C	degrees Celsius

Abstract

Transition metal-phosphine chemistry is the underpinning theme of this thesis. Chapter One briefly introduces the subject, with particular focus on *ortho*-aryl substituted phosphines, the DPEphos ligand and agostic and anagostic metal-hydrogen interactions. A comprehensive presentation of the developments in the field of phosphine-borane dehydropolymerisation is then provided.

Chapter Two describes the synthesis, characterisation and structural studies of a range of Schrock-Osborn type complexes containing *ortho*-aryl substituted DPEphos ligands of varying steric bulk, namely [Rh(*o*-R-DPEphos)(NBD)][BAr^F_4] [R = H, Me, OMe and ^{i}Pr, NBD = norbornadiene and Ar^F = 3,5-$(CF_3)_2C_6H_3$]. These complexes were all shown to contain a Rh···H–C anagostic interaction with an *ortho*-aryl proton, which were studied experimentally and computationally. The reactivity of the Schrock-Osborn complexes, upon hydrogenation of the alkene fragment in acetone, resulted in a range of Rh(I) and Rh(III) products, depending on the phosphine *ortho*-aryl substituent. In the bulkiest, *o*-^{i}Pr version, C–H activation is observed at the isopropyl group, which is shown to be reversible through reactivity with CO and D_2. This reactivity was used to form the first reported complex that contains both an anagostic interaction and an agostic bond.

Within Chapter Three, the coordination chemistry of the di-*ortho*-fluorine analogue of DPEphos, *o*-F,F-DPEphos, is described in comparison with the parent *o*-H-DPEphos and the bulkier *o*-Me-DPEphos. Rh···F interactions are observed in the Schrock-Osborn complex of *o*-F,F-DPEphos [Rh(o-F,F-DPEphos)(NBD)][BAr^F_4]. The hydrogenation products in 1,2-$F_2C_6H_4$ solvent are also compared, revealing the formation of a Rh dimeric complex Rh(H)(*fac*-κ^3-P,O,P-μ-CH-DPEphos)]$_2$[BAr^F_4]$_2$ with a bridging C–H agostic interaction for the parent DPEphos. The coordination chemistry of bimetallic gold complexes with these ligands is also explored, including an example of through-space F-F interactions.

The final chapter details an in depth study of the dehydropolymerisation of primary phosphine-boranes using a $[Rh(dppe)]^+$ catalyst. The mechanism is probed using in-situ NMR spectroscopy, stoichiometric reactivity and polymer molecular weight variation studies. Exploiting the mechanistic insight, the synthesis and characterisation of the first block copolymer of poly(phosphinoboranes) is described, which is also shown to self-assemble in solution to form spherical micelles.

Table of Contents

1 Chapter One – Introduction

1.1 Preamble

Within this thesis, the synthesis, characterisation and structural properties of rhodium complexes of *ortho*-substituted diphosphine ligands will be discussed. This will include an assessment of the structural consequences of *ortho*-aryl substitution, and an experimental investigation of anagostic interactions. The final chapter describes the application of rhodium-phosphine complexes as catalysts in the dehydropolymerisation of phosphine-boranes. To introduce these results and discussion chapters, Chapter One provides an introduction into the tuneability of phosphine ligands, and how these manipulations can have a pronounced impact on reactivity and homogeneous catalysis upon coordination to a transition metal centre, with particular attention paid to *ortho*-aryl substitution. The main focus will be on rhodium-phosphine chemistry and the DPEphos ligand. Metal-hydrogen interactions, specifically, agostic bonds and anagostic interactions, are also introduced, highlighting the key differences between the two interactions. The developments in dehydrocoupling and dehydropolymerisation of phosphine-boranes will be discussed, from initial discovery to the current mechanistic understanding.

1.2 Rhodium-phosphine complexes as homogeneous catalysts

Rhodium-phosphine complexes are of great synthetic importance as they can be used as catalysts for the synthesis of highly useful compounds.[1-3] Rhodium-catalysed hydroformylation is used to produce millions of tonnes of aldehydes and alcohols each year using highly designed, often bespoke, rhodium-diphosphine complexes.[4] One of the earliest, and possibly the most famous example of the use of an organometallic rhodium complex as a homogeneous catalyst is [$RhCl(PPh_3)_3$], commonly termed Wilkinson's catalyst.[5, 6] Wilkinson's catalyst was shown to catalytically hydrogenate olefins and alkynes with molecular H_2 (Scheme 1.1A). The mechanism of this reaction was separately studied by Tolman[7, 8] and Halpern,[9-11] and although it was revealed that the mechanism contained many on- and off-cycle intermediates, and was very dependent on the reaction conditions, it can be summarised by a core mechanism (Scheme 1.1A).[3] One PPh_3 ligand is reversibly displaced by a solvent molecule, such as

methanol, and then dihydrogen oxidatively adds before alkene coordination. The alkene then inserts into the Rh–H bond and a subsequent reductive elimination step releases the alkyl product.

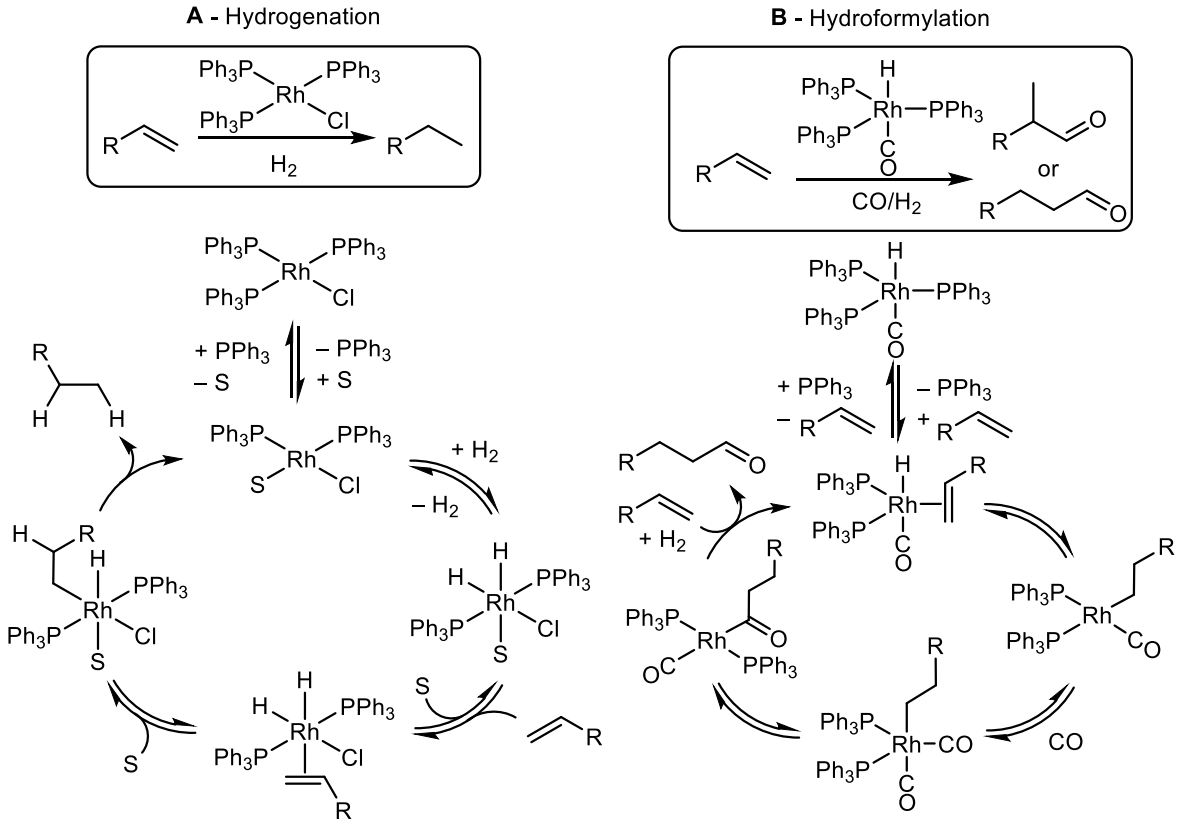

Scheme 1.1. **A**) Catalytic hydrogenation of olefins using Wilkinson's catalyst and the core, "hydrogen-first" mechanism for the hydrogenation of olefins.[3] **B**) Catalytic hydroformylation of terminal alkenes to form linear or branched aldehydes using a rhodium-phosphine catalyst (linear aldehyde formation is shown in the mechanism).

The related complex [$RhH(CO)(PPh_3)_3$] was reported to combine H_2 and CO with olefins to form either branched or linear aldehydes in the hydroformylation reaction (Scheme 1.1B).[12] The simplified mechanism for linear aldehyde formation is shown, as first deduced by Heck and Breslow.[13-15] An alkene ligand displaces PPh_3, and then insertion of the alkene into the Rh–H bond, before CO coordination and then CO insertion into the Rh–alkyl bond. Addition of H_2 results in the release of aldehyde.[16] In both of these reactions, the coordinated phosphine can influence the selectivity in the products formed, therefore, offering the opportunity for catalyst control by altering the phosphine design.[17]

Today, rhodium-phosphine complexes are used in many industrial scale reactions, such as asymmetric hydrogenation, which is vitally important in the pharmaceutical industry.[3] Other highly

influential applications of this chemistry in the industry and academic settings include C–H activation reactions,[18] and new bond-forming reactions, such as hydrosilylation.[19]

1.3 Rhodium-ligand coordination chemistry

Rhodium's use in catalysis spans a wide range of applications, from the synthesis of 1,4-hexadiene which is used to make synthetic rubber,[20] to the Monsanto acetic acid process.[21] One of the reasons for such a broad range of applications is the rich coordination chemistry of rhodium.[22, 23] The different possible ligands include neutral donor L-type ligands, and anionic X-type ligands. Examples of rhodium-ligand bonds with neutral ligands include, but are certainly not limited to: aromatic compounds, small solvent molecules (acetone, acetonitrile etc.), gaseous diatomic molecules (H_2, O_2, CO, N_2), alkenes, boranes, amines and phosphines (Figure 1.1). Some of the anionic ligands include: halides, alkyls, aryls, hydrides, alkoxides, acyls, acetates, phoshides and amidos.[3, 20] It is evident from the list in Figure 1.1 that there is a complex range of tolerated functional groups, coordinating atoms and bonding modes.

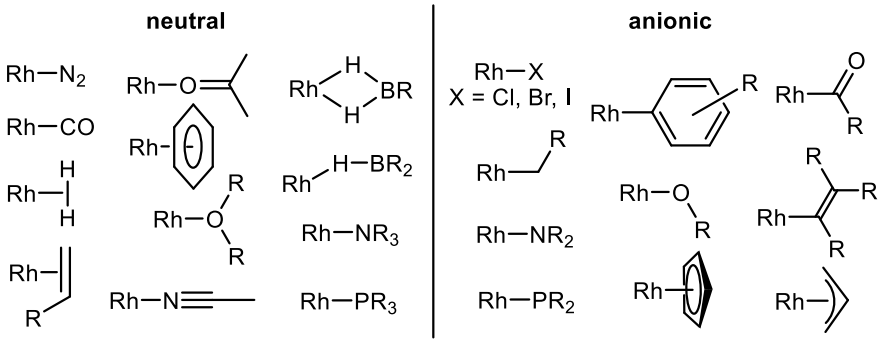

Figure 1.1. Some examples of organic ligands that can bind to rhodium.

Rhodium can adopt an oxidation state of anywhere between –1 and +6.[24, 25] The most stable oxidation states in organorhodium complexes, and therefore the most common, are +1 and +3 with a d^8 and d^6 configuration, respectively. Transitioning between these two oxidation states is key to the effectiveness of organorhodium complexes in homogeneous catalysis.[3] A high proportion of organorhodium catalysts contain phosphine ligands. This is due to the stabilising properties they bring to the organometallic complex, and in turn, facilitate the key catalytic steps in a cycle (Scheme 1.1).[26]

1.4 Phosphines as ligands

Phosphines are compounds with the generic formula PR_3, where R is typically an alkyl or aryl group, but can also be a halide or a heteroatom bound moiety, e.g. $P(NEt_3)_2Cl$.[3] The phosphorus atom is in the +3 oxidation state and therefore a lone pair of electrons is available for further coordination to a transition metal atom. One of the defining features of phosphines is the ability to change and tune the substituents on the phosphorus atom, with great predictability. This in turn modifies the phosphorus to metal bonding interaction, affecting the electronic properties of the complex. Different phosphine substituents can also impact the steric congestion around the metal centre.[16]

By modifying both electronic and steric influences the overall reactivity of the organometallic complex and subsequent catalytic activity can be controlled.[27] The universal aspect of the phosphine-metal bonding interaction is lone pair donation from the phosphorus into unoccupied orbitals in the metal (Figure 1.2). A second component is back-donation from filled metal orbitals into a vacant σ*(P–R) orbital in the phosphine.[28] However, this contribution is completely dependent on the π-acidity of the phosphine, which is directly related to the substituents present. As the substituent gets more electronegative the π-acceptor abilities increase. This is due to two reasons: the P–R σ* orbital is lower in energy which brings the orbital into a better energy match with the filled metal orbitals, and the P–R σ* orbital has more P character and therefore has a greater radial extension. At the extreme end of this spectrum, PF_3 is a better π-acceptor than even CO.[20]

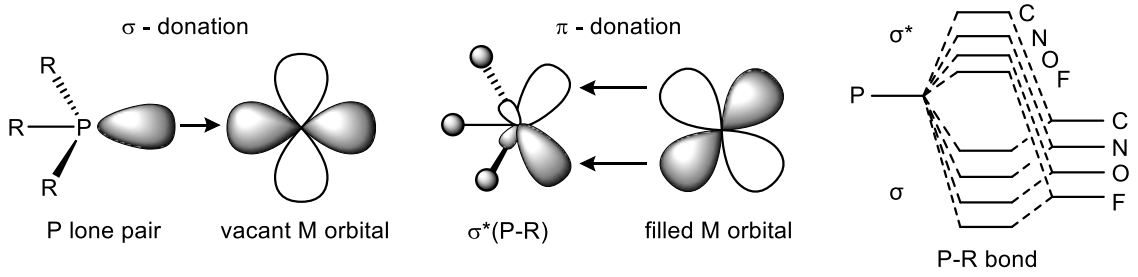

Figure 1.2. σ and π bonding components of phosphine-transition metal bonds and the molecular orbital diagram of the σ component of the P-R bond. The more electronegative atoms substituents have a lower σ and σ* orbital.

A measurement of the electronic contribution from the phosphine to the metal was described by Chadwick Tolman in 1977.[29] In this review, Tolman quantified the electronic effect of the phosphine

ligand through the change of the symmetric A_1 CO stretching frequency [v(CO)] in $(PR_3)Ni(CO)_3$ complexes. Stronger electron donors increase the electron density on the Ni centre which in turn decreases the v(CO). Computational methods have since been developed that can predict the same properties without the use of toxic Ni compounds.[30] Changing the steric bulk on the phosphine substituent can be as influential to the reactivity of an organometallic complex as the electronic contributions from the ligand.[31] An example of this is the stabilisation of low coordinate intermediates.[32] One descriptive measurement for this influence is the Tolman cone angle.[29, 30, 33] This measurement is determined from the space filling model of MPR_3. The cone angle is defined as the apex cone angle, positioned 2.28 Å from the centre of the P atom when the edges of the cone just touch the outermost part of the R fragments (Figure 1.3). Bulkier groups give a larger cone angle, e.g. PMe_3 = 118°, compared to P^iPr_3 = 160°.[29] NMR spectroscopy has been utilised as an alternative method to determine the cone angle, and it has been shown that there are direct correlations between cone angle and reaction and equilibrium rate constants.[34]

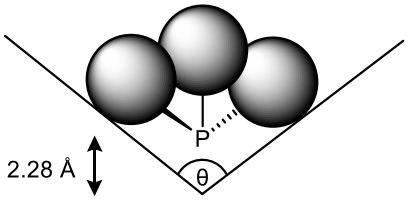

Figure 1.3. Visual description of the Tolman cone angle (θ) for phosphine bulk quantification.

More recently, sophisticated software, such as SambVca, has become publicly available. This software can be used to measure the steric volume within an organometallic complex, which provides insight into the most congested regions of the complex as well as the potential catalytic pockets.[35]

1.4.1 Diphosphines

One of the opportunities for phosphine modification is the insertion of an organic fragment that bridges two P(III) atoms. This forms a diphosphine which can coordinate to a metal with both P lone pairs, forming a chelating κ^2 ligand, which drastically effects the resulting organometallic reactivity.[16] The first diphosphine synthesised was 1,2-bis(diphenylphosphino)ethane (dppe) in 1959 (Figure 1.4).[36] However, it was several years later when the beneficial use of diphosphines was reported in Fe-

catalysed co-dimerisation of butadiene and ethene to form 1,4-hexadiene. In this early report, iron-halides and phosphines of varying backbone length were used as catalysts, with the propyl backbone bis(diphenylphosphino)propane (dppp) giving the best selectivity and conversion.[37] As well as simply changing the backbone length, more elaborate modifications, such as phenyl bridges (dppbe), ethers (DPEphos) or ferrocene (dppf) further modify the phosphine's properties (Figure 1.4).

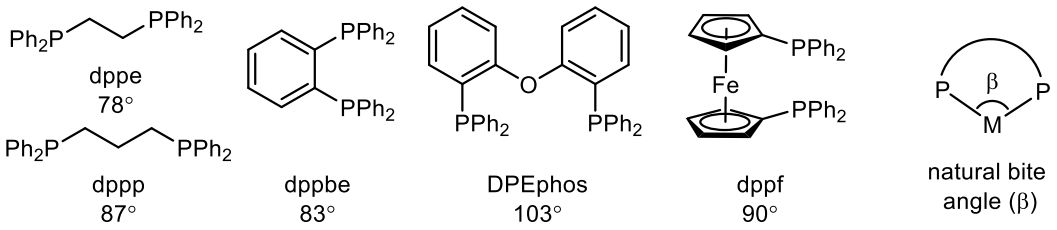

Figure 1.4. Some examples of diphosphines with different backbones. A diagram of the natural P–M–P bite angle (β) is shown and the values for the different diphosphines are quoted.[38, 39]

The coordination mode of the diphosphine can stabilise or destabilise catalytic intermediates and transitions states, thus influencing the lowest energy pathway in catalysis.[40] One measure of this influence is in the "ligand-preferred" or "natural" P–M–P bite angle β (example values shown in Figure 1.4), which varies with the ligand backbone and phosphorus substituents e.g. β = 78° for dppe and β = 103° for DPEphos.[38] Ligands with natural bite angles close to 90°, 109° or 120° are inherent to complexes with a square planar, tetrahedral or trigonal bipyramidal geometry, respectively.[38] There is also a measure of the flexibility of the backbone, described as the "flexibility range", which includes the bite angles of all of the low energy conformations the ligand can occupy.[41] For instance, DPEphos has a natural bite angle of roughly 103° but a flexibility range of 86-120°.[42] An example of the bite angle of a chelating diphosphine impacting catalysis is observed in the hydroxycarbonylation of styrene to form either the linear or branched carboxylic acid product under acidic conditions (Scheme 1.2).[38] It was shown that both the conversion of styrene and the regioselectivity of the linear product increased as the bite angle of the diphosphine increased. This was a result of the greater steric encumbrance of the larger bite angle ligands (i.e. DPEphos) promoting carbonylation at the least sterically congested alkene carbon.[43]

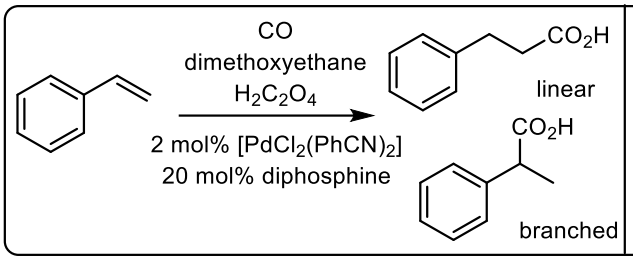

diphosphine	β (°)	conversion(%)	l:b
dppe	78	< 1	53:47
dppp	87	2	77:23
dppf	90	39	84:16
DPEphos	103	93	86:14

Scheme 1.2. Hydroxycarbonylation of styrene catalysed by Pd(diphosphine) complexes. The table shows the conversion of styrene and linear:branched selectivity with respect to the different diphosphines used. β = natural bite angle.[38]

1.5 *Ortho*-aryl substitution in phosphines

Another synthetic tool to control catalysis is via variation of the substituent in the *ortho*-position in the phosphine aromatic groups (Figure 1.5).

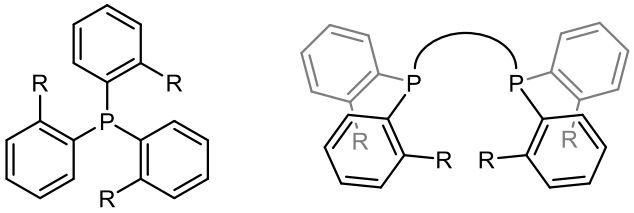

Figure 1.5. *Ortho*-aryl substitution in mono- and diphosphines.

An example of this approach has been reported in small bite angle, methylene bridged, diphosphines, $CH_2(PAr_2)_2$ (Ar = *o*-R-C_6H_4, R = H, Me, Et, OMe or ^{i}Pr) and similar amine-bridged diphosphines, $N(CH_3)(PAr_2)_2$ (**i-1-R**). Palladium(II) four-membered chelates of these amine-bridged ligands were shown to copolymerise ethene and CO to form polyketones (Scheme 1.3). The most bulky ligand, containing an *ortho*-aryl isopropyl group (Ar = *o*-^{i}Pr-C_6H_4), (**i-1-^{i}Pr**), gave the fastest rate of reaction and the largest molecular weight polyketone.[44] **i-1-R** were also reported as effective ligands in Ni(II) ethylene polymerisation catalysts. Once again, the bulkiest, isopropyl variant gave the highest molecular weight polymer and shortest reaction time.[45] *Ortho*-methoxy substitution was also exploited in **i-1-OMe** with $CrCl_3$ and methyl aluminoxane to catalyse the trimerization of ethene.[46] The same methodology was expanded to ligands with different backbones, such as ethyl, propyl, phenyl and Xantphos, which also effectively catalysed ethylene oligomerisation and polymerisation in Ni(II) systems [Xantphos = 4,5-bis(diphenylphosphino)-9,9-dimethylxanthene]. The most bulky substituents prevented formation of off-

cycle multinuclear species.[47] *Ortho*-aryl methyl substitution was also reported by Roy and Hartwig, who showed that bulkier monophosphines increased the rate of haloarene reductive elimination in {Pd[P(*o*-Me-C_6H_4)$_3$](Ar)(μ-X)}$_2$ complexes (Ar = 2-Me-5-^{t}Bu-C_6H_3 or 4-^{t}Bu-C_6H_4, X = Cl, Br or I).[48]

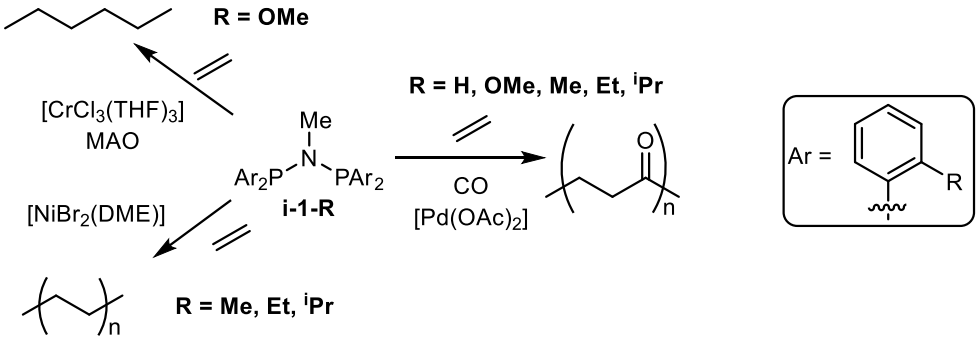

Scheme 1.3. Ethene polymerisation, oligomerisation and copolymeriation catalysed by transition metal complexes of *ortho*-substituted diphosphines. MAO = methyl aluminoxane. DME = 1,2-dimethoxyethane.

Extensive investigations into the special effects of *ortho*-aryl substitution in monophosphines was conducted by Howell[49-52] and others.[53, 54] Howell showed that there was a significant energy barrier for rotation around the P–C bonds in [M(CO)$_5$(P(*o*-Me-C_6H_4)$_3$)] complexes (M = Cr, Mo or W) of 36-42 kJ mol^{-1}, as well as restricted rotation about the M–P bond, compared to the least bulky *ortho*-H analogues.[50] This geometric constraint resulted in discrete orientations of the aromatic groups in the solution and solid-state (Figure 1.6). The geometries observed are dependent on the phosphine, the metal and the other coordinated ligands.[49] Rotamers of this form were first reported in triphenylcarbonium ions in 1965,[55] but the most logical description to date was published by Pringle and co-workers.[56, 57] The helical conformations in a range of *ortho*-substituted monophosphines in *trans*-[Pt(diphosphine)Cl$_2$] and *trans*-[Pd(diphosphine)Cl$_2$] complexes were described by the M–P–C_{ipso}–C_{ortho} torsion angle, deduced from the solid-state structures. The calculated values naturally fell into two groups: values of around ±50°, i.e. a *gauche*-orientation, denoted g^+ and g^-, or roughly ±180°, i.e. an *anti*-orientation, denoted *a* (Figure 1.6).

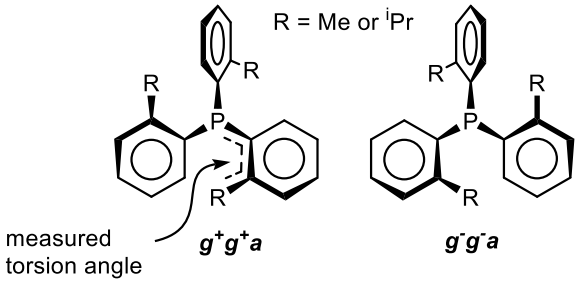

Figure 1.6. Conformational arrangements of the g^+g^+a and g^-g^-a chiral rotamers of *ortho*-substituted trisaryl phosphines, looking down the M-P bond.

Pringle and co-workers also studied the conformational arrangement of a range of *ortho*-methyl and *ortho*-isopropyl substituted monophosphines in monomeric Pt and Pd complexes; *trans*-$[MCl_2(PAr_3)_2]$ (Ar = *o*-Me-C_6H_4, *o*-Me,*p*-OMe-C_6H_3, *o*-^{i}Pr-C_6H_4, *o*-^{i}Pr,*p*-OMe-C_6H_3, and M = Pd or Pt). The crystal structure of *trans*-$[PtCl_2(P\{o\text{-}^i\text{Pr-}C_6H_4\}_3)_2]$ (**i-2**) revealed that the phosphine adopted a ***g*⁻*g*⁻*a*** conformation (Figure 1.7). Using variable temperature NMR studies, the energy barrier to P–C bond rotation was estimated to be 80 (±2) kJ mol^{-1}. In comparison, the less bulky equivalent *trans*-$[PtCl_2(P\{o\text{-Me},p\text{-OMe-}C_6H_3\}_3)_2]$ also adopted the ***g*⁻*g*⁻*a*** conformation in the solid-state but the P–C bond rotation energy was calculated to be only 65 (±2) kJ mol^{-1}. This highlights the greater rotational restriction with bulkier ligands. Four different isomers were observed in solution for *trans*-$[PtCl_2(P\{o\text{-Me},p\text{-OMe-}C_6H_3\}_3)_2]$, assigned as *rac* and *meso* conformations of the two phosphines, and only two in complex **i-2**, attributed to the greater bulk making some of the isomers inaccessible. Further detailed studies using the Cambridge Crystallographic Database revealed that four and six coordinate complexes containing the P(*o*-Me-$C_6H_4)_3$ ligand all have the *gga* conformation, but two/three coordinate complexes adopt the more sterically encumbering *ggg* conformation.[56] Other conformations are not observed, possibly due to steric clash causing the energy of these systems to be too high.

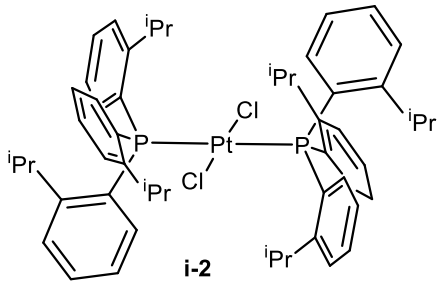

Cone angle: 195°

Pt-P-C_{ipso}-C_{ortho} torsion angles:
-66.0, -65.6 and 177.5

Conformation: ***g*⁻*g*⁻*a***

Figure 1.7. Depiction of the solid-state structure of *trans*-$[PtCl_2(P\{o\text{-}^i\text{Pr-}C_6H_4\}_3)_2]$, showing the g^-g^-a arrangement of the phosphines.

Ortho-aryl substitution in chelating phosphines has also been shown to promote enantioselectivity in catalytic processes. Specifically, *ortho*-methoxy substitution was used in the chiral *R*-*R*-DIPAMP diphosphine in the asymmetric hydrogenation of α-acylaminocinnamic acid with a rhodium precatalyst, [Rh((*R*-*R*-DIPAMP)(COD)]BF_4 (Scheme 1.4). The *S*-amino acid was preferred in all cases, with a higher enantiomeric excess (ee) obtained when the Z precursor was used. It was suggested that the increased bulk, and potentially coordinating ability of the *ortho*-methoxy groups, locked the metal complex in a geometry that favoured the binding of a linear, and flat conformation of the amino acid precursor. This geometry exposes the *re* face of the double bond to the rhodium, which subsequently produces the *S* isomer upon H_2 addition.[58]

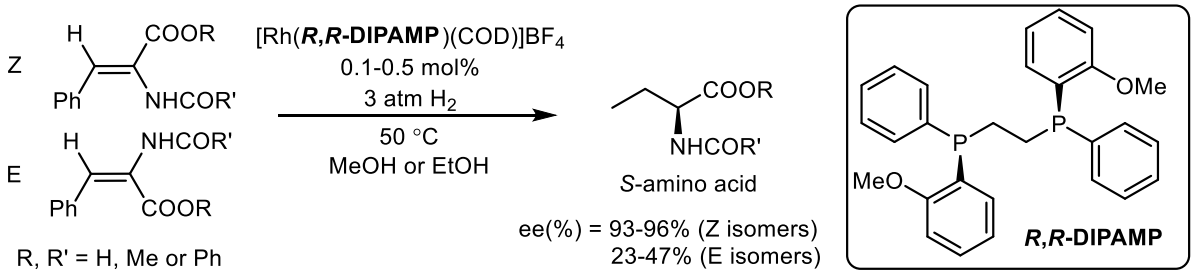

Scheme 1.4. Asymmetric hydrogenation of α-acylaminocinnamic acids with a chiral rhodium catalyst that contains an *ortho*-methoxy substituted diphosphine ligand.

Regioselectivity can also be induced by *ortho*-aryl substitution in a metal bound diphosphine ligand. One example was reported by Weller and Willis on the intermolecular hydroacylation of alkynes (Scheme 1.5). Diphosphine ligands based upon the dppe scaffold, **i-6-R**, with *ortho*- substituents of differing steric bulk, were used with a rhodium precursor to catalyse the formation of branched (**i-4**) and linear (**i-5**) enone products in the hydroacylation between phenylacetylene and a β-S-substituted aldehyde (**i-3**) (Scheme 1.5). It was shown that the least bulky ligand, when R = H, favoured formation of the linear product in a 10:1 ratio, whereas when the bulkier ligands were used (R = Cy or ^{i}Pr), the branched product was formed preferentially. It was postulated that the irreversible and rate limiting reductive elimination of the product was the selectivity inducing step, and the more rotationally restricted bulkier aryl groups had a greater influence on this selectivity.[59]

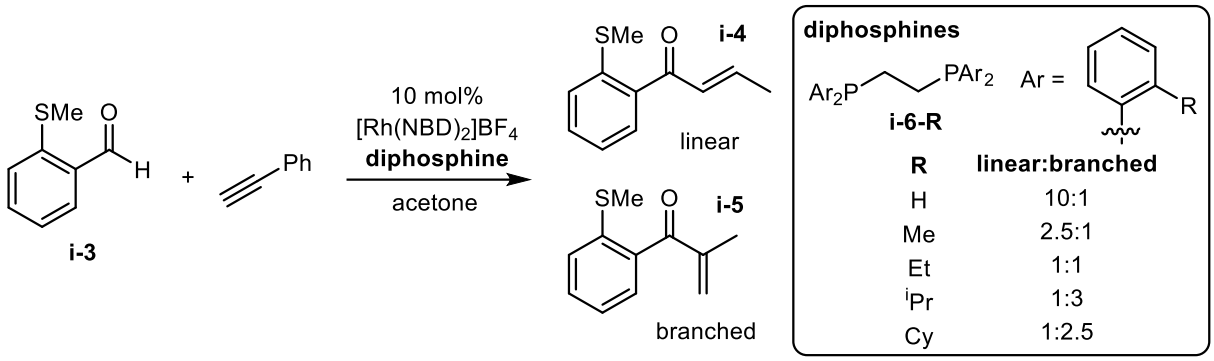

Scheme 1.5. Rhodium-catalysed hydroacylation of phenylacetylene and **i-3** to form branched (**i-4**) and linear (**i-5**) enone products, using *ortho*-substituted dppe ligands (**i-6-R**) of differing steric bulk.

1.5.1 *Ortho*-fluorine substitution

Fluorinated phosphorus substituents have been known since the 1960's, when the synthesis of $P(C_6F_5)_3$, $PPh(C_6F_5)_2$ and $PPh_2(C_6F_5)$ were reported by Peacock and co-workers.[60, 61] It was soon discovered that the presence of fluorine in these ligands affected the ligand lability in $PtCl_2L_2$ complexes. The order of complex stability was: $P(C_6F_5)_3 < PPh(C_6F_5)_2 < P(2\text{-}6\text{-}F_2C_6H_3)_3 < PPh_2(C_6F_5) < PPh_3$.[62] Fluorine atoms have a greater covalent radius than hydrogen (0.57 and 0.31 Å respectively)[63] and therefore $1,2\text{-}F_2C_6H_4$ substituted phosphines have a greater steric profile than those with C_6H_5 groups. Electronically, distinctions are more nuanced, as fluorine atoms are σ-withdrawing but π-donating.[64] The effects of *ortho*-aryl fluorine substitution on the structural characteristics of organometallic complexes with phosphine ligands was investigated by Saunders et al. using $PPh_x(2,6\text{-}F_2C_6H_3)_{3-x}$ (x = 0, 1 or 2) ligands and platinum complexes thereof: *trans*-$[PtCl_2(PEt_3)(PPh_x\{2,6\text{-}F_2C_6H_3\}_{3-x})]$. From the solid-state structures of these complexes, it was shown that the cone angle of *ortho*-aryl fluorinated phosphines was much larger than the *ortho*-H analogues, i.e. PPh_3 and $P(3,4,5\text{-}F_3C_6H_2)_3$ = 145°, $P(2,6\text{-}F_2C_6H_3)_3$ = 176° and $P(C_6F_5)_3$ = 172°. A fluxional process was observed in solution for *trans*-$[PtCl_2(PEt_3)(P\{2,6\text{-}F_2C_6H_3\}_3)]$ (**i-7**), attributed to restricted aryl rotation on the NMR timescale. At low temperature, three ^{19}F signals were observed in the ^{19}F NMR spectrum, due to a fixed orientation of the *ortho*-substituted ligands in a *gaa* arrangement (using Pringle's labelling method[56]) (Figure 1.8). The ^{19}F signals coalesced to one signal as the temperature of the sample was increased to 298 K, illustrating rapid P–C rotation on the NMR timescale. In the solid-state, a *gga* arrangement was observed.[65]

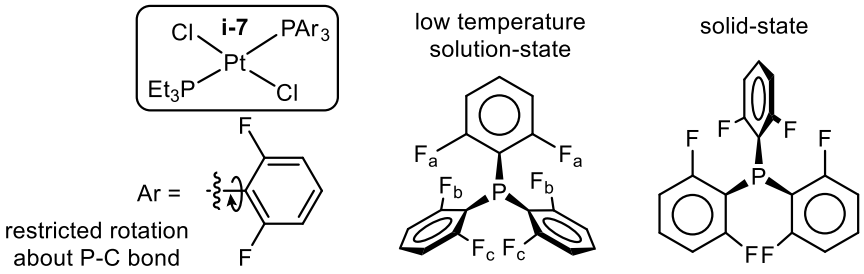

Figure 1.8. The conformational arrangement of the *ortho*-fluorinated phosphine ligand in **i-7** in the low temperature solution state and in the solid-state.

The corresponding *trans*-[MCl(CO)(PPh_x{2,6-$F_2C_6H_3$}$_{3-x}$)$_2$] (M = Rh or Ir) complexes were also synthesised, showing a similar dynamic process of restricted aryl-group rotation. The CO stretching frequency of these complexes was compared with PPh_3 and $P(C_6F_5)_3$ equivalents (Table 1.1). Overall, 2,6-C_6H_3 groups are more electron-donating than C_6F_5, being very similar to Ph in donation ability [ν(CO) for $P(2,6\text{-}F_2C_6H_3)_3$ = 1965 cm^{-1}, and 1961 cm^{-1} for PPh_3]. However, the steric profile of 2,6-$F_2C_6H_3$ was shown to be more similar to C_6F_5 and much larger than Ph.[65] This is shown by the Tolman cone angles of 184°, 176° and 145° for $P(C_6F_5)_3$, $P(2,6\text{-}F_2C_6H_3)_3$ and PPh_3 respectively.[29]

Table 1.1. CO stretching frequencies [ν(CO) / cm^{-1}] within *trans*-[MCl(CO)(phosphine)$_2$].[65]

Phosphine	ν(CO) / cm^{-1} (M = Rh)	ν(CO) / cm^{-1} (M = Ir)
PPh_3	1961	1951
$PPh(2,6\text{-}F_2C_6H_3)_2$	1961	1952
$P(2,6\text{-}F_2C_6H_3)_3$	1965	1952
$PPh_2(2,6\text{-}F_2C_6H_3)$	1967	1953
$PPh_2(C_6F_5)$	1982	-
$P(4\text{-}F\text{-}C_6H_4)$	1984	1960
$PPh(C_6F_5)_2$	2002	
$P(C_6F_5)_3$	2008	1996

The application of *ortho*-aryl fluorine substituted dppe ligand, $Ar_2PCH_2CH_2PAr_2$ (**i-8**) (Ar = 2,6-$F_2C_6H_3$), was reported by Saunders and co-workers. When this ligand was reacted with [{Rh(Cp*)Cl_2}] (Cp* = pentamethylcyclopentadiene), C–F activation occurred at two of the *ortho*-positions, forming C–C bonds with two of the methyl groups on Cp* (Scheme 1.6).[66] This demonstrates the potentially reactive sites at the C–F bonds and the *ortho*-substituents are not always innocent in reactivity.

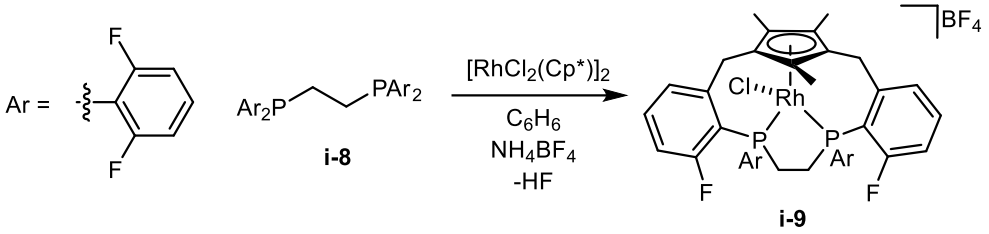

Scheme 1.6. Formation of a C–F activated complex **i-9** by addition of **i-8** to $[RhCl_2(Cp^*)]_2$ (Ar = 2,6-$F_2C_6H_3$).

A series of fluorinated dppe ligands were studied in the reductive elimination of biphenyl from Pt(diphosphine)$(Ph)_2$ complexes (Scheme 1.7) (**i-10-R**). It was shown that the ligands containing *ortho*-fluorine atoms promoted the reductive elimination of biphenyl, and the kinetics were measured over a temperature range to determine $\Delta S^{\ddagger}$ and $\Delta H^{\ddagger}$. It was shown that the *ortho*-F ligands strongly influenced the conformation of the starting Pt(II) complex and this in turn explained the lower $\Delta S^{\ddagger}$ values calculated for the substituents bearing more fluorine atoms (Scheme 1.7), although these values were all small. These differences were predominantly dictated by restricted aryl group rotation influencing the phenyl ligand positioning. Smaller $\Delta H^{\ddagger}$ values were also calculated for the more fluorinated groups, which was attributed to the electron-poor ligands lowering the energy of the transition state prior to reductive elimination.[67] The enthalpic component dominates, leading to an overall faster reaction with the more fluorinated substituents.

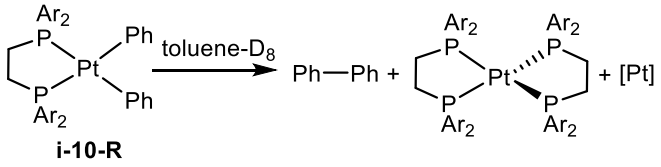

Ar	$\Delta H^{\ddagger}$	$\Delta S^{\ddagger}$	$\Delta G^{\ddagger(100^\circ C)}$
Ph	38	12	34
4-F-C_6H_4	37	12	33
3,5-$F_2C_6H_3$	35	11	32
2,6-$F_2C_6H_3$	32	1	30
C_6F_5	29	1	28

Scheme 1.7. Investigation of the effect of fluorinated dppe ligands in the reductive elimination of biphenyl from Pt(diphosphine)$(Ph)_2$ complexes, **i-10-R**. Activation parameters were determined from the Arrhenius plots from the thermolysis of the [Pt(diphosphine)$(Ph)_2$] complexes. Units of $\Delta H^{\ddagger}$ are kJ mol^{-1} and $\Delta S^{\ddagger}$ are J K^{-1} mol^{-1}.

Ortho-aryl fluorine substitution has also been used in Cr-catalysed ethene oligomerisation to form 1-hexene and 1-octene (with a small proportion of longer hydrocarbons) (Scheme 1.8).[68, 69] The diphosphines explored (**i-11-R**) contained the rigid C=C backbone and were varied via different backbones substituent and *ortho*-fluorine substitution in one of each of the phosphorus aromatics.

Irrespective of whether a fluorine atom was present in either or both aryl groups, a higher productivity of the catalyst was observed (in terms of kg of product/g Cr/h). It was proposed that C–F···H–C interactions stabilised intermediates for the formation of C_6 and C_8 products.[68]

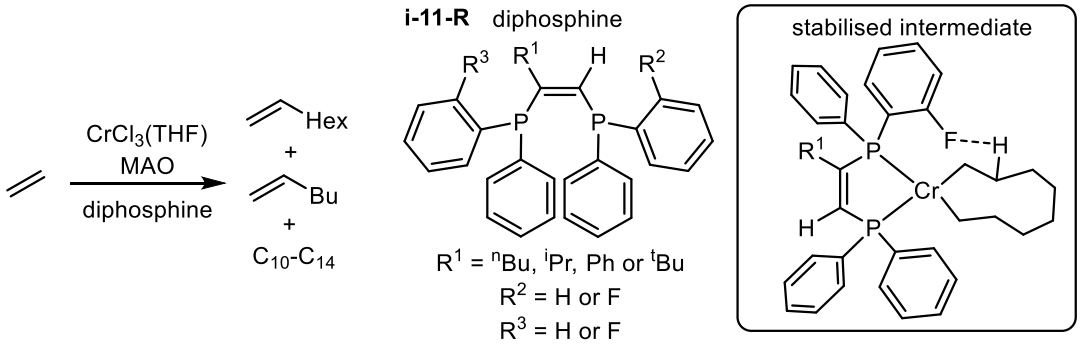

Scheme 1.8. Cr-catalysed ethylene oligomerisation utilising fluorinated diphosphines to promote catalyst productivity. MAO = methylaluminoxane. A proposed stabilised intermediate is also shown.

Evidently, *ortho*-aryl substitution can have a pronounced influence on reactivity. It would be an oversimplification to attribute this purely due to increased steric bulk. Pringle and co-workers revealed the greater restriction in P–C bond rotation for the bulkier ligands,[56] which could in turn, influence the selectivity inducing step,[59] or stabilise low coordinate intermediates.[70] However, the electronic differences upon the introduction of alkyl groups or fluorine atoms in the *ortho*-aryl position must not be discounted,[71] and as has been demonstrated in the last example, potential intramolecular interactions may stabilise catalytic intermediates.[68]

1.6 POP-type ligands

The backbone in traditional κ^2-bidentate diphosphines can be modified by addition of a bridging donor ligand, forming a pincer ligand, once bound κ^3 to a transition metal centre. This can include a coordinated carbon, “PCP”; nitrogen, “PNP”; or oxygen; “POP” (Figure 1.9). Pincer-type ligands have been used in a wide variety of transition metals catalysts,[72] with particular success in Pd-catalysed organic synthesis,[73] and the iridium catalysed dehydrogenation of alkanes.[74] POP-type ligands have been of increasing interest as κ^3 ligands in the past decade.[75] The first example of a ligand coordinating to a transition metal via two phosphorus atoms and a bridging ether was $[P(Ph)_2CH_2CH_2]_2O$ (Figure 1.9), in a Rh(I) complex: $\{Rh(CO)(\kappa^3\text{-}P,O,P\text{-}[P(Ph)_2CH_2CH_2]_2O)\}$.[76]

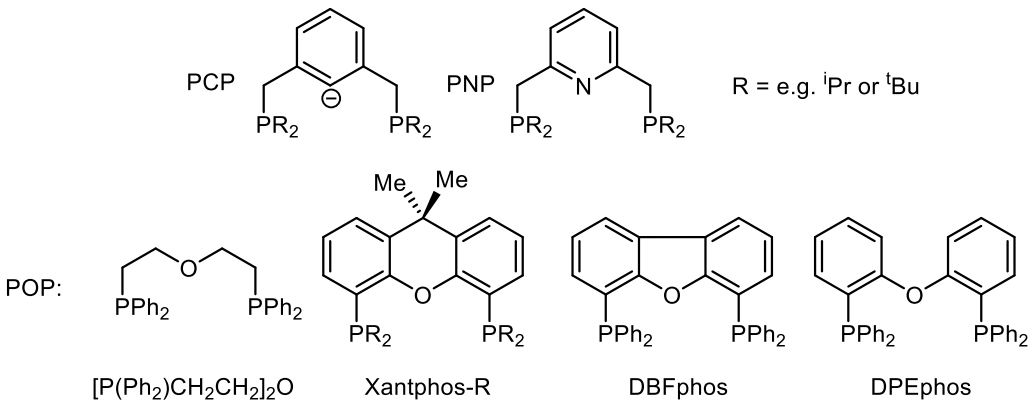

Figure 1.9. Examples of POP-type ligands.

Aryl-bridging POP ligands such as Xantphos-R, DBFphos and DPEphos (Figure 1.9) have since been synthesised and are popular due to their larger natural bite angle in the κ^2 geometry (DPEphos, β = 103° and Xantphos, β = 111°).[38, 75] Xantphos and DPEphos were originally prepared as wide bite angle κ^2 diphosphines for use in rhodium hydroformylation catalysis.[77] However, more recently, interest has grown in POP-type ligands due to their ability to form a κ^3-P,O,P bonding mode, giving rise to a range of coordination geometries with a transition metal.

1.6.1 Hemilability and coordination modes

Depending on the ligand bite angle, metal, oxidation state and other coordinated ligands, different coordination modes are possible with POP-type ligands (Figure 1.10). These include μ^2,κ^1,κ^1-P,P with the phosphorus atoms bridging two metal nuclei, or κ^2-P,P and κ^3-P,O,P arrangements with the chelating phosphorus atoms bound either *cis* or *trans* to one another. One of the defining characteristics of the chelating arrangements is the P–M–P bond angle, which is typically 130-180° for *trans*-κ^2 and *mer*-κ^3, and 90-130° for *cis*-κ^2 and *fac*-κ^3. The M···O distance defines ether coordination. Distances shorter than 2.4 Å suggests either a *fac*-κ^3 or *mer*-κ^3 geometry whereas longer than 2.5 Å is indicative of the κ^2 geometries, *trans*-κ^2 or *cis*-κ^2.[75] The oxygen linker can reversibly coordinate, i.e. hemilability, which facilitates the transition between these geometries.[75] Hemilability is a process which leaves the metal centre operationally unsaturated upon ligand decoordination, but the donor ligand (i.e. the ether linkage) is still within the coordination sphere due to constraints imposed by binding of other parts of the ligand (i.e. the phosphines).[78] Coordination flexibility allows for a ligand that is responsive to metal oxidation

state, coordination geometry and the binding and elimination of substrates and products, essential for many catalytic processes.[79, 80] Specific examples of the implication of hemilability in the DPEphos ligand are discussed in the next section.

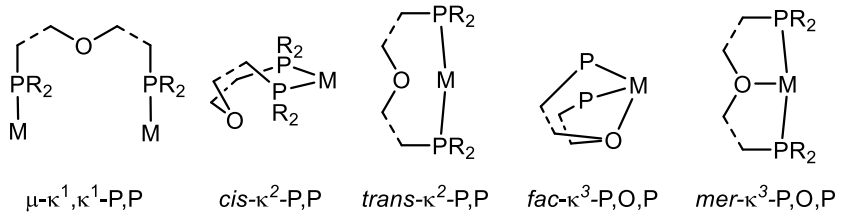

Figure 1.10. Different coordination modes of POP-type ligands with transition metals. M = transition metal.

1.7 DPEphos

First synthesised for use as a κ²-P,P wide bite angle diphosphine ligand in hydroformylation catalysis in 1995 by van Leeuwen,[77] DPEphos has since received significant attention in homogeneous transition metal catalysis (649 hits in Reaxys on 26/05/22). This is attributed to the wide bite angle of 103° in the *cis*-κ² geometry but also the hemilability of the oxygen atom facilitating the transition between a range of coordination geometries.[75] In a review by Weller and Adams, the coordination geometry of chelating DPEphos in 290 transition metal complexes were collated. It was shown that 93% of all DPEphos containing complexes existed in the *cis*-κ²-P,P conformation, with the rest in *fac*-κ³-P,O,P or *mer*-κ³-P,O,P (Figure 1.11).[75, 81]

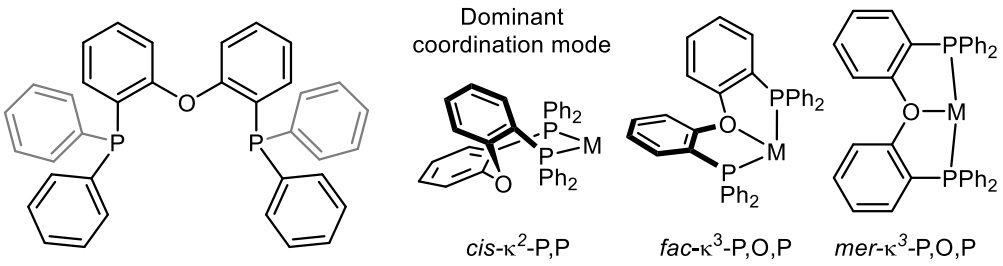

Figure 1.11. DPEphos ligand and the coordination modes adopted in transition metal complexes.

1.7.1 Metal-DPEphos complexes in catalysis

The conformational flexibility of DPEphos was exploited by van Leeuwen et al. in [Pd(DPEphos)] catalysed methanolysis (Scheme 1.9). The initial Pd(II) complex **i-12** exhibited a *mer*-κ^3-P,O,P arrangement of the DPEphos ligand. Addition of methanol resulted in the Pd–O bond breaking, and a *cis*-κ^2-P,P geometry was adopted, allowing a molecule of MeOH to bind (**i-13**). This step was shown to be rate limiting, and therefore DPEphos rearrangement was crucial to the reaction rate. The activation energy (ΔG‡) for this step was shown to be +83 kJ mol^{-1}, which is 9 kJ mol^{-1} lower than the Xantphos equivalent, highlighting the benefits of the greater flexibility in DPEphos. Reductive elimination of methyl propanoate under a CO atmosphere irreversibly afforded a palladium dimer (**i-15**).[82]

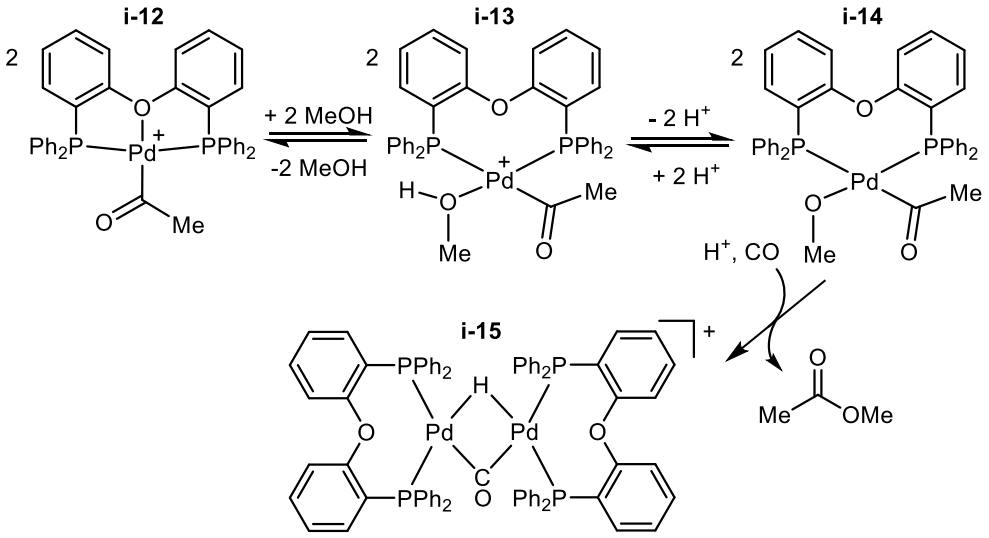

Scheme 1.9. Proposed mechanism of methanolysis catalysed by [Pd(DPEphos)]. OTf$^-$ anion omitted for clarity (OTf = SO_3CF_3).

There is an abundance of metal-DPEphos complexes used as catalysts for important synthetic reactions, such as: ruthenium catalysed regioselective alkylation of indoles (Scheme 1.10A),[83] palladium catalysed cross-coupling of difluoromethyl and aryl boronic acids (Scheme 1.10B)[84] and platinum-catalysed amination of allylic alcohols (Scheme 1.10C).[85] In the latter example, it was shown that the electron donating ability of the oxygen linker in DPEphos increased the product yield, not solely the wide bite angle, shown by a comparison with diphosphines with similar bite angles but no bridging oxygen giving poorer conversion.

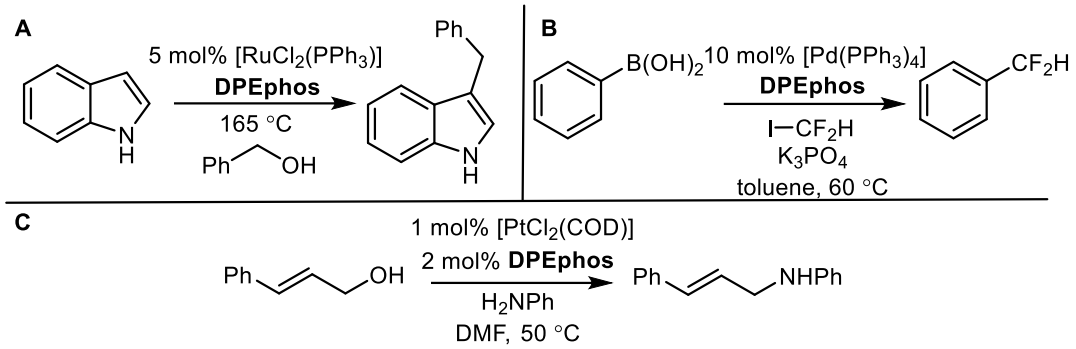

Scheme 1.10. **A**) Ru-DPEphos catalysed benzylation of indole. **B**) Pd-DPEphos catalysed fluoromethylation of aryl boronic acids. **C**) Pt-DPEphos catalysed amination of allylic alcohols.

1.7.1.1 Schrock-Osborn precatalysts

The combination of rhodium 2-electron catalytic processes and DPEphos hemilability are combined in the popular $[Rh(DPEphos)]^+$ system. A common precursor, [Rh(DPEphos)(diene)][anion], is based upon the original Schrock-Osborn precatalyst, i.e. $[Rh(phosphine)_x(diene)][anion]$ (Figure 1.12).[86, 87] Within this class of precatalyst, two η^2-C=C alkene moieties bind to the rhodium centre, these can be chelating dienes: such as 1,5-cyclooctadiene (COD) or norbornadiene (NBD), as well as monoenes, such as cyclooctene, or ethene. A plethora of mono- and diphosphines are tolerated,[88] which makes this complex type so popular.[89] The anions are weakly-coordinating, and examples include: $[PF_6]^-$,[86] $[BF_4]^-$,[90] $[BAr^F_4]^-$,[88] carboranes, such as: $[CB_{11}H_{12}]^-$,[91] or even more recently $[B(3,5\text{-}(SF_5)_2\text{-}C_6H_3)_4]^-$ (Ar^F = 3,5-CF_3-C_6H_3).[92]

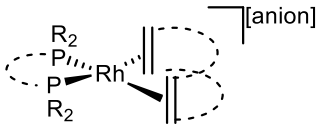

Figure 1.12. General structure of Schrock-Osborn type precatalysts. A range of mono- and diphosphines, dienes and non-coordinating anions are applicable.

1.7.1.2 Rh-DPEphos complexes and catalysis

The $[Rh(DPEphos)(diene)]^+$ system can be used directly as a drop-in precatalyst or it can be made in-situ with $[RhCl(diene)]_2$ / anion salt / DPEphos, or $[Rh(diene)_2][anion]$ and DPEphos added into the catalytic mixture.[93] An example of the former is the application of $[Rh(DPEphos)(COD)]BF_4$ as a

precatalyst in the rhodium-catalysed anti-Markovnikov hydroamination of vinylarenes (Scheme 1.11A).[90] In-situ formation of [Rh(DPEphos)] was used in the diastereoselective cycloaddition of allenyl-sulfonylcarbamates (Scheme 1.11B).[94]

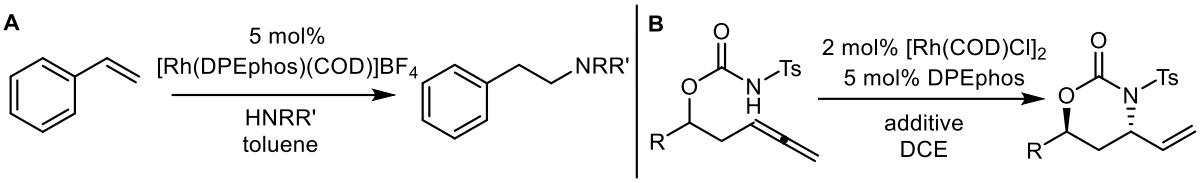

Scheme 1.11. **A**) Hydroamination of vinylarenes with a [Rh(DPEphos)(COD)]$^+$ precatalyst. **B**) Diastereoselective cycloaddition of allenyl-sulfonylcarbamates with an in-situ formed [Rh(DPEphos)] catalyst.

Schrock and Osborn reported that pre-activating the [Rh(L_2)(diene)][X] complex via hydrogenation of the diene moiety in a coordinating solvent, such as acetone or methanol, produces a more reactive precatalyst.[86, 87] [Rh(DPEphos)(NBD)][BAr^F_4] (**i-16**) has been exposed to an atmosphere of H_2 in a range of coordinating solvents, including *o*-xylene, acetone and C_6H_5F. This resulted in the hydrogenation of NBD to norbornane and subsequent coordination of local solvent molecule(s) to form [Rh(κ^2-P,P-DPEphos)(η^6-*o*-xylene)][BAr^F_4] (**i-17**),[95] [Rh(κ^2-P,P-DPEphos)(η^1-O-acetone)$_2$][BAr^F_4] (**i-18**)[91, 96] and [Rh(κ^2-P,P-DPEphos)(η^6-C_6H_5F)][BAr^F_4] (**i-19**)[97] respectively (Scheme 1.12). NMR spectroscopy is a good tool for detecting a solvated complex due to the large *J*(RhP) values observed (~200 Hz for this system) in the $^{31}P\{^1H\}$ NMR spectrum, which are indicative of weakly binding solvent ligands, compared to a chelating NBD ligand (~ 160 Hz).[91] The solvent molecules are more easily displaced than the NBD fragment, allowing for substrate binding and further reactivity.[95]

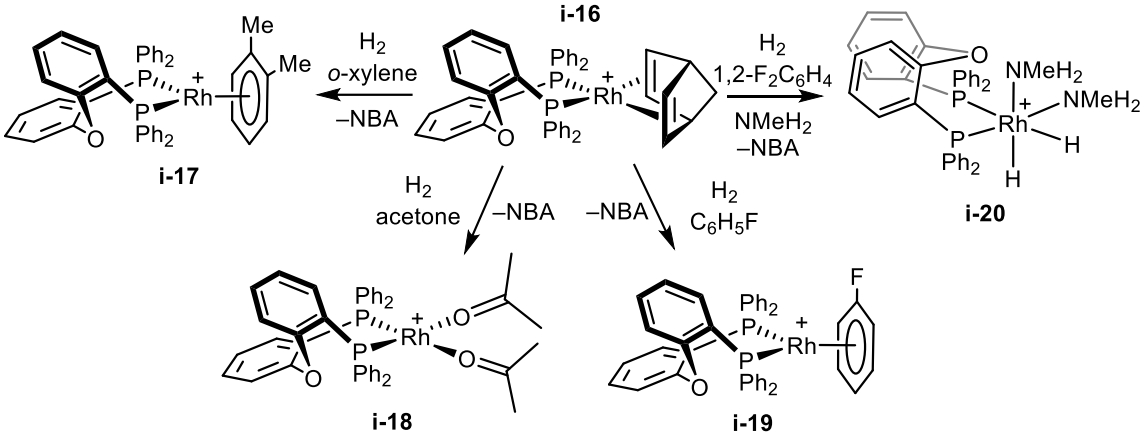

Scheme 1.12. Resultant solvated complexes after the hydrogenation of [Rh(DPEphos)(NBD)][BAr^F_4] in various coordinating solvents and the formation of [Rh(DPEphos)($NMeH_2$)$_2$(H_2)][BAr^F_4] upon hydrogenation in the presence of $NMeH_2$. [BAr^F_4]$^-$ anions are omitted for clarity.

These more active precatalysts have been employed in a range of catalytic reactions. Firstly, **i-18** was used in the intermolecular alkyne hydroacylation of β-carbonyl substituted aldehydes to form the linear (**i-22**) and branched (**i-23**) enone products as well as a small proportion (10%) of the cyclotrimerized product (**i-24**, Scheme 1.13). A detailed mechanistic investigation was conducted on this system – revealing the delicate balance of substrate concentrations with product selectivity, resulting in low catalyst loadings (0.1 mol%) giving the best selectivity for enone products (99%) and linear to branched ratios of up to 15:1 with no excess of either reagent.[98]

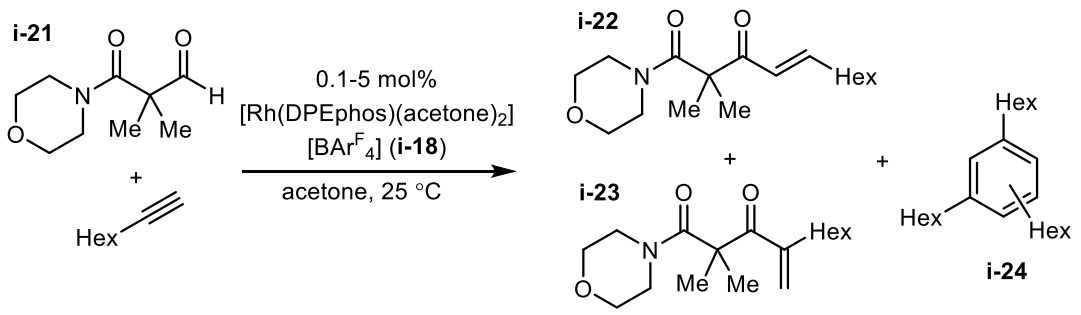

Scheme 1.13. [Rh(DPEphos)]$^+$ catalysed intermolecular alkyne hydroacylation of β-carbonyl substituted aldehydes.

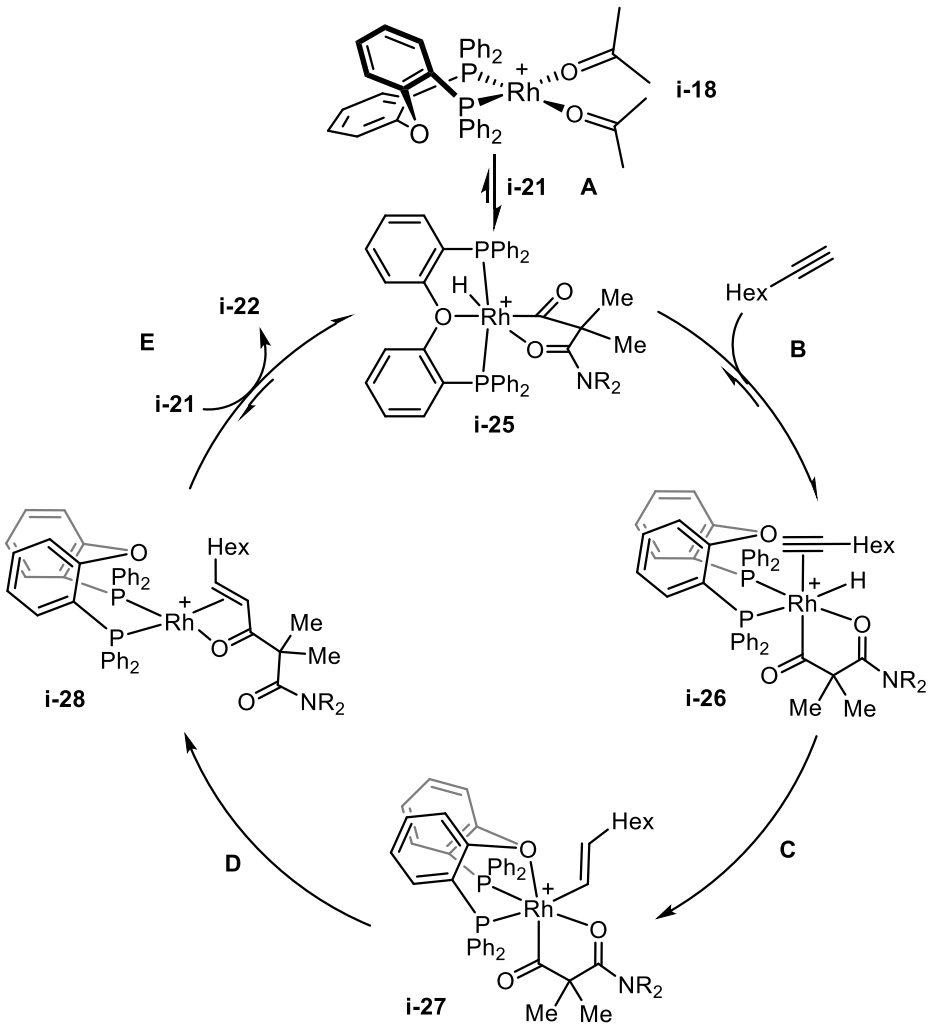

Scheme 1.14. Proposed mechanism of [Rh(DPEphos)]$^{+}$ catalysed hydroacylation of **i-21** and phenylacetylene. [BAr^{F}_{4}]$^{-}$ anions omitted for clarity.

The mechanism of this hydroacylation reaction exploits the flexibility and hemilability of the DPEphos ligand and highlights a few key catalytic steps (Scheme 1.14). Firstly, the κ^2-P,P arrangement in the starting precatalyst, **i-18**, transforms to a *mer*-κ^3-P,O,P geometry to stabilise the oxidative addition of the aldehyde (**A**) forming a Rh(III) centre (**i-25**). The oxygen linker then decoordinates to allow 1-octyne to bind (**B**), reforming the κ^2-P,P bonding geometry in **i-26**. Hydride insertion into the alkyne (**C**), forming an alkenyl ligand is followed by oxygen coordination and the formation of *fac*-κ^3-P,O,P, **i-27**. Reductive elimination of the product then follows (**D**), forming product bound Rh(I) κ^2-P,P complex **i-28**, until another aldehyde molecule oxidatively adds and the product is released (**E**).[98]

[Rh(κ^2-P,P-DPEphos)(η^6-*o*-xylene)][BAr^{F}_{4}] (**i-17**) was also shown to be an effective precatalyst for the hydroacylation reaction.[98] Initially, however, the complex was synthesised as a precatalyst for

carbothiolation of aryl methyl sulfides (Scheme 1.15).[95] A range of different alkyl and aryl groups gave product of high yield. It was shown that the rate of reaction was far quicker when the pre-activated complex **i-17** was used instead of [Rh(DPEphos)(NBD)][BAr^F_4] (**i-16**). When 1-SMe-2-C(O)Me-C_6H_4 **i-29** and phenylacetylene were used as the substrates in *o*-xylene at 130 °C, **i-16** yielded 90% isolated product after one hour, compared to 98% after 0.25 hours when **i-17** was used. The transition between *cis*-κ^2-P,P and *mer*-κ^3-P,O,P bonding modes was shown to facilitate catalysis.[95]

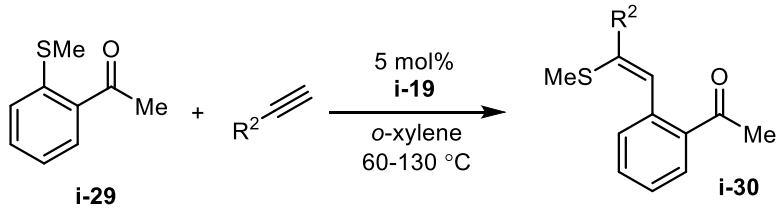

Scheme 1.15. [Rh(DPEphos)]$^+$ catalysed carbothiolation of aryl methyl sulfides. R^1 and R^2 = alkyl and aryl groups.

Other coordinating molecules can be added before hydrogenation of the diene, which then preferentially coordinate to the rhodium centre over the solvent. Examples of complexes formed include σ-amine-borane complexes[97] (see section 1.8) and amine bound species (Scheme 1.12).[81] For example, the Rh(III) complex [Rh(H)$_2$(NMeH$_2$)$_2$(DPEphos)][BAr^F_4] (**i-20**) was prepared by hydrogenation of **i-17** in the poorly-coordinating solvent[99] 1,2-$F_2C_6H_4$ in the presence of $NMeH_2$. This complex was then used to study the mechanism of methylamine-borane dehydropolymerisation to form poly(methylaminoborane). Unlike other related precatalysts, there was no observable induction period, with a simple 1st order kinetic profile observed. Variation of the catalyst loading, $H_{2(sol)}$ concentration and addition of $NMeH_2$ gave control of the polymer molecular weight.[97]

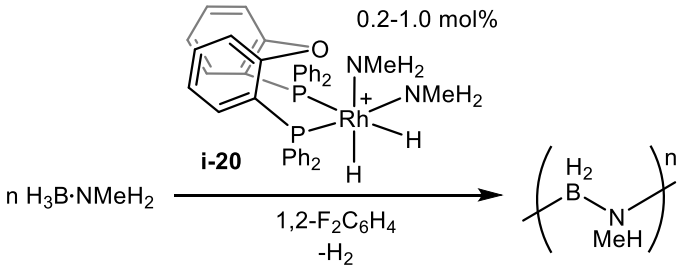

Scheme 1.16. [Rh(DPEphos)]$^+$ catalysed methylamine-borane dehydropolymerisation, starting from a cationic precursor. [BAr^F_4]$^-$ anion omitted for clarity.

Further investigations revealed that the catalyst resting-state was in fact a neutral complex. Addition of $H_3B{\cdot}NMeH_2$ to $[Rh(NMeH_2)_2(DPEphos)][BAr^F{}_4]$ (**i-31**), which could be formed upon degassing of $[Rh(H)_2(NMeH_2)_2(DPEphos)][BAr^F{}_4]$ (**i-20**), gave the same neutral dimeric-tetrahydride product $[Rh_2(\mu\text{-}H)_3(H)(DPEphos)_2]$ (**i-32**) as starting from the neutral precatalyst $[Rh(\eta^3\text{-}H_2CPh)(DPEphos)]$ (**i-33**) (Scheme 1.17). It was proposed that fast and reversible dissociation of the dimer to a monomeric hydride gets the catalyst onto the catalytic cycle. This allowed development of multigram-scale poly(aminoborane) synthesis, a key development in this field.

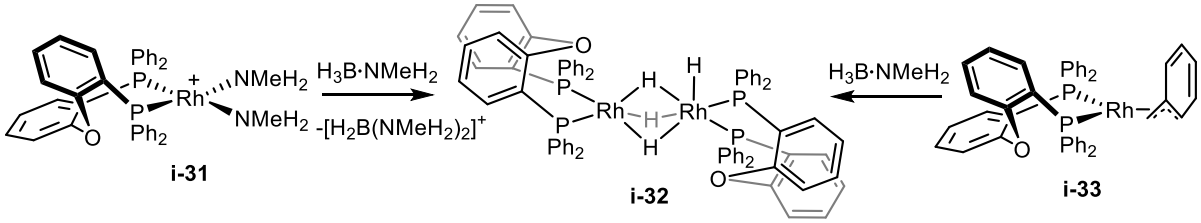

Scheme 1.17. Formation of neutral $[Rh(H)_2(DPEphos)]_2$ from either cationic or neutral precursors. $[BAr^F{}_4]^-$ anion omitted for clarity.

1.7.1.3 Au-DPEphos complexes

The DPEphos ligand has also been used as a bridging κ^1 ligand in bimetallic gold complexes.[100, 101] $[Au_2Br_2(\mu^1\text{-}\kappa^1,\kappa^1\text{-}P,P\text{-}DPEphos)]$ (**i-33-Br**) was synthesised by Gray and co-workers, who reported a linear P–Au–Br geometry.[100] **i-33-Br** was shown to contain a close Au···Au contact [2.976(1) Å] assigned as an aurophilic interaction.[102] Similar aurophilic interactions were observed in $[Au_2Br_2(\mu^1\text{-}\kappa^1,\kappa^1\text{-}P,P\text{-}Xantphos)]$ [2.9233(6) Å] but not in $[Au_2Br_2(\mu^1\text{-}\kappa^1,\kappa^1\text{-}P,P\text{-}DPFphos)]$ [> 7.2 Å] (Figure 1.13).[100] This is an example of how ligand design can be used to control organometallic structural properties.

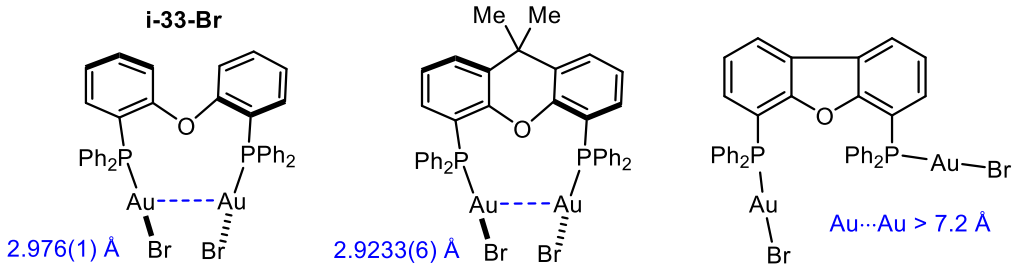

Figure 1.13. Depictions of the solid-state structures of $[Au_2Br_2(\mu^1\text{-}\kappa^1,\kappa^1\text{-}P,P\text{-}diphosphine)]$, diphosphine = DPEphos, Xantphos or DBFphos.

The chloride analogue, $[Au_2Cl_2(\mu^1\text{-}\kappa^1,\kappa^1\text{-P,P-DPEphos})]$ (**i-33-Cl**), has been employed catalytically in the heterocyclisation of 1-(ethynylphenyl)urea (Scheme 1.18). This complex exploits the σ and π activating properties of bimetallic Au(I) complexes, i.e. one Au(I) coordinated to the π-bonds in the alkyne.[101]

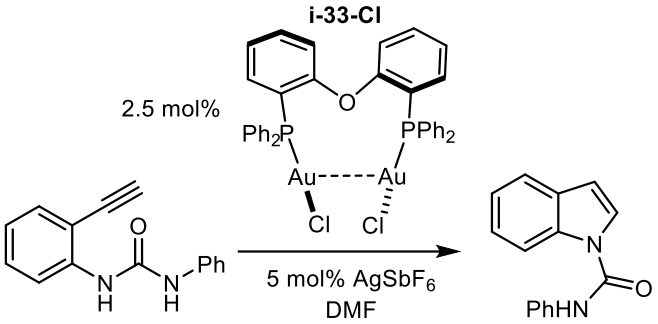

Scheme 1.18. Heterocylisation of 1-(ethynylphenyl)urea with $[Au_2Cl_2(\mu^1\text{-}\kappa^1,\kappa^1\text{-P,P-DPEphos})]$.

1.7.2 *Ortho*-substituted DPEphos

Ortho-aryl substitution (discussed in section 1.5) at the phosphorus substituents has also been studied with the parent DPEphos ligand, albeit with only a handful of examples and limited to *ortho*-methyl and *ortho*-methoxy substituted ligands (Figure 1.14).[103-106]

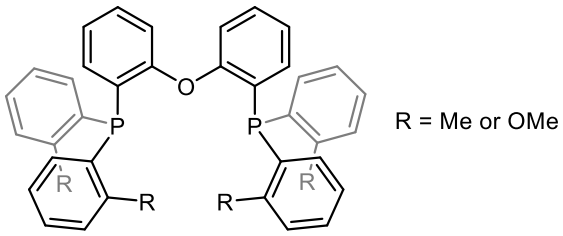

Figure 1.14. *Ortho*-substituted DPEphos ligands: *o*-Me-DPEphos and *o*-OMe-DPEphos.

The first example of this ligand design was reported by Hartwig and Hamann. They reported that using the bulkier, *o*-Me-DPEphos variant in a palladium catalyst system gave higher yields of monoarylated amine and a faster rate of reaction in the Buchwald-Hartwig amination of aryl halides (Scheme 1.19).[106]

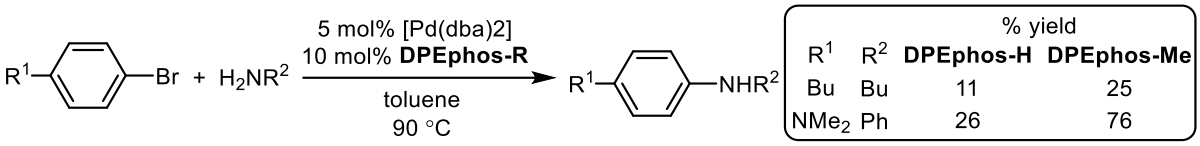

		% yield	
R^1	R^2	**DPEphos-H**	**DPEphos-Me**
Bu	Bu	11	25
NMe_2	Ph	26	76

Scheme 1.19. Aryl halide amination catalysed by palladium catalysts of DPEphos and *ortho*-methyl DPEphos.

o-Me-DPEphos was used by van Leeuwen and co-workers in the hydroformylation of 1-octene (Scheme 1.20). They showed that the *ortho*-methyl version gave better conversion of the alkene but poorer selectivity for aldehyde formation due to alkene isomerisation. The linear to branched selectivity was also less with the methyl variant compared with standard DPEphos.[105]

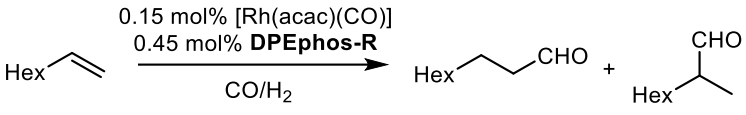

	% conv.	aldehyde selectivity	l/b ratio
DPEphos-H	67	100	6.7
DPEphos-Me	99	42	1.4

Scheme 1.20. Rh-DPEphos-R catalysed hydroformylation of 1-octene.

o-OMe-DPEphos has been used in Pd-catalysed C3 benzylation of indoles (Scheme 1.21A),[104] in which the DPEPhos catalyst yielded 82% of the desired product, whereas the modified ligand only achieved 49%. The same ligand was used in the synthesis of biaryls using polyfluoro magnesium species (Scheme 1.21B). Once again, the parent DPEphos returned a higher product yield (53% compared to 35%) but the selectivity for monosubstitution was much higher in the *ortho*-methoxy substituted ligand (17:1 and 45:1 respectively).[103]

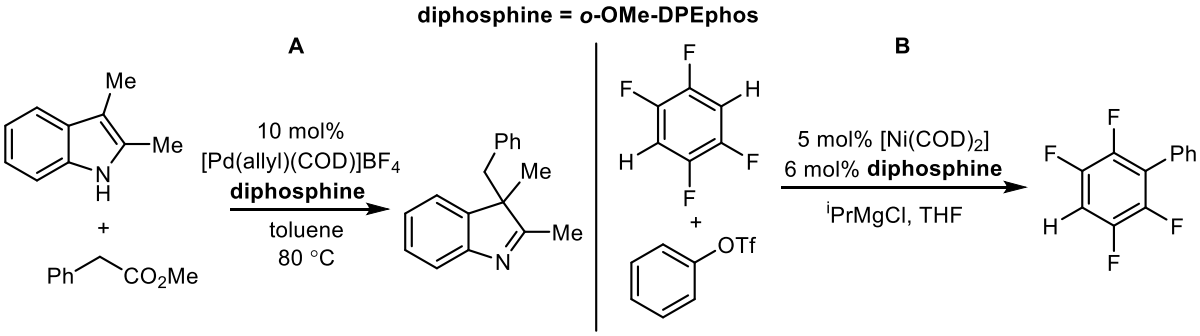

Scheme 1.21. Application of *o*-OMe-DPEphos in: **A**) Pd-catalysed C3 benzylation of indoles and **B**) Polyfluorobiaryl synthesis using Ni catalysts.

There is scope for a wider exploration of *ortho*-aryl substituted DPEphos ligands, including ortho-isopropyl and ortho-fluorine substitution, which have proved to beneficially influence catalysis by other metal-diphosphine complexes (vide-infra).[45, 46, 59]

1.8 Sigma and agostic complexes

Sigma complexes are described as organometallics that contain non-classical, 3-centre-2-electron bonds, in which two electrons are donated from a σ(E–H) bond (E = H, B, C, P, Si or Sn) into vacant metal orbitals. This interaction is augmented by back donation into the σ*(E–H), although this is normally only a minor component. Characteristic changes upon sigma coordination of the E–H bond include elongation of the E–H bond and a concurrent reduction in the *J*(EH) coupling constant.[20] Sigma-bonds are often considered to precede E–H oxidative cleavage, a key bond breaking step in alkane activation (E = C)[18] and the dehydrocoupling of amine-[107] and phosphine-boranes.[108] There are now many reported sigma complexes, despite their inherent instability,[109] including H_2,[110] silanes,[111] alkanes,[112] amine-boranes[113] and phosphine-boranes[114, 115] (Figure 1.15). E–H sigma bound ligands can bind either through solely the hydrogen atom, in a η^1 fashion, characterised by a wider M–H–E angle and a longer M···E distance, or via a η^2 bonding mode, that adopts a tighter M–H–E bond angle and a shorter M···E distance. Sigma-borane complexes often coordinate via two B–H bonds, i.e. $\eta^2\eta^2$, defined by two close M···H and one M···B contacts.[116] Agostic ligands also contain the same M–H–E 3c-2e bond but differ in the fact that they contain a secondary coordination site, so the M–H–E bond creates a chelating, and stabilising, motif (Figure 1.15).

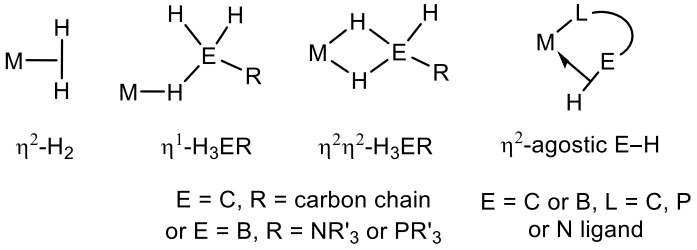

Figure 1.15. Sigma and agostic complexes.

1.8.1 Phosphine-borane sigma complexes

P–B bonds are valence isoelectronic with C–C bonds. Therefore, η^1 and η^2 sigma M···H–BH_2PR_3 interactions are a useful model for C–H coordination prior to oxidative cleavage, a synthetically important step for alkane activation.[108, 117] Moreover, sigma η^1-(BH) and $\eta^2\eta^2$-(BH_2) phosphine-borane complexes have been shown as key intermediates in metal-catalysed phosphine-borane dehydrocoupling and dehydropolymerisation (see section 1.10).[108, 115] The most commonly reported complexes are of tertiary phosphine-boranes ($H_3B{\cdot}PR_3$, R = Me or Ph). The first reported phosphine-borane sigma complexes were reported by Shimoi and co-workers. They synthesised [$M(CO)_5$(η^1-$H_3B{\cdot}PR_3$)] (M = Cr or W, R = Me and Ph) complexes (**i-34**) via the photolysis of [$M(CO)_6$] in the presence of $H_3B{\cdot}PR_3$ (Figure 1.16).[114] In the ^{1}H NMR spectra, broad resonances were assigned as bridging and terminal BH_3 hydrogens, rapidly exchanging on the NMR timescale with a calculated energy barrier of only 30 kJ mol^{-1}. A computational study on these systems showed the lowest energy bonding mode is η^1-(BH), but exchange occurred via an $\eta^2\eta^2$-(BH_2) intermediate. The bonding contribution was found to come from the σ(B–H) with minimal π back-donation due to the high energy σ*(B–H).[118] This is one reason for end-on coordination rather than side-on, in contrast to that observed in sigma complexes of H_2. Increased steric bulk also encourages end-on coordination.

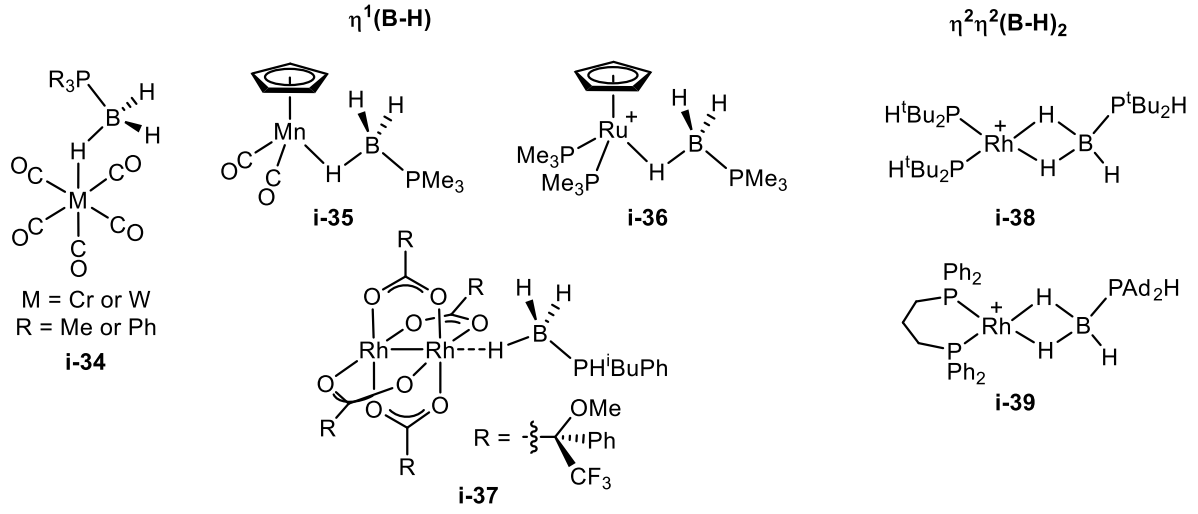

Figure 1.16. Examples of η^1-(BH) and η^2-(BH_2) coordinated phosphine-borane complexes. [$BAr^F{}_4$]$^-$ anions omitted for clarity.

Other examples of η^1-(BH) bonding modes include: $[CpMn(CO)_2(\eta^1\text{-}H_3B{\cdot}PMe_3)]$ (**i-35**),[119] and $[CpRu(PMe_3)_2(\eta^1\text{-}H_3B{\cdot}PMe_3)][BAr^F{}_4]$ (**i-36**).[120] Secondary phosphine-boranes ($H_3B{\cdot}PHR_2$) have also been shown to coordinate via η^1-(BH) in $[Ru(Xantphos)(PPh_3)(\eta^1\text{-}H_3B{\cdot}PHPh_2)H][BAr^F{}_4]$,[121] and a Rh(II) paddlewheel complex (**i-37**) to help determine phosphine-borane chirality via NMR analysis.[122] The $\eta^2\eta^2$-(BH_2) bonding mode in secondary phosphine-borane sigma complexes has been highlighted as a key bonding mode in the mechanism of secondary phosphine-borane dehydrocoupling, which can be used as a model for primary phosphine-borane dehydropolymerisation.[115, 123] The solid-state structure of $[Rh(PH^tBu_2)_2(\eta^2\eta^2\text{-}H_3B{\cdot}PH^tBu_2)][BAr^F{}_4]$ (**i-38**) shows two close Rh···H contacts [1.87(3) and 1.90(3) Å], as well as a short Rh···B distance of 2.188(3), highlighting the $\eta^2\eta^2$-M-(BH_2) bonding motif.[115] There are no reported examples of primary phosphine-borane sigma complexes. It should be noted that M–H–B sigma bonds are reasonably weak {~ 20 kcal mol^{-1} in calculated $[M(CO)_5(H_3B{\cdot}PH_3)]$ complexes, M = Cr and Mo}.[118] However, a chelating moiety can stabilise this interaction, namely, an agostic B–H complex.[124]

1.8.2 E–H Agostic complexes

1.8.2.1 Phosphine-borane B–H agostic complexes

The borane adduct of dppm [bis(diphenylphosphino)methane], $Ph_2PCH_2PPh_2{\cdot}BH_3$, has been used as a chelate ligand to form five-membered metallocycles in $[Rh(COD)(\eta^2\eta^2\text{-}H_3B{\cdot}dppm)][PF_6]$ (**i-40**),[124] $[Cr(CO)_4(\eta^1\text{-}H_3B{\cdot}dppm)]$ (**i-41**), and $[Cp^*Ru(\eta^2\eta^2\text{-}H_3B{\cdot}dppm)][PF_6]$ (**i-43**) (Figure 1.17).[125]

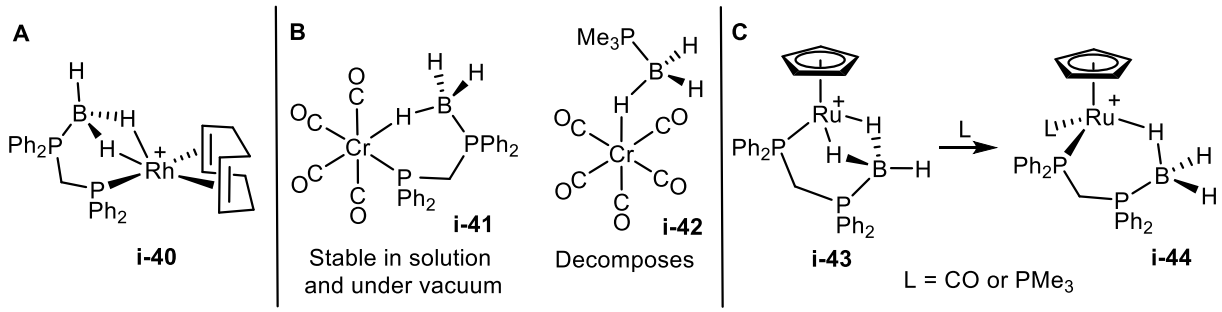

Figure 1.17. Metal complexes of $H_3B{\cdot}dppm$. **A**) $[Rh(COD)(\eta^2\eta^2\text{-}H_3B{\cdot}dppm)]^+$ (**i-40**). **B**) $[Cr(CO)_4(\eta^1\text{-}H_3B{\cdot}dppm)]$ (**i-41**) in comparison with an equivalent non-chelating phosphine-borane sigma complex, **i-42**. **C**) Addition of CO or PMe_3 to $[Cp^*Ru(\eta^2\eta^2\text{-}H_3B{\cdot}dppm)]^+$ (**i-43**) to form $[Cp^*Ru(L)(\eta^1\text{-}H_3B{\cdot}dppm)]^+$ (**i-44**). PF_6^- anions omitted for clarity.

Within this set of complexes both η^1-(BH) and $\eta^2\eta^2$-(BH_2) bonding motifs are observed. The enhanced stability associated with the chelate ring is highlighted in the comparison between $Cr(CO)_4(\eta^1$-$H_3B{\cdot}$dppm) (**i-41**) and the sigma complex $Cr(CO)_5(\eta^1$-$H_3B{\cdot}PMe_3$) (**i-42**); the metallacycle complex was stable in solution and under vacuum, whereas the sigma complex decomposed under both conditions.[125] Only one signal relating to the BH_3 group was observed in the ^{1}H NMR spectrum of **i-41** at δ –2.71 at all temperatures, suggesting a rapid exchange between bridging M···H–B and terminal B–H, on the NMR timescale. In **i-43**, a transition from $\eta^2\eta^2$ to η^1 bonding was forced by addition of CO or PMe_3. This was highlighted by the ^{1}H NMR spectrum that showed two distinct signals for the two bridging (δ –8.0, integral 2H) and one terminal (δ 5.2, integral 1H) B–H signals in **i-43** at room temperature and only one signal for the rapidly rotating BH_3 in $[Cp^*Ru(PMe_3)(\eta^2\eta^2$-$H_3B{\cdot}$dppm)][$PF_6$] (**i-44**) (δ –3.41), which split into three at low temperature, showing arrested fluxionality. In all three of these examples, the B–H agostic proton signals are shifted upfield compared to the BH_3 in free $H_3B{\cdot}$dppm (δ 0.99).

Several other B–H agostic complexes have been observed in-situ during the investigation of rhodium-catalysed phosphine-borane dehydrocoupling. These include chelating phosphine-borane ligands, coordinating via phoshine/phosphido moieties as well as sigma B–H bonds, such as [Rh(H)(dppp)($Ph_2PBH_2PPh_2BH_3$)][BAr^F_4] (Scheme 1.22). This complex was synthesised via the stoichiometric addition of $Ph_2PBH_2PPh_2BH_3$ to [Rh(dppp)(η^6-C_6H_5F)][BAr^F_4] and was shown to be the catalyst resting state in the dehydrocoupling of $H_3B{\cdot}PPh_2H$ (more detail in section 1.10).[126]

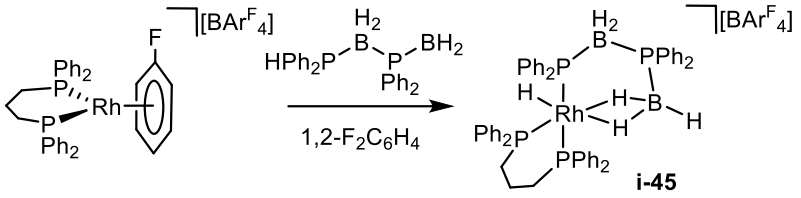

i-45

Scheme 1.22. Formation of [Rh(H)(dppp)($Ph_2PBH_2PPh_2BH_3$)][BAr^F_4], **i-45**.

1.8.2.2 Other examples of metal B–H and C–H agostic complexes

Two further examples highlight the upfield ^{1}H chemical shift observed for the interacting E–H groups in β-agostic complexes: $[Ru(H)_2(PCy_3)_2(HB(N^iPr_2)C_6H_4(o$-$PPh_2)]$ (**i-46**)[127] and [Ni(Et)(d^tbpe)][BF_4] (**i-47**,

Figure 1.18).[128] The ^{1}H NMR spectrum of **i-46** showed a broad signal at δ –6.4, assigned to the agostic B–H signal. At room temperature, the coordinated CH_3 group in **i-47** was shown to rotate on the NMR timescale, once cooled to 173 K, a distinct signal for the agostic C–H was observed at δ –5.8. This was corroborated by the solid-state structures of **i-46** and **i-47** which showed close agostic M···H contacts of 1.79(3) and 1.64(2) Å respectively.[127, 128]

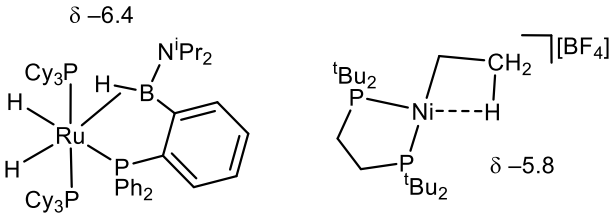

i-46 **i-47**

Figure 1.18. Examples of metal B–H and C–H agostic complexes.

1.8.2.3 Defining and characterising agostic bonding

Agostic complexes are important intermediates prior to E–H bond activation, as well as providing essential stabilising interactions. Therefore, it is important to define and characterise them. In 2009, Brookhart and co-workers defined a M–H–C 3c-2e interaction as an agostic bond,[129] but there are many examples of other bonds being involved in similar interactions, such as C–H, B–H, C–C or Si–C bonds.[130] This thesis focuses on M–H–B 3c-2e bonds, in both fundamental bonding, and catalytic investigations. Structural characterisation of C–H agostic bonds was summarised by Brookhart and co-workers.[129] In this report, they characterise an agostic bond to have a relatively short M···H distance (≈ 1.8-2.3 Å) and a small M–H–C bond angle (≈90-140°) in the solid-state structure (Figure 1.19). Spectroscopically, distinctive traits include a lower ^{1}J(CH) value as well as an upfield shift of the ^{1}H signal compared to the free ligand.[129]

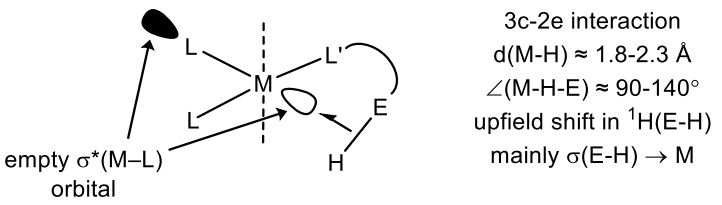

Figure 1.19. Simple depiction and summary of agostic bonds.

The precise electronic character of E–H agostic bonds can be complicated, and can be sensitive to the ligand and the metal d-orbital occupancy. However, commonly, the main electronic contribution is from the σ(E–H) bond into vacant orbitals on the metal. There can also be a small contribution from filled metal orbitals into the σ*(E–H) and typically a non-negligible interaction between the metal and the E atom, hence the non-linear E–H–M coordination geometry.[130, 131]

Upfield shifted signals in the ^{1}H NMR spectrum compared to the free ligand are characteristic of agostic bonds, but there are also reports of close M···H interactions resulting in downfield shifted ^{1}H signals. A different electronic and magnetic environment must therefore be influencing these protons.

1.9 Anagostic Interactions

1.9.1 Definition and characterisation

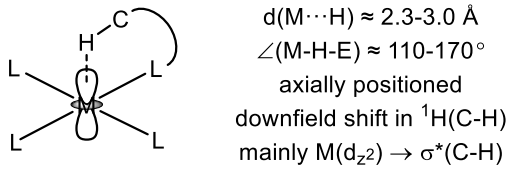

Figure 1.20. Description of an anagostic interaction in d^8-ML_4 complexes.

A somewhat less explored and less reported M···H contact is an anagostic interaction. These interactions have been reported in d^{10} complexes,[132] but by far the most common examples are of square planar d^8 complexes,[129, 133] and this will be the focus within this thesis. The M···H–C interaction arises when a C–H bond is positioned in the apical position of a square planar ML_4 complex, giving rise to distinctly different geometrical, spectroscopic and electronic characteristics to agostic bonds (Figure 1.20). Anagostic interactions are geometrically characterised as having a much wider M–H–C bond angle, defined by Brookhart et al. between 110-170°, and a longer D(M···H) (2.3-2.9 Å).[134] The spectroscopic signature of this interaction is a downfield shift in the ^{1}H NMR signal, in the opposite direction to an agostic bond. There has been much discussion on the electronic character of this interaction.[135-137] The prevailing theory is that the main contribution comes from a filled metal d_{z^2} orbital into the vacant σ*(C–H), with a smaller contribution from σ(C–H) into vacant metal orbitals.[138] However,

the current descriptions of the electronic arrangement are complicated and something this thesis hopes to shed light on.

1.9.2 What causes the chemical shift changes in agostic and anagostic interactions?

An in-depth computational study was conducted by Scherer and co-workers on the ^{1}H chemical shift of agostic and anagostic interactions.[138] Why do the two interactions result in a ^{1}H chemical shift in opposite directions? Scherer computed the $\delta(^{1}H)$ of the protons in M···H-C interactions in a series of [RhCl(CO)(L)] complexes (L = a range of NHCs with differing backbones) (Figure 1.21). Through the use of charge density maps, he deduced that if the proton approaches the metal through a region of topological charge concentration, such as a filled metal orbital, then the proton would experience a downfield chemical shift [i.e. $\Delta\delta(^{1}H)$ is positive for an anagostic proton]. If the proton approaches through a region of charge depletion an upfield shift was observed [$\Delta\delta(^{1}H)$ is negative for an agostic proton] (Figure 1.21).

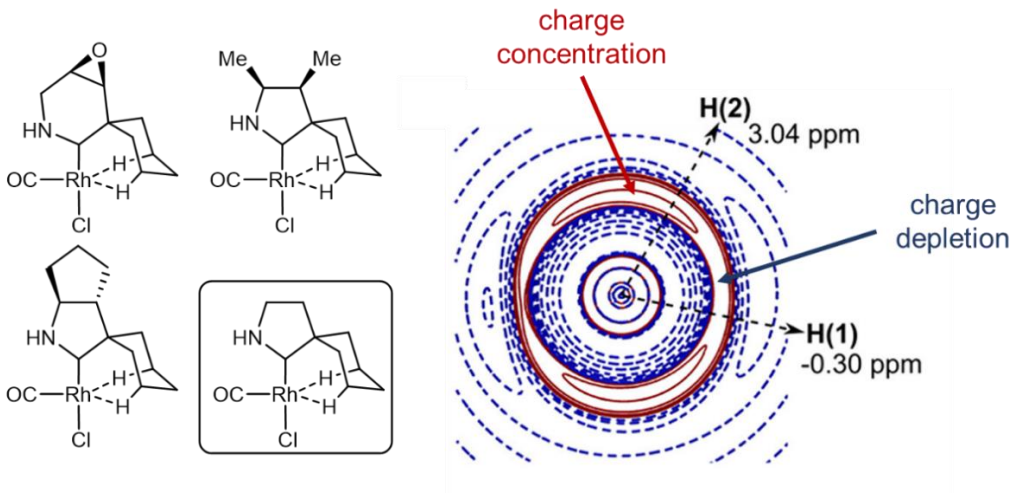

Figure 1.21. Left – some examples of the Rh(I)-NHC complexes analysed by Scherer. Right - a modified figure taken from Scherer's analysis (reference 138), showing the charge density map of the Rh-NHC complex in the box on the left. If the proton approaches through a region of charge concentration (red lines) a downfield shift is observed. If the M···H interaction approaches via a charge depletion zone (blue lines), an upfield shift is observed in the ^{1}H NMR spectrum.

Scherer expanded on this concept by analysing the computed ^{1}H chemical shift in a hypothetical d^{8} $NiMe_2$ complex at varying positionings of the approaching hydrogen to the Ni centre. Two angles were highlighted as influencing the chemical shift change, θ and Φ (Figure 1.22A). If the proton approaches in the axial direction (i.e. an anagostic interaction) $\Delta\delta(^{1}H)$ was positive. $\Delta\delta(^{1}H)$ was negative if the proton

approached from the equatorial direction (i.e. agostic). The reason for this was shown to be due to the induced magnetic current (the blue ring in Figure 1.22B) and the concurrent induced magnetic field (red ring) experienced in the complex when in the large magnetic field from the NMR spectrometer. Protons in the apical position are in regions of induced magnetic field that deshield the proton and therefore are observed shifted downfield. Protons in the equatorial position experience a shielded effect and are consequently observed shifted upfield. Summarised, it is the topological placing of the proton which dictates the change in chemical shift,[138] rather than the differences in M···H–C bonding electronics. Brookhart's definition of C–H anagostic interactions and agostic bonds, presented via the geometric differences in D(M···H) and ∠(M···H–C), perhaps oversimplifies the situation, and subsequently, does not account for the differences in observed ^{1}H chemical shift.[129]

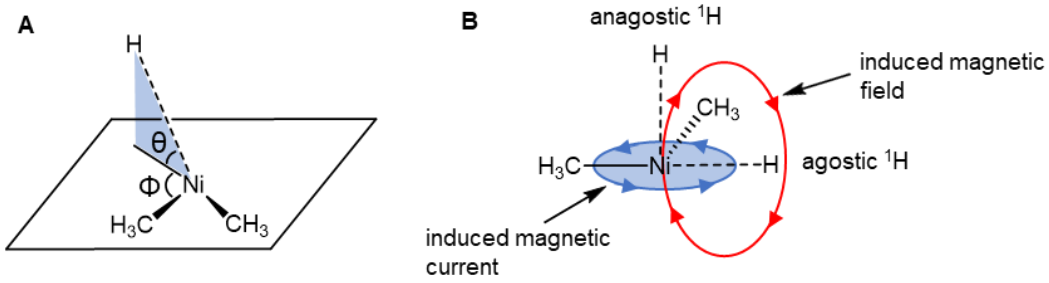

Figure 1.22. Adaptions of Figures in reference 138 showing the topological placing of the protons which dictates the change in chemical shift.

1.9.3 Examples of anagostic interactions

There are a growing number of examples of anagostic interactions in the literature, which are dominated by square planar d^{8} complexes. Bergman and co-workers reported a downfield shifted aryl proton in [RhCl(^{i}Pr$_2$POXy)(PPh$_3$)]$_2$ (Xy = 2,3-xylyl) (**i-48**, Figure 1.23). An aromatic proton was geometrically positioned in the apical position of the rhodium square planar complex and was observed shifted 3.2 ppm downfield compared to the free ligand. The Rh···H distances in the dimer were measured as 2.77 and 2.84 Å and the Rh–H–C angles as 141.3 and 139.3°.[139] A rarer alkyl anagostic interaction was reported by Hor and co-workers in *trans*-[NiX$_2$(N-RBzTh)$_2$] complexes (X = Br or I, BzTh = benzothiazolin-2-ylidene). In the R = isopropyl complex (**i-49**, Figure 1.23) the methine proton in both NHC ligands interact with the Ni centre placed 2.63 Å from the Ni centre, shifting the protons downfield by ≈ 1.5 ppm.[140] Palladium(II) complexes of bidentate cycloimmidate ligand systems (**i-50**) were shown

to contain both aryl and alkyl anagostic interactions by Dyker *et al*., resulting in the downfield shift of both signals by 3.3 and 4.1 ppm respectively, compared to the free ligand.[141]

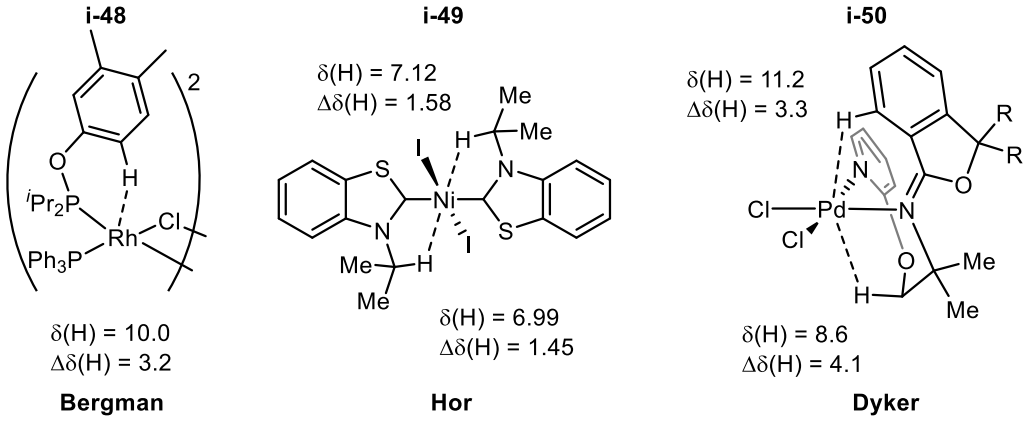

Figure 1.23. Examples of complexes containing anagostic M···H-C anagostic interactions. R = *p*-anisole.

Ortho-aryl substituted ligands have been shown to sterically encourage aromatic protons to lie in the apical position of square planar complexes. Downfield shifted signals were reported in the aforementioned $[PtCl_2(PAr_3)_2]$ complexes (Ar = *o*-Me,*p*-OMe-C_6H_3 and *o*-^{i}Pr-C_6H_4, **i-2-Me** and **i-2-^{i}Pr**) between δ 8.5-9.5. When cooled these signals were observed as doublet of doublets, comprising ^3J(PH) and ^3J(HH) consistent with an *ortho*-protons on the substituted aromatic rings.[56] This was corroborated by the crystal structure of $[PtCl_2(PAr_3)_2]$ (Ar = *o*-^{i}Pr-C_6H_4) (**i-2-^{i}Pr**), in which two crystallographically equivalent *ortho*-hydrogens are located 3.01 Å from the Pt centre (Figure 1.24). Two isomers were observed in the low temperature ^{1}H NMR analysis of **i-2-^{i}Pr**, both exhibiting downfield aromatic signals (δ 9.25 and 8.74). Although not assigned as an anagostic interaction, they have the same spectroscopic and structural characteristics. This highlights the lack of proper assignment of anagostic interactions in the literature.

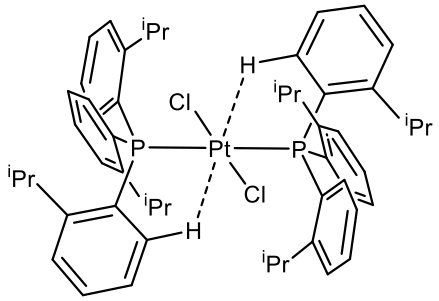

Figure 1.24. Diagram of the solid-state structure of $[PtCl_2(PAr_3)_2]$ (Ar = *o*-^{i}Pr-C_6H_4) (**i-2-^{i}Pr**). The Pt···H interactions were not mentioned in the publication but we suggest they are the cause of the downfield ^{1}H chemical shifts observed at δ 9.25 and 8.74.

Despite numerous experimental examples and Scherer's pioneering analysis, the field is lacking a systematic experimental and computational investigation on anagostic interactions which allows for easy assignment in organometallic complexes.

1.10 Catalytic dehydrocoupling and dehydropolymerisation of phosphine-boranes

1.10.1 Properties and applications of poly(phosphinoboranes)

Main group polymers are of increasing interest due to their distinctly different properties to those made of olefins, i.e. hydrocarbons.[142, 143] Polymers with alternating P-B backbone units are formally valence isoelectronic with polyolefins, but possess different electronic and materials properties to the ubiquitous organic analogue.[108] Transition metal catalysed dehydropolymerisation of primary-phosphine boranes to form poly(phosphinoborane) is one method in which to form such polymers (Scheme 1.23).[144] The polarised P-B bond in poly(phosphinoborane) is > 1.9 Å, compared to a typical non-polar C–C bond of 1.54 Å in polyolefins. This gives rise to application as etch resists in lithography,[145, 146] in flame retardant materials,[147] and as ceramic precursors to boron-phosphide.[148] The remaining P–H bond in the polymer backbone can be exploited for post-polymerisation manipulation. This has been done via thermally induced cross-linking to form gel-like materials,[149] as well as hydrophosphination with alkenes.[150] However, the field of poly(phosphinoboranes) is still in its relative infancy.[151]

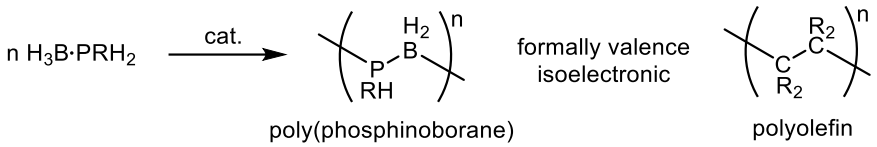

Scheme 1.23. Transition metal catalysed dehydropolymerisation of primary phosphine-boranes.

1.10.2 Discovery and early catalysts

The first attempts to form macromolecular materials containing P-B repeat units come from attempts to dehydropolymerise the secondary phosphine-borane adduct, $H_3B{\cdot}PPh_2H$, using thermal conditions (150-250 °C). This resulted in ill-defined mixtures of trimers, tetramers and low molecular weight polymer.[152, 153] In 1999, Manners and co-workers published the first transition metal catalysed approach to the dehydrocoupling of $H_3B{\cdot}PPh_2H$ and dehydropolymerisation of $H_3B{\cdot}PPhH_2$ (Scheme 1.24). This was the first example of isolated, soluble and fully characterised high molecular weight poly(phosphinoborane), which was obtained as a white, air-stable powder. Analysis by static light scattering revealed the polymer had a weight averaged molecular weight of 31,000 g mol^{-1} (M_w).[144]

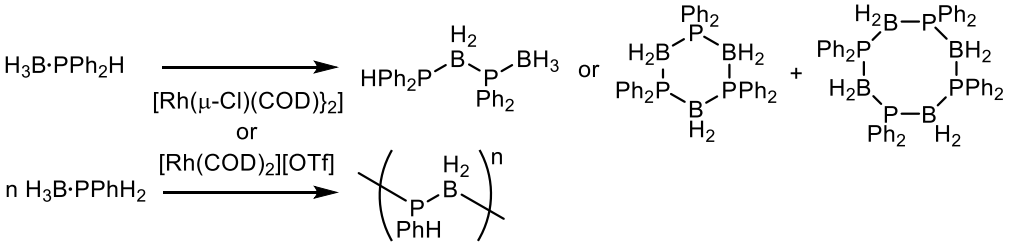

Scheme 1.24. The dehydrocoupling of $H_3B{\cdot}PPh_2H$ and dehydropolymerisation of $H_3B{\cdot}PPhH_2$ using Rh(I) catalysts $[Rh(COD)(\mu\text{-}Cl)]_2$ and $[Rh(COD)_2][OTf]$.

The catalysts used were: $[Rh(\mu\text{-}Cl)(COD)]_2$ and $[Rh(COD)_2][OTf]$, and neat, melt conditions were employed (90-130 °C). Dehydrocoupling of the secondary phosphine-borane at 90 °C yielded linear dimer, and at 120 °C the cyclic trimer and tetramer products were formed (Scheme 1.24).[154] In terms of polymerisation of primary phosphine-boranes, these early catalysts suffered with poor selectivity, forming polymer of very wide dispersity ($M_w/M_n > 5$).[149] Moreover, using neat melt conditions hindered the exploration of mechanistic studies and overall less control of the transition metal catalyst and the resultant poly(phosphinoborane). Primary phosphine-boranes undergo thermally induced

dehydropolymerisation in the absence of a catalyst, however, only low molecular weight polymer and ill-defined oligomeric material are formed.[154]

1.10.3 Different phosphorus substituents in poly(phosphinoboranes)

From 2000-2005 Manners and co-workers reported the dehydropolymerisation of primary phosphine boranes with different substituents on the phosphorus atom, $H_3B{\cdot}PRH_2$, to form poly(R-phosphinoborane) of high molecular weight using the same Rh(I) catalysts (90 °C, neat conditions). These included ^{i}Bu, *p*-^{n}Bu-C_6H_4, *p*-dodecyl-C_6H_4 and *p*-CF_3-C_6H_4 substituents.[146, 149] $H_3B{\cdot}P^{i}BuH_2$ required harsher conditions (120 °C, 15 hours), ascribed to the alkyl group reducing the polarity of the P–H bond and thus activity in P–H activation.[155] Since then, different catalysts have been employed and the range of different substituents has grown to include ferrocenyl substituents,[156] and a wide range of aryl[145] and alkyl groups (Figure 1.25).[157, 158] These different polymers exhibited a diverse range of spectroscopic characteristics, glass transition temperatures, thermal stability (Table 1.2), and surface properties as thin films.[157, 158] The general pattern is that the glass transition temperature increases with bulkier phosphorus R groups. Poly(alkylphosphinoboranes) also lose mass more readily at higher temperatures than poly(arylphosphinoboranes), i.e. a lower ceramic yield.

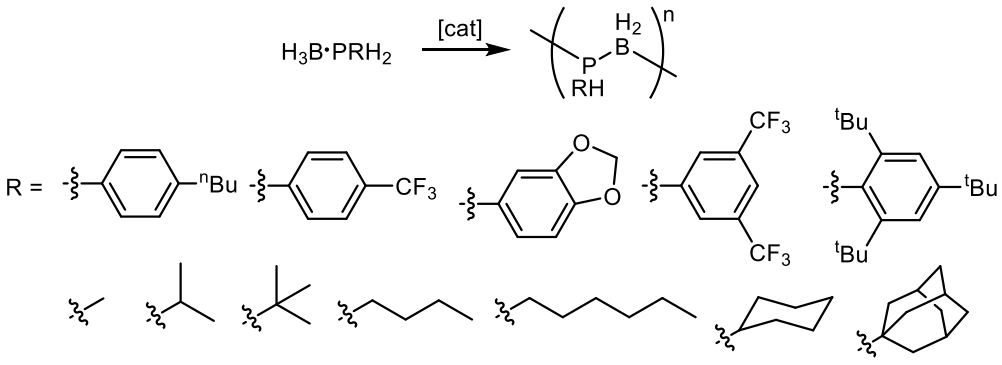

Figure 1.25. A range of the published poly(phosphinoboranes) with differing phosphorus substituents.

Table 1.2. Summary of the thermal properties of some poly(phosphinoboranes).[145, 157]

$[H_2BPRH]_n$, R =	M_n (g mol^{-1})	T_g (°C)	$T_{5\%}$ (°C)[a]
Ph	45,000	38	180
3,5-CF_3-C_6H_3	209,000	52	150
2,4,6-$(CH_3)_3$-C_6H_2	95,000	>135	160
^{i}Pr	18,000	-22	135
^{t}Bu	31,500	36	129
^{n}Hex	57,000	-76	140

[a] Temperature at 5% weight loss.

The P atoms in poly(phosphinoboranes) are chiral, therefore, there is potential for tacticity within the polymer. This has most clearly been observed via ^{31}P NMR spectroscopy in which different ^{31}P environments are assigned as different tactic environments. The observation of tacticity is dependent on the R group. The most commonly used phenyl variant only exhibits a single broad resonance,[144] however, for ^{t}Bu,[159] Ad, ^{n}Hex,[157] and 3,5-$(CF_3)_2$-C_6H_3 variants tacticity is observed (Figure 1.26).[145] The different geometric possibilities that give rise to tacticity are best described in triads containing adjacent P atoms of the same configuration meso (m) or different configurations racemo (r) (Figure 1.26). This brings about four theoretical possibilities: syndiotactic rr, heterotactic mr and rm (which are equivalent) and isotactic mm.[157, 159] While there have been reports of different synthetic methods selectively producing polymer of different tacticity,[157, 159] there is no controlled and rational methodology to control tacticity.

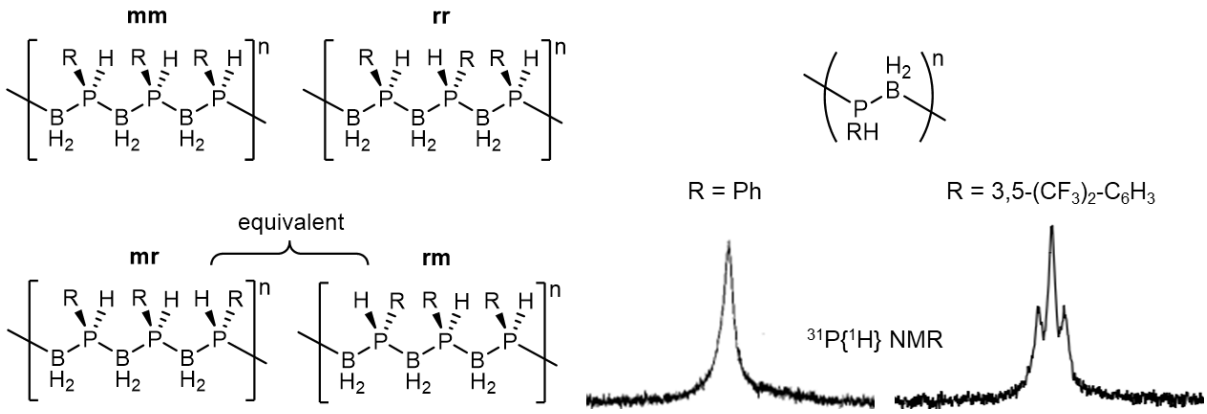

Figure 1.26. Left – the hypothetical tacticity triads of poly(phosphinoboranes). Right – the ^{31}P signals of $[H_2BPRH]_n$ (R = Ph and 3,5-$(CF_3)_2$-C_6H_3 respectively) in the $^{31}P\{^1H\}$ NMR spectra.[145, 154]

1.10.4 Rh-based catalysts and mechanistic investigations

For many years, very little was known about the mechanism of the initially reported Rh(I) catalysts, $[Rh(COD)_2][OTf]$ and $[\{Rh(\mu\text{-}Cl)(COD)\}_2]$, and neat conditions made it hard for any in-situ reaction monitoring. One report concluded that the reaction mechanism proceeded homogeneously by a series of tests to distinguish between heterogeneous and homogeneous catalysts. These included the lack of observation of metal particles using transmission electron microscopy (TEM) and UV-vis, as well as analysis of kinetic data, and attempted catalyst poisoning using mercury or PPh_3 and filtration of the reaction mixture.[160]

The Wilkinson catalyst analogue $[RhCl(PHCy_2)_3]$ was also shown to dehydrocouple $H_3B{\cdot}PPh_2H$ in neat conditions at 90 °C to form exclusively the linear dimer product, $H_3B{\cdot}PPh_2BH_2{\cdot}PPh_2H$. Dissociation of the phosphine-borane adduct was evident by observation of $H_3B{\cdot}PCy_2H$ in the catalytic mixture by NMR spectroscopy. Additional information on the likely catalyst came from the fact that free phosphine is likely formed in the reaction that may coordinate to the rhodium centre.[161]

A mechanistic investigation was conducted by Weller and Huertos using secondary phosphine-borane dehydrocoupling as a model for dehydropolymerisation. Interrogation of the catalytic mixture of the dehydrocoupling of $H_3B{\cdot}P^tBu_2H$ with the precatalyst $[Rh(COD)_2][BAr^F{}_4]$ in melt conditions was conducted by dilution of the neat mixture in 1,2-$F_2C_6H_4$. After partial conversion the reaction was stopped and analysed by NMR spectroscopy and electrospray ionisation mass spectrometry (ESI-MS). The $\eta^2\eta^2$-(BH_2) linear dimer bound sigma cation $[Rh(P^tBu_2H)_2(\eta^2\eta^2\text{-}H_3B{\cdot}P^tBu_2BH_2{\cdot}P^tBu_2H)]^+$ (**i-53-^{t}Bu$_2$**) was observed. This highlighted P–B dissociation of the phosphine-borane and thus the potential for phosphine-bound intermediates. The monomer bound complex $[Rh(P^tBu_2H)_2(\eta^2\eta^2\text{-}H_3B{\cdot}P^tBu_2H)][BAr^F{}_4]$ (**i-51**) was also prepared, and addition of H_2 to this resulted in oxidative addition to form a Rh(III) species, $[Rh(P^tBu_2H)_2(\eta^2\eta^2\text{-}H_3B{\cdot}P^tBu_2H)(H)_2][BAr^F{}_4]$ (**i-52**). Linear dimer bound **i-53-^{t}Bu$_2$** was also formed via addition of excess $H_3B{\cdot}P^tBu_2H$ to $[Rh(COD)_2][BAr^F{}_4]$ in 1,2-$F_2C_6H_4$ at 75 °C. In light of these results, a mechanism was proposed which coupled two phosphine-boranes via rhodium sigma complexes of the monomer and linear dimer (Scheme 1.25).[115]

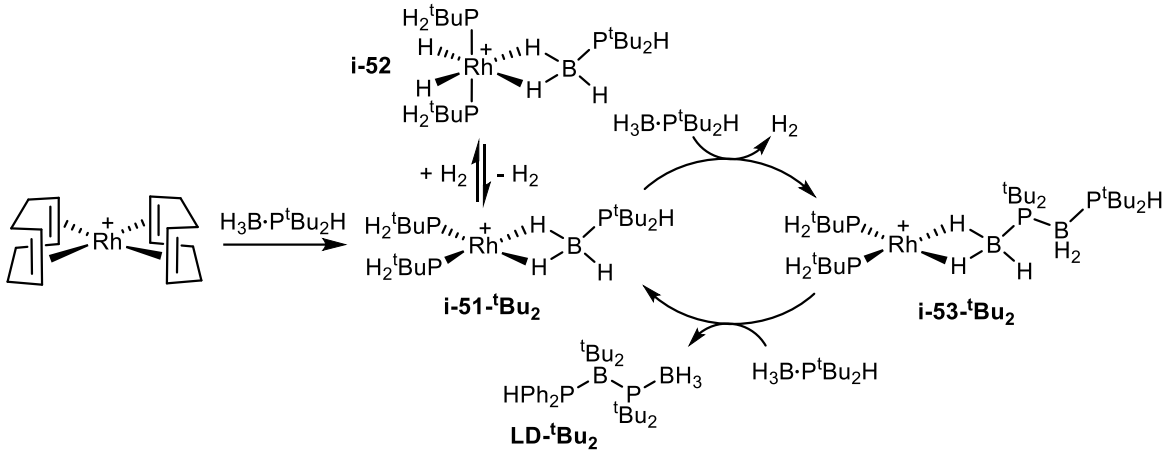

Scheme 1.25. Proposed mechanism for the rhodium-catalysed dehydrocoupling of $H_3B{\cdot}P^tBu_2H$. $[BAr^F{}_4]^-$ anions omitted for clarity.

A more extensive study was conducted with the precatalyst $[Rh(dppp)(\eta^6\text{-}C_6H_5F)][BAr^F{}_4]$ (**i-54**) which was shown to quantitatively dehydrocouple $H_3B{\cdot}PPh_2H$ under melt conditions to form the linear dimer, $H_3B{\cdot}PPh_2BH_2{\cdot}PPh_2H$ (**LD-Ph$_2$**), in 4 hours at 5 mol% catalyst loading. Stoichiometric addition of two equivalents of $H_3B{\cdot}PPh_2H$ to the precatalyst, **i-54**, resulted in dissociation of the fluorobenzene and coordination of two phosphine-borane units, one of which is P–H activated to form a Rh(III) complex, $[RhH(dppp)(\sigma,\eta^1\text{-}PPh_2BH_3)(\eta^1\text{-}H_3B{\cdot}PPh_2H)][BAr^F{}_4]$ **i-55-Ph$_2$** (Scheme 1.26). The two phosphine borane units couple together at room temperature, forming $[RhH(dppp)(\sigma,\eta^2\eta^2\text{-}PPh_2{\cdot}BH_2PPh_2{\cdot}BH_3)][BAr^F{}_4]$ **i-56-Ph$_2$**. This was shown to be an overall first order process. The same complex could also be formed via addition of diphenyl linear dimer, **LD-Ph$_2$**, to **i-54**. When $D_3B{\cdot}PPh_2H$ was added to **i-54**, incorporation of D was observed at all of the B, P and Rh sites, suggesting rapid and reversible B–H and P–H activation was occurring. The KIE of the overall reaction was determined to be 1.9(1), suggesting either B–H or P–H activation are involved in the rate determining process. The bound linear dimer was displaced by dppe, illustrating that the product can be removed and thus catalytic turnover is possible.

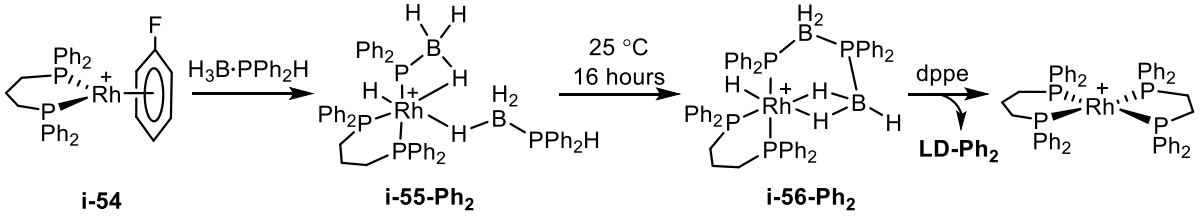

Scheme 1.26. Speciation experiments in the $[Rh(dppp)]^+$ catalysed phosphine-borane dehydrocoupling. $[BAr^F{}_4]^-$ anions omitted for clarity.

A mechanism for dehydrocoupling was subsequently proposed (Scheme 1.27). Displacement of the fluorobenzene by $H_3B{\cdot}PPh_2H$ gives the $\eta^2\eta^2$-(BH_2) sigma complex $[Rh(dppp)(\eta^2\text{-}H_3B{\cdot}PPh_2H)][BAr^F{}_4]$ (**i-51-Ph$_2$**). A second $H_3B{\cdot}PPh_2H$ unit binds, forming $[RhH(dppp)(\sigma,\eta^1\text{-}PPh_2BH_3)(\eta^1\text{-}H_3BPPh_2H)][BAr^F{}_4]$ **i-56-Ph$_2$** after P–H activation. The Rh–H unit undergoes exchange with the agostic B–H to form **i-57.** The B–H activation and then H_2 formation form a five coordinate Rh species (**i-58**) which would rapidly lose H_2 and couple the activated B and P fragments to form bound linear dimer. The $\eta^2\eta^2$-(BH_2) linear dimer bound Rh(I) complex $[Rh(dppp)(\eta^2\eta^2\text{-}H_3B{\cdot}PPh_2BH_2{\cdot}PPh_2H)][BAr^F{}_4]$, **i-53-Ph$_2$**, was never observed and suggested to be in equilibrium with the off-cycle P–H activated complex, $[RhH(dppp)(\sigma,\eta^2\eta^2\text{-}PPh_2{\cdot}BH_2PPh_2{\cdot}BH_3)][BAr^F{}_4]$ (**i-56-Ph$_2$**), which was the observed resting state during catalysis. Displacement of the linear dimer with monomer was proposed to be turnover limiting for catalysis.[126] A chain transfer mechanism has also been proposed for amine-borane dehydropolymerisation, but it is irreversible.[151] However, these discoveries were limited by the use of melt conditions for catalytic turnover and due to rapid H/D exchange at B and P, the exact order and rate of the B–H/P–H activation steps could not be deciphered.

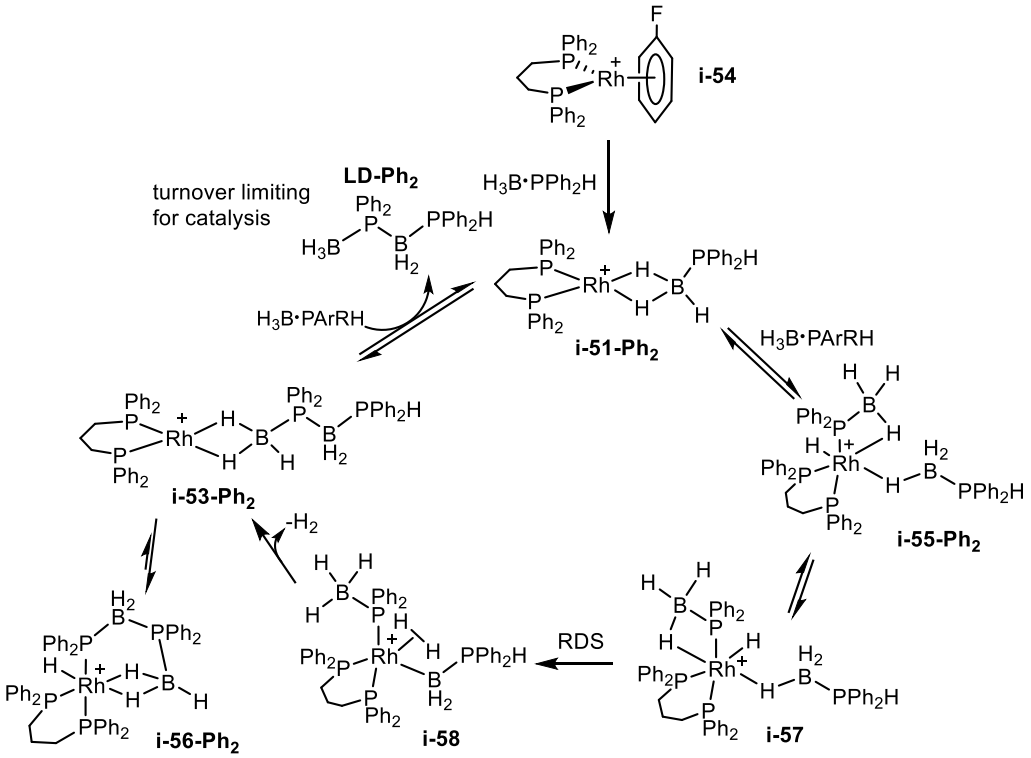

Scheme 1.27. Proposed mechanism for the $[Rh(dppp)]^+$ catalysed dehydrocoupling of $H_3B{\cdot}PPh_2H$. $[BAr^F{}_4]^-$ anions omitted for clarity. RDS = rate determining step.

The rhodium-mediated dehydrocoupling process described above was investigated further with a range of phosphine-boranes with different substituents with electron-withdrawing and electron-donating aryl groups. The electron withdrawing substituents underwent the dehydrocoupling process faster than more electron rich phosphine-boranes, e.g. for $H_3B{\cdot}PAr_2H$, when Ar = 3,5-$(CF_3)_2$-C_6H_3 the reaction took six hours at 25 °C and when Ar = *p*-OMe-C_6H_4 the reaction took 16 hours at 35 °C. P–H bond weakening was suspected to be the cause of this. Furthermore, a side reaction was observed with the more electron-withdrawing substituents, in which the formation of $[Rh(dppp)(PAr_2H)_2][BAr^F{}_4]$ was observed, due to a greater propensity for P–B adduct dissociation. The same dehydrocoupling reaction with primary phosphine-borane, $H_3B{\cdot}PCyH_2$ revealed the inherent chirality at the coordinated P atom. Two complexes were observed in a 1:1 ratio when $H_3B{\cdot}PCyH_2$ was added to $[Rh(dppp)(\eta^6\text{-}C_6H_5F)][BAr^F{}_4]$ (Scheme 1.28), assigned as two diastereomers of $[RhH(dppp)(\sigma,\eta^1\text{-}PCyHBH_3)(\eta^1\text{-}H_3B{\cdot}PCy_2H)][BAr^F{}_4]$, **i-55-CyH**, formed upon P–H activation of the prochiral P. Both isomers underwent dehydrocoupling at room temperature to form two diastereomers of $[RhH(dppp)(\sigma,\eta^2\text{-}PCy_2BH_2PCy_2BH_3)][BAr^F{}_4]$ **i-56-CyH** in a 1:6 ratio. The diastereomeric pair, **i-56-CyH**, could also be prepared via addition of the linear dimer, $H_3B{\cdot}PCyHBH_2{\cdot}PCyH_2$, (**LD-CyH**) directly to $[Rh(dppp)(\eta^6\text{-}C_6H_5F)][BAr^F{}_4]$ (**i-54**), forming in a 1:1 diastereomeric ratio after five minutes and settling at a 1:6 ratio after 18 hours at 25 °C. It was suggested that the reductive elimination of P–H, rotation about the P–B bond, then oxidative addition of the other P–H occurs, with an observed thermodynamic ratio of 1:6 for the two isomers. It was not determined which isomer was preferred. Excess dppe was shown to displace the linear dimer ligand.[123]

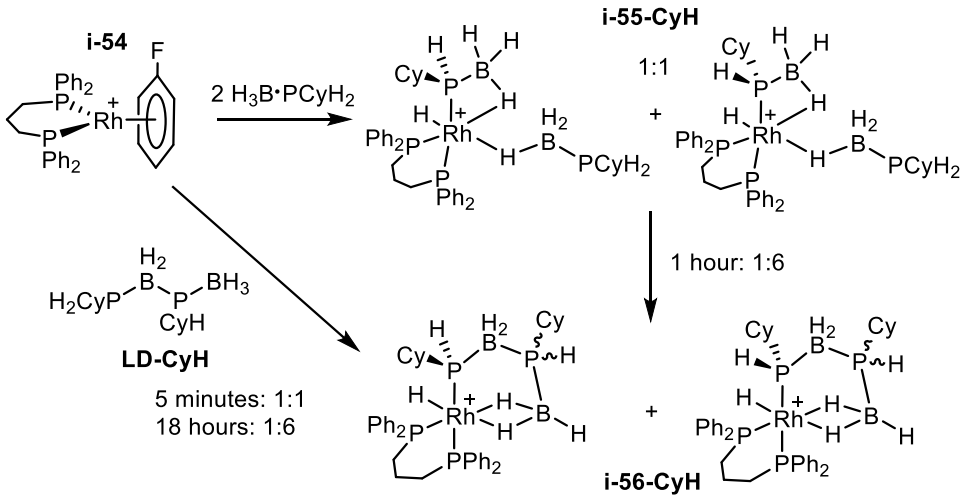

Scheme 1.28. Observed chirality in the rhodium-mediated dehydrocoupling of $H_3B{\cdot}PCyH_2$. $[BAr^F{}_4]^-$ anions omitted for clarity.

[Cp*Rh(Me)(PMe_3)(CH_2Cl_2)][BAr^F_4] (**i-59**) has been reported to dehydropolymerise $H_3B{\cdot}PPhH_2$ in toluene solution (1 M) at 100 °C over 72 hours. A high catalyst loading of 5 mol% was required. The resultant polymer was shown by GPC analysis to be of moderate chain length and dispersity (M_n = 13,000 g mol^{-1}, PDI = 2.2). Monitoring of the reaction by ^{11}B NMR spectroscopy revealed complete conversion of monomer after 4 hours but only to short chain oligomers and the linear dimer $H_3B{\cdot}PPhHBH_2{\cdot}PPhH_2$ (**LD-PhH**), which was present in a relatively large proportion (≈ 30 % mixture after one hour). The linear dimer was isolated and shown to undergo polymerisation to form low molecular weight polymer with further added rhodium precatalyst (5 mol% in toluene, 100 °C) (Scheme 1.29). However, $H_3B{\cdot}PPhH_2$ was also observed during catalysis, suggesting P–B bond scission of oligomer/polymer or linear dimer.

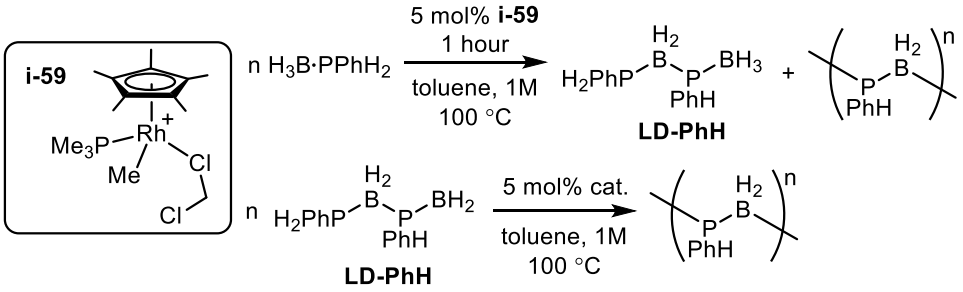

Scheme 1.29. Dehydropolymerisation of $H_3B{\cdot}PPhH_2$ and **LD-PhH** with the precatalyst **i-59**.

Stoichiometric addition of secondary phosphine-boranes $H_3B{\cdot}PPh_2H$, $H_3B{\cdot}PCy_2H$ and $H_3B{\cdot}P^tBu_2H$ to complex **i-59** was studied to explore role of the catalyst in dehydropolymerisation. The resultant β-B agostic phosphido-borane complexes, [RhCp*(PR_2BH_3)(PMe_3)][BAr^F_4] (**i-63-R**) were fully characterised (R = Ph, Cy or ^{t}Bu) and suggested to be key intermediates in the P–H/B–H activation process. Computational and deuterium labelling studies were used to determine the mechanism of phosphido-borane formation. It was shown that initially B–H activation occurs at a sigma η^1(BH) complex (**i-60-R**) to form a base-stabilised α-B agostic boryl complex with concomitant loss of CH_4 (**i-61-R**), then subsequent P–H activation to a hydrido-phosphino-borane intermediate (**i-62-R**) before hydride insertion into the Rh–B bond and formation of the phosphido-borane (**i-63-R**, Scheme 1.30).[162] This shows that P–H activation actually occurs via an initial B–H activation.

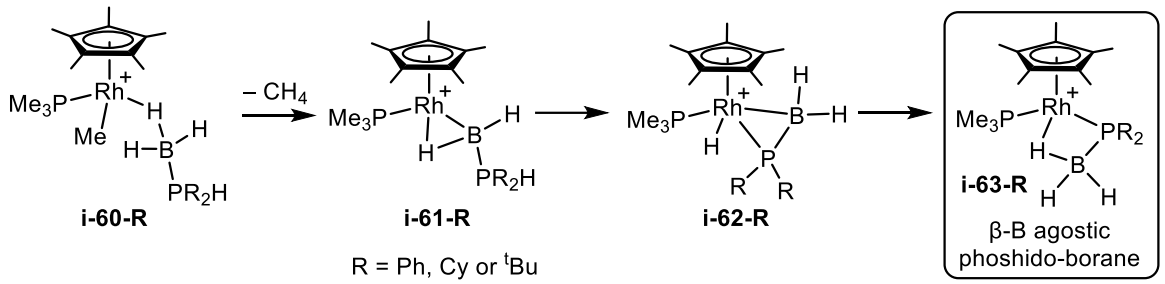

Scheme 1.30. Formation of [Cp*Rh(PMe$_3$)(PR$_2$BH$_3$)][BAr$^F_4$] phosphido-borane complexes. [BAr$^F_4$]$^-$ anions omitted for clarity.

1.10.5 Iron-based catalysts

An iron-based catalyst, specifically [Cp(CO)$_2$Fe(OTf)] (**i-64**), was shown by Manners and co-workers to selectively, and quantitatively convert H$_3$B·PPH$_2$ into high molecular weight [H$_2$BPPhH]$_n$ (M_n = 59,000 g mol^{-1}, PDI = 1.6) with low catalyst loadings (0.1 mol%, toluene, 100 °C, 24 hours). It was discovered that variation of catalyst loading allowed for molecular weight control, with low loadings giving higher molecular weight polymer (0.1 mol%: Mn ≈ 78,000 g mol^{-1}) compared to higher catalyst loadings (10 mol%: Mn ≈ 40,000 g mol^{-1}). A chain growth mechanism was postulated for this system (Scheme 1.31), which was supported by further experiments: the catalysis was stopped after only 35% conversion of the monomer (H$_3$B·PPH$_2$) and high molecular weight polymer was observed (Mn = 40,000 g mol^{-1}) alongside free monomer. The polymer chain length did not increase after 100% conversion of the monomer, suggesting no further coupling was occurring. The catalytic mechanism was shown to be homogeneous, via a lack of catalyst poisoning with a substoichiometric addition of PMe$_3$ and no polymer was formed when Fe nanoparticles were added at the start of the reaction instead of [Cp(CO)$_2$Fe(OTf)] (**i-64**).[163] However, very little in-situ data was obtained and the proposed mechanism is very speculative.

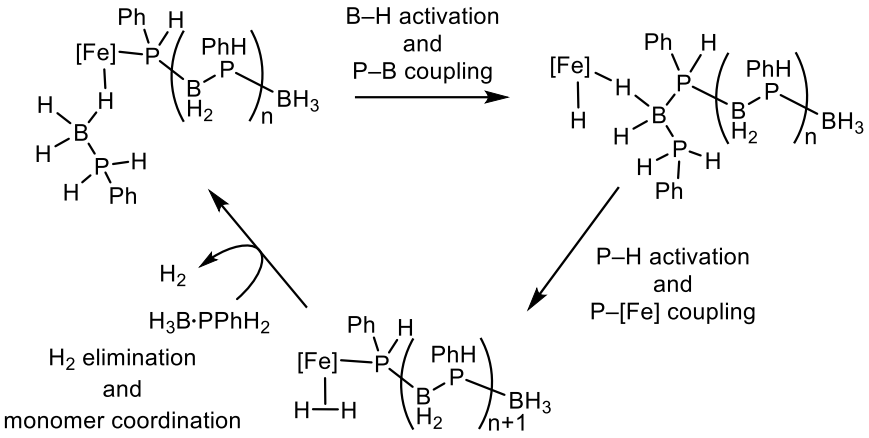

Scheme 1.31. Proposed chain growth dehydropolymerisation mechanism with $[Cp(CO)_2Fe(OTf)]$ precatalyst. [Fe] = $[Cp(CO)_xFe]$.

The high activity of **i-64** in this reaction was exploited to expand the reported substrate tolerance of the phosphine-borane dehydropolymerisation, with a broad range of aryl[145] and alkyl[157] substituents shown to polymerise (Figure 1.25). Cross-linking through activation of internal P–H bonds, using $H_3B{\cdot}PArH_2$ [Ar = 3,5-$(CF_3)_2$-C_6H_3] was proposed to cause gel-like substances formed at 5 mol% catalyst loading, which was not observed with any other substrate. Relatively deactivated alkylphosphine-boranes (compared to arylphosphine-boranes) subsequently required a much longer reaction time (96 hours) to fully convert all of the monomer in a toluene solution at 100 °C. It was shown that the polymer molecular weight could be controlled by addition of $^tBuPH_2$ as this capped the terminal BH_3 of the polymer, as shown by ESI-MS, and prevented further dehydrocoupling.[157]

1.10.6 Other transition metal catalysts

$[CpRu(CO)_2(PPh_2BH_3)]$ has been used in the dehydrocoupling of $H_3B{\cdot}PPh_2H$, although neat conditions at 120 °C were required for only 60% conversion.[164] Iridium bis-phosphinite pincer complexes, $[(^tBuPOCOP)IrH_2]$ (**i-64**) and [(^{t}BuPOCOP)IrHPh], have been reported by Radius and co-workers as catalysts for $H_3B{\cdot}PArH_2$ dehydropolymerisation (Ar = Ph, *p*-tolyl or mesityl), (Scheme 1.32). 5 mol% catalyst loadings of **i-64** in toluene gave longer polymer by GPC analysis, M_w = 66,000-300,000 g mol^{-1} but with very wide polydispersity (PDI = 13.2-30.0). Reducing the catalyst loading to 2.5 mol% gave lower M_W with much reduced PDI (2.6). 0.5 mol% gave even shorter polymer. A two-stage polymerisation mechanism was proposed, whereby an initial dehydrogenation from the phosphine-

borane by **i-64** occurs slowly. The resultant phosphinoborane H_2B-PArH then undergoes rapid chain growth polymerisation to form $[H_2BPArH]_n$.[165] This similar to the dehydrogenation-polymerisation mechanism proposed for metal catalysed methylamine-borane dehydropolymerisation,[166] but is different to the Rh studies on phosphine-borane dehydropolymerisation.[115, 126] It was suggested that the concentration of H_2B-PArH would be the rate limiting factor and explained the polymer length dependence on catalyst loading. However, no evidence of dehydrogenation or chain propagation steps was presented.[165]

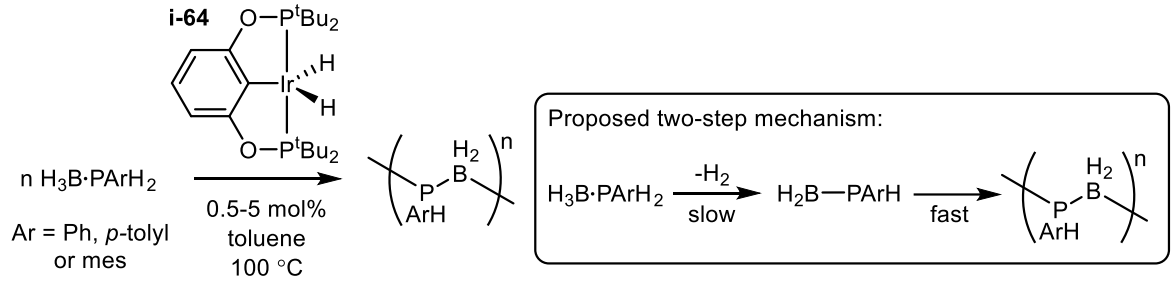

Scheme 1.32. Iridium-catalysed dehydropolymerisation of primary aryl phosphine-boranes.

1.10.7 Transition metal free routes

There are also reports of metal-free dehydropolymerisation routes, using cyclic(alkyl)(amino)carbenes as hydrogen acceptors[167] and head-to-tail polymerisation of transient phosphino-boranes (Scheme 1.33). Lewis base stabilised monomeric phosphanylboranes were synthesised from the free phosphine, which could then undergo thermally induced oligomerisation/polymerisation with concurrent release of the Lewis base. Only oligomeric material was formed via this method with H and Ph substituents, but polymeric material was formed with the R^1 = ^{t}Bu, R^2 = H substrate with M_n = 27,800-35,000 g mol^{-1} and polydispersity of 1.6-1.9. At the time of publication, this was the only method to form poly(phosphinoboranes) with bulky P–R groups.[159] The ^{31}P NMR of $[H_2BP^tBuH]_n$ formed via this manner, revealed three tactic environments, compared to the Fe-catalysed route, for which only one tactic environment was reported.[157]

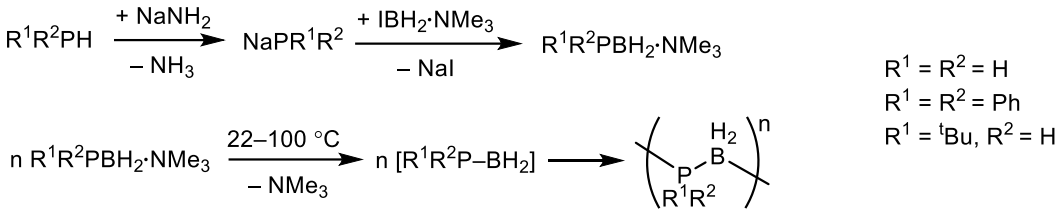

Scheme 1.33. Synthesis of Lewis base stabilised organosubstituted phosphanylboranes and the thermally induced polymerisation.

The most recent development in the field of phosphine-borane dehydropolymerisation is the use of calix[4]pryyrolato aluminates (**i-65**) as catalysts for the synthesis of high molecular weight poly(phenylphosphinoborane) (Scheme 1.34). This is the first example of a non-transition metal catalysing the dehydropolymerisation reaction. Polymer of up to M_n = 43,000 g mol^{-1} was formed over 72 hours in a 1:4 mixture of 1,2-$Cl_2C_6H_4$/toluene. This method overcomes the issue of residual transition metal in the isolated polymer but limited mechanistic information is known.[168]

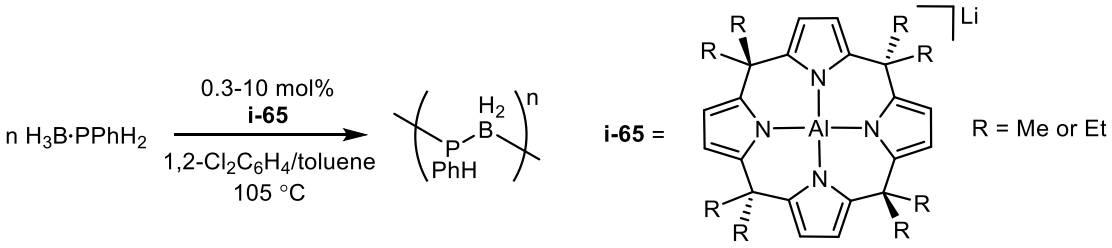

Scheme 1.34. Dehydropolymerisation of $H_3B{\cdot}PPhH_2$ using **i-65**.

1.11 Summary

This introduction has only briefly touched upon the vast field of transition metal-diphosphine chemistry, in particular, focussing on rhodium, the impact of *ortho*-aryl substitution in metal-phosphine complexes and the POP-type ligand, DPEphos. There are a vast number of examples of how diphosphine design, via manipulation of the backbone and substituents, can have a pronounced effect on reactivity and homogeneous catalysis.[3, 17, 43] One particular approach is *ortho*-aryl substitution, which has been shown to increase productivity in a range of catalyses. This has been largely attributed to restricted rotation about the P–C bond with bulkier *ortho*-substituents which influences the catalytic activity.[56, 57]

Diphosphine ligands with a bridging ether linkage can be used as wide bite angle κ^2 ligands,[77] but they also have the ability to reversibly coordinate via the oxygen as well, giving rise to κ^3-P,O,P

bonding arrangements.[75] This allows for the stabilisation of catalytic intermediates.[95, 98] DPEphos also features this capability. The number of examples of *ortho*-substituted DPEphos ligands, however, is limited, and we believe there is potential in the yet unreported *ortho*-isopropyl and *ortho*-fluorine analogues.

The characteristics of agostic bonds and anagostic interactions have also been introduced, alongside several examples. One of the defining features of these M···H interactions is the upfield (agostic) or downfield (anagostic) ^{1}H chemical shift.[129] Pioneering work by Scherer explains these opposing observations by the topological placing of the proton in difference regions of charge density, which in turn, gives rise to different local magnetic fields.[138] However, the field is lacking a comprehensive experimental investigation that relays this detailed computational understanding into real examples, making it more accessible for the organometallic chemist.

The developments in transition metal catalysed phosphine-borane dehydropolymerisation, since the initial report in 1999, have been presented. The earliest Rh catalysts, e.g. $[Rh(COD)_2][OTf]$, suffered with poor control over polymer chain length.[144, 149, 154, 169] Iron catalysts, based upon $[Cp(CO)_xFe(OTf)]$, have been used to expand the range of substituents, producing polymer of high molecular weight and some control via catalyst loading or addition of free primary phosphine.[145, 157, 163] However, little is known about the mechanism of these systems. Rhodium catalysts, such as $[Rh(dppp)]^+$ and $[Cp^*Rh(PMe_3)]^+$ have been used to provide some important mechanistic insights into the dehydrocoupling of secondary phosphine-boranes, but dehydropolymerisation was not reported or resulted in low molecular weight and polydisperse polymer.[115, 126, 170] There is an absence in the literature of a catalytic system in which the mechanism is not just understood, but also exploited to give polymer of designed molecular weight. This also introduces the opportunity for incorporation of two different substrates – namely, poly(phosphinoborane) block-copolymers.

1.12 References

[1] T. Shilpa, R. Dhanya, S. Saranya, G. Anilkumar, *ChemistrySelect,* **2020,** 5, 898-915.
[2] P. A. Evans, *Modern Rhodium-Catalyzed Organic Reactions*. Wiley, Weinheim, **2005**.
[3] J. F. Hartwig, *Organotransition Metal Chemistry. From Bonding to Catalysis Edited By John F. Hartwig*. University Science Books, Sausalito, **2010**.
[4] K.-D. Wiese, D. Obst, Hydroformylation. In *Catalytic Carbonylation Reactions. Topics in Organometallic Chemistry*, Beller, M., Ed. Springer: Heidelberg, Berlin, **2006**; Vol. 18.
[5] J. A. Osborn, F. H. Jardine, J. F. Young, G. Wilkinson, *J. Chem. Soc. A,* **1966,** 1711-1732.
[6] J. F. Young, J. A. Osborn, F. H. Jaiidine, G. Wilkinson, *Chem. Commun.,* **1965,** 7, 131-132.

[7] P. Meakin, J. P. Jesson, C. A. Tolman, *J. Am. Chem. Soc.,* **1972,** 94, 3240-3242.
[8] C. A. Tolman, J. P. Jesson, *Science,* **1973,** 181, 501-505.
[9] J. Halpern, *Science,* **1982,** 217, 401-407.
[10] J. Halpern, D. P. Riley, A. S. C. Chan, J. J. Pluth, *J. Am. Chem. Soc.,* **1977,** 99, 8055-8057.
[11] J. Halpern, T. Okamoto, A. Zakhariev, *J. Mol. Catal.,* **1977,** 2, 65-68.
[12] D. Evans, J. A. Osborn, G. Wilkinson, *J. Chem. Soc. A,* **1968,** 3133-3142.
[13] R. F. Heck, *Acc. Chem. Res.,* **1969,** 2, 10-16.
[14] R. F. Heck, D. S. Breslow, *J. Am. Chem. Soc.,* **1962,** 84, 2499-2502.
[15] R. F. Heck, D. S. Breslow, *J. Am. Chem. Soc.,* **1961,** 83, 4023-4027.
[16] P. W. N. M. Van Leeuwen, C. Claver, *Rhodium Catalyzed Hydroformylation* Kluwer Academic Publishers, Dordrecht, **2000**.
[17] P. W. N. M. Van Leeuwen, *Homogeneous Catalysis: Understanding the Art*. Kluwer Academic Publishers, **2004**.
[18] R. H. Crabtree, *J. Organomet. Chem.,* **2004,** 689, 4083-4091.
[19] S. Medici, M. Peana, A. Pelucelli, M. A. Zoroddu, *Molecules,* **2021,** 26,
[20] R. H. Crabtree, *The Organometallic Chemistry of the Transition Metals*. 6th ed., John Wiley & Sons, New Jersey, **2014**.
[21] I. Omae, *Appl. Organomet. Chem.,* **2009,** 23, 91-107.
[22] K. Fagnou, M. Lautens, *Chem. Rev.,* **2003,** 103, 169-196.
[23] J. T. Mague, Rhodium: Organometallic Chemistry. In *Encyclopedia of Inorganic and Bioinorganic Chemistry*, Scott, R. A., Ed. John Wiley & Sons: New York, **2011**.
[24] N. N. Greenwood, A. Earnshaw, 26 - Cobalt, Rhodium and Iridium. In *Chemistry of the Elements*, 2nd ed.; Butterworth-Heinemann: Oxford, **1997**.
[25] V. Varela-Izquierdo, J. A. López, B. De Bruin, C. Tejel, M. A. Ciriano, *Chem. Eur. J.,* **2020,** 26, 3270-3274.
[26] P. W. N. M. Van Leeuwen, C. P. Casey, G. T. Whiteker, Phosphines as ligands. In *Rhodium Catalyzed Hydroformylation*, Leeuwen, P. W. N. M. v., Ed. Springer: Dordrecht, **2000**.
[27] P. B. Dias, M. E. M. De Piedade, J. a. M. Simões, *Coord. Chem. Rev.,* **1994,** 135-136, 737-807.
[28] A. G. Orpen, N. G. Connelly, *J. Chem. Soc., Chem. Commun.,* **1985,** 1310-1311.
[29] A. T. Chadwick, *Chem. Rev.,* **1977,** 77, 313-348.
[30] L. Perrin, E. Clot, O. Eisenstein, J. Loch, R. H. Crabtree, *Inorg. Chem.,* **2001,** 40, 5806-5811.
[31] A. T. Chadwick, *J. Am. Chem. Soc.,* **1970,** 92, 2956-2965.
[32] G. M. Adams, F. M. Chadwick, S. D. Pike, A. S. Weller, *Dalton Trans.,* **2015,** 44, 6340-6342.
[33] A. T. Chadwick, *J. Am. Chem. Soc.,* **1970,** 92, 2953-2956.
[34] W. C. Trogler, L. G. Marzilli, *J. Am. Chem. Soc.,* **1974,** 96, 7589-7591.
[35] L. Falivene, Z. Cao, A. Petta, L. Serra, A. Poater, R. Oliva, V. Scarano, L. Cavallo, *Nature Chem.,* **2019,** 11, 872-879.
[36] K. Issleib, D.-W. Müller, *Chem. Ber.,* **1959,** 92, 3175-3182.
[37] M. Iwamoto, S. Yuguchi, *J. Org. Chem.,* **1966,** 31, 4290-4291.
[38] P. W. N. M. Van Leeuwen, P. C. J. Kamer, J. N. H. Reek, P. Dierkes, *Chem. Rev.,* **2000,** 100, 2741-2770.
[39] J. Holz, A. Monsees, H. Jiao, J. You, I. V. Komarov, C. Fischer, K. Drauz, A. Börner, *J. Org. Chem.,* **2003,** 68, 1701-1707.
[40] M. Kranenburg, P. C. J. Kamer, P. W. N. M. V. Leeuwen, D. Vogtb, W. Keim, *J. Chem. Soc. Chem. Commun.,* **1995,** 2177-2178.
[41] C. P. Casey, G. T. Whiteker, *Isr. J. Chem.,* **1990,** 30, 299-304.
[42] P. Dierkes, P. W. N. M. Van Leeuwen, *J. Chem. Soc., Dalton Trans.,* **1999,** 1519-1530.
[43] M. Schreuder Goedheijt, J. N. H. Reek, P. C. J. Kamer, P. W. N. M. Van Leeuwen, *Chem. Commun.,* **1998,** 2431-2432.
[44] S. J. Dossett, A. Gillon, A. G. Orpen, J. S. Fleming, P. G. Pringle, D. F. Wass, M. D. Jones, *Chem. Commun.,* **2001,** 699-700.
[45] N. A. Cooley, S. M. Green, D. F. Wass, K. Heslop, A. G. Orpen, P. G. Pringle, *Organometallics,* **2001,** 20, 4769-4771.
[46] A. Carter, S. A. Cohen, N. A. Cooley, A. Murphy, J. Scutt, D. F. Wass, *Chem. Commun.,* **2002,** 858-859.
[47] J. N. L. Dennett, A. L. Gillon, K. Heslop, D. J. Hyett, J. S. Fleming, C. E. Lloyd-Jones, A. G. Orpen, P. G. Pringle, D. F. Wass, J. N. Scutt, R. H. Weatherhead, *Organometallics,* **2004,** 23, 6077-6079.
[48] A. H. Roy, J. F. Hartwig, *Organometallics,* **2004,** 23, 1533-1541.
[49] J. S. Howell, J. D. Lovatt, P. Mcardle, D. Cunningham, E. Maimone, H. E. Gottlieb, Z. Goldschmidt, *Inorg. Chem. Commun.,* **1998,** 1, 118-120.
[50] J. S. Howell, P. C. Yates, M. G. Palin, P. Mcardle, D. Cunningham, Z. Goldschmidt, H. E. Gottlieb, D. Hezroni-Langerman, *J. Chem. Soc., Dalton Trans.,* **1993,** 2775-2780.
[51] J. S. Howell, M. G. Palin, P. Mcardle, D. Cunningham, Z. Goldschmidt, H. E. Gottlieb, D. Hezroni-Langerman, *Inorg. Chem.,* **1993,** 32, 3493-3500.
[52] J. S. Howell, N. Fey, J. D. Lovatt, P. C. Yates, P. Mcardle, D. Cunningham, E. Sadeh, H. E. Gottlieb, Z. Goldschmidt, M. B. Hursthouse, M. E. Light, *J. Chem. Soc., Dalton Trans.,* **1999,** 3015-3028.
[53] M. R. Whitnall, K. K. Hii, M. Thornton-Pett, T. P. Kee, *J. Organomet. Chem.,* **1997,** 529, 35-50.

[54] J. Forniés, A. Martín, R. Navarro, V. Sicilia, P. Villarroya, *Organometallics,* **1996,** 15, 1826-1833.
[55] A. K. Colter, I. I. Schuster, R. J. Kurland, *J. Am. Chem. Soc.,* **1965,** 87, 2279-2281.
[56] R. A. Baber, A. G. Orpen, P. G. Pringle, M. J. Wilkinson, R. L. Wingad, *Dalton Trans.,* **2005,** 659-667.
[57] A. G. Orpen, P. G. Pringle, M. B. Smith, K. Worboys, *J. Organomet. Chem.,* **1998,** 550, 255-266.
[58] B. D. Vineyard, W. S. Knowles, M. J. Sabacky, G. L. Bachman, D. J. Weinkauff, *J. Am. Chem. Soc.,* **1977,** 99, 5946-5952.
[59] C. Gonzalez-Rodriguez, R. J. Pawley, A. B. Chaplin, A. L. Thompson, A. S. Weller, M. C. Willis, *Angew. Chem. Int. Ed.,* **2011,** 50, 5134-5138.
[60] R. D. W. Kemmitt, D. I. Nichols, R. D. Peacock, *Chem. Commun.,* **1967,** 599b-601.
[61] R. D. W. Kemmitt, D. I. Nichols, R. D. Peacock, *J. Chem. Soc. A,* **1968,** 1898-1902.
[62] R. D. W. Kemmitt, D. I. Nichols, R. D. Peacock, *J. Chem. Soc. A,* **1968,** 2149-2152.
[63] B. Cordero, V. Gómez, A. E. Platero-Prats, M. Revés, J. Echeverría, E. Cremades, F. Barragán, S. Alvarez, *Dalton Trans.,* **2008,** 2832-2838.
[64] D. T. Clark, J. N. Murrell, J. M. Tedder, *J. Chem. Soc.,* **1963,** 1250-1253.
[65] C. Corcoran, J. Fawcett, S. Friedrichs, J. H. Holloway, E. G. Hope, D. R. Russell, G. C. Saunders, A. M. Stuart, *J. Chem. Soc., Dalton Trans.,* **2000,** 161-172.
[66] J. Fawcett, S. Friedrichs, J. H. Holloway, E. G. Hope, V. Mckee, M. Nieuwenhuyzen, D. R. Russell, G. C. Saunders, *J. Chem. Soc., Dalton Trans.,* **1998,** 1477-1484.
[67] T. Korenaga, K. Abe, A. Ko, R. Maenishi, T. Sakai, *Organometallics,* **2010,** 29, 4025-4035.
[68] H. Lee, Y. Joe, H. Park, *Catal. Commun.,* **2019,** 121, 15-18.
[69] H. Lee, S. H. Hong, *Applied Catalysis A: General,* **2018,** 560, 21-27.
[70] L. J. Sewell, A. B. Chaplin, J. a. B. Abdalla, A. S. Weller, *Dalton Trans.,* **2010,** 39, 7437-7439.
[71] M. T. Tribble, J. G. Traynham, *J. Am. Chem. Soc.,* **1969,** 91, 379-388.
[72] D. Morales-Morales, C. Jensen, *The Chemistry of Pincer Compounds*. Elsevier, Amsterdam, **2007**.
[73] N. Selander, K. J. Szabó, *Chem. Rev.,* **2011,** 111, 2048-2076.
[74] J. Choi, A. H. R. Macarthur, M. Brookhart, A. S. Goldman, *Chem. Rev.,* **2011,** 111, 1761-1779.
[75] G. M. Adams, A. S. Weller, *Coord. Chem. Rev.,* **2018,** 355, 150-172.
[76] N. W. Alcock, J. M. Brown, J. C. Jeffery, *J. Chem. Soc., Chem. Commun.,* **1974,** 829-830.
[77] M. Kranenburg, Y. E. M. Van Der Burgt, P. C. J. Kamer, P. W. N. M. Van Leeuwen, K. Goubitz, J. Fraanje, *Organometallics,* **1995,** 14, 3081-3089.
[78] J. C. Jeffrey, T. B. Rauchfuss, *Inorg. Chem.,* **1979,** 18, 2658-2666.
[79] Z. Weng, S. Teo, T. S. A. Hor, *Acc. Chem. Res.,* **2007,** 40, 676-684.
[80] A. Bader, E. Lindner, *Coord. Chem. Rev.,* **1991,** 108, 27-110.
[81] G. M. Adams, D. E. Ryan, N. A. Beattie, A. I. Mckay, G. C. Lloyd-Jones, A. S. Weller, *ACS Catal.,* **2019,** 9, 3657-3666.
[82] P. W. N. M. Van Leeuwen, M. A. Zuideveld, B. H. G. Swennenhuis, Z. Freixa, P. C. J. Kamer, K. Goubitz, J. Fraanje, M. Lutz, A. L. Spek, *J. Am. Chem. Soc.,* **2003,** 125, 5523-5539.
[83] A. E. Putra, K. Takigawa, H. Tanaka, Y. Ito, Y. Oe, T. Ohta, *Eur. J. Org. Chem.,* **2013,** 2013, 6344-6354.
[84] K. Hori, H. Motohashi, D. Saito, K. Mikami, *ACS Catal.,* **2019,** 9, 417-421.
[85] T. Ohshima, Y. Miyamoto, J. Ipposhi, Y. Nakahara, M. Utsunomiya, K. Mashima, *J. Am. Chem. Soc.,* **2009,** 131, 14317-14328.
[86] R. R. Schrock, J. A. Osborn, *J. Am. Chem. Soc.,* **1976,** 98, 4450-4455.
[87] J. R. Shapley, R. R. Schrock, J. A. Osborn, *J. Am. Chem. Soc.,* **1969,** 91, 2816-2817.
[88] A. J. Martínez-Martínez, B. E. Tegner, A. I. Mckay, A. J. Bukvic, N. H. Rees, G. J. Tizzard, S. J. Coles, M. R. Warren, S. A. Macgregor, A. S. Weller, *J. Am. Chem. Soc.,* **2018,** 140, 14958-14970.
[89] A. Meißner, E. Alberico, H. Drexler, W. Baumann, D. Heller, *Catal. Sci. Technol.,* **2014,** 4, 3409-3425.
[90] M. Utsunomiya, R. Kuwano, M. Kawatsura, J. F. Hartwig, *J. Am. Chem. Soc.,* **2003,** 125, 5608-5609.
[91] G. L. Moxham, H. E. Randell-Sly, S. K. Brayshaw, R. L. Woodward, A. S. Weller, M. C. Willis, *Angew. Chem. Int. Ed.,* **2006,** 45, 7618-7622.
[92] L. R. Doyle, E. A. Thompson, A. L. Burnage, A. C. Whitwood, H. T. Jenkins, S. A. Macgregor, A. S. Weller, *Dalton Trans.,* **2022,** 51, 3661-3665.
[93] T. J. Coxon, M. Fernández, J. Barwick-Silk, A. I. Mckay, L. E. Britton, A. S. Weller, M. C. Willis, *J. Am. Chem. Soc.,* **2017,** 139, 10142-10149.
[94] P. A. Spreider, A. M. Haydl, M. Heinrich, B. Breit, *Angew. Chem. Int. Ed.,* **2016,** 55, 15569-15573.
[95] J. F. Hooper, A. B. Chaplin, C. Gonzaíez-Rodríguez, A. L. Thompson, A. S. Weller, M. C. Willis, *J. Am. Chem.Soc,* **2012,** 134,
[96] G. L. Moxham, H. Randell-Sly, S. K. Brayshaw, A. S. Weller, M. C. Willis, *Chem. Eur. J.,* **2008,** 14, 8383-97.
[97] D. E. Ryan, K. A. Andrea, J. J. Race, T. M. Boyd, G. C. Lloyd-Jones, A. S. Weller, *ACS Catal.,* **2020,** 10, 7443-7448.
[98] J. Barwick-Silk, S. Hardy, M. C. Willis, A. S. Weller, *J. Am. Chem. Soc.,* **2018,** 140, 7347-7357.
[99] A. I. Mckay, J. Barwick-Silk, M. Savage, M. C. Willis, A. S. Weller, *Chem. Eur. J.,* **2020,** 26, 2883-2889.
[100] D. V. Partyka, J. B. Updegraff Iii, M. Zeller, A. D. Hunter, T. G. Gray, *Dalton Trans.,* **2010,** 39, 5388-5397.
[101] M. Lankelma, V. Vreeken, M. A. Siegler, J. I. Van Der Vlugt, *Inorganics,* **2019,** 7,

[102] H. Schmidbaur, A. Schier, *Chem. Soc. Rev.,* **2012,** 41, 370-412.
[103] J. Wang, G. Meng, K. Xie, L. Li, H. Sun, Z. Huang, *ACS Catal.,* **2017,** 7, 7421-7430.
[104] Y. Zhu, V. H. Rawal, *J. Am. Chem. Soc.,* **2012,** 134, 111-114.
[105] Y. Jiao, M. S. Torne, J. Gracia, J. W. Niemantsverdriet, P. W. N. M. Van Leeuwen, *Catal. Sci. Techol.,* **2017,** 7, 1404-1414.
[106] B. C. Hamann, J. F. Hartwig, *J. Am. Chem. Soc.,* **1998,** 120, 3694-3703.
[107] H. C. Johnson, C. L. Mcmullin, S. D. Pike, S. A. Macgregor, A. S. Weller, *Angew. Chem. Int. Ed.,* **2013,** 52, 9776-9780.
[108] A. Staubitz, A. P. M. Robertson, M. E. Sloan, I. Manners, *Chem. Rev.,* **2010,** 110, 4023-4078.
[109] G. J. Kubas, *Metal dihydride and σ-bond complexes*. Kluwer, New York, **2001**.
[110] G. J. Kubas, *J. Organomet. Chem.,* **2014,** 751, 33-49.
[111] G. S. Mcgrady, P. Sirsch, N. P. Chatterton, A. Ostermann, C. Gatti, S. Altmannshofer, V. Herz, G. Eickerling, W. Scherer, *Inorg. Chem.,* **2009,** 48, 1588-1598.
[112] A. J. Bukvic, A. L. Burnage, G. J. Tizzard, A. J. Martínez-Martínez, A. I. Mckay, N. H. Rees, B. E. Tegner, T. Krämer, H. Fish, M. R. Warren, S. J. Coles, S. A. Macgregor, A. S. Weller, *J. Am. Chem. Soc.,* **2021,** 143, 5106-5120.
[113] A. G. Algarra, L. J. Sewell, H. C. Johnson, S. A. Macgregor, A. S. Weller, *Dalton Trans.,* **2014,** 43, 11118-11128.
[114] M. Shimoi, S. Nagai, M. Ichikawa, Y. Kawano, K. Katoh, M. Uruichi, H. Ogino, *J. Am. Chem. Soc.,* **1999,** 121, 11704-11712.
[115] M. A. Huertos, A. S. Weller, *Chem. Commun.,* **2012,** 48, 7185-7187.
[116] R. Dallanegra, A. P. M. Robertson, A. B. Chaplin, I. Manners, A. S. Weller, *Chem. Commun.,* **2011,** 47, 3763-3765.
[117] W. E. Piers, *Angew. Chem. Int. Ed.,* **2000,** 39, 1923-1925.
[118] A. Ariafard, M. M. Amini, A. Azadmehr, *J. Organomet. Chem.,* **2005,** 690, 1147-1156.
[119] T. Kakizawa, Y. Kawano, M. Shimoi, *Organometallics,* **2001,** 20, 3211-3213.
[120] Y. Kawano, M. Hashiva, M. Shimoi, *Organometallics,* **2006,** 25, 4420-4426.
[121] A. E. W. Ledger, C. E. Ellul, M. F. Mahon, J. M. J. Williams, M. K. Whittlesey, *Chem. Eur. J.,* **2011,** 17, 8704-8713.
[122] J. Mattiza, D. Albert, M. Stankevič, K. Dziuba, A. Szmigielska, K. M. Pietrusiewicz, H. Duddeck, *Tetrahedron: Asymmetry,* **2006,** 17, 2689-2696.
[123] T. N. Hooper, M. A. Huertos, T. Jurca, S. D. Pike, A. S. Weller, I. Manners, *Inorg. Chem.,* **2014,** 53, 3716-3729.
[124] M. Ingleson, N. J. Patmore, G. D. Ruggiero, C. G. Frost, M. F. Mahon, M. C. Willis, A. S. Weller, *Organometallics,* **2001,** 20, 4434-4436.
[125] N. Merle, G. Koicok-Köhn, M. F. Mahon, C. G. Frost, G. D. Ruggerio, A. S. Weller, M. C. Willis, *Dalton Trans.,* **2004,** 3883-3892.
[126] M. A. Huertos, A. S. Weller, *Chem. Sci.,* **2013,** 4, 1881-1888.
[127] Y. Gloaguen, G. Alcaraz, A. S. Petit, E. Clot, Y. Coppel, L. Vendier, S. Sabo-Etienne, *J. Am. Chem. Soc.,* **2011,** 133, 17232-17238.
[128] F. M. Conroy-Lewis, L. Mole, A. D. Redhouse, S. A. Litster, J. L. Spencer, *J. Chem. Soc., Chem. Commun.,* **1991,** 1601-1603.
[129] M. Brookhart, L. H. Green Malcolm, G. Parkin, *PNAS,* **2007,** 104, 6908-6914.
[130] E. Clot, O. Eisenstein, Agostic Interactions from a Computational Perspective: One Name, Many Interpretations. In *Principles and Applications of Density Functional Theory in Inorganic Chemistry II*, Kaltsoyannis, N.; McGrady, J. E., Eds. Springer: Berlin, **2004**; Vol. 113.
[131] M. Lein, *Coord. Chem. Rev.,* **2009,** 253, 625-634.
[132] G. Dos Passos Gomes, G. Xu, X. Zhu, L.-M. Chamoreau, Y. Zhang, O. Bistri-Aslanoff, S. Roland, I. V. Alabugin, M. Sollogoub, *Chem. Eur. J.,* **2021,** 27, 8127-8142.
[133] W. Scherer, A. C. Dunbar, J. E. Barquera-Lozada, D. Schmitz, G. Eickerling, D. Kratzert, D. Stalke, A. Lanza, P. Macchi, N. P. M. Casati, J. Ebad-Allah, C. Kuntscher, *Angew. Chem. Int. Ed.,* **2015,** 54, 2505-2509.
[134] M. Brookhart, M. L. H. Green, *J. Organomet. Chem.,* **1983,** 250, 395-408.
[135] M. P. Mitoraj, M. G. Babashkina, K. Robeyns, F. Sagan, D. W. Szczepanik, Y. V. Seredina, Y. Garcia, D. A. Safin, *Organometallics,* **2019,** 38, 1973-1981.
[136] W. Scherer, A. C. Dunbar, J. E. Barquera-Lozada, D. Schmitz, G. Eickerling, D. Kratzert, D. Stalke, A. Lanza, P. Macchi, N. P. M. Casati, J. Ebad-Allah, C. Kuntscher, *Angew. Chem. Int. Ed.,* **2015,** 127, 2535-2539.
[137] W. Scherer, V. Herz, A. Brück, C. Hauf, F. Reiner, S. Altmannshofer, D. Leusser, D. Stalke, *Angew. Chem. Int. Ed.,* **2011,** 50, 2845-2849.
[138] J. E. Barquera-Lozada, A. Obenhuber, C. Hauf, W. Scherer, *J. Phys. Chem. A,* **2013,** 117, 4304-4315.
[139] J. C. Lewis, J. Wu, R. G. Bergman, J. A. Ellman, *Organometallics,* **2005,** 24, 5737-5746.
[140] N. Ding, J. Zhang, T. S. A. Hor, *Dalton Trans.,* **2009,** 1853-1858.
[141] S. Schöler, M. H. Wahl, N. I. C. Wurster, A. Puls, C. Hättig, G. Dyker, *Chem. Commun.,* **2014,** 50, 5909-5911.
[142] F. Vidal, F. Jäkle, *Angew. Chem. Int. Ed.,* **2019,** 58, 5846-5870.
[143] A. M. Priegert, B. W. Rawe, S. C. Serin, D. P. Gates, *Chem. Soc. Rev.,* **2016,** 45, 922-953.

[144] H. Dorn, R. A. Singh, J. A. Massey, A. J. Lough, I. Manners, *Angew. Chem. Int. Ed.,* **1999,** 38, 3321-3323.
[145] J. R. Turner, D. A. Resendiz-Lara, T. Jurca, A. Schäfer, J. R. Vance, L. Beckett, G. R. Whittell, R. A. Musgrave, H. A. Sparkes, I. Manners, *Macromol. Chem. Phys.,* **2017,** 218, 1700120.
[146] T. J. Clark, J. M. Rodezno, S. B. Clendenning, S. Aouba, P. M. Brodersen, A. J. Lough, H. E. Ruda, I. Manners, *Chem. Eur. J.,* **2005,** 11, 4526-4534.
[147] A. W. Knights, M. A. Nascimento, I. Manners, *Polymer,* **2022,** 247, 124795.
[148] E. M. Leitao, T. Jurca, I. Manners, *Nature Chem.,* **2013,** 5, 817-829.
[149] H. Dorn, J. M. Rodezno, B. Brunnhöfer, E. Rivard, J. A. Massey, I. Manners, *Macromolecules,* **2003,** 36, 291-297.
[150] A. W. Knights, S. S. Chitnis, I. Manners, *Chem. Sci.,* **2019,** 10, 7281-7289.
[151] A. L. Colebatch, A. S. Weller, *Chem. Eur. J. ,* **2019,** 25, 1379-1390.
[152] A. B. Burg, R. I. Wagner, *J. Am. Chem. Soc.,* **1953,** 75,
[153] V. V. Korshak, V. A. Zamyatina, A. I. Solomatina, E. I. Fedin, P. V. Petrovskii, *J. Organomet. Chem.,* **1969,** 17, 201-212.
[154] H. Dorn, R. A. Singh, J. A. Massey, J. M. Nelson, C. A. Jaska, A. J. Lough, I. Manners, *J. Am. Chem. Soc.,* **2000,** 122, 6669-6678.
[155] A. Bartole-Scott, C. A. Jaska, I. Manners, *Pure Appl. Chem.,* **2005,** 77, 1991-2002.
[156] S. Pandey, P. Lönnecke, E. Hey-Hawkins, *Eur. J. Inorg. Chem.,* **2014,** 2014, 2456-2465.
[157] D. A. Resendiz-Lara, V. T. Annibale, A. W. Knights, S. S. Chitnis, I. Manners, *Macromolecules,* **2021,** 54, 71-82.
[158] H. Cavaye, F. Clegg, P. J. Gould, M. K. Ladyman, T. Temple, E. Dossi, *Macromolecules,* **2017,** 50, 9239-9248.
[159] C. Marquardt, T. Jurca, K.-C. Schwan, A. Stauber, A. V. Virovets, G. R. Whittell, I. Manners, M. Scheer, *Angew. Chem. Int. Ed.,* **2015,** 54, 13782-13786.
[160] C. A. Jaska, I. Manners, *J. Am. Chem. Soc.,* **2004,** 126, 9776-9785.
[161] M. E. Sloan, T. J. Clark, I. Manners, *Inorg. Chem.,* **2009,** 48, 2429-2435.
[162] T. N. Hooper, A. S. Weller, N. A. Beattie, S. A. Macgregor, *Chem. Sci.,* **2016,** 7, 2414-2426.
[163] A. Schäfer, T. Jurca, J. Turner, J. R. Vance, K. Lee, V. A. Du, M. F. Haddow, G. R. Whittell, I. Manners, *Angew. Chem. Int. Ed.,* **2015,** 54, 4836-4841.
[164] K. Lee, T. J. Clark, A. J. Lough, I. Manners, *Dalton Trans.,* **2008,** 2732-2740.
[165] U. S. D. Paul, H. Braunschweig, U. Radius, *Chem. Commun.,* **2016,** 52, 8573-8576.
[166] C. N. Brodie, T. M. Boyd, L. Sotorríos, D. E. Ryan, E. Magee, S. Huband, J. S. Town, G. C. Lloyd-Jones, D. M. Haddleton, S. A. Macgregor, A. S. Weller, *J. Am. Chem. Soc.,* **2021,** 143, 21010-21023.
[167] N. L. Oldroyd, S. S. Chitnis, V. T. Annibale, M. I. Arz, H. A. Sparkes, I. Manners, *Nature Communications,* **2019,** 10, 1370.
[168] F. Schön, L. M. Sigmund, F. Schneider, D. Hartmann, M. A. Wiebe, I. Manners, L. Greb, *Angew. Chem. Int. Ed.,* **2022,** 61, e202202176.
[169] H. Dorn, E. Vejzovic, A. J. Lough, I. Manners, *Inorg. Chem.,* **2001,** 40, 4327-4331.
[170] T. N. Hooper, A. S. Weller, N. A. Beattie, S. A. Macgregor, *Chem. Sci.,* **2016,** 7, 2414-2426.

2 Chapter Two – Rhodium complexes of *ortho*-aryl substituted DPEphos ligands. Reactivity and structural studies.

2.1 Preamble

In Chapter One, the [Rh(DPEphos)]$^+$ system was introduced, and several applications of this system in homogeneous catalysis were highlighted, such as: intermolecular hydroacylation,[1-3] hydroamination,[4] carbothiolation[5] and amine-borane dehydropolymerisation.[6, 7] The Schrock-Osborn precatalyst, [Rh(DPEphos)(diene)][anion] was used as a precursor in all of these examples. Schrock-Osborn complexes[8, 9] are a popular precatalyst, as they are easily prepared and a wide range of diphosphines are tolerated.[10] These complexes can also be activated by hydrogenation of the diene fragment in solution, leading to the formation of solvated or hydridic species, the nature of which is dependent on the solvent and the diphosphine ligand used.[11]

Ortho-aryl substituted phosphines were also presented in Chapter One, with many examples highlighting the effect that *ortho*-aryl substitution can have on fundamental coordination chemistry[12] and homogeneous catalysis.[13-16]

Within Chapter Two, a detailed investigation on the structure and reactivity of a range of Schrock-Osborn complexes with different *ortho*-aryl substituted DPEphos ligands is described. This Chapter will focus on the fundamental coordination chemistry of these *ortho*-aryl substituted complexes, with particular attention paid to M···H–C anagostic interactions observed. Following this, an investigation of the reactivity of these complexes, which gave rise to some previously unreported coordination chemistry, is described. The resultant products are highly influenced by the *ortho*-aryl substituent.

2.2 *Ortho*-aryl substituted DPEphos ligands

Four DPEphos-based ligands, which vary only by the *ortho*-aryl substituent, are used in this study (Figure 2.1). The four ligands are: *o*-H-DPEphos (**1-H**), *o*-Me-DPEphos (**1-Me**), *o*-OMe-DPEphos (**1-OMe**) and *o*-^{i}Pr-DPEphos (**1-^{i}Pr**). **1-H** and **1-Me** are commercially available, and were used as

received, whereas **1-OMe** was prepared via a literature procedure.[17] **1-^{i}Pr** is a novel ligand, newly synthesised for this investigation.

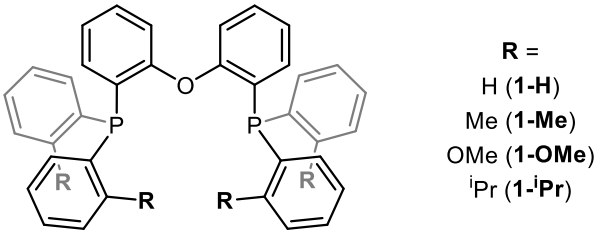

Figure 2.1. *Ortho*-aryl substituted DPEphos ligands used in this study.

2.2.1 Synthesis and characterisation of *ortho*-^{i}Pr-DPEphos

1-^{i}Pr was prepared via addition of in-situ formed Li[2-^{i}Pr-C_6H_4] to 2,2'-$(PCl_2)_2(C_6H_4)_2O$[17] at –78 °C (Scheme 2.1). The resultant air-stable phosphine was isolated via an aqueous work-up and recrystallised from pentane, yielding **1-^{i}Pr** as an analytically pure, white, crystalline material in a moderate yield (30%). **1-^{i}Pr** was fully characterised by NMR spectroscopy and single-crystal X-ray diffraction. C_1 symmertry is observed in the solid-state structure which also revealed no remarkable bond lengths or angles (Figure 2.2). At 298 K, a single ^{31}P environment is observed in the $^{31}P\{^{1}H\}$ NMR spectrum at δ –37.6 ($CDCl_3$), shifted upfield compared to the parent *o*-H-DPEphos, **1-H** (δ –16.4), but similar to **1-Me** (δ –34.6).[18]

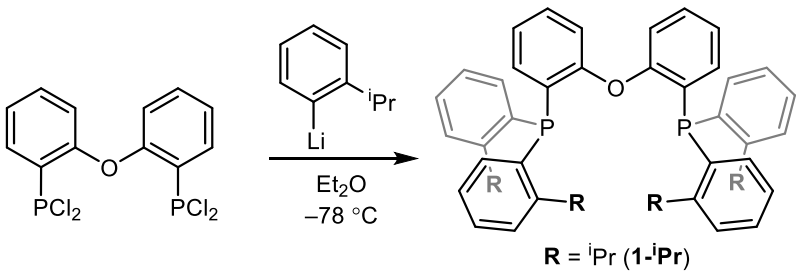

Scheme 2.1. Synthesis of **1-^{i}Pr**.

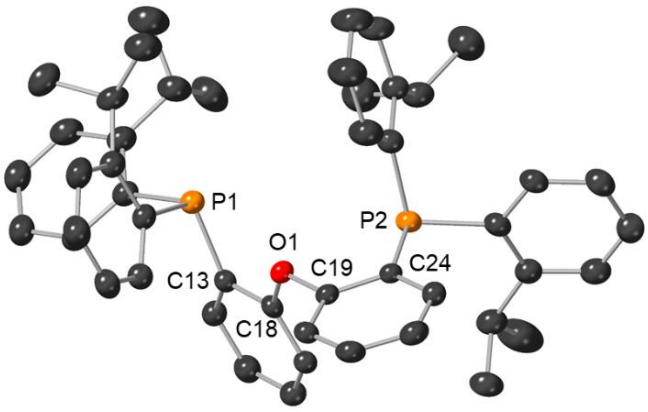

Figure 2.2. Crystallographically determined structure of **1-^{i}Pr**. Ellipsoids at the 50% probability level. Hydrogen atoms omitted for clarity. Key bond lengths (Å) and angles (°): P1-C13, 1.828(3); C13-C18, 1.403(4); C18-O1, 1.386(4); O1-C19, 1.390(4); C19-C24, 1.396(5); C24-P2, 1.839(3); C18-O1-C19, 1.218(4).

Interestingly, at 298 K, there is only one isopropyl methyl environment observed (δ 1.06, integral 24H) in the ^{1}H NMR spectrum, despite the diastereotopic nature of the isopropyl groups in the solid-state structure. This suggests low-energy inversion at the P atoms and rotation about the P–C(diphenylether) and C–C(isopropyl) bonds is accessible at room temperature, which makes the methyl groups equivalent on the NMR timescale (Scheme 2.2). Phosphorus inversion has been shown to be promoted by *ortho*-isopropyl substitution, for example, the energy barrier for planarisation of P(2,6-(^{i}Pr)$_2$-C$_6$H$_3$)$_3$ was calculated to be 37.5 kJ mol^{-1}.[19] For **1-^{i}Pr** at 203 K in CD_2Cl_2, multiple ^{31}P environments are observed and the ^{1}H spectrum becomes much more complex, consistent with the freezing out of different isomers. Multiple isomers could arise from restricted rotation about the P–C bond, giving different arrangments of the *ortho*-substituted aryl groups, similar to the gauche (g) and anti (a) arrangements observed for *trans*-[MCl$_2$(P{o-^{i}Pr-C$_6$H$_4$}$_3$)$_2$] (M = Pt and Pd).[12]

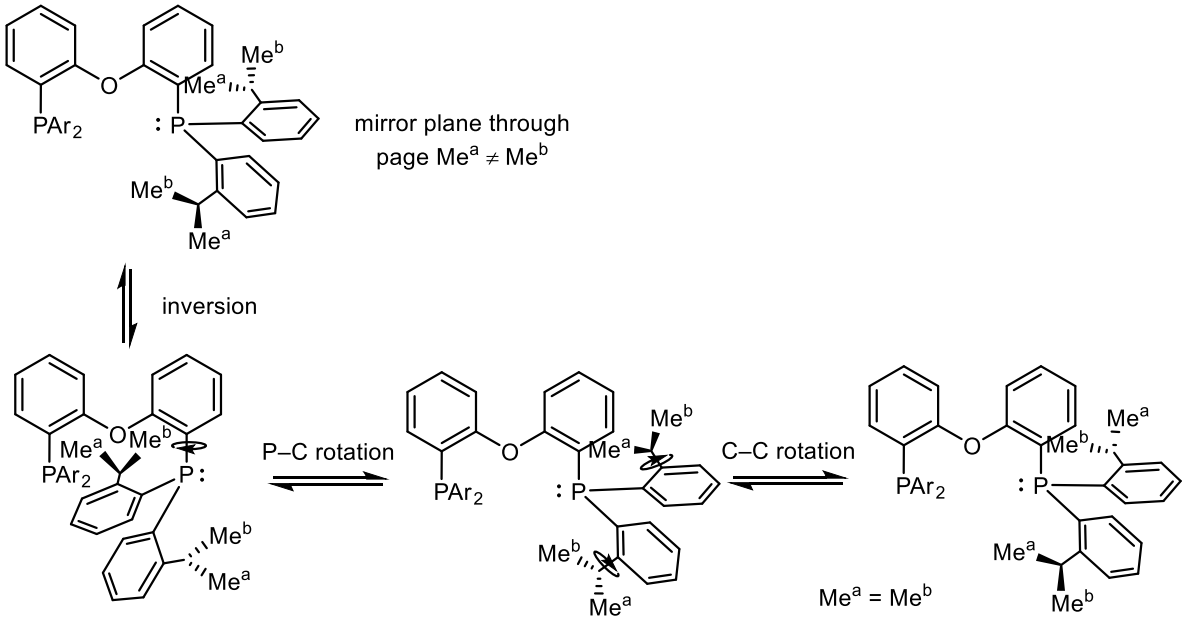

Scheme 2.2. Inversion and rotation process that makes the methyl groups in **1-^{i}Pr** equivalent.

2.3 Schrock-Osborn complexes of *ortho*-aryl substituted DPEphos ligands

2.3.1 Synthesis and solid-state characterisation

The respective Schrock-Osborn complexes of these ligands, [Rh(*o*-R-DPEphos)(NBD)][BAr$^{F}_{4}$] (**2-R**) were synthesised via addition of the appropriate ligand to a suitable Rh precursor in 1,2-$F_2C_6H_4$ solution at ambient temperature (Scheme 2.3). For **1-H**, **1-Me** and **1-OMe**, the precursor used was [Rh(NBD)(μ-Cl)]$_2$, followed by the addition of Na[BAr$^{F}_{4}$], acting as a halide extractor, to give [Rh(*o*-R-DPEphos)(NBD)][BAr$^{F}_{4}$] (R = H, **2-H**; R = Me, **2-Me** or R = OMe, **2-OMe**). The bulkiest ligand, **1-^{i}Pr**, did not coordinate via this method and only ^{31}P signals relating to free ligand were observed in the ^{31}P{^{1}H} NMR spectrum. Instead, stoichiometric addition of **1-^{i}Pr** to the precursor [Rh(NBD)$_2$][BAr$^{F}_{4}$] resulted in the formation of [Rh(*o*-^{i}Pr-DPEphos)(NBD)][BAr$^{F}_{4}$] (**2-^{i}Pr**). All four complexes were isolated as analytically pure orange microcrystalline solids in good yields (65-85%). Crystals suitable for single crystal X-ray diffraction were obtained via slow diffusion of pentane into 1,2-$F_2C_6H_4$ solutions of **2-R** at room temperature.

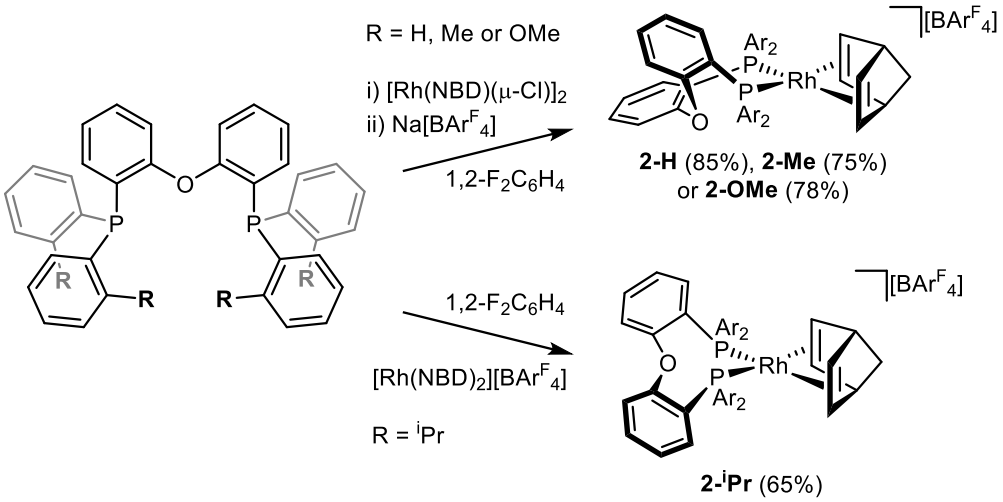

Scheme 2.3. Synthesis of Schrock-Osborn type complexes **2-R**.

Complex **2-H** has been published previously,[3] but the solid-state structure was not reported, and thus is included in this study. The solid-state structures of **2-R** all show a *cis*-κ²-P,P bonding arrangement of the *o*-R-DPEphos, and a η²η² NBD fragment, producing an overall pseudo square planar geometry around a Rh(I) centre for all for complexes (Figure 2.3A). In all cases, the oxygen atom is not coordinated to the rhodium [D(Rh···O) = 3.498(8)–3.5545(18) Å]. However, there is a difference in the P-O-P backbone arrangement. Closer inspection of the structures of **2-H**, **2-Me** and **2-OMe** reveals that the oxygen linker sits off the P1–Rh1–P2 plane with an O1 to P1–Rh1–P2 plane distance calculated at ~ 1.5 Å (Figure 2.3B). This backbone geometry has previously been described as envelope-like[20] and would result in overall C_1 symmetry if retained in solution. In contrast, the oxygen linker of the *o*-^{i}Pr-DPEphos ligand in **2-^{i}Pr**, sits closer to P1–Rh1–P2 plane (~0.4 Å). This also results in a non-crystallographic C_2 axis presumably forced by the bulky isopropyl groups.

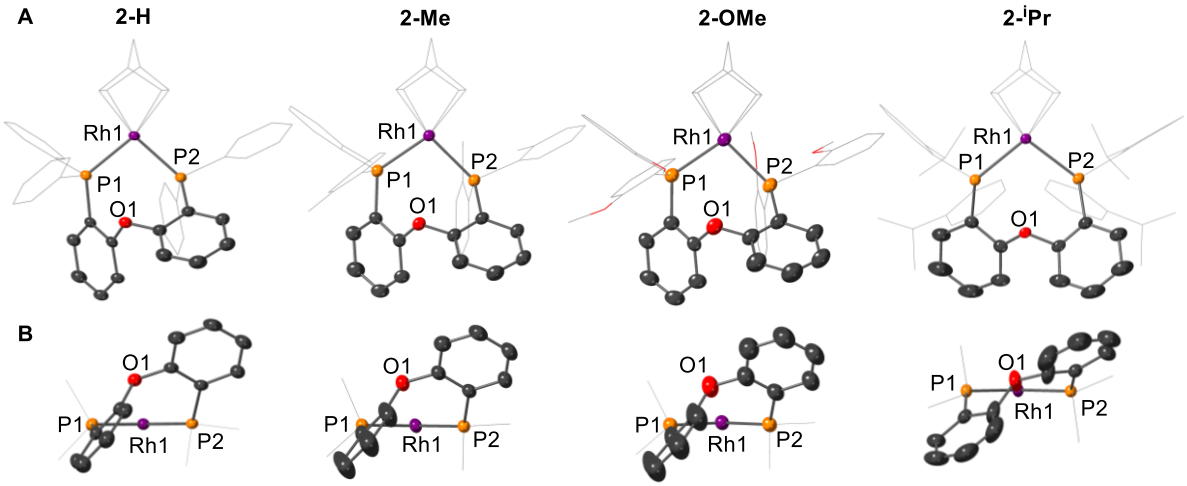

Figure 2.3. **A**) Crystallographically determined structures of the cationic portion of **2-R**. Ellipsoids are shown at the 50% probability level. Hydrogen and $[BAr^{F}{}_{4}]^{-}$ anions are not shown. Selected aryl groups and NBD ligands are shown in wireframe. **B**) End-on view of **2-R**, highlighting the backbone orientation.

The difference in ligand orientation is also reflected in the Rh–P bond lengths, which are ~ 0.1 Å longer in **2-^{i}Pr** compared to the other complexes (Table 2.1). The higher symmetry is also shown in the Rh–$C_{(NBD)}$ bond lengths, which are much more uniform in **2-^{i}Pr**. The Rh–P distances of 2.3368(6)-2.4256(5) Å and P–Rh–P angles of 98.58-103.91° within **2-R** are similar to those reported for [Rh(*cis*-κ^{2}-DPEphos)(NBD)][$CB_{11}H_{6}Br_{6}$]: 2.340(2) and 2.346(1) Å, and 100.12(5)° respectively.[2, 21]

Table 2.1. Key bond lengths and angles calculated from the solid-state structures of **2-R**.

Bond (Å) / Angle (°)	2-H	2-Me	2-OMe	2-^{i}Pr
Rh–P1	2.3392(9)	2.3514(6)	2.3813(7)	2.4482(7)
Rh–P2	2.3438(7)	2.3949(7)	2.3368(6)	2.4256(5)
Rh–O1	3.547(2)	3.5529(16)	3.5545(18)	3.498(8)
Rh–$C_{(NBD)}$ range	2.179(3)–2.215(3)	2.164(3)–2.236(3)	2.160(3)–2.210(3)	2.178(2)–2.184(2)
P1–Rh–P2	98.58(3)	100.79(2)	100.67(2)	103.91(2)

2.3.2 Solution-state NMR characterisation and behaviour

The room temperature NMR spectra of **2-R** in d_{6}-acetone solvent reflect the different substitution patterns on the DPEphos aryl groups. A single, sharp signal at δ 16.7 with doublet multiplicity [J(RhP) = 159 Hz] is observed in the $^{31}P\{^{1}H\}$ NMR spectrum of **2-H**, which matches the reported $^{31}P\{^{1}H\}$ signal (δ 17.0 in $CD_{2}Cl_{2}$).[3] In the ^{1}H NMR spectrum, three NBD ^{1}H environments in a 4:2:2 ratio are assigned to the alkene, methine and methylene signals respectively, suggestive of time-averaged C_{2v} symmetry,

different from that observed in the solid-state structure. For **2-Me** and **2-OMe**, on the other hand, broad resonances in the $^{31}P\{^{1}H\}$ and ^{1}H NMR spectrum are observed that provided no structural information. ESI-MS analysis gave molecular ions (m/z) of 789.20 and 853.18 respectively, consistent with the calculated values of 789.19 and 853.17 respectively and isotope patterns consistent with their formulations, and in agreement with solid-state structures of **2-Me** and **2-OMe**. The higher symmetry observed for **2-H**, and the broad resonances observed for **2-Me** and **2-OMe**, suggest that fluxional processes are operating at room temperature. Therefore, samples of **2-R** were cooled in d_6-acetone. At 183 K, the previously sharp ^{31}P signal for **2-H** had broadened and the doublet multiplicity was lost. The ^{1}H signals were too broad to provide useful structural information. Evidently, any fluxional process is not frozen out at 183 K for **2-H**, so a sample was further cooled to 140 K in $CDCl_2F$ solvent (m.p. = 138 K).[22] This revealed two distinct ^{31}P environments at δ 21.5 and 13.8, observed as broad doublets with coincidentally the same *J*(RhP) values of 154 Hz (Figure 2.4). P-P coupling was not resolved due to the broad linewidth of the signals (FWHM = 80 Hz). The ^{1}H signals are still broad and not useful for assignment at this temperature, however, one aromatic signal was observed shifted downfield compared to the others, at δ 8.32. **2-Me** and **2-OMe** did not require to be cooled as low for the observation of the low temperature regime. Two distinct ^{31}P signals are observed in the $^{31}P\{^{1}H\}$ NMR spectrum of **2-Me** at 203 K in d_6-acetone (δ 18.0 and 1.8). The signals exhibit doublet of doublet multiplicity, comprising of coupling to rhodium [*J*(RhP) = 161 and 152 Hz] and *cis*-P,P coupling [*J*(PP) = 28 Hz].[21] Four methyl environments and four NBD alkene signals are also observed in the ^{1}H NMR spectrum, their assignment confirmed by a HSQC experiment at 203 K. These data are reflective of a complex with C_1 symmetry. As the sample is warmed, the two ^{31}P signals broaden, and a new doublet signal appears at δ 8.5 with *J*(RhP) = 154 Hz. At 363 K, only one broad ^{31}P signal, centred at δ 10 is observed, suggestive of C_2 symmetry.

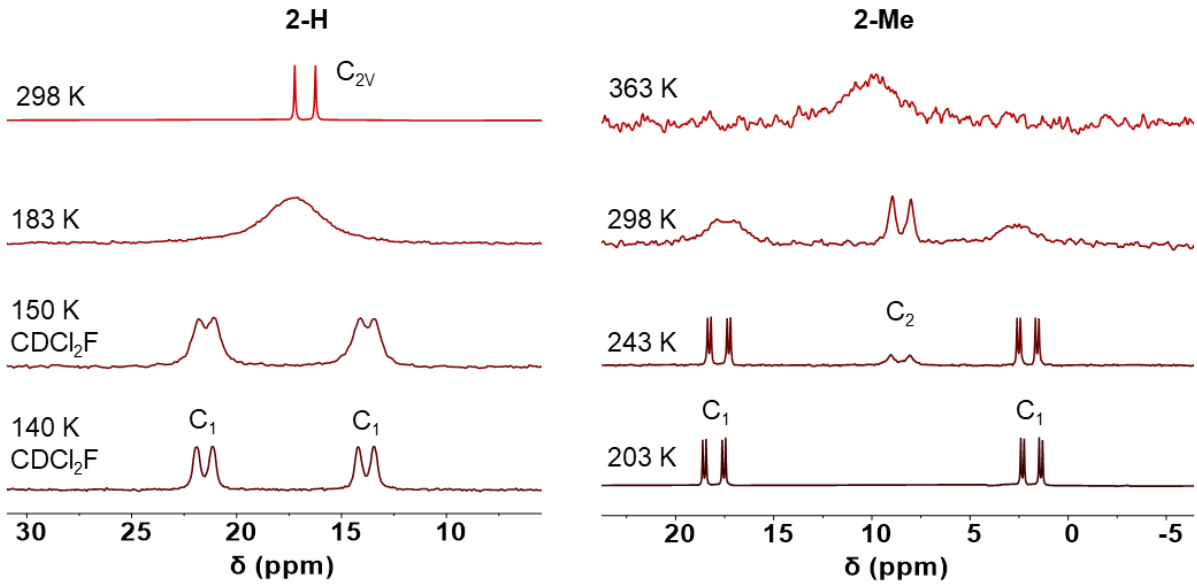

Figure 2.4. Variable temperature $^{31}P\{^{1}H\}$ NMR of **2-H** and **2-Me** (202 MHz, d_6-acetone unless specified otherwise).

The same pattern and changes with temperature were observed with **2-OMe**, albeit that the spectrum at 363 K showed broad doublet multiplicity. It is clear that a fluxional process is occurring, which can be frozen out at low temperature to give C_1 species. For **2-Me** and **2-OMe**, a species with C_2 symmetry is also observed at intermediate temperatures. As the temperature is raised the dynamic process occurs on the NMR timescale and the signals broaden, until eventually, at even higher temperatures the signals coalesce to a single peak with time-averaged C_{2V} symmetry. It is clear that this process is occurring fastest in the least bulky **2-H**. The low temperature regimes of **2-H**, **2-Me** and **2-OMe** reflects the envelope-like[20] arrangement of the *o*-R-DPEphos ligands (i.e. C_1 symmetry). We propose that there is an equilibrium between two enantiomers of this C_1 arrangement in which a ring-flipping process interconverts the two isomers via a symmetric C_2 state (Scheme 2.4). At higher temperatures, this process occurs faster than the NMR timescale and time-averaged C_{2V} symmetry is observed. The C_2 state is seen in the intermediate temperatures in the $^{31}P\{^{1}H\}$ NMR spectra of **2-Me** and **2-OMe** and we propose this complex is more similar to the solid-state structure of **2-^{i}Pr** in which the oxygen sits in the equatorial plane, giving non-crystallographic C_2 symmetry.

Line-shape analysis was conducted by Dr Alex Heyam (University of York) using Spinach[23] line-shape modelling software (Figure 2.5). The energy barriers for this process were calculated. Linear regression of the line-shape modelling of **2-Me** and **2-OMe** provided $\Delta G^{\ddagger}$(183 K) values of 43 (±1) and

38 (±1) kJ mol^{-1} respectively for the exchange between two C_1 enantiomers via a ring-flipping process. The fact that both C_1 and C_2 symmetry species are observed for **2-Me** and **2-OMe** suggests that they must be in slow equilibrium with one another, and on raising the temperature to 363 K, all of the isomers start to rapidly interconvert. This equilibrium was incorporated into the line-shape fitting (Figure 2.5). For **2-H**, the use of unlocked $CDCl_2F$ solvent gave unreliable line-shape modelling data but simple calculations from the coalescence point at 183 K gave a rate of exchange of 3400 (±100) s^{-1} and a corresponding energy barrier of $\Delta G^{\ddagger}$(183 K) = 31 (±1) kJ mol^{-1}. This is consistent with the variable temperature NMR data, i.e. the rate of exchange is in the order **2-H** > **2-Me** ≳ **2-OMe**. The lowest energy barrier is with the least bulky ligand. The barrier to fluxionality in **2-Me** is slightly lower than **2-OMe**, and we attribute this to the larger steric encumbrance of the hydrogens on CH_3 compared to oxygen lone pair on the ether in **2-OMe** which has more flexibility to twist the methyl group and reduce the steric congestion.

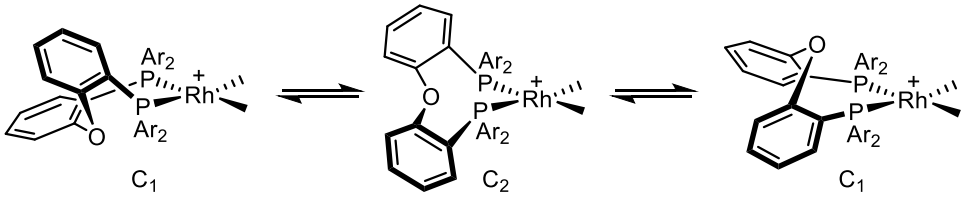

Scheme 2.4. Proposed fluxional process occurring in **2-H**, **2-Me** and **2-OMe** in solution.

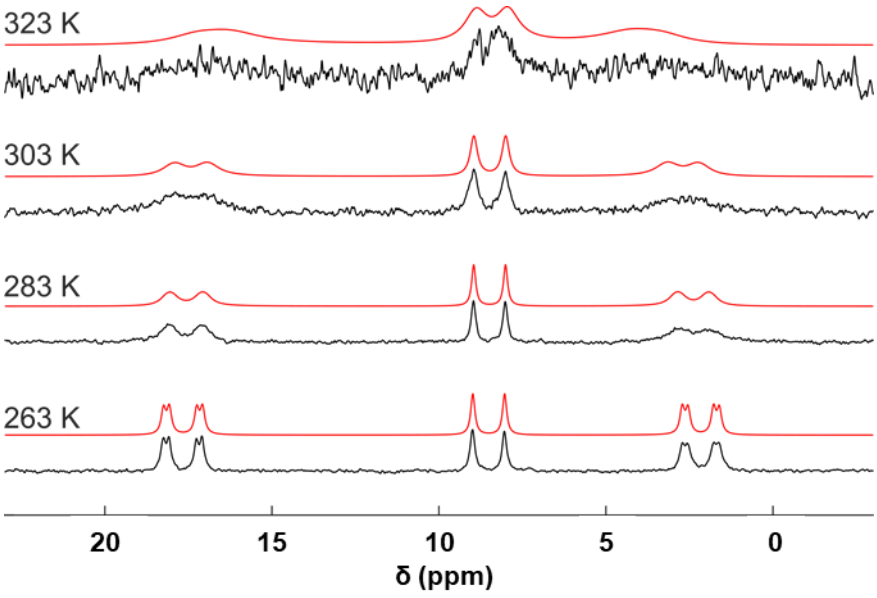

Figure 2.5. Experimental (black) and simulated (red) $^{31}P\{^1H\}$ NMR spectra of **2-Me** at different temperatures (CD_2Cl_2, 202 MHz). Line-shape simulation was conducted using Spinach.[23]

Similar backbone flipping processes have been reported in [RuHCl(CO)(PPh_3)(Xantphos)]. In this complex, the backbone in the Xantphos ligand flips between above and below the equatorial plane with a coalescence point at 328 K and an energy barrier of 57 (±5) kJ mol^{-1}.[24] Similarly, Thixantphos-based ligands (Thixantphos = 4,6-bis(diphenylphosphanyl)-2,8-dimethylphenoxathiine) also undergoes a similar backbone flipping process in Ni(Thixantphos)$_2$ complexes [$\Delta G^{\ddagger}$(293 K) ≈ 60 kJ mol^{-1}].[25]

2-^{i}Pr exhibits a non-crystallographic C_2 axis in the solid-state structure (*vide infra*) and this is carried forward into solution. In the $^{31}P\{^{1}H\}$ NMR spectrum in d_6-acetone, a sharp doublet is observed for [*J*(RhP) = 153 Hz], shifted 58.4 ppm downfield compared to free **1-^{i}Pr**, consistent with phosphine coordination.[26] It is important to note that **2-^{i}Pr** exhibited no signs of fluctuation as on cooling to 183 K there is essentially no change in the chemical shift or line shape. The $^{31}P\{^{1}H\}$ and ^{1}H NMR spectra remained unchanged between 183 and 298 K (Figure 2.6) and therefore we suspect the bulky isopropyl groups lock the complex into a fixed position.

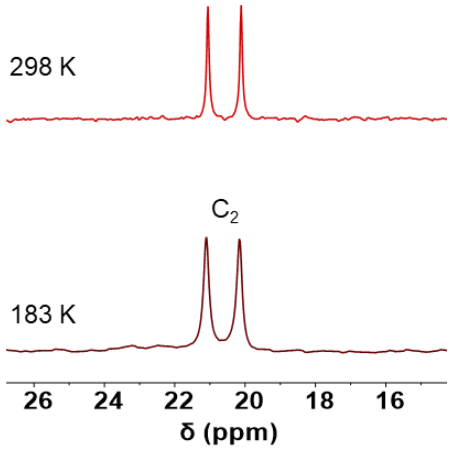

Figure 2.6. $^{31}P\{^{1}H\}$ NMR spectrum of **2-^{i}Pr** at 298 and 183 K, showing no major change (202 MHz, d_6-acetone).

The C_2 symmetry of **2-^{i}Pr** is also apparent in the ^{1}H NMR spectrum. Four CH_3 and two C*H*(CH_3) signals are assigned to the isopropyl groups, and four NBD signals in a 2:2:2:2 ratio are observed, which is consistent with every signal comprising of two chemically equivalent groups (Figure 2.7). Interestingly, a downfield shifted aromatic signal, integral 2H, was observed at δ 9.34, exhibiting doublet of doublet multiplicity. Selective ^{31}P and ^{1}H decoupling experiments revealed values of *J*(PH) = 17 Hz and *J*(HH) = 7 Hz for this multiplet, which suggests this signal corresponds to an *ortho*-aryl proton, with three-bond coupling to both a ^{31}P and a ^{1}H. This signal was observed at all temperatures for **2-^{i}Pr**. Similar downfield

chemical shifts between δ 8.5-9.5 have been reported by Pringle and co-workers in *ortho*-methyl and *ortho*-isopropyl monophosphine ligands in Pt complexes, namely, $[PtCl_2(PAr_3)_2]$ (Ar = *o*-Me,*p*-OMe-C_6H_3 and *o*-^{i}Pr-C_6H_4, **i-2**).[12] Upon closer inspection of the low temperature NMR data of **2-H**, **2-Me** and **2-OMe**, similar downfield shifted signals are also observable and are discussed in detail next.

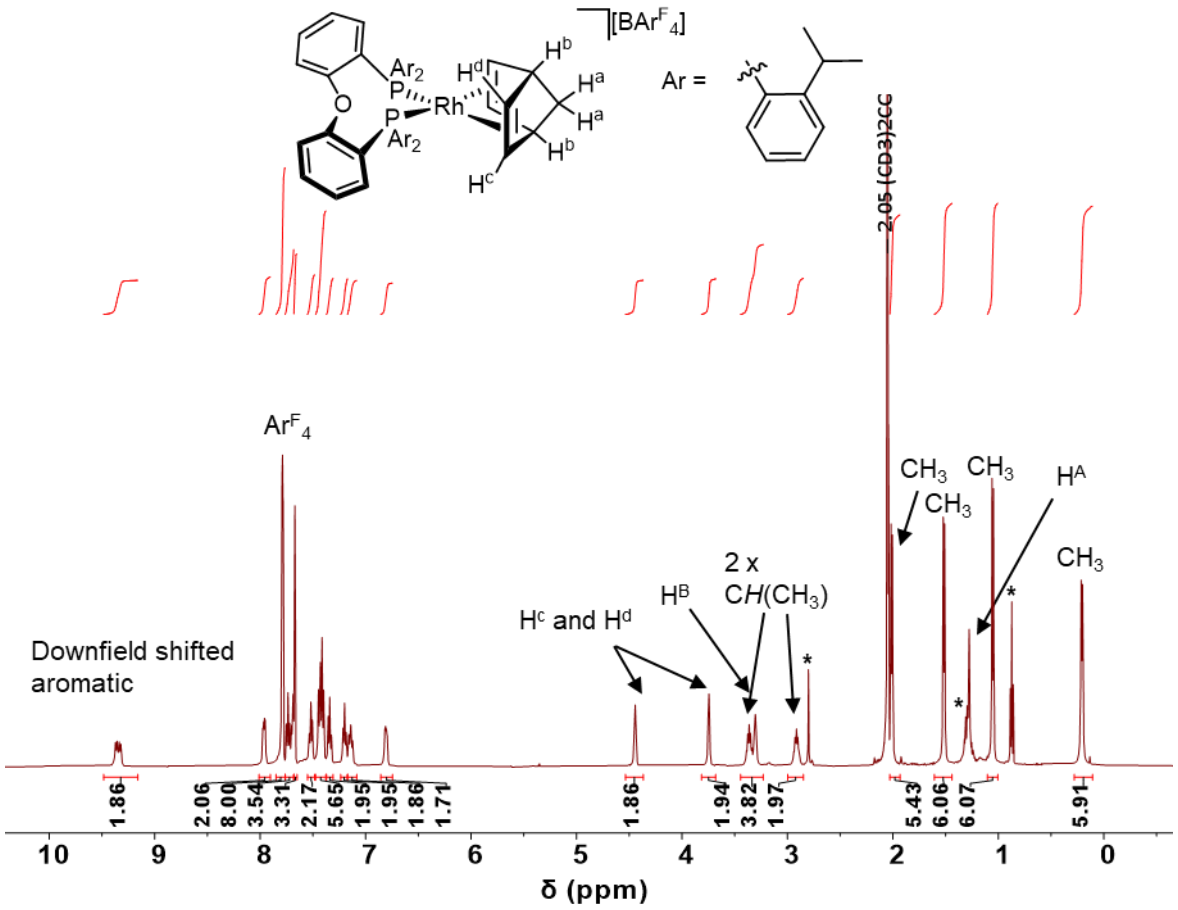

Figure 2.7. ^{1}H NMR spectrum of **2-^{i}Pr**, highlighting the C_2 symmetry and an unusual downfield shifted aromatic signal (500 MHz, d_6-acetone, 298 K). * Denotes a pentane or unknown impurity.

2.3.3 Assignment and comparison of Rh···H–C anagostic interactions

Downfield shifted ^{1}H signals are one of the characteristics of M···H–C anagostic interactions[27] (see section 1.9). Figure 2.7 shows the downfield shifted signal in **2-^{i}Pr**, which were not observed in the room temperature spectra of **2-H**, **2-Me** and **2-OMe**. However, cooling the samples also revealed downfield signals for these three complexes (Figure 2.8). The temperature required to see these signals could be correlated to the fluxional processes observed in the $^{31}P\{^1H\}$ NMR spectra. **2-H** required cooling to 140 K, **2-Me** 183 K and **2-OMe** 223 K. The same doublet of doublet multiplicity, comprising *J*(PH) (~ 17 Hz)

and *J*(HH) (~ 7 Hz), was observed in all of them apart from **2-H**, which is likely due to the low temperature limit not being reached, even at 140 K. The relative integral of each signal, compared to the Ar^F aromatic signals, are not the same: **2-H**, 2H; **2-Me**, 1H, **2-OMe**, 1H and **2-^{i}Pr**, 2H. Minor isomers are also present in **2-OMe**, these could be due to the freezing out of slightly different aryl group arrangements which are not observed for the *o*-methyl variant, potentially due to the increased steric bulk of OMe compare to Me.

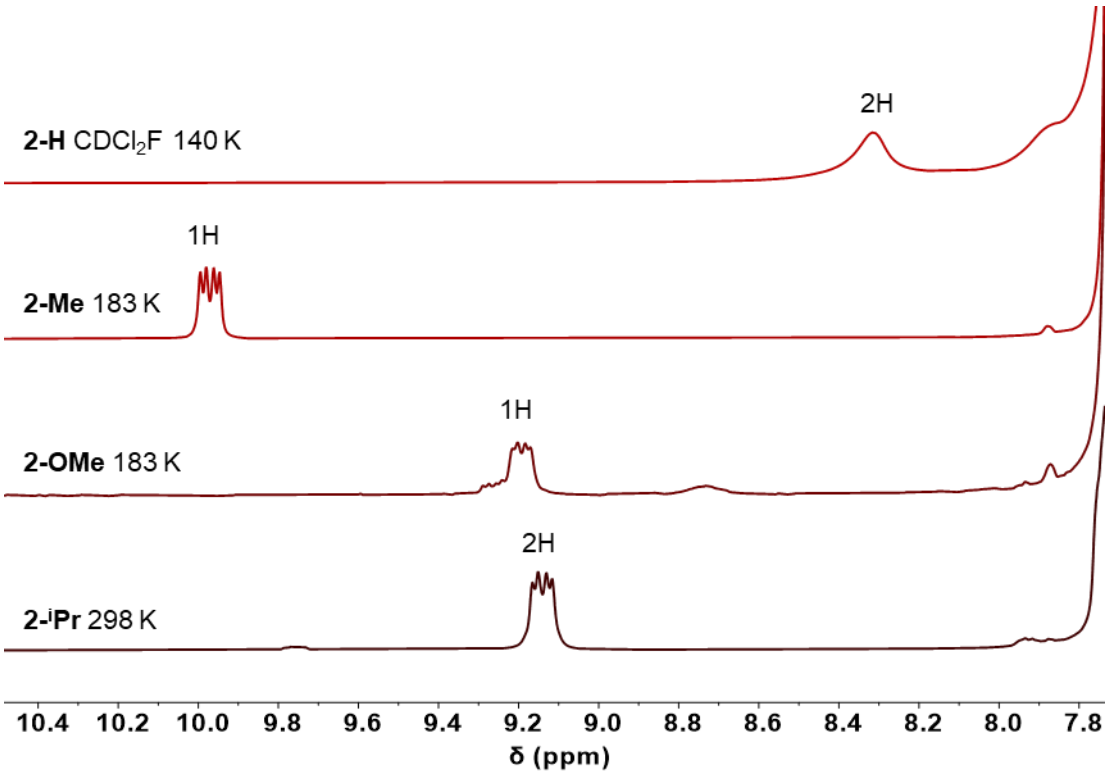

Figure 2.8. The downfield region of the ^{1}H NMR spectra of **2-R** (500 MHz, d_6-acetone unless specified otherwise).

Returning to the solid-state structures reveals that the integral of these signals coincide with the number of axially positioned *ortho*-aryl protons from the *o*-R-DPEphos ligand that are in a relatively close approach to the rhodium (Figure 2.9). The coupling patterns observed in the downfield shifted signals [^3J(PP) (~ 17 Hz) and ^3J(HH) (~ 7 Hz)], are consistent with the assignment of them as *ortho*-protons on the substituted aromatic groups. All of the protons were geometrically placed in calculated positions for **2-R**. The solid-state structure of **2-H** shows two *ortho*-protons in the apical position (H1 and H36), situated 2.92 and 2.97 Å from the rhodium centre respectively. The Rh–H–C bond angles are 114.7(2)° (H1) and 122.6(2)° (H36). **2-Me** contains one *ortho*-aryl proton (H1), positioned 2.57 Å from the Rh in the apical position. *Trans* to this proton is a methyl proton (H47a), only 2.63 Å from the Rh atom. This

is an example of a rarer alkyl anagostic interaction.[28] **2-OMe** also contains one *ortho*-aryl proton (H1) in a similar apical position to that in **2-Me** [D(Rh···H–C) = 2.88 Å], whereas **2-^{i}Pr** shows two aryl C–H to be in close approach to the rhodium [D(Rh···H–C) = 2.47 and 2.58 Å] (Figure 2.9) with Rh–H–C bond angles of 135.5(1)° and 132.7(1)°. These characteristics sit confidently within the definition of an anagostic interaction.[27] These data show that these four complexes contain an *ortho*-aryl anagostic interaction, and thus present an excellent opportunity for a detailed study of these interactions in a coherent set of complexes. **2-^{i}Pr** contains two crystallographically inequivalent anagostic protons so we suggest a very low energy fluxional process makes them equivalent in solution.

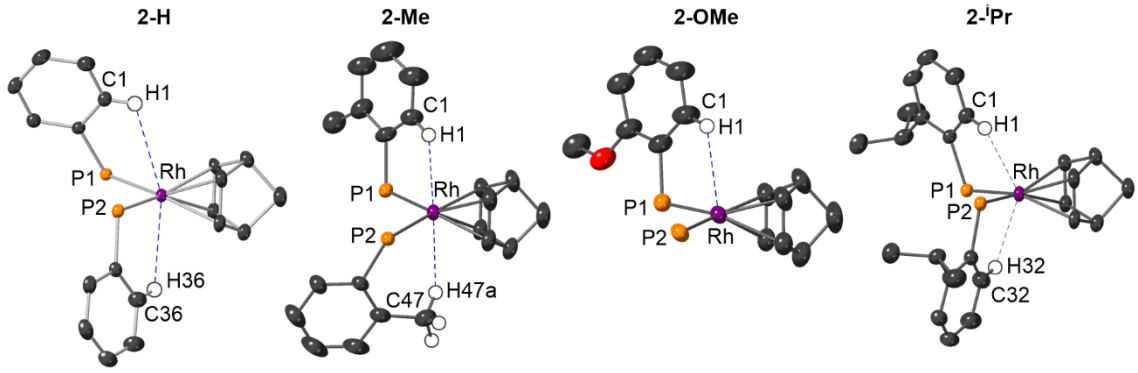

Figure 2.9. Reduced solid-state structures of **2-R**, highlighting the Rh···H-C anagostic interactions. Ellipsoids are shown at the 50% probability level. Aromatic groups and hydrogen atoms not involved in anagostic interactions are removed for the sake of clarity. Hydrogen atoms are placed in calculated positions.

As the downfield shifted ^{1}H signals can be correlated with relatively close Rh···H–C interactions in the solid-state, the change in chemical shift of the effected protons between the free ligands (**1-R**), and the subsequent rhodium complexes (**2-R**) can be compared. The *ortho*-aryl proton signals were assigned in **1-R** via a series of 2D NMR experiments. The change in chemical shift values on coordination to the metal are summarised in Table 2.2. CD_2Cl_2 was used as the solvent because the not all of the free ligands are soluble in d_6-acetone. The sample temperatures for **2-R** are 203 K (or 140 K for **2-H**) in order to observe the downfield shifted signals of the anagostic protons, whereas the ligands, **1-R**, were measured at 298 K as different isomers were present at low temperature due to restricted rotation of the aromatic groups.[12] The *ortho*-protons in question shifted downfield between 0.99 and 2.82 ppm. These are slightly smaller changes than the aryl anagostic interactions reported by Bergman for $[RhCl(^{i}Pr_2POXy)(PPh_3)]_2$ (Xy = 2,3-xylyl, **i-48**) [$\Delta\delta(^{1}H)$ = 3.2 ppm][29] and Dyker's palladium

cycloimmidate complexes (Figure 2.11) [$\Delta\delta(^1H)$ = 3.3 ppm],[28] but consistent in shift direction. A comparison of the chemical shifts for **2-Me** at 203 K and **1-Me** at 298 K is shown in Figure 2.10. One aromatic signal and one CH_3 signal are shifted downfield by 2.82 and 1.30 ppm respectively, compared to free **1-Me**. Although only one methyl proton is positioned in the region for an anagostic interaction in the solid-state structure, it is assumed that the CH_3 group is rotating freely in solution, and we are observing a time-averaged signal in the ^1H NMR spectrum, which is shifted 1.30 ppm downfield at δ 3.53. This is a smaller change in shift compared to the methylene anagostic in Dyker's palladium cycloimmidate complexes (Figure 2.11) [$\Delta\delta(^1H)$ ~ 4 ppm]. However, the downfield shifted methyl signal in **2-Me** is a weighted average of one anagostic proton and two terminal protons. Computationally calculated ^1H chemical shifts from a fixed geometry of **2-Me** were conducted by Arron Burnage using nuclear independent chemical shifts (NICS). The chemical shift of the methyl anagostic proton was calculated to be at δ 6.0, with an average of δ 3.9 for all three protons within the methyl group – in good agreement with the experimental observation (δ 3.53) (see later for more computational details). Using the same weighted average approach in the experimental data produces a rough value for the bridging Rh···H–C proton, to be δ 6.07 (assuming the terminal C–H ^1H signals are at the same chemical shift as the free ligand, at δ 2.26). Moreover, this CH_3 signal is still shifted noticeably downfield compared to the other three CH_3 signals in **2-Me** (δ 1.80, 1.72 and 1.55).

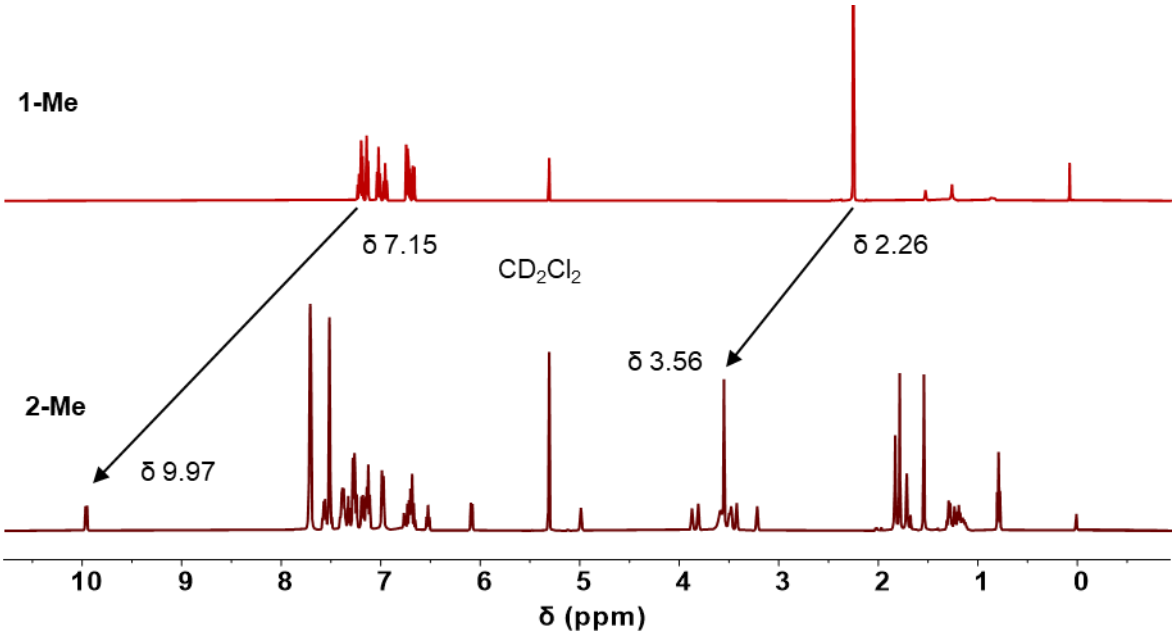

Figure 2.10. ^1H NMR chemical shift changes of the anagostic protons in the free ligand, **1-Me**, and in the rhodium complex, **2-Me** (500 MHz, CD_2Cl_2 measured at 298 K for **1-Me** and 203 K for **2-Me**).

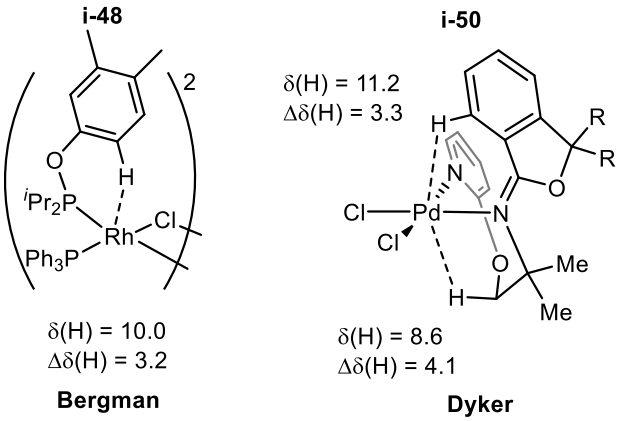

Figure 2.11. Previously reported examples of anagostic interactions.[28, 29]

Scherer's pioneering work on the chemical shift changes in agostic and anagostic protons (see section 1.9) describes the influence of the topological orientation of the interacting C–H group on chemical shift.[30] In light of this, we have analysed the same geometrics as Scherer's investigations using the solid-state structures of **2-R** (Figure 2.12) and compared them with the spectroscopic observations (Table 2.2). These geometrics include: D(Rh···H), the C–H–Rh angle (θ), the Rh···H to RhP_2 plane angle (Φ) and the Rh–P/C–H torsion angle (Ψ) (Figure 2.12). Firstly, the magnitude of the change in chemical shift of the *ortho*-aryl proton goes as follows: **2-Me** > **2-OMe** > **2-^{i}Pr** > **2-H**. This trend does not correlate with the D(Rh···H) values, in which the shortest distance is in **2-^{i}Pr**.

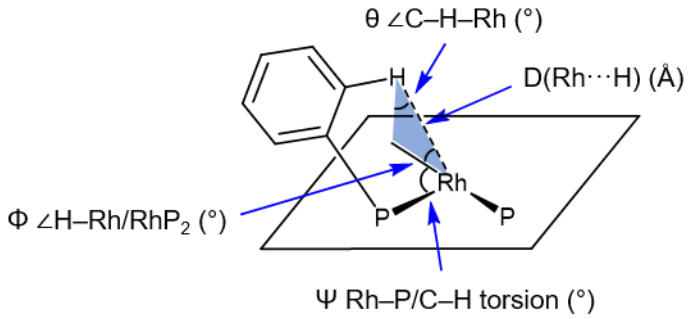

Figure 2.12. Geometrics used to structurally analyse the aryl-anagostic interactions in **2-R**.

The C–H···Rh angles (θ) are all reasonably wide (114 to 136 °), but once again, do not correlate with the trend in the Δδ(^{1}H) values. The angle between the Rh···H bond and the RhP_2 plane (Φ) is a measure of how axial the proton is positioned with regard to the RhP_2 plane. Values closer to 90° reflect a more apical proton, and values nearer to 0° are in the equatorial plane. In all four cases, the protons are positioned closer to the apical position, with similar Φ values of 58.0-64.3°. Lastly, the Rh–P/C–H torsion

angle (Ψ), indicates how twisted the C–H bond is compared to the Rh–P vector. Similar Ψ values throughout **2-R** (–8.2° to 1.7°) suggest that there is minimal twisting of the phenyl group and does not appear to affect the chemical shift change observed. One of the protons in **2-H** is twisted away compared to the other complexes [θ = 114.7°, Φ = 42.0°] but has a similar D(Rh···H) distance [2.92 Å]. The methyl anagostic interaction in **2-Me** is positioned in a similar manner, albeit with a slightly wider C–H–Rh angle (θ = 144.2°) and positioned closer to the 'perfectly' axial position (Φ = 69.3°).

Table 2.2. Solid-state and spectroscopic metrics of the aryl-anagostic interactions in **2-R**.

	2-H	**2-Me**	**2-OMe**	**2-^{i}Pr**
θ ∠C–H–Rh (°)[a]	114.7(2) 122.6(2)	129.8(2) (144.2(2))[c]	121.6(7)	135.5(1) 132.7(1)
Φ ∠H–Rh/RhP$_2$ (°)[a]	63.1, 58.0	64.3, (69.3)[c]	63.9	64.3, 64.3
Ψ Rh–P/C–H torsion (°)[a]	42.0, 1.7	1.3	– 6.2	– 1.4, –8.2
D(Rh···H) (Å)	2.92, 2.97	2.57, (2.63)[c]	2.88	2.47, 2.58
δ(^{1}H) (ppm)	8.32	9.97 (3.56)[c]	9.19	9.14
Δδ(^{1}H) (ppm)[b]	+0.99-1.11[d]	+2.82 (+1.3)[c]	+2.34	+1.85

[a] See Figure 2.12 for diagram of metrics. [b] Difference in chemical shift of the *ortho*-aryl proton in **2-R** (500 MHz, CD_2Cl_2, 203 K) and the free ligands **1-R** (CD_2Cl_2, 295 K). [c] Numbers in parenthesis associated with anagostic methyl group. [d] The *ortho*-protons could not be unambiguously assigned.

One noticeable relationship is between the Rh···H distance and the Rh–H-C angle of the aryl anagostic interactions. The shortest contacts are observed in **2-^{i}Pr** [2.47 and 2.58 Å] which also reflects with widest Rh–H-C angles [135.5(1) and 132.7(1)°]. **2-Me** shows the next closest contact and widest Rh–H–C angles in this respect, followed by **2-OMe**, then **2-H**. This also correlates with the steric bulk of the ligand. This may be a result of the bulkier ligands forcing the aromatic group into the position which leads to the anagostic interaction. As we have seen in **2-^{i}Pr**, the steric bulk fixes the ligand into one position with overall C_2 symmetry, compared to the less bulky alternatives that undergo fluxional processes on the NMR timescale with C_1 symmetry observed at low temperature and time-average C_{2V} symmetry at higher temperature.

With no clear correlations between chemical shift and structural positioning of the Rh···H–C in the experimental data, we turned to our computational collaborators, Arron Burnage and Professor Stuart Macgregor (Heriot-Watt University) for a deeper study of the anagostic bonding interactions within **2-R**. Beginning from the experimental solid-state structures, as determined by single-crystal X-ray crystallography, the cationic portion of **2-R**, **[2-R]$^{+}$**, were optimised with the heavy atoms fixed at their observed positions and the H atoms optimised. This resulted in slightly shorter calculated Rh···H

distances. The electronic structures were then interrogated by Quantum Theory of Atoms In Molecules (QTAIM) and Non-Covalent Interactions (NCI) plots. The molecular graph showing the contour plot of the charge density and the non-covalent interactions plot of **[2-Me]**$^+$ are shown in Figure 2.13, and is used as example of the anagostic interactions observed in all of **[2-R]**$^+$. There is a clear critical bond point between the Rh and H1 (*ortho*-aryl proton) and H47a (methyl proton) with small electron densities [$\rho(r)$] calculated at these bond critical points, indicative of weak interactions (0.022 and 0.020 au respectively). For all of **[2-R]**$^+$, only minimal electron density was calculated at thee bond critical points [$\rho(r)$ = 0.011-0.026, Table 2.3]. Notably, both of the bonding pathways pass through regions of charge concentration around the Rh (red contours). This is consistent with Scherer's work, which stated that anagostic protons approach a metal centre through regions of charge concentration,[30] quite often filled d_{z2} orbitals, which results in a downfield shift of the ^{1}H signal.[31] The non-covalent interactions plot suggests that there is some hydrogen-bonding character, as there are weakly stabilising (turquoise regions) interactions between Rh and H1 and H47a. These observations are consistent across all four cations, **[2-R]**$^+$.

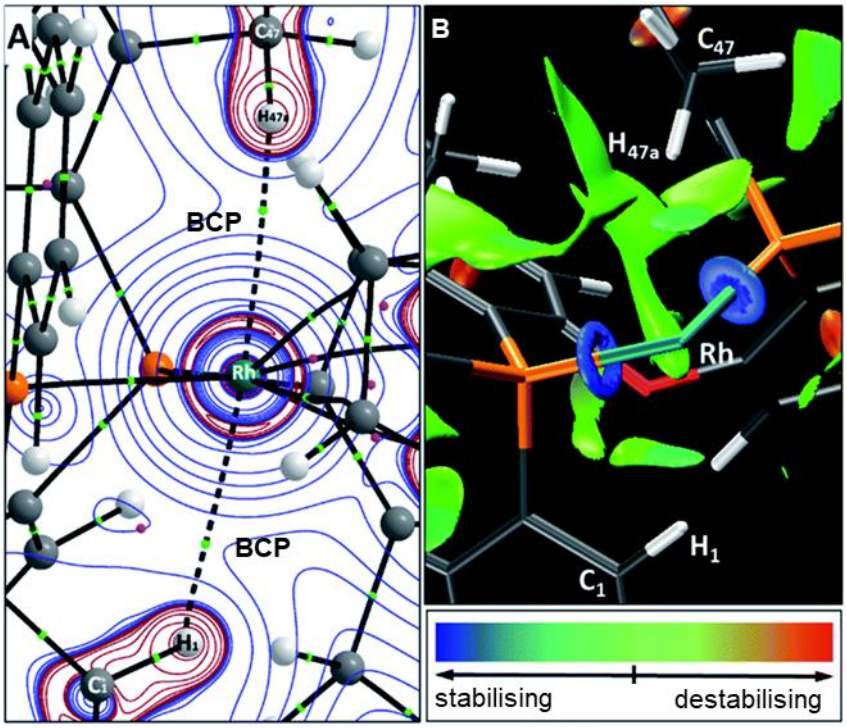

Figure 2.13. **A**) Molecular graph of **[2-Me]**$^+$ showing the contour plot of the charge density. BCP = bond critical point. Blue contours show areas of charge depletion and red contours show areas of charge concentration. **B**) Non-covalent interactions plot, highlighting the weakly stabilising interactions between Rh and H1 and H47a. The NBD ligand is removed for clarity. Key shows isosurface colouring.

The computed chemical shifts of these protons match well with the experimental data, albeit calculated to be slightly more downfield (Table 2.3). The largest difference between experimental and computational is observed in **[2-H]$^+$** (~ 1 ppm) which is attributed to the low temperature regime not being fully frozen out, as shown by the broadness of the ^{1}H signal. As previously mentioned, the experimental methyl anagostic shift in **[2-Me]$^+$** (δ 3.56) is an average of a freely rotating methyl group. The specific shift for the methyl proton in contact with the rhodium, H47a, is calculated to be δ 6.0. This equates as a change in chemical shift of $\Delta\delta(^1H)$ = 2.7 ppm, which is similar to Dyker's report of an alkyl anagostic interaction (Figure 2.11, $\Delta\delta(^1H)$ = 4.1 ppm).[28]

The electronic contributions of these interactions, as shown by a natural bonding orbitals analysis, were the same in all four cases. The main bonding contribution is from filled Rh orbitals, namely a d_{z2} orbital, into the vacant σ*(C–H). Although the main contribution, these donations are still weak, with the strongest being in **[2-^{i}Pr]$^+$** (8.98 and 6.70 kcal mol^{-1}) and the weakest in **[2-H]$^+$** (1.33 and 1.22 kcal mol^{-1}) (Table 2.3). A minor component was calculated to be donation from the σ(C–H) into vacant metal orbitals, although this was only between 0.5 and 2.1 kcal mol^{-1}.

Table 2.3. Calculated bonding metrics for the anagostic interactions in **2-R**.

	[2-H]$^+$	**[2-Me]$^+$**	**[2-OMe]$^+$**	**[2-^{i}Pr]$^+$**
D(Rh···H)$_{calc.}$	2.83, 2.87	2.45, (2.51)[e]	2.79	2.33, 2.45
Rh → σ*(C–H) (kcal mol^{-1})[a,b]	1.33, 1.22	4.38, (4.29[e]	1.91	8.98, 6.70
σ(C–H) → Rh (kcal mol^{-1})[a,c]	0.57, 0.52	0.69, (0.49)[e]	0.33	2.08, 1.71
δ(^{1}H)$_{calc.}$[d]	9.5, 9.1	10.6, (3.9)[e,f]	9.6	9.9, 9.8
δ(^{1}H)$_{exp.}$	8.32	9.97, (3.56)[e]	9.19	9.14
***ρ*(*r*) (au)[a]**	0.012, 0.011	0.022, 0.020	0.013	0.026, 0.021

[a] QTAIM and natural bonding orbitals data are based on the experimental crystal structures. [b] Sum of donation into the two σ*(C–H) natural bonding orbitals. [c] Sum of donation from the Rh lone pairs and σ(Rh–P) bonding orbitals. [d] Data are weighted averages taking into account all low energy conformations. [e] Data in parenthesis is for alkyl anagostic. [f] Average for all three methyl hydrogens.

A plot of these different orbital contributions against the Rh··· H distances in **[2-R]$^+$** reveals a correlation between the two (Figure 2.14). The closer the proton is situated to the metal, unsurprisingly, the stronger the electronic contributions are. The extremes of this correlation are exhibited in **[2-^{i}Pr]$^+$** and **[2-H]$^+$** that possess Rh··· H distances of ~2.4 and ~2.9 respectively, and subsequent Rh → σ*(C–H) contributions of ~1 and ~ 8 kcal mol^{-1}, respectively. The bulkiest ligands result in the *ortho*-aryl protons coming into closer contact with the rhodium. However, there does not appear to be a correlation between Rh··· H

distances with the observed or calculated chemical shifts (Figure 2.14). Therefore, we can conclude that the orbital interactions are not directly related to the ^{1}H chemical shift.

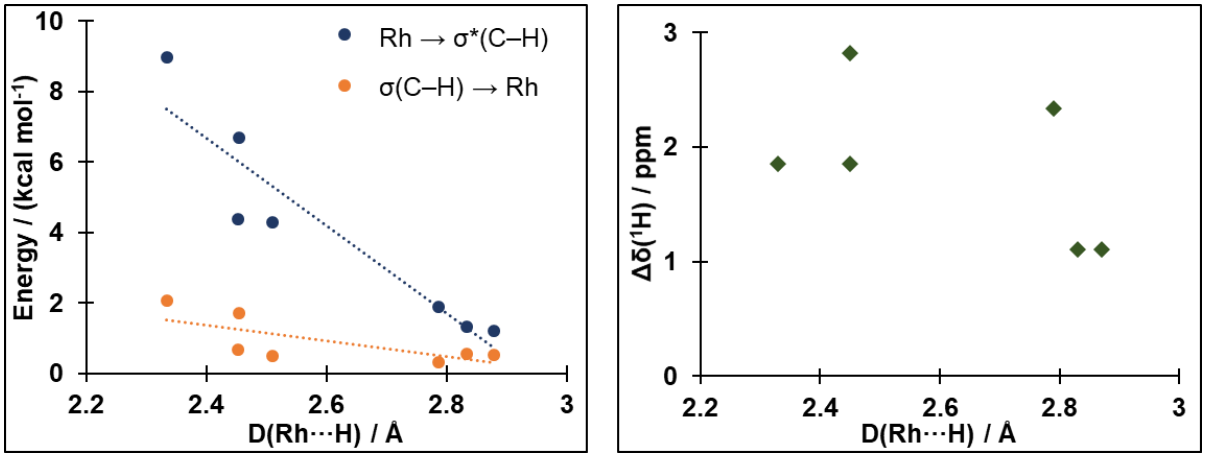

Figure 2.14. **Left** - plot of the electronic contributions in the anagostic interactions in [**2-R**]$^{+}$ compared to the calculated Rh···H interatomic distances. Energy values calculated by natural bonding orbital calculations. **Right** - comparison of the calculated chemical shift change and the D(Rh···H) in **[2-R]**$^{+}$.

Turning back to Scherer's computational studies, we are reminded that it is the induced magnetic fields within the complex that influence the change in chemical shift of protons in close approach to a metal centre (Figure 2.15).[30] Consequently, the precise positioning of the proton, which encompasses a complex interplay of different structural metrics, is the likely cause for the changes in chemical shift. The definition of anagostic interactions can thus be dissected into two different observations: structural and spectroscopic. Firstly, the structural metrics can be indicative of the strength of the interaction, with closer metal-proton contacts resulting in stronger interactions in which the major the electronic contribution comes from Rh → σ*(C-H) donation, albeit weak. Scherer has previously described these interactions as a consequence of the ligand framework which puts the proton into this position or observed chemical shift, and it is not the stabilising effect of the interaction itself that determines the geometry.[31] Secondly, we have shown that the characteristic downfield ^{1}H chemical shift of an anagostic interaction is not directly related to the strength of the interaction. Rather these spectroscopic observations are more like a ring current effect,[32] as a similar downfield chemical shift is observed when a proton is positioned above an aromatic moiety in an area of charge concentration.[33] Scherer also noticed that anagostic protons approached through regions of charge concentration (i.e. towards filled orbitals), whereas agostic protons approached through regions of charge depletion. This results in a chemical shift change in opposite directions. A useful tool for the comparison of these two motifs would

be a complex that contains both an anagostic interaction and an agostic bond. This would allow for direct comparison of the topological placing and subsequent magnetic environments of the two motifs. In search of this, the reactivity of **2-R** was explored.

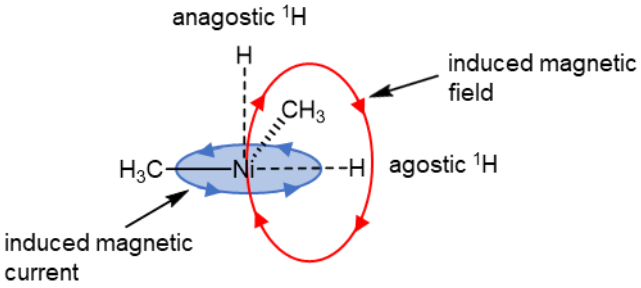

Figure 2.15. Adaption of a figure from reference 30, which illustrates the topological placing of the protons which dictates the change in chemical shift.

2.4 Reactivity of Schrock-Osborn precatalysts

2.4.1 Hydrogenation in d_6-acetone

The activation of Schrock-Osborn complexes via hydrogenation of a NBD fragment in the presence of a coordinating solvent is a common method to form more active precatalysts.[5, 6, 9] This methodology has previously been reported with **2-H** in d_6-acetone solvent, which resulted in the hydrogenation of NBD to NBA and concurrent formation of [Rh(*o*-H-DPEphos)(d_6-acetone)$_2$][BAr$^F_4$], **3-H** (Scheme 2.5).[2] Application of the same procedure with other complexes containing POP-type ligands has resulted in the formation of rhodium-hydride complexes, such as the preparation of [Rh(*mer*-κ^3-P,O,P-Xantphos)(H)$_2$][BAr$^F_4$].[11, 34] Whether a Rh(I) or a Rh(III) dihydride is formed is dependent on the bite angle of the P-P chelate, the cone angle and donating ability of the phosphine substituents.[35]

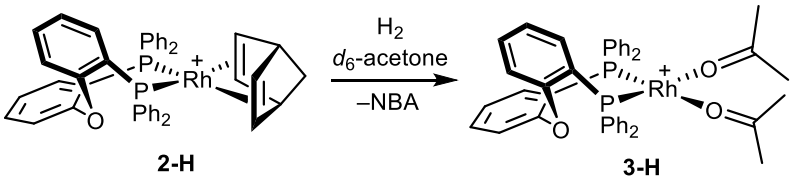

Scheme 2.5. Hydrogenation products of **2-H** after application of H_2 in acetone solvent. [BAr$^F_4$]$^-$ omitted for clarity.

We have used the same activation method with complexes **2-Me**, **2-OMe** and **2-^{i}Pr**, and very different products result depending on the *ortho*-aryl substituent of the ligands. When a sample of **2-Me** in d_6-

acetone exposed to 15 PSI of H_2, the solution immediately changed from orange to yellow (Scheme 2.6). The subsequent complex, **4-Me**, could not be isolated, as persistent vacuum required for the removal of the solvent resulted in decomposition, therefore, **4-Me**, was characterised by in-situ NMR spectroscopy.

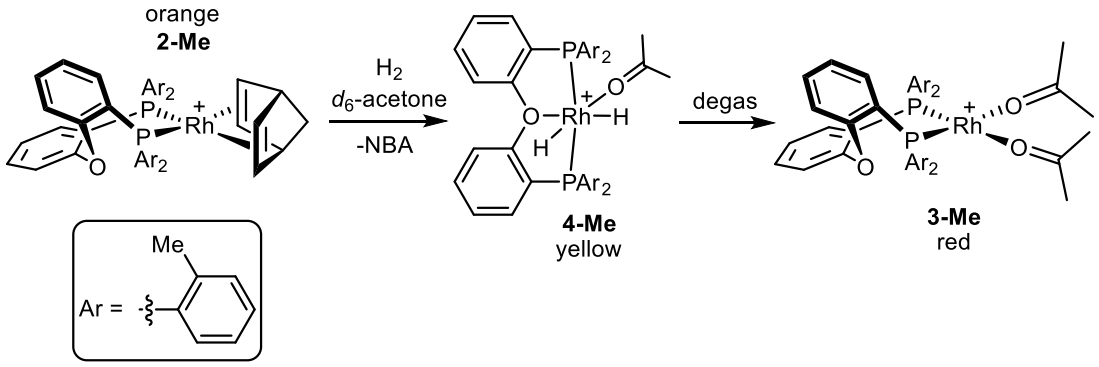

Scheme 2.6. Hydrogenation of **2-Me** in d_6-acetone. $[BAr^F{}_4]^-$ omitted for clarity.

The $^{31}P\{^1H\}$ spectrum of **4-Me** revealed complete conversion of **2-Me** and only a single broad resonance centred at δ 26.0 was observed for **4-Me** (Figure 2.16). Signals corresponding to free NBA and broad aromatic and methyl signals are observed in the ^1H NMR spectrum. An upfield broad signal at δ –19.51 (FWHM = 99 Hz), integral 2H compared to all of the aromatic signals, is also observed indicative of two equivalent metal-hydrides.[36] The hydride signal was broad at 298 K. Cooling the sample to 183 K (CD_2Cl_2) resulted in sharper signals being observed, suggestive of a fluxional process at room temperature. At this temperature, the ^{31}P signals separated into two doublet of doublets, comprising large *J*(PP) of 343 Hz and smaller *J*(RhP) of 121 and 114 Hz (Figure 2.16). These data are suggestive of a *trans*-P,P arrangement on a Rh(III) centre.[21] Four hydride resonances are observed, as two sets of two, in a 5:1 set ratio at 183 K, both coupling to one ^{103}Rh, two *cis*-^{31}P and one cis-hydride (30, 12 and 8 Hz respectively, Figure 2.17). Four corresponding methyl signals are also observed for each complex. As only one set of ^{31}P signals are observed, it is likely the signals relating to the two species are coincident in the $^{31}P\{^1H\}$ NMR spectrum. In light of this data, **4-Me** is assigned as a Rh(III) dihydride complex: [Rh(*mer*-κ^3-P,O,P-*o*-Me-DPEphos)(acetone)$(H)_2$][$BAr^F{}_4$] (Scheme 2.6), similar to the previously reported complex [Rh(*mer*-κ^3-P,O,P-Xantphos)(acetone)$(H)_2$][$BAr^F{}_4$] for which, two hydride signals were observed at δ –19.25 and –20.27 at 223 K in d_6-acetone.[37] The two complexes observed in the ^1H NMR spectra are attributed to two isomers of the same complex, related by restricted P–C bond rotation of the substituted aromatic groups.[12, 38]

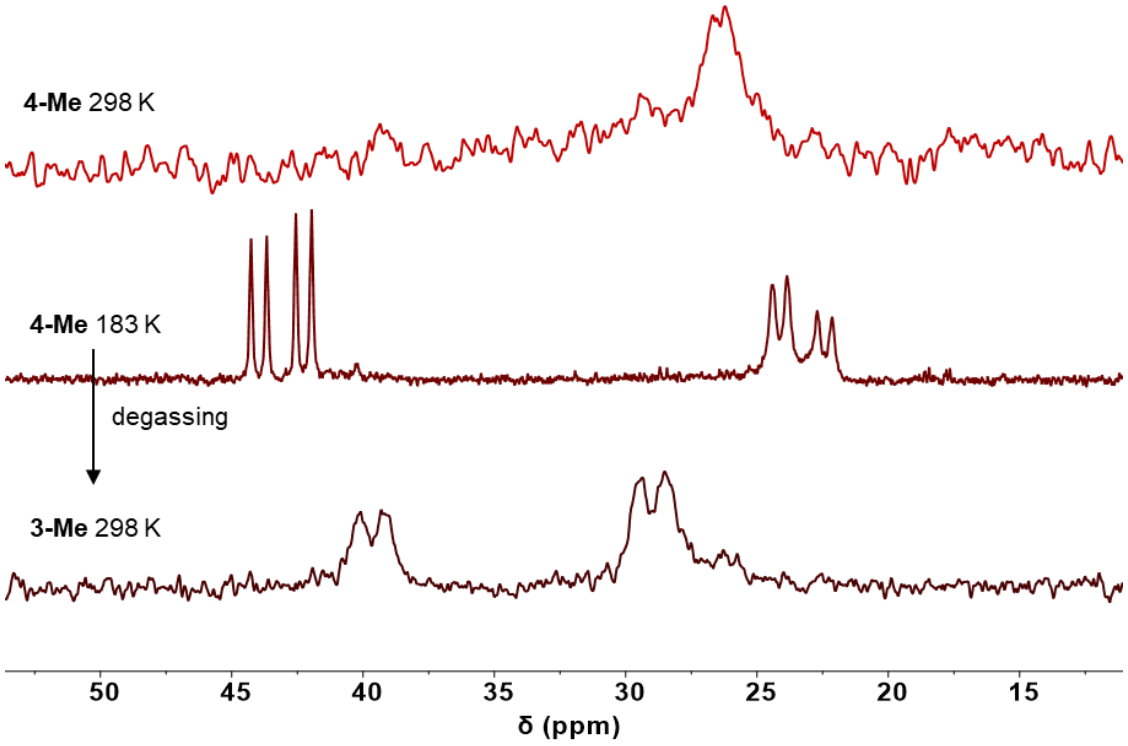

Figure 2.16. $^{31}P\{^{1}H\}$ NMR spectra of **4-Me** before degassing. Top, 298 K, middle, 183 K. The bottom spectrum is representative of the same sample after six successive freeze-pump-thaws, i.e. **3-Me** (202 MHz, d_6-acetone).

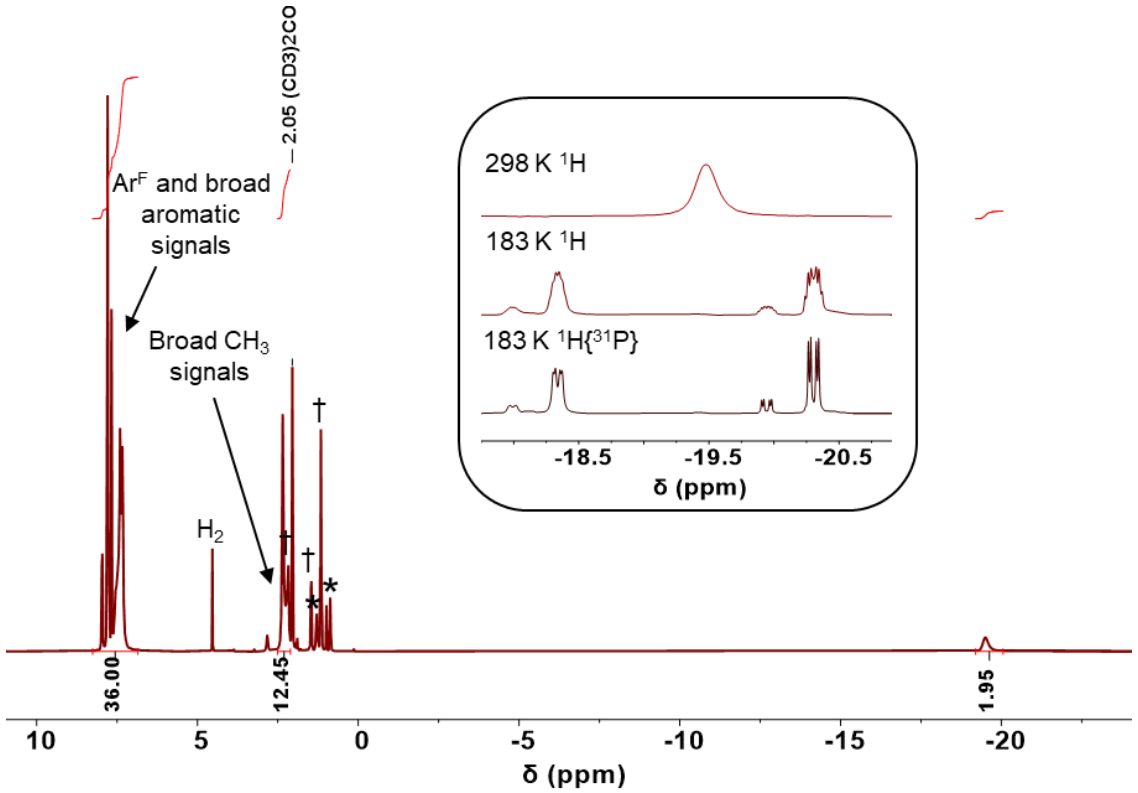

Figure 2.17. ^{1}H NMR spectrum of **4-Me** (500 MHz, d_6-acetone, 298 K). Integrals relative to the total aromatic signals integral. * Denotes a pentane impurity and † denotes free NBA. The inset shows the hydride signals at 298 K, 183 K and with ^{31}P-decoupling at 183 K.

Upon degassing a sample of **4-Me** by successive freeze-pump-thaws the solution turned dark red and the NMR signals completely changed. Notably, the hydride signals are no longer observable and the ^{31}P NMR signals changed to two broad doublets, *J*(RhP) = 194 and 199 Hz, which are much larger than those observed in **2-Me** (~ 160 Hz) and **4-Me** (~120 Hz), being indicative of weakly binding solvent molecules on a Rh(I) centre *trans* to the phosphine.[21] Therefore, **3-Me** is assigned as [Rh(*cis*-P,P-*o*-Me-DPEphos)(acetone)$_2$][BAr$^F_4$] formed upon loss of H_2 from **4-Me**, with a similar bonding arrangement to **3-H**.[2, 3]

The same methodology was applied with the methoxy variant, **2-OMe** (Scheme 2.7). The solution turned from orange to dark red when H_2 was added to **2-OMe** in d_6-acetone. Free NBA was observed in the ^{1}H NMR spectrum and no metal-hydride signals were observed. The resultant complex is tentatively assigned as [Rh(*cis*-P,P-*o*-OMe-DPEphos)(acetone)$_2$][BAr$^F_4$] (**3-Me**). The room temperature ^{1}H and ^{31}P{^{1}H} spectra show broad signals that do not allow for definitive characterisation. Cooling to 183 K resulted in the observation of multiple isomers as shown in the ^{31}P{^{1}H} NMR spectrum (Figure 2.18). Although difficult to individually assign, the symmetry of the *o*-OMe-DPEphos ligand within some of the isomers can be identified. C_2 symmetric arrangements do not contain observable *J*(PP) coupling. The asymmetric, C_1 isomers appear as doublet of doublets, containing large *J*(*cis*-PP) of ~ 60 Hz. The central isomers, observed between δ 39-28, all exhibit large *J*(RhP) values (205-223 Hz), very characteristic of weakly bound acetone ligands and similar to **3-H** (209 Hz) and **3-Me** (~ 200 Hz). The isomers observed at δ 45-43 and δ 21-18 contain smaller *J*(RhP) and *J*(PP) constants of ~160 Hz and ~35 Hz respectively, and could potentially be mono-acetone complexes, but this is very speculative. Multiple isomers were also observed in the ^{1}H NMR spectrum. Analysis by ESI-MS only gave a mass value that corresponds to [Rh(*o*-OMe-DPEphos)]$^+$ (observed 761.11, calc. 761.11 m/z). Degassing of the sample resulted in no change in solution colour or spectroscopic signals.

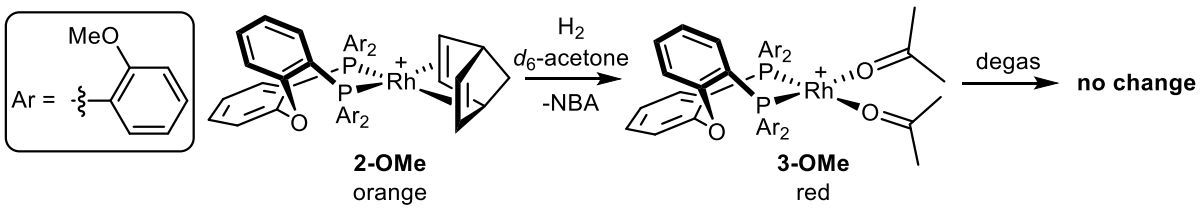

Scheme 2.7. Hydrogenation of **2-OMe** in d_6-acetone. [BAr$^F_4$]$^-$ omitted for clarity.

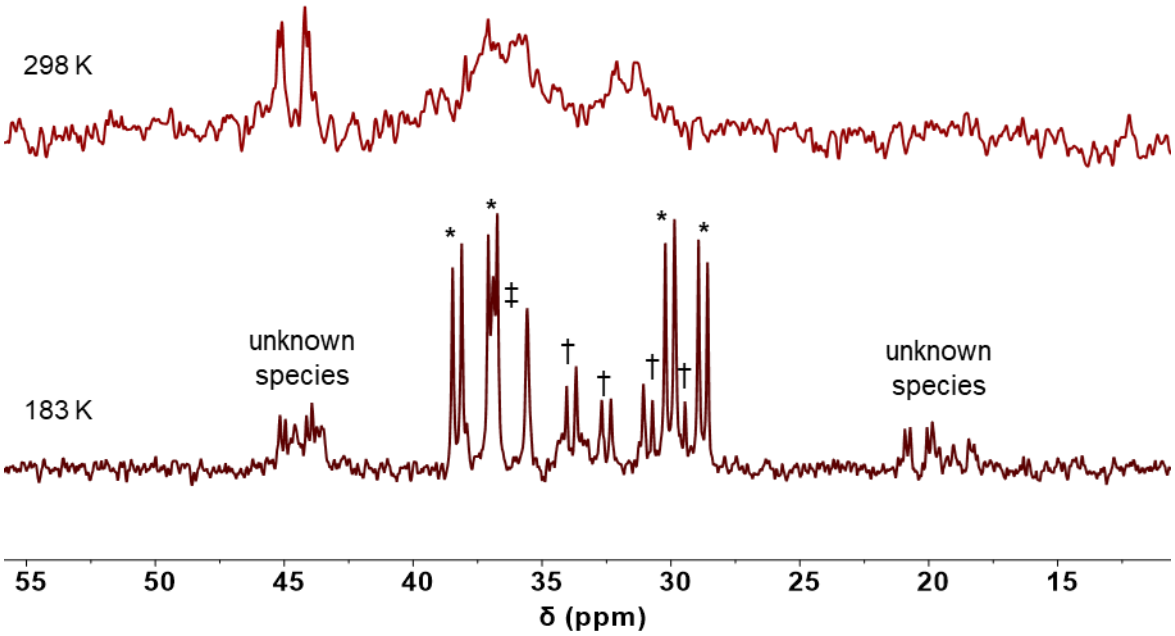

Figure 2.18. $^{31}P\{^{1}H\}$ NMR spectra of in-situ formed **3-OMe** at 298 K (top) and 183 K (bottom) (202 MHz, d_6-acetone). Three different isomers have been highlighted by different symbols.

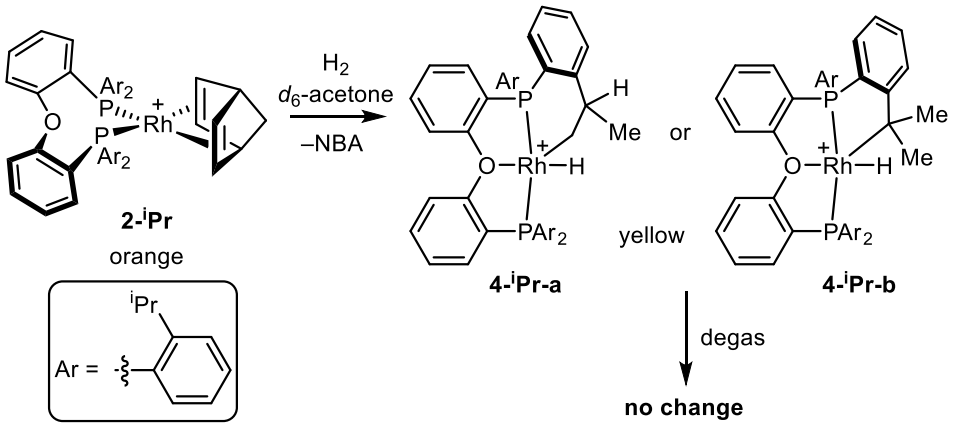

Scheme 2.8. Hydrogenation of **2-^{i}Pr** to form C–H activated product, **4-^{i}Pr**. $[BAr^{F}_{4}]^{-}$ omitted for clarity.

A different product was produced when this methodology was applied to **2-^{i}Pr**. The hydrogenation product of **2-^{i}Pr** in d_6-acetone is assigned as a Rh(III) cyclometallated complex, formed upon reversible C–H activation at one of the isopropyl groups, giving a yellow solution of either **4-^{i}Pr-a** or **4-^{i}Pr-b** (Scheme 2.8). Unfortunately, crystals suitable for X-ray diffraction could not be obtained, thus we cannot definitively state whether C–H activation has occurred at the methyl position to produce a six-membered metallocycle (**4-^{i}Pr-a**) or at the methine position to give a five-membered metallocycle (**4-^{i}Pr-b)** (Scheme 2.8). There are examples in the literature of methyl activation of isopropyl groups,[12] such as $[OsH(\eta^5\text{-}C_9H_7)(\kappa^2\text{-}P,C\text{-}CH_2CH(CH_3)P^iPr_2\}(P^iPr_3)]OTf$,[39] and $[Rh\{P^iBu_2(CH_2CHCH_3CH_2)\}(P^iBu_3)(\mu\text{-}$

Br)]$_2$[BAr$^F{}_4$]$_2$,[40] and methine activation has been reported in dimeric, chloro-bridged platinacycles [(κ^2-P,C-*o*-P^{t}Bu$_2$,CMe$_2$-C$_6$H$_4$))Pt(μ-Cl)]$_2$.[41] However, it is important to note that C–H activation has not occurred at the aryl C–H bonds that were involved in the anagostic interactions.

The ^{31}P{^{1}H} NMR spectrum of **4-^{i}Pr** is broad at 298 K, but cooling to 183 K revealed at least three different isomers with large *J*(PP) (~ 360 Hz) and small *J*(RhP) (112-121 Hz), typical of a *trans*-P,P arrangement at a Rh(III) centre (Figure 2.19).[36]

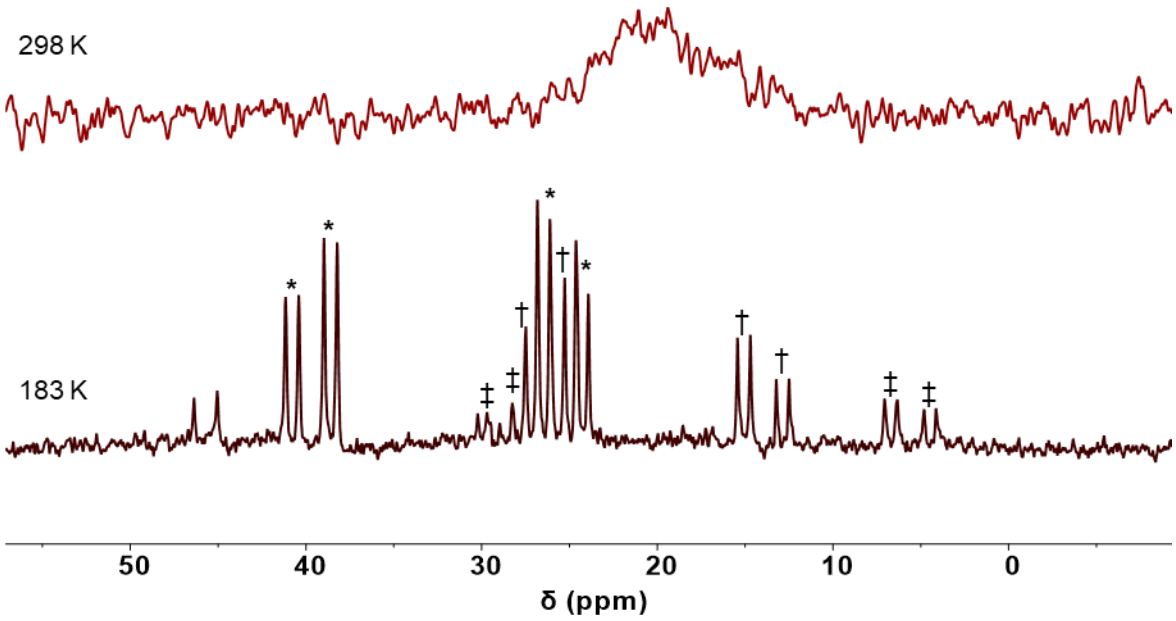

Figure 2.19. ^{31}P{^{1}H} NMR spectra of in-situ formed **4-^{i}Pr** at 298 K (top) and 183 K (bottom) (202 MHz, *d*$_6$-acetone). Three different isomers have been highlighted by different symbols.

In the ^{1}H NMR spectrum of **4-^{i}Pr** at 298 K, free NBA, broad aromatic and isopropyl groups and a sharper hydride resonance at δ –19.81 are observed (Figure 2.20). The hydride signal integrates to 1H compared to the total aromatic signals, and is observed with observed doublet of triplet multiplicity. Selective decoupling revealed this comprised of two equivalent *J*(*cis*-PH) 15 Hz and one *J*(RhH) 29 Hz. Upon cooling to 183 K, this signal split into at least three different signals. We discount the formation of a dihydride, as seen in **4-Me**, as the integral of the hydride is 1H (even when a long delay of 20 seconds is used in the acquisition), no apparent hydride-hydride coupling is observed, and there is no change in the signals upon removal of the H$_2$ atmosphere. Moreover, H/D exchange occurs in **4-^{i}Pr** but not **4-Me**, as discussed later.

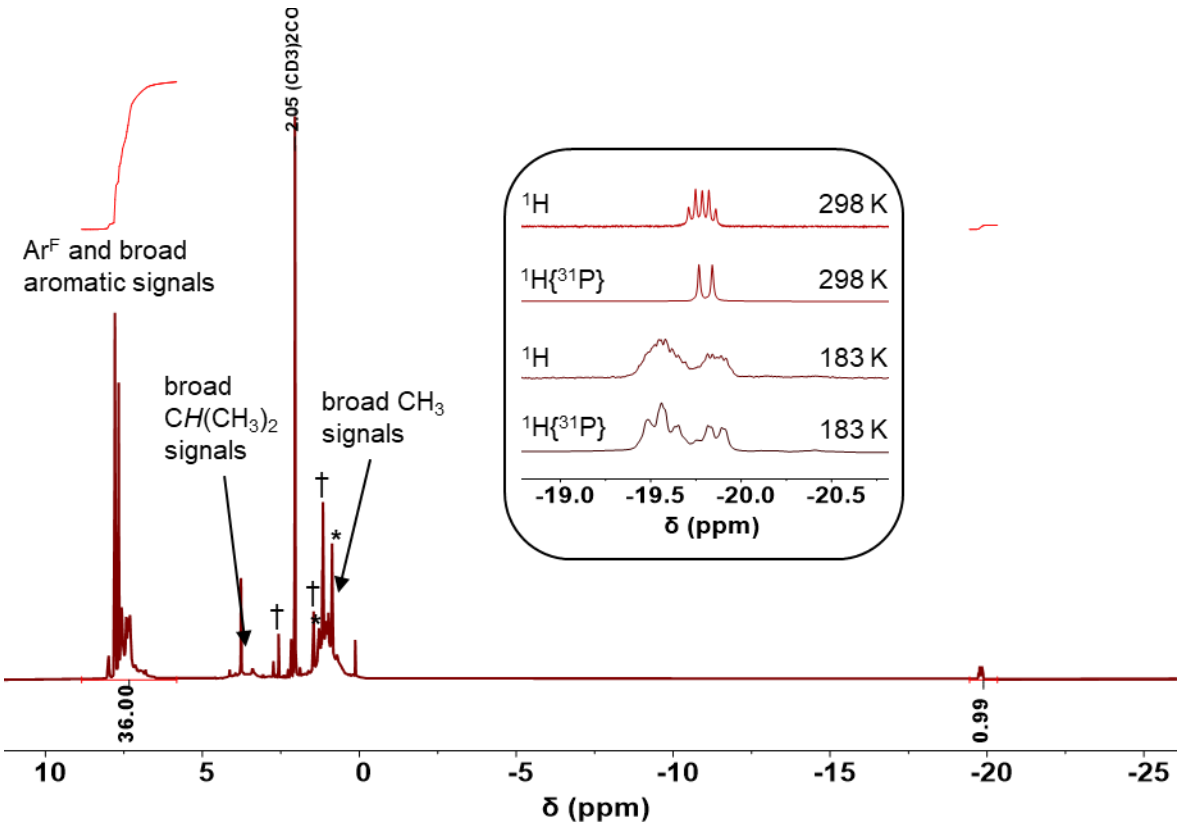

Figure 2.20. ^{1}H NMR spectrum of **4-^{i}Pr** (500 MHz, d_6-acetone, 298 K). Integrals relative to the total aromatic signals integral. * Denotes a pentane impurity and † denotes free NBA. The inset shows the hydride signals at 298 K, 183 K and with and without ^{31}P-decoupling.

Evidently, a fluxional process is occurring in **4-^{i}Pr**. However, *J*(RhH) is observable between 183-298 K and therefore Rh–H is not broken on the NMR timescale.[42-44] Therefore, it is proposed that the fluxional process is caused by restricted rotation of the bulky aromatic groups, as previously reported,[12, 38] and also suggested in Rh(I) complexes **3-Me**, **4-Me** and **3-OMe.** It is also important to note that the same hydride signal and ^{31}P{^{1}H} characteristics of **4-^{i}Pr** were observed when 1,2-$F_2C_6H_4$ or *o*-xylene solvents were used instead of d_6-acetone, so reversible solvent binding is unlikely the cause of the fluxional process. We also suggest methyl activation has occurred in **4-^{i}Pr** (i.e. isomer **4-^{i}Pr-a**) due to evidence of close (< 5 Å) contacts between the hydride and methyl, methine and aryl protons deduced from a NOESY NMR experiment at 183 K (Figure 2.21). Methine activation, to form **4-^{i}Pr-b**, is unlikely to show methine/hydride correlations.[36] We also suggest the hydride is *trans* to the more weakly bound oxygen in the *o*-^{i}Pr-DPEphos backbone rather than the P atoms, based upon its relatively upfield chemical shift.[45]

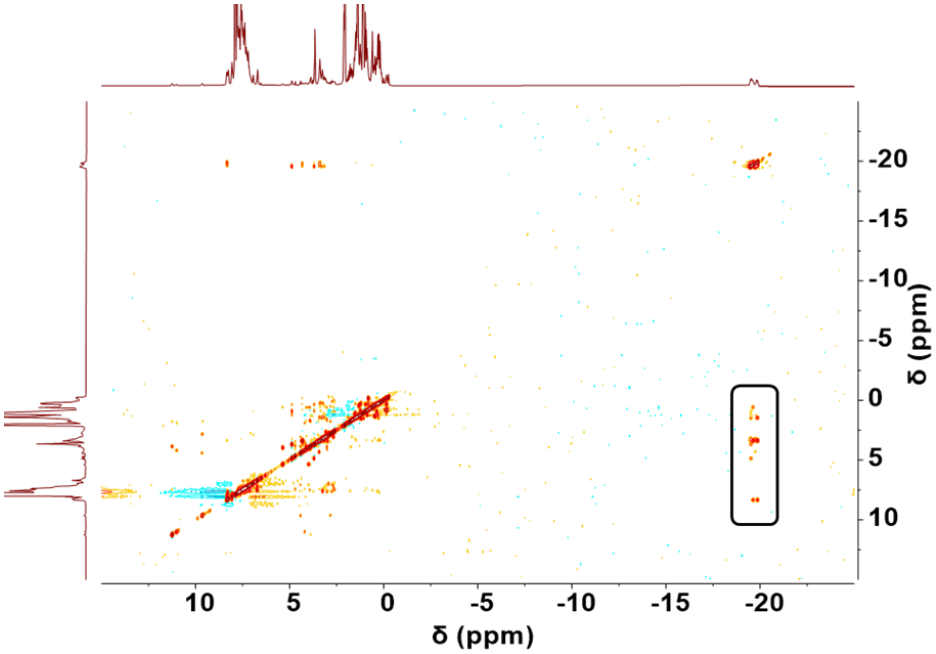

Figure 2.21. $^{1}H/^{1}H$ NOESY spectrum of **4-^{i}Pr** (500/500 MHz, d_6-acetone, 183 K). Region highlighted shows interactions between the hydride signals and alkyl and aryl protons that are within close proximity (< 5 Å).

2.4.2 Reactivity of C–H activated product 4-^{i}Pr

2.4.2.1 Deuterium incorporation

While C–H activation was not reversible on the NMR timescale, on the laboratory timescale it is reversible. When D_2 (15 PSI gauge pressure) was added to a sample of **4-^{i}Pr** in *o*-xylene (Scheme 2.9) a signal due to Rh–D at δ –20.21 in the ^{2}H NMR spectrum appeared within two hours, at a similar chemical shift to the equivalent hydride in **4-^{i}Pr** (δ –19.81). Multiplicity could not be observed in the ^{2}H spectrum. Acetone solvent was initially used for these studies but H/D exchange was observed in the solvent which suggested additional C–H activation processes were occurring. Thus, *o*-xylene was used as a solvent for subsequent H/D exchange studies. A small amount of deuterium was also observed to be incorporated into the methyl position of the isopropyl groups after two hours, which then greatly increased over a two-week period and multiple D_2 recharges (Figure 2.22). Incorporation into the methine position was also observed after two weeks. These observations suggest that there is initial formation of a deuterated isopropyl group and a Rh–D which then enriches the isopropyl group on successive D addition. A proposed mechanism for H/D exchange is discussed in section 2.4.2.3. No 2H signals were observed in a blank sample of *o*-xylene under a D_2 atmosphere. This complex was

tentatively assigned to **4-^{i}Pr-D$_x$** and suggests that H/D exchange via C–H activation occurs on the laboratory timescale.

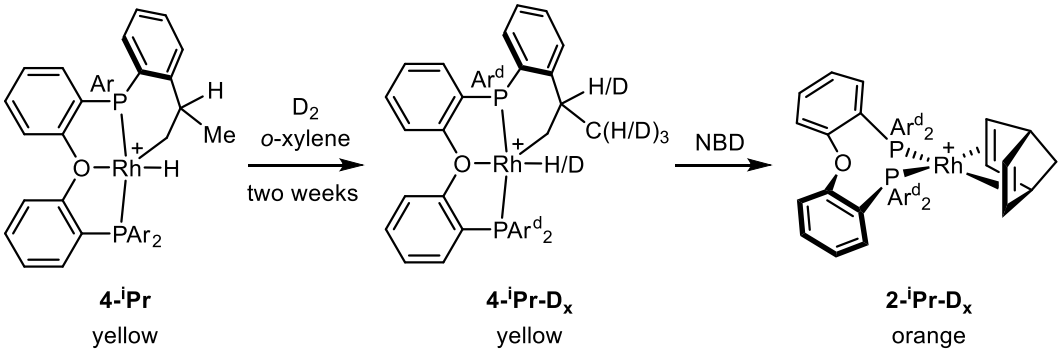

4-^{i}Pr
yellow

4-^{i}Pr-D$_x$
yellow

2-^{i}Pr-D$_x$
orange

Scheme 2.9. Evidence for reversible C–H activation in **4-^{i}Pr**: addition of D_2 to **4-^{i}Pr** to form deuterium incorporated **4-^{i}Pr-D$_x$** and addition of NBD to form **2-^{i}Pr-D$_x$**. $[BAr^F{}_4]^-$ omitted for clarity.

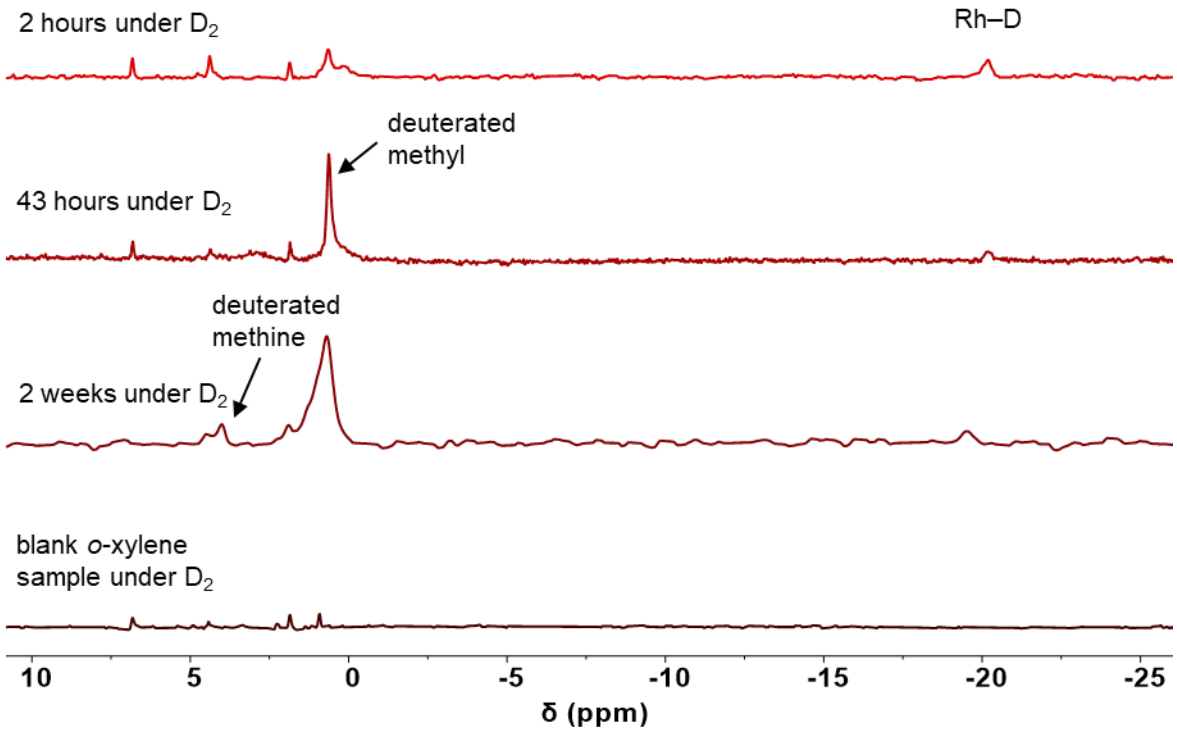

Figure 2.22. ^{2}H NMR spectra of a sample of **4-^{i}Pr-D$_x$** under an atmosphere of 15 PSI D_2 for 2 hours, 43 hours and two weeks compared to a blank sample of *o*-xylene also under 15 PSI D_2 (61 MHz, o-xylene, 298 K).

C–H activation in **4-^{i}Pr** was also shown to be reversible by the addition of excess NBD (10 equiv.) to **4-^{i}Pr**, which resulted in the formation of **2-^{i}Pr** on time of mixing, as shown by multinuclear NMR spectroscopy and ESI-MS. This reaction was exploited to ascertain the deuterium incorporation within

4-^{i}Pr-D$_x$. Attempts to analyse **4-^{i}Pr-D$_x$** by ESI-MS did not produce the expected mass values as decomposition occurred. Instead, excess NBD was added to **4-^{i}Pr-D$_x$** which resulted in the formation of **2-^{i}Pr-D$_x$** (Scheme 2.9), which is air stable and could be analysed by ESI-MS.

The isotope pattern of **2-^{i}Pr-D$_x$** from these ESI-MS studies revealed that isotopologues of up to D_{14} had formed and the distribution was centred at D_6/D_7. This illustrates that multiple CH_3 or CH groups must undergo C-H activation at the rhodium. A coding script, produced by Dr Timothy Morgan Boyd, was used to plot the isotopologues in terms of % of total distribution (Figure 2.23). The ^{1}H NMR spectrum of **2-^{i}Pr-D$_x$** showed that the methyl and methine signals had lost intensity compared to **2-^{i}Pr**. Using $BAr^F{}_4$ as an internal standard, revealed a deuterium incorporation of 40% in the methine position and 20% into the methyl positions. This equates to roughly 6 out of 28 of the total isopropyl protons had exchanged for deuterium atoms, consistent with the ESI-MS data. It is important to note that no deuterium incorporation is observed in the aromatic region. This highlights the fact that anagostic interactions do not necessarily precede C–H activation in this system, unlike agostic bonds which are known to do so.[26, 46]

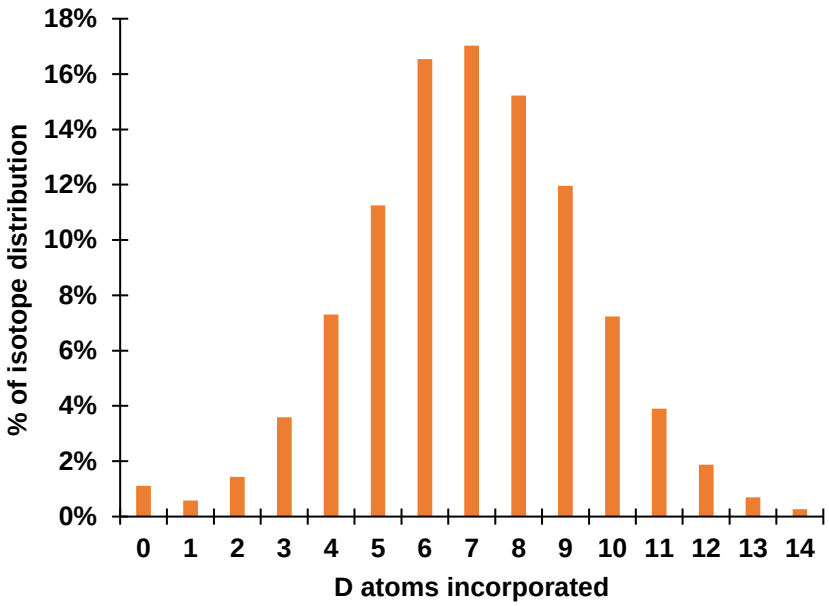

Figure 2.23. Deuterium isotope distribution calculated via a coding script of the ESI-MS data of **2-^{i}Pr-D$_x$**.

A repeat of this experiment was stopped after just 48 hours under 15 PSI D_2 and an almost identical isotope distribution pattern was observed. A closer inspection of the ^{1}H NMR of **2-^{i}Pr-D$_x$** revealed that

two of the CH_3 signals (which each correspond to two chemically equivalent CH_3 groups, i.e. integral 6H) have reduced in intensity by ~ 40% whereas the other two signals have only reduced by a few %. Both methine ^1H signals are reduced by ~ 40%, which suggests all four methine environments undergo H/D exchange if we assume that the chemically equivalent environments undergo the same H activation processes. In light of this, we propose that predominantly, only four out of the eight CH_3 groups and all four methine C–Hs undergo C–H activation and subsequent H/D exchange, which could be due to geometric constraints only allowing certain structural arrangements to undergo C–H activation. This would explain why the maximum D incorporation is D_{14}. Why the distribution centres around D_7 is unclear, but could be caused by a complex interplay of kinetic isotope effects and statistical probabilities.[47, 48]

2.4.2.2 Reactivity with CO to form [Rh(o-^{i}Pr-DPEphos)(CO)[BAr$^F_4$] 5-^{i}Pr

The reversibility of the C–H activation in **4-^{i}Pr**, as shown by the reaction with NBD, was also shown to occur with CO. A sample of **4-^{i}Pr** was degassed and exposed to 15 PSI of CO. This led to the quantitative formation of [Rh(κ^3-P,O,P-*o*-^{i}Pr-DPEphos)(CO)][BAr$^F_4$], **5-^{i}Pr** (Scheme 2.10), which was characterised by NMR spectroscopy and single crystal X-ray diffraction.

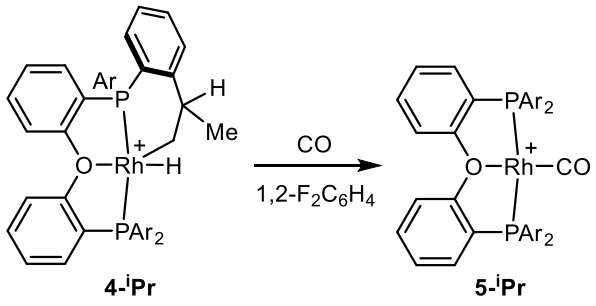

4-^{i}Pr **5-^{i}Pr**

Scheme 2.10. Formation of **5-^{i}Pr** by addition of CO to **4-^{i}Pr**.

The solid-state structure of **5-^{i}Pr**, as determined by x-ray crystallography, reveals a P–Rh–P bond angle of 162.41(4)° and an Rh–O distance of 2.128(3) Å (Figure 2.24). This is diagnostic of a *mer*-κ^3-P,O,P arrangement of the *o*-^{i}Pr-DPEphos ligand. A CO ligand is also bound, confirmed by the observation of a CO stretch in the IR spectrum at 2023 cm^{-1} collected in the solid-state. This gives the complex overall pseudo square planar geometry on a Rh(I) centre. There are reported examples of [Rh(*mer*-κ^3-P,O,P-diphosphine)CO][X] complexes with Xantphos,[49] *o*-H-DPEphos[1] and [P(Ph)$_2$CH$_2$CH$_2$]$_2$O.[50] The P–Rh–

P bond angle in [Rh(*mer*-κ^3-P,O,P-Xantphos)CO][BF_4], was reported to be 164.42(5)° and the Rh–O(backbone) distance is 2.126(3) Å,[51] which is similar to **5-^{i}Pr**. The CO stretching frequency in [Rh(*mer*-κ^3-P,O,P-Xantphos)CO][BF_4] was reported to be 1999 cm^{-1},[51] reasonably similar to **5-^{i}Pr**. In the solid-state structure of **5-^{i}Pr**, two methine protons are positioned in the apical positions to the rhodium within reasonably close contact [2.67 and 2.82 Å]. These are reminiscent of the anagostic interactions observed in the Schrock-Osborn complexes, **2-R**. A non-crystallographic C_2 axis is also present, which is retained in solution: a single ^{31}P peak at δ 19.9 is observed in the $^{31}P\{^1H\}$ NMR spectrum as a doublet with a small *J*(RhP) value of 123 Hz. In the ^{1}H NMR spectrum of **5-^{i}Pr**, however, only three broad CH_3 signals in a 1:2:1 ratio are observed at 298 K. Cooling to 183 K revealed four signals in a 1:1:1:1 ratio, i.e. C_2 symmetry. Two methine environments are observed at all temperatures at δ 4.74 and 3.10. Clearly, one of these signals is shifted slightly more downfield than the other, which is shift of $\Delta\delta(^1H)$ = 1.1 ppm compared to the free ligand. We therefore suggest the presence of two methine anagostic interactions in **5-^{i}Pr**, as well as a dynamic process at room temperature that makes two CH_3 groups equivalents on the NMR timescale, but is frozen out in an overall C_2 geometry at 183 K, which reflects the solid-state structure. Methyl groups on an isopropyl moiety cannot interchange via rotation (they are diastereotopic), and therefore a small movement that creates a time-averaged local mirror plane through the isopropyl group is more likely. Local mirror planes have been described before in isopropylchloroformate and isopropylcyanoformate,[52] as well as in the intermediates of alkyne reduction by nitrogenase.[53]

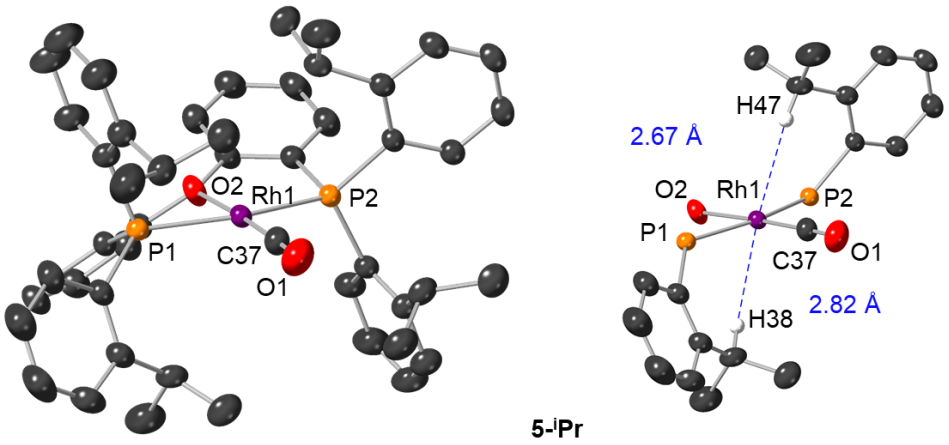

Figure 2.24. Left – crystallographically determined structure of **5-^{i}Pr**. Hydrogens and $[BAr^{F}{}_{4}]^{-}$ anion omitted for clarity. Right – reduced solid-state structure of **5-^{i}Pr**, highlighting the close Rh···H contacts. Ellipsoids at the 50% probability level. Key bond lengths (Å) and angles (°): Rh1–P1, 2.3145(7); Rh1–P2, 2.3027(8); Rh1–O2, 2.128(3); Rh1–C37, 1.819(4); C37–O1, 1.135(5); Rh1–H47, 2.67; Rh1–H38, 2.82; P1–Rh1P2, 162.41(4); O2–Rh1–C37, 177.0(1); Rh1–C37–O1, 177.8(3).

2.4.2.3 Mechanisms of reactivity

We consider several different mechanisms for the reactivity observed in **4-^{i}Pr** (i.e. C–H activation). Firstly, an equilibrium between **4-^{i}Pr** and a low-coordinate 14-electron Rh(I) complex, [Rh(κ^{3}-P,O,P-*o*-^{i}Pr-DPEphos)]$^{+}$ (**A**), via reductive elimination of the alkyl and hydride to reform the C–H bond (Scheme 2.11-**Route I**). Similar "masked" rhodium-phosphine complexes have been reported before, such as [Rh(H)(κ^{2}-P,C-$CH_2CH(CH_3)CH_2P^{t}Bu^{i}Bu$)($P^{t}Bu^{i}Bu_2$)][$BAr^{F}{}_{4}$], which was shown to be in rapid equilibrium with the 12-electron Rh(I), reductive elimination product, [Rh($P^{t}Bu^{i}Bu_2$)$_2$][$BAr^{F}{}_{4}$].[54] Others have also reported examples of reversible H–C(sp^{3}) activation within organometallic complexes.[55-57] Most notably, Caulton showed that [($^{t}Bu_2PCH_2SiMe_2$)$_2$N]Rh is in rapid equilibrium with a Rh(III) hydride,[58] and reacted as a 'masked' 14-electron complex with NO to form [($^{t}Bu_2PCH_2SiMe_2$)$_2$N]Rh(N_2) and [($^{t}Bu_2PCH_2SiMe_2$)$_2$N]Rh(NO).[59] Such reversible reductive elimination and oxidative addition (**Route I**) would explain the reactivity with NBD and CO, which reforms Rh(I) complexes, **2-^{i}Pr** and **5-^{i}Pr**. However, this would not facilitate H/D exchange.

H/D exchange and CO/NBD coordination could also occur via ligand assisted reductive elimination[60, 61] (Scheme 2.11-**Route II**). A vacant site is suggested to be present on **4-^{i}Pr**. A small molecule, such as NBD or CO, could bind at this site, and promote reductive elimination, forming **2-^{i}Pr**

or **5-^{i}Pr** respectively. This small molecule could also be H_2, and a subsequent σ-CAM mechanism[62] (i.e. a rearrangement of σ-ligands without a change in metal oxidation state) could interchange the hydride and σ-bound D–D ligand and then reductive elimination/oxidative addition of the deuteride into the isopropyl group could occur, leading to the formation of **4-^{i}Pr-D_x**.

A third mechanism pathway is via β-hydrogen elimination at the coordinated alkyl to form an alkene moiety (intermediate **B**) with concurrent loss of H_2 (Scheme 2.11 - **Route III**). β-hydrogen elimination has been reported before in $[Rh(P^{i}Pr_3)_3][BAr^{F}_4]$ to form an alkene bound ligand and concomitant loss of H_2.[63] D_2 coordination and insertion into the alkene moiety followed by reductive elimination would explain for D insertion at both the methine and methyl sites. A reversible reductive elimination step to reform **A**, and flexibility within the ligand must be accessible to account for multiple isopropyl groups incorporating deuterium (D_x > 7, bottom of Scheme 2.11). The observation of HD [δ 4.39, *J*(HD) = 43 Hz] is consistent with either **Route II** or **Route III**. **Route III** provides an explanation for incorporation into both the methine and methyl positions via formation of the alkene moiety. Deuterium incorporation into the methine site is also possible via the σ-CAM and reductive elimination route (**Route II**) if the methine proton C–H activates, however, C-H activation was not observed at the methyl group in the *ortho*-methyl variant **4-Me**, therefore, methine activation is considered less likely. Furthermore, β-hydrogen elimination is impossible at **4-Me** and therefore **Route III** is inaccessible.

Why D incorporation into **4-^{i}Pr** is only available up to D_{14} is not completely clear, but most likely due to geometric constraints preventing half of the CH_3 groups from approaching the rhodium centre in the required manner.

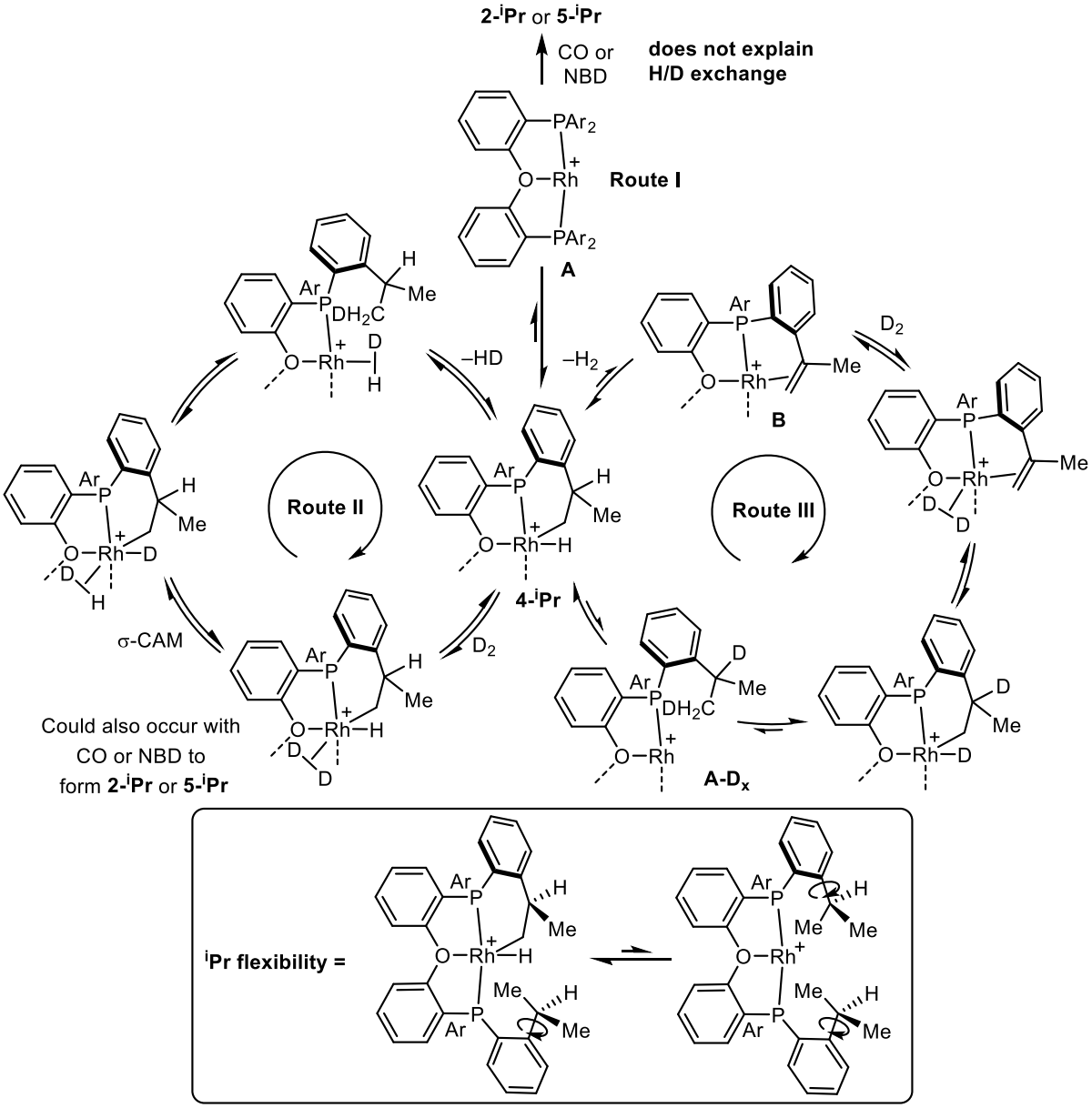

Scheme 2.11. Potential reactivity pathways for the formation of **2-^{i}Pr**, **4-^{i}Pr-D$_x$** and **5-^{i}Pr** from **4-^{i}Pr**. The bottom scheme shows the required flexibility in the ligand to allow for D insertion into multiple isopropyl groups. $[BAr^F{}_4]^-$ anions omitted for clarity.

2.4.2.4 Formation and characterisation of $H_3B{\cdot}NMe_3$ incorporated product, [Rh(o-^{i}Pr-DPEphos'')-η^2-BH_2NMe_3)][$BAr^F{}_4$] 7-^{i}Pr

Further support for the dehydrogenative route (**Route III**) being a plausible pathway comes from reactivity with the well-known hydrogen acceptor, tertiary butyl ethene[64, 65] (TBE) in the presence of $H_3B{\cdot}NMe_3$ with **4-^{i}Pr** in 1,2-$F_2C_6H_4$ solvent.[66, 67] $H_3B{\cdot}NMe_3$ has previously been shown to undergo rhodium-catalysed hydroboration with alkenes[68, 69] and therefore a useful chemical trap to ascertain

whether **Route III** is operating (albeit in the presence of TBE). There was an immediate colour change from yellow to dark blue when **4-^{i}Pr**, TBE and $H_3B{\cdot}NMe_3$ were combined. NMR spectroscopy confirmed quantitative conversion of **4-^{i}Pr** to what is tentatively assigned as a sigma bound $\eta^2(BH_2)$-$H_3B{\cdot}NMe_3$ complex: [Rh(κ^2-P,P-*o*-^{i}Pr-DPEphos)($\eta^2\eta^2$-$H_3B{\cdot}NMe_3$)][BAr$^F_4$], **6-^{i}Pr** (Scheme 2.12). Upon the addition of TBE to **4-^{i}Pr** without $H_3B{\cdot}NMe_3$, a complex mixture of unknown hydrido complexes were observed.

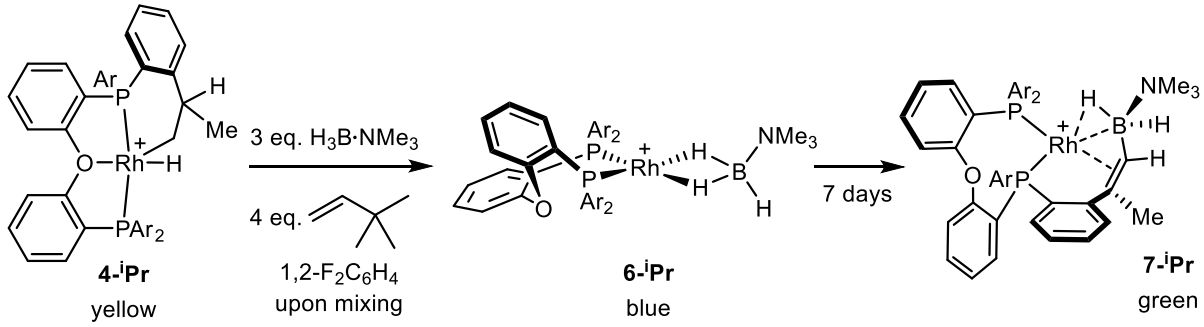

Scheme 2.12. Formation of sigma complex **6-^{i}Pr** and agostic complex **7-^{i}Pr** by the addition of $H_3B{\cdot}NMe_3$ and TBE to **4-^{i}Pr**, upon mixing and after 7 days respectively. [BAr$^F_4$]$^-$ anions omitted for clarity.

Dark blue/green colours are unusual for Rh–Phosphine complexes, but have been reported previously for Rh(I)-Xantphos and Rh(I)-DPEphos sigma and agostic B-H complexes.[6, 7, 68] A broad ^{11}B signal at δ 21.4 was observed in the ^{11}B{^{1}H} NMR spectrum (Figure 2.25), which is very similar to the previously reported *o*-H-DPEphos equivalent [Rh(*o*-H-DPEphos)($\eta^2\eta^2$-$H_3B{\cdot}NMe_3$)][BAr$^F_4$], **6-H** (δ 20.7),[7] and [Rh(P^{i}Pr$_2$(CH$_2$)$_3$P^{i}Pr$_2$)($\eta^2\eta^2$-$H_3B{\cdot}NMe_3$)][BAr$^F_4$] (δ 24.5).[70] A sharp singlet at δ –6.4 was also observed which corresponds to [BAr$^F_4$]$^-$. A very broad ^{1}H signal centred at δ –2.8, integral 3H, in the ^{1}H NMR spectrum of **6-^{i}Pr** is observed, which sharpened upon ^{11}B-decoupling, that is diagnostic of a rapid exchange between Rh···H–B and terminal B–H. A similar characteristically upfield signal has been observed in **6-H** (δ –1.74, 3H)[70] and [Rh(P^{i}Pr$_2$(CH$_2$)$_3$P^{i}Pr$_2$)($\eta^2\eta^2$-$H_3B{\cdot}NMe_3$)][BAr$^F_4$] (-1.9, 3H).[70] Unfortunately, the 1,2-$F_2C_6H_4$ solvent aromatic signals overwhelmed the aromatic signals in **6-^{i}Pr**, and the alkyl region is complicated with the presence of free NBA and excess $H_3B{\cdot}NMe_3$ and TBE. In the ^{31}P{^{1}H} NMR spectrum, two ^{31}P signals are observed for **6-^{i}Pr** at δ 31.4 and 19.4 as broad doublets [*J*(RhP) = 209 and 176 Hz] (Figure 2.25). This is indicative of a *cis*-κ^2-P,P arrangement of the DPEphos-type ligand bound to a Rh(I) centre, with a reasonably weakly binding co-ligand.[2] This is in contrast with **6-^{i}Pr** and [Rh(P^{i}Pr$_2$(CH$_2$)$_3$P^{i}Pr$_2$)(η^2-$H_3B{\cdot}NMe_3$)][BAr$^F_4$], which both showed a symmetric arrangement of the diphosphine by ^{31}P NMR spectroscopy.[7, 70] Therefore, we suggest that restricted rotation of the bulky aromatic groups[12] locks the *o*-^{i}Pr-DPEphos ligand.

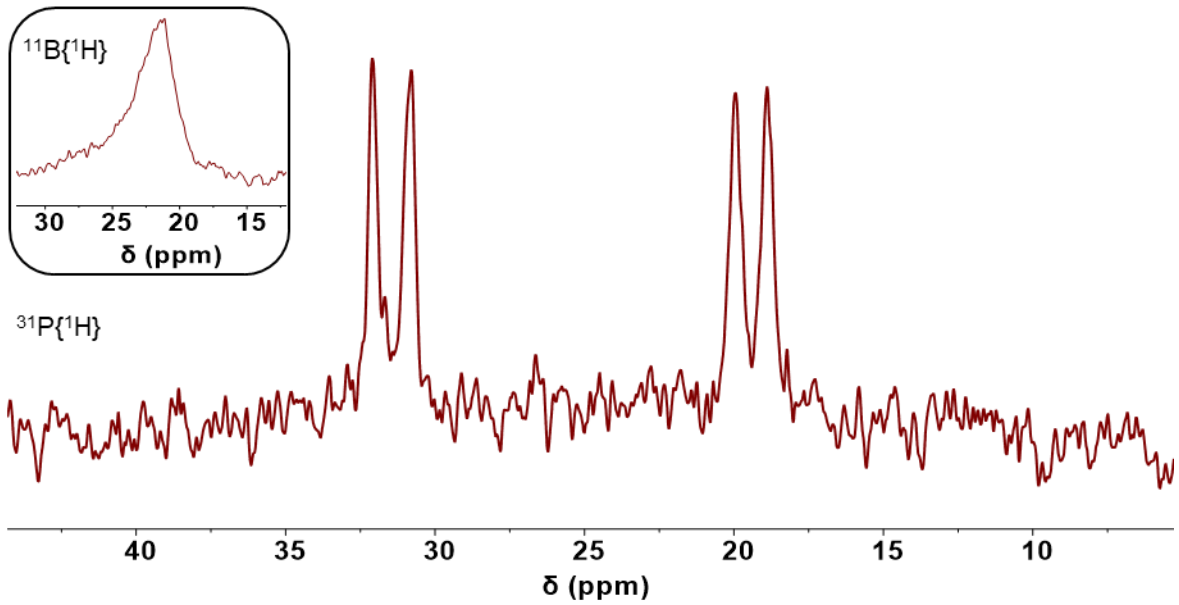

Figure 2.25. $^{31}P\{^{1}H\}$ NMR spectra of in-situ formed **6-^{i}Pr** (202 MHz, 1,2-$F_2C_6H_4$, 298 K). The inset shows the selected regions of the $^{11}B\{^{1}H\}$ NMR spectrum (128 MHz, 1,2-$F_2C_6H_4$, 298 K).

Attempts to isolate **6-^{i}Pr** led to decomposition of the complex. However, after leaving the reaction mixture for several days, the solution started to turn dark green and the spectroscopic analysis revealed a new complex had quantitatively formed after seven days. NMR and single crystal X-ray crystallography showed that this new complex has undergone C–H activation followed by a double dehydrogenative borylation with $H_3B{\cdot}NMe_3$ to form a vinyl borane moiety within the *o*-^{i}Pr-DPEphos ligand (Scheme 2.12). Rhodium catalysed borylation[71] and dehydrogenative borylation[72] are known. Simple precatalysts such as $RhCl(CO)(PPh_3)_2$ have been shown to form vinyl borate esters from substituted alkenes and diboron reagents via dehydrogenative borylation.[73] However, this is the first example, that we know of, that this has occurred within the ligand framework. The resultant product is assigned as [Rh(κ^2-P,P-(*o*-^{i}Pr-DPEphos'')-η^2-BH_2NMe_3)][BAr^F_4], **7-^{i}Pr** which is isolated as a green analytically pure solid in good yield (88%) (Scheme 2.12). A solid-state structure was obtained via single-crystal X-ray crystallography (Figure 2.26). This revealed that one $H_3B{\cdot}NMe_3$ incorporated *o*-^{i}Pr-DPEphos'' ligand binds to the rhodium centre via two P, an η^2(C=C) ethenyl moiety [D(Rh1–C37), D(Rh1–C39) and D(C=C) = 2.266(3), 2.152(3) and 1.392(6) Å respectively] and an agostic B–H [D(Rh1–B1) = 2.391(6) Å and D(Rh1–H1B) = 1.99 Å). The tight Rh1–H1B–B1 angle of 87.8(2)° is suggestive an η^2(BH) agostic coordination.[74] The P atom trans to the more weakly bound B–H agostic bond is ~0.1 Å closer to the rhodium that the P trans to the ethenyl moiety due to the stronger *trans*

influence of alkenes.[75] Overall there is a pseudo square planar geometry in the solid-state at the metal centre.

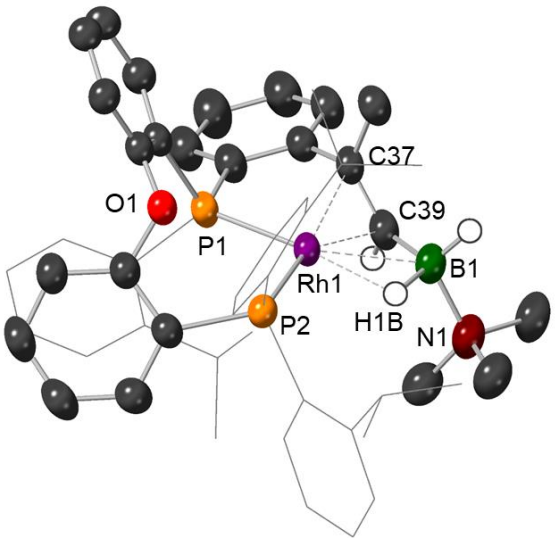

Figure 2.26. Crystallographically determined structure of **7-^{i}Pr**. Selected aryl groups in wire frame and $[BAr^{F}_{4}]^{-}$ anion omitted for clarity. Only key hydrogens are shown. Ellipsoids at the 50% probability level. Key bond lengths (Å) and angles (°): Rh1–P1, 2.3361(9); Rh1–P2, 2.270(1); Rh1–H1B, 1.99; Rh1–B1, 2.391(6); Rh1–C37, 2.266(3); Rh1–C39, 2.152(3); Rh1–H46, 2.47; Rh1–H49, 2.75; C37–C39, 1.392(6); C39–B1, 1.557(6); B1–H1B, 1.41(4); Rh1–H1B–B1, 87.8(2); P1–Rh1–P2, 100.59(4); C37–Rh1–C39, 36.6(2).

The NMR spectroscopic data (CD_2Cl_2, 298 K) are fully consistent with the solid-state structure. Two ^{31}P environments at δ 29.5 and 8.5, both observed as doublet of doublets, reflect the C_1 symmetry of **7-^{i}Pr** in the solid-state (Figure 2.27). The *J*(RhP) values of 187 and 165 Hz also support the fact that one ^{31}P atom is more tightly bound than the other, and a mutual *J*(PP) value of 31 Hz suggests a *cis*-κ^2-P,P arrangement. In the ^{11}B NMR spectrum, a broad resonance observed at δ –10.2 is assigned as the BH_2 moiety, which sharpened upon ^{1}H-decoupling. A sharper $[BAr^{F}_{4}]^{-}$ signal at δ –9.1 overlaps with this broad BH_2 resonance. In the ^{1}H NMR spectrum, seven isopropyl CH_3 (integral 3H) and one $N(CH_3)_3$ (δ 2.48, 9H) signals are observed. A broad signal at δ –7.54 (integral 1H), which sharpened and revealed ddd multiplicity upon ^{11}B-decoupling, is assigned as the agostic B–H proton. Via selected decoupling experiments the multiplicity of this characteristically upfield shift could be deconvoluted as *J*(RhH) = 14 Hz, ^{2}J(HH) = 14 Hz and *J*(PH-*trans*) = 52 Hz. The terminal B–H signal could also be pinpointed after ^{11}B-decoupling was applied, with the same ^{2}J(HH) of 14 Hz. Interestingly, two of the methine signals of the ^{i}Pr are observed shifted notably downfield compared to the third (δ 4.92, 4.75 and 2.32) (Figure 2.28). Correspondingly, these are shifted 1.29 and 1.12 ppm [Δδ(^{1}H)] compared to the free ligand.

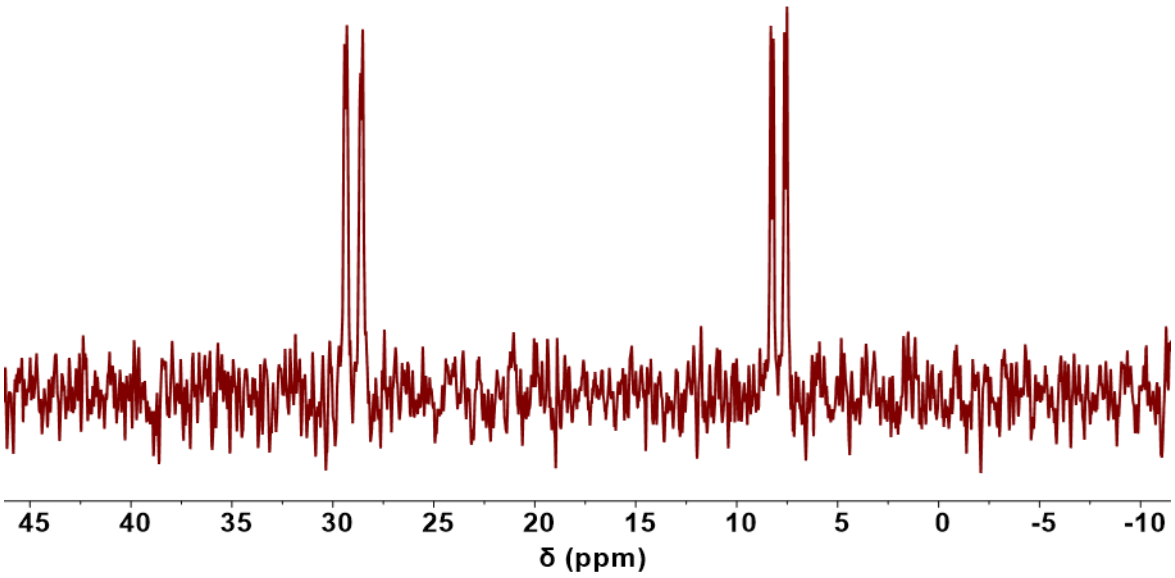

Figure 2.27. $^{31}P\{^{1}H\}$ NMR spectrum of **7-^{i}Pr** (202 MHz, CD_2Cl_2, 298 K).

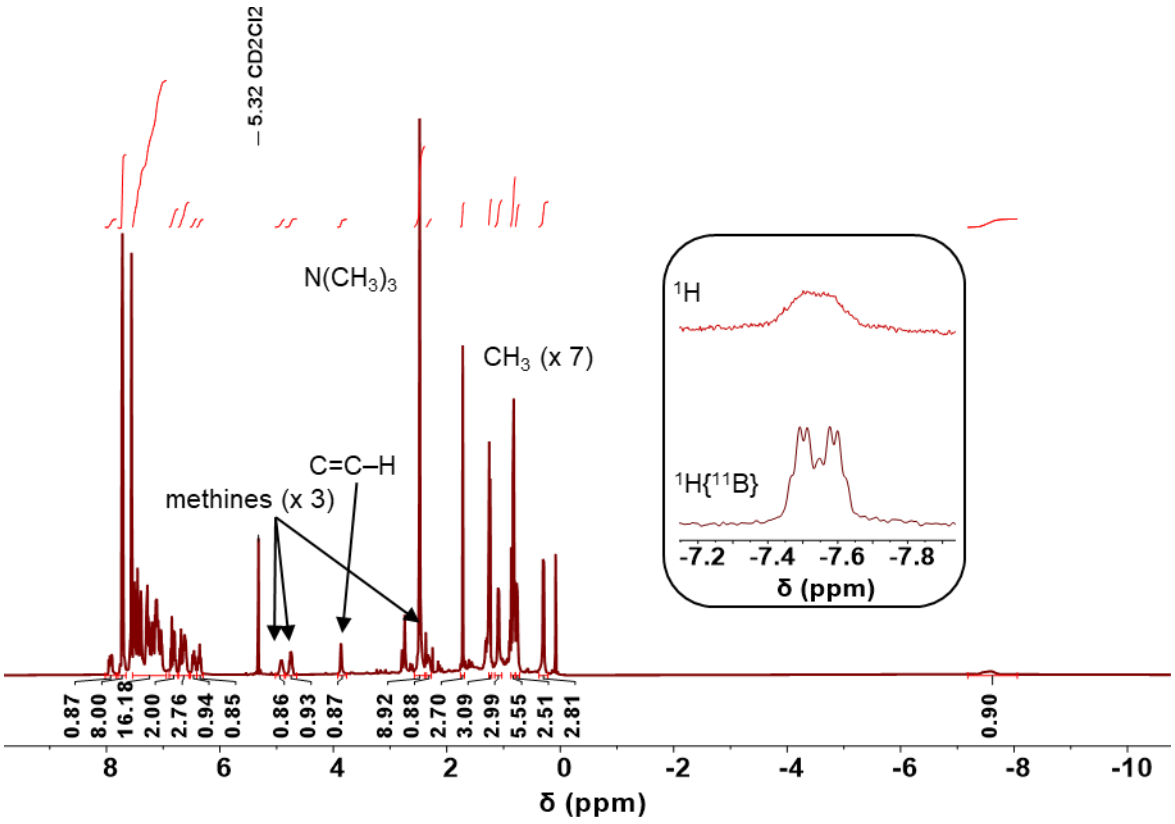

Figure 2.28. ^{1}H NMR spectrum of **7-^{i}Pr** (500 MHz, CD_2Cl_2, 298 K). Integrals relative to the *meta*-H $[BAr^{F}_{4}]^{-}$ signal. The inset shows the signal corresponding to the agostic B–H moiety, with and without ^{11}B-decoupling.

Closer inspection of the solid-state structure revealed that two methine protons were indeed axially positioned and in relatively close contact with the rhodium [D(Rh1···H46) = 2.47 and D(Rh1···H49) = 2.75 Å] (Figure 2.29). These are very similar to the methine anagostic interactions observed in **5-^{i}Pr**. Therefore, serendipitously, we have isolated and fully characterised the first known complex that contains both an anagostic C–H interaction and an agostic B–H bond. The anagostic C–H protons are axially positioned *trans* to one another, in the apical position on the rhodium with Φ values (Figure 2.12) of 66.2° and 64.8°. The values for this metric are similar to those already measured for the aromatic anagostic protons in **2-R** (63-65°), the methyl anagostic in **2-Me** (69.2°) and the similar methine protons in **5-^{i}Pr** (59.0 and 64.0°). The B–H agostic, however, is situated on the equatorial plane of the molecule (Φ = 6.6°). The resultant difference in chemical shift is dramatic (Table 2.4). The agostic proton is shifted upfield by Δδ(^{1}H) = –10.00, compared to the model vinyl borane PhCH=CPh($H_2B{\cdot}NMe_3$) [δ(^{1}H) 2.4],[69] whereas the anagostic methine protons are shifted downfield by 1.29 and 1.12 ppm respectively (compared to free **1-^{i}Pr**). This is consistent with Scherer's analysis, and our own, in which is it the placing of the C–H bonds that defines the chemical shift.[30]

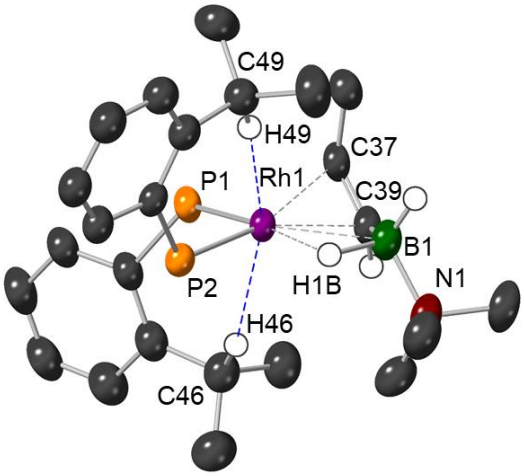

Figure 2.29. Reduced solid-state structure of **7-^{i}Pr**, showing only the fragments specifically involved with rhodium binding, highlighting the agostic B–H and anagostic C–H motifs. Ellipsoids at the 50% probability level. Structural and electronic data are shown in Table 2.4.

Our computational collaborators, Stuart Macgregor and Arron Burnage, calculated the electronic structure of the Rh···H–E interactions within **7-^{i}Pr**. The methine anagostic interactions, Rh1···H46–C46 and Rh1···H49–C49, are electronically very similar to the aryl anagostic interactions in **2-R**. Thus, the major bonding component was calculated to be from a filled rhodium orbital into a vacant σ*(C–H)

orbital. The strength of this interaction is similar to the strongest aryl anagostic interactions previously calculated in **2-^{i}Pr**, e.g. **7-^{i}Pr**: 10.95 and 9.59 kcal mol^{-1} and **2-^{i}Pr**: 8.98 and 6.70 kcal mol^{-1}. Moreover, the minor component to the bonding in this interaction is also from σ(C–H) to the rhodium. This bonding description sharply contrasts with the agostic B–H. The major contribution in this Rh–H–B, 3-centre-2-electron bond, is from the σ(B–H) orbital into a vacant rhodium orbital, which was calculated to be five times stronger than the methine anagostic interactions, at 52.38 kcal mol^{-1}. This is reflected by the E–H–Rh bond angle in the B–H agostic bond being much more acute [87.8(2)°] compared to the anagostic motifs (~160°) to allow for good orbital overlap, as well as the considerably shorter Rh···H distance (2.47, 2.75 and 1.99 Å respectively). A minor component of the agostic bond is donation from the Rh into the σ*(B–H) orbital, but this is ~10% of the electronic contributions.

Table 2.4. Structural and electronic metric of the Rh···H interactions within **7-^{i}Pr**.

	Rh···H46–C46	**Rh···H49–C49**	**Rh···H1B–B1**
θ ∠E–H–Rh (°)[a]	167.6(3)	157.4(3)	87.8(2)
Φ ∠H–Rh/RhP$_2$ (°)[a]	64.8	66.2	6.6
D(Rh···H) (Å)	2.47	2.75	1.99(5)
δ(^{1}H) (ppm)	4.92	4.75	–7.54
Δδ(^{1}H) (ppm)[b]	1.29	1.12	–10.00[d]
Rh → σ*(E–H) (kcal mol^{-1})[c]	10.95	9.59	6.71
σ(E–H) → Rh (kcal mol^{-1})[c]	0.95	0.73	52.38

E = C or B. [a] See Figure 2.12 for diagram of metrics. [b] Difference in chemical shift of the methine proton in **7-^{i}Pr** and the free ligand **1-^{i}Pr** (500 MHz, CD_2Cl_2, 298 K). [c] NBO donor-acceptor interactions. [d] Chemical shift compared with the model free vinyl borane PhCH=CPh($H_2B{\cdot}NMe_3$).[69]

Utilising the same computational methods as Scherer,[30] the current densities within **7-^{i}Pr** were plotted (Figure 2.30). The small arrows describe the direction of the current density that arise from the implementation of B_0 in a fixed direction, mimicking NMR conditions. The dark blue arrows highlight the direction that the current density is moving and there is clearly a counter-clockwise nature to the current, or more formally termed: a paratropic ring current. As a consequence, an induced magnetic field, B_{ind}, manifests perpendicular to the ring current and parallel with B_0.[30] This then has the implication that any protons approaching the metal from the axial direction, i.e. an anagostic proton, will experience a deshielding effect ($B_{eff} = B_0 + B_{ind}$). Any protons approaching on the equatorial plane (agostic protons) will experience a shielding effect. This is just one orientation of B_0 relative to the complex, and in reality, when also considering molecular tumbling, there is in fact an extremely complex interplay of topological placing and experienced magnetic fields.[76] However, the observed experimental chemical shifts within

7-^{i}Pr are in good agreement with the proposed theoretical and computational analysis.[30] This reinforces the previous comments on **2-R** complexes that the spectroscopic observations of anagostic interactions are similar to ring current effects, as observed in protons approaching aromatics.[32, 33, 77]

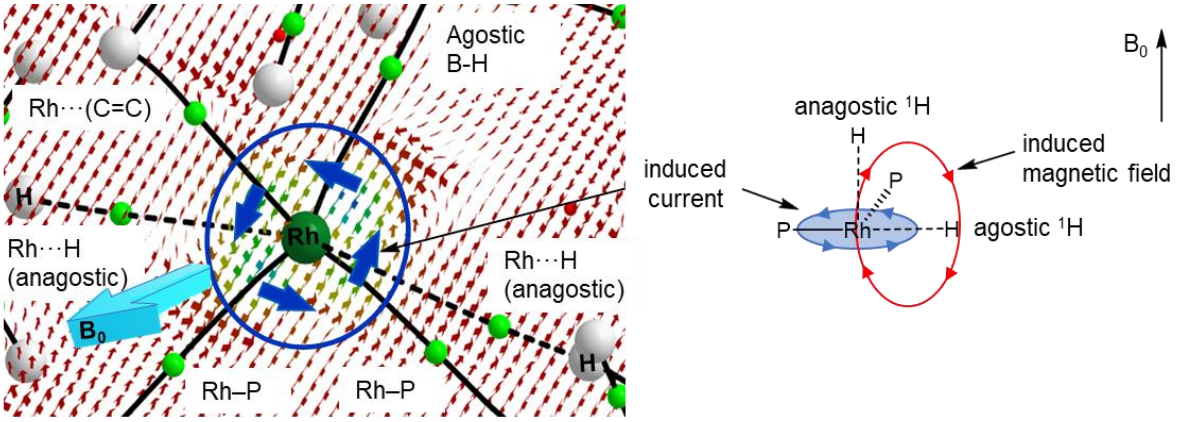

Figure 2.30. Current densities in **7-^{i}Pr** induced by a magnetic field, B_0, in the direction of the light blue arrow coming out of the page. The colour code for the magnitude of the current density is based on a logarithmic scale (dark blue, light blue, green, yellow and red correspond to 100%, 10%, 1%, 0.1% and 0.01% of the induced current density). A Schematic representation of the induced current and concurrent induced magnetic field (B_{ind}) is shown on the right.

We propose a mechanism for the formation of **7-^{i}Pr** that proceeds via an ethenyl bound complex (intermediate **B**) formed through β-hydrogen elimination from **4-^{i}Pr** and concurrent liberation of H_2, thermodynamically encouraged by sacrificial TBE (Scheme 2.13).[63, 78] $H_3B{\cdot}NMe_3$ then undergoes hydroboration with the double bond to form a base stabilised alkyl borane (**C**). A second dehydrogenation step must then occur to obtain **7-^{i}Pr**. This is most likely to occur via a second C-H activation/β-hydrogen elimination sequence and is suggested in other dehydrogenative rhodium catalysed hydroboration reactions.[72, 73] No evidence of catalytic dehydrocoupling[68] or hydroboration of TBE[69, 79] was observed when 20 equivalents of TBE and $H_3B{\cdot}NMe_3$ were added to **7-^{i}Pr**, which suggests that no further reactivity with either TBE or $H_3B{\cdot}NMe_3$ occurs.

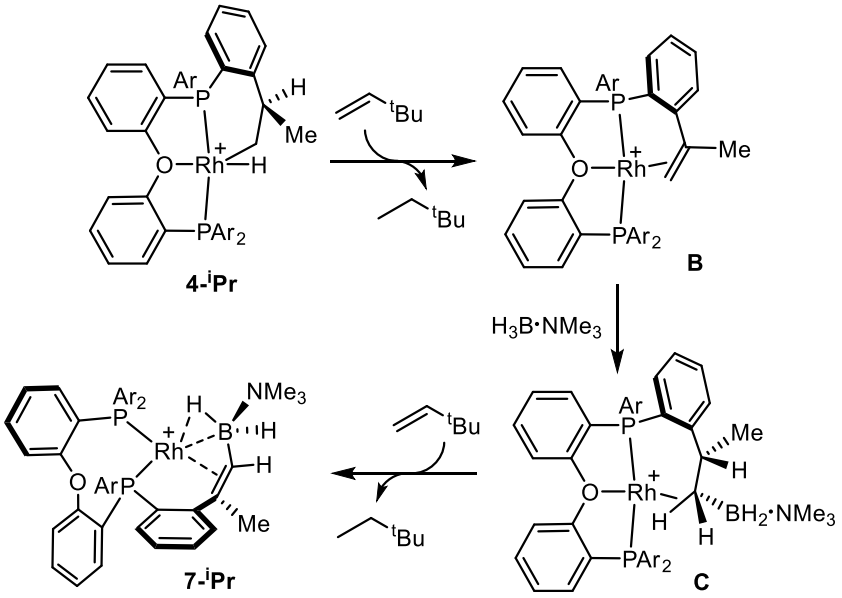

Scheme 2.13. Proposed mechanism for the formation of **7-^{i}Pr** via a dehydrogenative borylation from **4-^{i}Pr**.

2.5 Conclusion

In this chapter, a series of novel Schrock-Osborn type complexes[8, 9] containing DPEphos ligands varying in steric bulk at the *ortho*-position, [Rh(*o*-R-DPEphos)(NBD)][BAr$^{F}_{4}$] (**2-R**), have highlighted the influence *ortho*-aryl substitution can have on solid-state structure, fluxionality, reactivity and anagostic interactions. A backbone ring flipping process[24, 25] was observed on the NMR timescale when R = H, Me or OMe, and also downfield shifted aromatic signals in the ^{1}H NMR spectrum in the low temperature regime. The bulkiest variant, when R = ^{i}Pr, was fixed in one position, and a downfield shift, characteristic of an anagostic interaction, was observed at all temperatures. These downfield shifts coincided with close Rh···H contacts, as previously described in metal d^{8} anagostic interactions.[27, 28, 80] With the aid of a computational collaboration we deduced that the structural positioning of the proton influenced the strength of the electronic bonding contributions, which was predominantly Rh(d_{z^2}) → σ*(C–H) and a small component of σ(C–H) → Rh. However, this did not correlate with the change in downfield chemical shift.

Distinct reactivities were observed for each of the *ortho*-aryl substituted DPEphos ligands upon application of H_2. The least bulky ligands formed Rh(I) solvated complexes, whereas C–H activation occurred at the isopropyl group of the bulkiest variant (R = ^{i}Pr), which was shown to be reversible

through addition of CO, NBD and D_2. In search of a mechanism for the reactivity of the C–H activated product, we synthesised the first complex that exhibits both a C–H anagostic interaction and a B–H agostic bond. Importantly, C–H activation did not occur at the anagostic proton. With this complex in hand, we highlighted the reasoning behind the chemical shift changes observed in both metal-H motifs as well as the vastly different electronic make-up between anagostic Rh···H–C interactions and agostic Rh–H–B bonds. The dominant electronic contribution in the B–H agostic bond [σ(B–H) → Rh] was shown to be five times stronger than the Rh···H–C anagostic interactions. When a hydrogen atom is forced into the apical position (Φ → 90°), the proton approaches the metal through a region of charge concentration, and the local magnetic environment creates a deshielding effect on the proton (i.e. an anagostic proton). When the proton approaches on the equatorial plane (Φ → 0°), such as an agostic bond in a square planar ML_4 complex, the local magnetic environment has a shielding effect on the proton. Therefore, it is the topological placing of the proton that influences the observed changes in chemical shift similar to ring current effects in arenes.[32, 33, 77] This is all consistent with Scherer's analysis on [Rh(CAAC)(CO)Cl] and $[NiMe_2]^+$ systems (CAAC = cyclic alkyl-aminocarbenes).[30]

Further work on this subject could involve a detailed investigation of the influence of anagostic interactions in catalysis. How much do these relatively weak interactions impact the stabilisation of catalytic intermediates and rates of reaction? This would be challenging as there would also be a major influence of the ligand steric bulk on reactivity and deciphering the exact effect of the anagostic interactions alone would require computational collaboration.

2.6 References

[1] J. Barwick-Silk, S. Hardy, M. C. Willis, A. S. Weller, *J. Am. Chem. Soc.,* **2018,** 140, 7347-7357.
[2] G. L. Moxham, H. Randell-Sly, S. K. Brayshaw, A. S. Weller, M. C. Willis, *Chem. Eur. J.,* **2008,** 14, 8383-97.
[3] G. L. Moxham, H. E. Randell-Sly, S. K. Brayshaw, R. L. Woodward, A. S. Weller, M. C. Willis, *Angew. Chem. Int. Ed.,* **2006,** 45, 7618-7622.
[4] M. Utsunomiya, R. Kuwano, M. Kawatsura, J. F. Hartwig, *J. Am. Chem. Soc.,* **2003,** 125, 5608-5609.
[5] J. F. Hooper, A. B. Chaplin, C. Gonzaíez-Rodríguez, A. L. Thompson, A. S. Weller, M. C. Willis, *J. Am. Chem.Soc,* **2012,** 134,
[6] G. M. Adams, D. E. Ryan, N. A. Beattie, A. I. Mckay, G. C. Lloyd-Jones, A. S. Weller, *ACS Catal.,* **2019,** 9, 3657-3666.
[7] D. E. Ryan, K. A. Andrea, J. J. Race, T. M. Boyd, G. C. Lloyd-Jones, A. S. Weller, *ACS Catal.,* **2020,** 10, 7443-7448.
[8] J. R. Shapley, R. R. Schrock, J. A. Osborn, *J. Am. Chem. Soc.,* **1969,** 91, 2816-2817.
[9] R. R. Schrock, J. A. Osborn, *J. Am. Chem. Soc.,* **1976,** 98, 4450-4455.
[10] A. Meißner, E. Alberico, H. Drexler, W. Baumann, D. Heller, *Catal. Sci. Technol.,* **2014,** 4, 3409-3425.
[11] P. Ren, S. D. Pike, I. Pernik, A. S. Weller, M. C. Willis, *Organometallics,* **2015,** 34, 711-723.
[12] R. A. Baber, A. G. Orpen, P. G. Pringle, M. J. Wilkinson, R. L. Wingad, *Dalton Trans.,* **2005,** 659-667.

[13] B. D. Vineyard, W. S. Knowles, M. J. Sabacky, G. L. Bachman, D. J. Weinkauff, *J. Am. Chem. Soc.,* **1977,** 99, 5946-5952.
[14] S. J. Dossett, A. Gillon, A. G. Orpen, J. S. Fleming, P. G. Pringle, D. F. Wass, M. D. Jones, *Chem. Commun.,* **2001,** 699-700.
[15] J. N. L. Dennett, A. L. Gillon, K. Heslop, D. J. Hyett, J. S. Fleming, C. E. Lloyd-Jones, A. G. Orpen, P. G. Pringle, D. F. Wass, J. N. Scutt, R. H. Weatherhead, *Organometallics,* **2004,** 23, 6077-6079.
[16] N. A. Cooley, S. M. Green, D. F. Wass, K. Heslop, A. G. Orpen, P. G. Pringle, *Organometallics,* **2001,** 20, 4769-4771.
[17] J. Wang, G. Meng, K. Xie, L. Li, H. Sun, Z. Huang, *ACS Catal.,* **2017,** 7, 7421-7430.
[18] M. Kranenburg, Y. E. M. Van Der Burgt, P. C. J. Kamer, P. W. N. M. Van Leeuwen, K. Goubitz, J. Fraanje, *Organometallics,* **1995,** 14, 3081-3089.
[19] R. T. Boeré, A. M. Bond, S. Cronin, N. W. Duffy, P. Hazendonk, J. D. Masuda, K. Pollard, T. L. Roemmele, P. Tran, Y. Zhang, *New J. Chem. ,* **2008,** 32, 214-231.
[20] A. G. Orpen, *Chem. Soc. Rev.,* **1993,** 22, 191-197.
[21] G. M. Adams, A. S. Weller, *Coord. Chem. Rev.,* **2018,** 355, 150-172.
[22] J. S. Siegel, F. L. Anet, *J. Org. Chem.,* **1988,** 53, 2629-2630.
[23] H. J. Hogben, M. Krzystyniak, G. T. P. Charnock, P. J. Hore, I. Kuprov, *J. Magn. Reson. ,* **2011,** 208, 179-194.
[24] D. Pingen, T. Lebl, M. Lutz, G. S. Nichol, P. C. J. Kamer, D. Vogt, *Organometallics,* **2014,** 33, 2798-2805.
[25] W. Goertz, W. Keim, D. Vogt, U. Englert, M. D. K. Boele, L. A. Van Der Veen, P. C. J. Kamer, P. W. N. M. Van Leeuwen, *J. Chem. Soc., Dalton Trans.,* **1998,** 2981-2988.
[26] R. H. Crabtree, *J. Organomet. Chem.,* **2004,** 689, 4083-4091.
[27] M. Brookhart, L. H. Green Malcolm, G. Parkin, *PNAS,* **2007,** 104, 6908-6914.
[28] S. Scholer, M. H. Wahl, N. I. Wurster, A. Puls, C. Hattig, G. Dyker, *Chem. Commun.,* **2014,** 50, 5909-11.
[29] J. C. Lewis, J. Wu, R. G. Bergman, J. A. Ellman, *Organometallics,* **2005,** 24, 5737-5746.
[30] J. E. Barquera-Lozada, A. Obenhuber, C. Hauf, W. Scherer, *J. Phys. Chem. A,* **2013,** 117, 4304-4315.
[31] W. Scherer, A. C. Dunbar, J. E. Barquera-Lozada, D. Schmitz, G. Eickerling, D. Kratzert, D. Stalke, A. Lanza, P. Macchi, N. P. M. Casati, J. Ebad-Allah, C. Kuntscher, *Angew. Chem. Int. Ed.,* **2015,** 127, 2535-2539.
[32] C. W. Haigh, R. B. Mallion, *Prog. Nucl. Magn. Reson. Spectrosc.,* **1979,** 13, 303-344.
[33] C. S. Wannere, P. V. R. Schleyer, *Org. Lett.,* **2003,** 5, 605-608.
[34] M. C. Haibach, D. Y. Wang, T. J. Emge, K. Krogh-Jespersen, A. S. Goldman, *Chem. Sci.,* **2013,** 4, 3683-3692.
[35] A. D. Wilson, A. J. M. Miller, D. L. Dubois, J. A. Labinger, J. E. Bercaw, *Inorg. Chem.,* **2010,** 49, 3918-3926.
[36] P. S. Pregosin, *NMR in Organometallic Chemistry* Wiley, Zurich, **2012**.
[37] R. J. Pawley, G. L. Moxham, R. Dallanegra, A. B. Chaplin, S. K. Brayshaw, A. S. Weller, M. C. Willis, *Organometallics,* **2010,** 29, 1717-1728.
[38] A. G. Orpen, P. G. Pringle, M. B. Smith, K. Worboys, *J. Organomet. Chem.,* **1998,** 550, 255-266.
[39] M. A. Esteruelas, A. M. López, E. Oñate, E. Royo, *Organometallics,* **2005,** 24, 5780-5783.
[40] N. S. Townsend, A. B. Chaplin, M. A. Naser, A. L. Thompson, N. H. Rees, S. A. Macgregor, A. S. Weller, *Chem. Eur. J.,* **2010,** 16, 8376-8389.
[41] M.-E. Moret, S. F. Keller, J. C. Slootweg, P. Chen, *Inorg. Chem.,* **2009,** 48, 6972-6978.
[42] A. C. Albeniz, G. Schulte, R. H. Crabtree, *Organometallics,* **1992,** 11, 242-249.
[43] A. C. Cooper, J. C. Huffman, K. G. Caulton, *Organometallics,* **1997,** 16, 1974-1978.
[44] N. Phillips, L. Treasure, N. H. Rees, R. Tirfoin, J. E. Mcgrady, S. Aldridge, *Eur. J. Inorg. Chem.,* **2014,** 2014, 4877-4885.
[45] L. J. L. Häller, E. Mas-Marzá, M. K. Cybulski, R. A. Sanguramath, S. A. Macgregor, M. F. Mahon, C. Raynaud, C. A. Russell, M. K. Whittlesey, *Dalton Trans.,* **2017,** 46, 2861-2873.
[46] A. Staubitz, A. P. M. Robertson, M. E. Sloan, I. Manners, *Chem. Rev.,* **2010,** 110, 4023-4078.
[47] J. Atzrodt, V. Derdau, T. Fey, J. Zimmermann, *Angew. Chem. Int. Ed.,* **2007,** 46, 7744-7765.
[48] A. Sattler, *ACS Catal.,* **2018,** 8, 2296-2312.
[49] G. L. Williams, C. M. Parks, C. R. Smith, H. Adams, A. Haynes, A. J. H. M. Meijer, G. J. Sunley, S. Gaemers, *Organometallics,* **2011,** 30, 6166-6179.
[50] S. D. Pike, R. J. Pawley, A. B. Chaplin, A. L. Thompson, J. A. Hooper, M. C. Willis, A. S. Weller, *Eur. J. Inorg. Chem.,* **2011,** 2011, 5558-5565.
[51] A. J. Sandee, L. A. Van Der Veen, J. N. H. Reek, P. C. J. Kamer, M. Lutz, A. L. Spek, P. W. N. M. Van Leeuwen, *Angew. Chem. Int. Ed.,* **1999,** 38, 3231-3235.
[52] B. J. Van Der Veken, H. H. Liefooghe, *J. Mol. Struct.,* **1994,** 328, 211-220.
[53] H.-I. Lee, R. Y. Igarashi, M. Laryukhin, P. E. Doan, P. C. Dos Santos, D. R. Dean, L. C. Seefeldt, B. M. Hoffman, *J. Am. Chem. Soc.,* **2004,** 126, 9563-9569.
[54] L. J. Sewell, A. B. Chaplin, J. a. B. Abdalla, A. S. Weller, *Dalton Trans.,* **2010,** 39, 7437-7439.
[55] M. Albrecht, *Chem. Rev.,* **2010,** 110, 576-623.
[56] N. P. Tsvetkov, M. F. Laird, H. Fan, M. Pink, K. G. Caulton, *Chem. Commun.,* **2009,** 4578-4580.

[57] M. A. Rankin, D. F. Maclean, R. Mcdonald, M. J. Ferguson, M. D. Lumsden, M. Stradiotto, *Organometallics,* **2009,** 28, 74-83.
[58] A. Y. Verat, M. Pink, H. Fan, J. Tomaszewski, K. G. Caulton, *Organometallics,* **2008,** 27, 166-168.
[59] A. Y. Verat, M. Pink, H. Fan, B. C. Fullmer, J. Telser, K. G. Caulton, *Eur. J. Inorg. Chem.,* **2008,** 2008, 4704-4709.
[60] A. Johnson, C. G. Royle, C. N. Brodie, A. J. Martínez-Martínez, S. B. Duckett, A. S. Weller, *Inorg. Chem.,* **2021,** 60, 13903-13912.
[61] N. M. West, S. Reinartz, P. S. White, J. L. Templeton, *J. Am. Chem. Soc.,* **2006,** 128, 2059-2066.
[62] R. N. Perutz, S. Sabo-Etienne, *Angew. Chem. Int. Ed.,* **2007,** 46, 2578-2592.
[63] A. B. Chaplin, A. I. Poblador-Bahamonde, H. A. Sparkes, J. a. K. Howard, S. A. Macgregor, A. S. Weller, *Chem. Commun.,* **2009,** 244-246.
[64] T. W. Lyons, D. Bézier, M. Brookhart, *Organometallics,* **2015,** 34, 4058-4062.
[65] R. Ahuja, B. Punji, M. Findlater, C. Supplee, W. Schinski, M. Brookhart, A. S. Goldman, *Nature Chem.,* **2011,** 3, 167-171.
[66] A. I. Mckay, J. Barwick-Silk, M. Savage, M. C. Willis, A. S. Weller, *Chem. Eur. J.,* **2020,** 26, 2883-2889.
[67] S. D. Pike, M. R. Crimmin, A. B. Chaplin, *Chem. Commun.,* **2017,** 53, 3615-3633.
[68] H. C. Johnson, E. M. Leitao, G. R. Whittell, I. Manners, G. C. Lloyd-Jones, A. S. Weller, *J. Am. Chem. Soc.,* **2014,** 136, 9078-9093.
[69] M. Dietz, A. Johnson, A. Martínez-Martínez, A. S. Weller, *Inorg. Chim. Acta,* **2019,** 491, 9-13.
[70] A. Kumar, N. A. Beattie, S. D. Pike, S. A. Macgregor, A. S. Weller, *Angew. Chem. Int. Ed.,* **2016,** 55, 6651-6656.
[71] K. Burgess, W. A. Van Der Donk, S. A. Westcott, T. B. Marder, R. T. Baker, J. C. Calabrese, *J. Am. Chem. Soc.,* **1992,** 114, 9350-9359.
[72] J. M. Brown, G. C. Lloyd-Jones, *J. Am. Chem. Soc.,* **1994,** 116, 866-878.
[73] I. a. I. Mkhalid, R. B. Coapes, S. N. Edes, D. N. Coventry, F. E. S. Souza, R. L. Thomas, J. J. Hall, S.-W. Bi, Z. Lin, T. B. Marder, *Dalton Trans.,* **2008,** 1055-1064.
[74] A. Johnson, A. J. Martínez-Martínez, S. A. Macgregor, A. S. Weller, *Dalton Trans.,* **2019,** 48, 9776-9781.
[75] R. H. Crabtree, *The Organometallic Chemistry of the Transition Metals*. 6th ed., John Wiley & Sons, New Jersey, **2014**.
[76] A. D. Buckingham, P. J. Stephens, *J. Chem. Soc.,* **1964,** 4583-4587.
[77] M. Baranac-Stojanović, *RSC Advances,* **2014,** 4, 308-321.
[78] U. Fekl, K. I. Goldberg, *J. Am. Chem. Soc.,* **2002,** 124, 6804-6805.
[79] H. C. Johnson, R. Torry-Harris, L. Ortega, R. Theron, J. S. Mcindoe, A. S. Weller, *Cat. Sci. Technol.,* **2014,** 4, 3486-3494.
[80] H. V. Huynh, L. R. Wong, P. S. Ng, *Organometallics,* **2008,** 27, 2231-2237.

3 Chapter Three – Synthesis and coordination chemistry of *o*-F,F-DPEphos and a comparison with *o*-H-DPEphos and *o*-Me-DPEphos

3.1 Preamble

In Chapter Two, Schrock-Osborn complexes of *ortho*-substituted DPEphos ligands were explored, including: *o*-H-, *o*-Me-, *o*-OMe- and *o*-^{i}Pr-DPEphos. These complexes all contained *ortho*-aryl Rh···H–C anagostic interactions in the solid-state and solution. The hydrogenation products of these Schrock-Osborn complexes in d_6-acetone varied between Rh(I) solvated and Rh(III) hydrido complexes, depending on the *ortho*-aryl substituent. The question we next asked was, what if both of the *ortho*-aryl protons are exchanged for fluorine atoms? Through targeted ligand design we can prevent the formation of *ortho*-aryl anagostic interactions and also investigate the influence of *ortho*-fluorine substitution on the fundamental coordination chemistry of DPEphos ligands.

Within this chapter, the coordination chemistry of the new ligand *ortho*-F-F-DPEphos, **1-F,F**, is analysed and compared with the parent DPEphos, *o*-H-DPEphos (**1-H**) (Figure 3.1). In some instances, the equivalent *o*-Me-DPEphos (**1-Me**) complexes will also be compared, to ascertain if the effect of *ortho*-fluorine substitution is comparable to the bulky *ortho*-methyl variant.

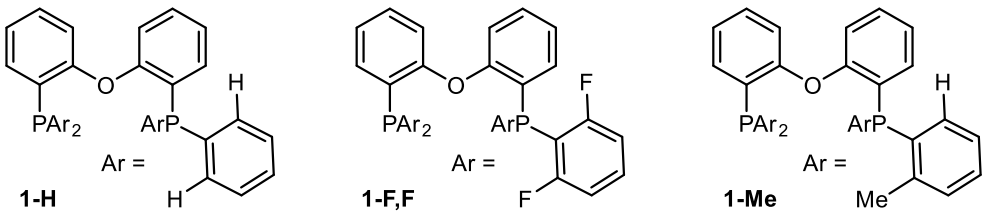

Figure 3.1. The three *ortho*-substituted DPEphos ligands explored within this chapter.

3.2 *Ortho*-F,F-DPEphos

The di-*ortho*-fluorine analogue of *o*-H-DPEphos, *o*-F,F-DPEphos (**1-F,F**) was prepared using the same method used for the preparation of **1-^{i}Pr** (section 2.2.1).[1] Stoichiometric addition of Li[2,6-$F_2C_6H_3$] to 2,2'-$(PCl_2)_2(C_6H_4)_2O$ at –78 °C resulted in the formation of **1-F,F** (Scheme 3.1). An aqueous workup followed by recrystallization in a CH_2Cl_2/pentane solution mixture afforded **1-F,F** as an analytically pure white solid in a modest yield (30%).

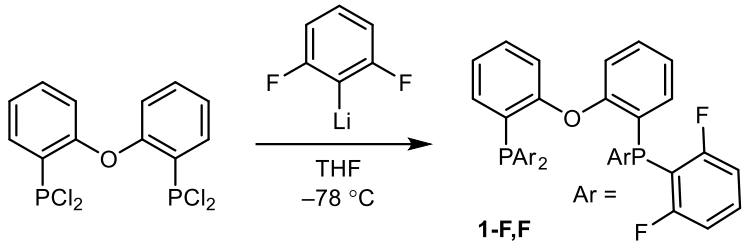

Scheme 3.1. Synthesis of **1-F,F**.

1-F,F was fully characterised by multinuclear NMR spectroscopy (CD_2Cl_2). In the $^{31}P\{^1H\}$ NMR spectrum a single resonance was observed at δ –62.5, coupling to four equivalent ^{19}F nuclei to give a quintet [*J*(PF) = 40 Hz] (Figure 3.2). This was also reflected in the $^{19}F\{^1H\}$ NMR spectrum, which showed a single doublet signal at δ –100.7, with an equivalent coupling constant [*J*(PF) = 40 Hz]. The ^{31}P signal is shifted 45.9 ppm upfield compared to **1-H**. A similar difference in shift is observed between PPh_3 (δ –4.7)[2] and $PPh(2,6\text{-}F_2C_6H_3)_2$ (δ –50.6).[3] The fact that only one ^{31}P and one ^{19}F environment are observed indicates that there is free rotation of the aryl groups[4] and flexibility within the backbone which makes all of the aryl groups and the ^{31}P nuclei equivalent on the NMR timescale. This is corroborated by the ^1H NMR data, which details six signals in an 8:4:2:2:2:2 ratio, corresponding to the *meta*-H and *para*-H on the substituted aryl groups, and the four backbone signals respectively (Figure 3.2).

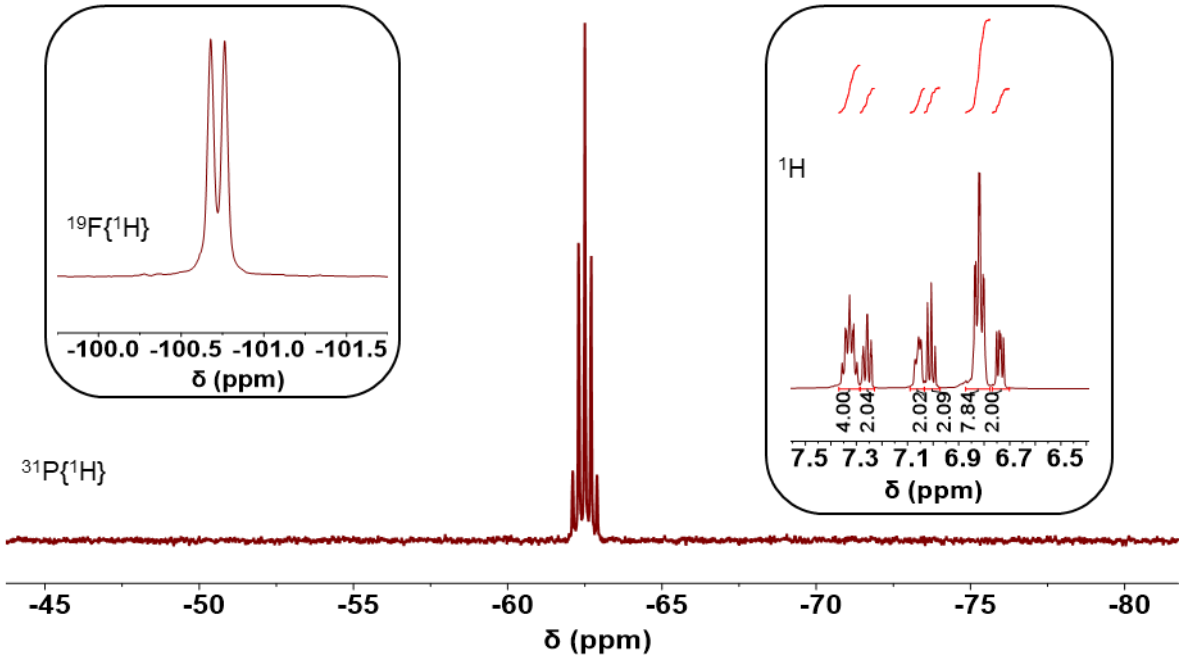

Figure 3.2. $^{31}P\{^1H\}$ NMR spectrum of **1-F,F** (202 MHz, CD_2Cl_2, 295 K). The insets show the $^{19}F\{^1H\}$ spectrum and the aromatic region of the ^1H NMR spectrum (471 and 500 MHz, CD_2Cl_2, 295 K).

3.3 Synthesis, characterisation and structural behaviour of [Rh(*o*-F,F-DPEphos)(NBD)][BAr$^F_4$]

Intrigued how the coordination chemistry with Rh(I) fragments will change if we remove the possibility of *ortho*-aryl Rh···H–C anagostic interactions, the corresponding Schrock-Osborn complex of **1-F,F**, [Rh(*o*-F,F-DPEphos)(NBD)][BAr$^F_4$] **2-F,F**, was synthesised in a similar manner to **2-^{i}Pr** in Chapter Two.[1] Stoichiometric addition of **1-F,F** to [Rh(NBD)$_2$][BAr$^F_4$] in 1,2-$F_2C_6H_4$ solvent resulted in the quantitative formation of **2-F,F** (Scheme 3.2), which was isolated as an analytically pure, orange powder. The solid-state structure does not match the symmetry observed in the solution-state.

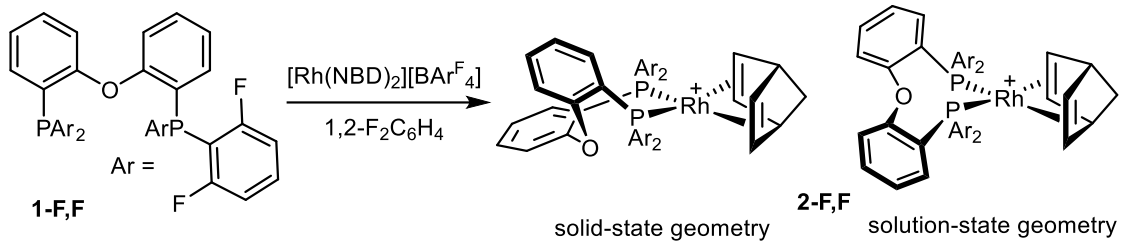

Scheme 3.2. Synthesis of [Rh(*o*-F,F-DPEphos)(NBD)][BAr$^F_4$], **2-F,F**. [BAr$^F_4$]$^-$ anions omitted for clarity.

A few crystals suitable for diffraction were obtained by slow diffusion of pentane into a 1,2-$F_2C_6H_4$ solution of **2-F,F**. The solid-state structure revealed a very similar overall bonding structure to **2-H**, **2-Me** and **2-OMe** studied in Chapter Two, i.e. a *cis*-κ^2-P,P arrangement of the *o*-F,F-DPEphos ligand [P–Rh–P = 101.48(2)°] with no ether coordination [D(Rh···O) = 3.480(2) Å] and the NBD fragment bound $\eta^2\eta^2$(C=C) to give an overall pseudo square planar geometry on a Rh(I) centre (Figure 3.3). The diphenylether backbone is twisted and the oxygen sits off the P1–Rh–P2 plane by 1.67 Å in an envelope-like[5] geometry, giving overall C_1 symmetry. The Rh–P and Rh–C bond lengths and angles are comparable to **2-H**, **2-Me** and **2-OMe**. There are two close F···F contacts between F2···F3 and F6···F7 of 2.820(2) and 2.859(2) Å respectively (Figure 3.3).

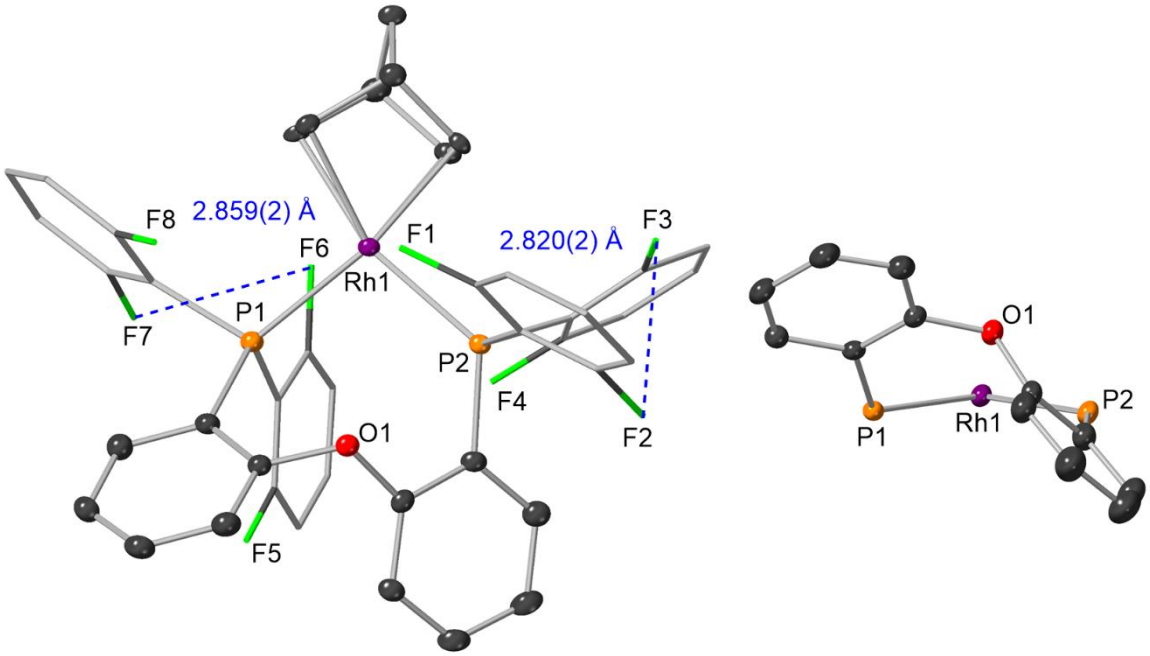

Figure 3.3. Crystallographically determined structure of **2-F,F**. Ellipsoids shown at the 50% probability level. Hydrogen atoms and $[BAr^{F}{}_{4}]^{-}$ anion omitted and substituted aryl groups in stick form for clarity. Selected bond lengths (Å) and angles (°): Rh1–P1, 2.3180(6); Rh1–P2, (2.3757(6); Rh1–O1, 3.480(2); Rh1–F1, 2.876(2); Rh1–F6, 3.147(2); P1–Rh1–P2, 101.48(2). An end on and reduced form of **2-F,F** is shown on the right, emphasising the envelope conformation.

In solution at 295 K, a single resonance is observed in the $^{31}P\{^{1}H\}$ spectrum as a sharp doublet at δ –17.4 with *J*(RhP) = 163 Hz (Figure 3.4). This is ~34 ppm more upfield than [Rh(*o*-H-DPEphos)(NBD)][$BAr^{F}{}_{4}$] (**2-H**), but both have similar *J*(RhP) values (159 Hz in **2-H**).[6] In the $^{19}F\{^{1}H\}$ NMR spectrum at 295 K, three, very broad signals are observed in an approximate 1:2:1 ratio (Figure 3.4). The ^{1}H NMR spectrum reveals a time-averaged C_{2V} symmetry of **2-F,F** at 295 K, as three NBD signals in a 4:2:2 are observed at δ 4.16, 3.80 and 1.44 respectively, corresponding to the alkene, methine and methylene protons respectively. The aromatic signals are broad and overlapping and provide no structural information. Upon cooling to 223 K, the ^{31}P signal in the $^{31}P\{^{1}H\}$ NMR spectrum splits into a doublet of doublets, retaining the original *J*(RhP) (163 Hz) combined with a new *J*(PF) of 38 Hz. In the ^{19}F NMR spectrum, four signals are observed in a 2:2:2:2 ratio, three of which are singlets (δ –90.8, –97.9 and –103.5) and one doublet signal at δ –98.1, showing the same *J*(PF) value of 38 Hz (Figure 3.4). Cooling to 140 K in $CDCl_2F$,[7] did not reveal any further coupling. In the ^{1}H NMR spectrum of **2-F,F** at 183 K, four NBD signals are observed in a 2:2:2:2 ratio, suggesting a C_2 symmetry. Therefore, the observation of four ^{19}F signals implies that there is restricted rotation about the P–C bonds, which makes

the *ortho*-fluorine atoms on the same aryl groups inequivalent. This has previously been reported in *trans*-[$PtCl_2(PEt_3)(P\{C_6F_5\}_3)$].[8] Upon warming **2-F,F** to 318 K, only one, very broad ^{19}F signal is observed, suggesting multiple isomers are coalescing at higher temperature. There are several observations to note here: 1) A fluxional process is occurring on the NMR timescale that makes the ^{19}F atoms become equivalent at higher temperature. 2) At 183 K, the NBD ^{1}H and ^{19}F signals show a complex of C_2 symmetry, but at 298 K C_{2v} symmetry is observed. 3) The P-F coupling between one ^{31}P and four ^{19}F nuclei, which gave quintet and doublet multiplicity respectively in **1-F,F**, is no longer apparent, and instead, there is only one observable *J*(PF) coupling. 4) No through-space ^{19}F-^{19}F coupling is observed, despite the close F···F contacts in the solid-state, unlike **6-F,F**, which will be discussed in section 3.6.

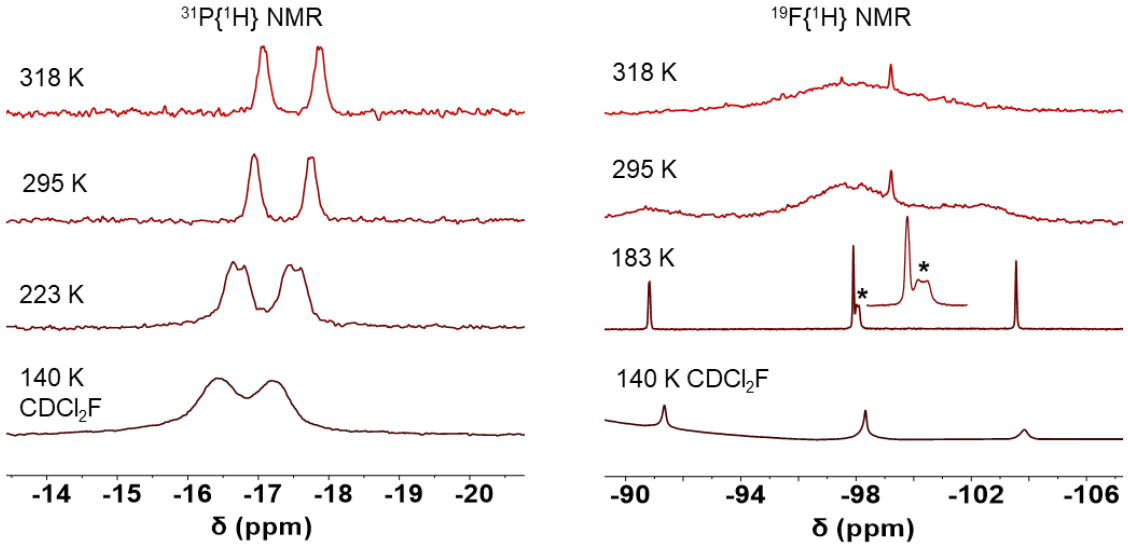

Figure 3.4. $^{31}P\{^{1}H\}$ NMR spectra (left) and $^{19}F\{^{1}H\}$ NMR spectra (right) of **2-F,F** at different temperatures (500 and 471 MHz respectively, CD_2Cl_2 unless otherwise stated). * Denotes the one ^{19}F signal that shows *J*(PF) which is highlighted in the inset.

An unexpected lack of P-F coupling has been reported before by Saunders and co-workers in *trans*-[$PtCl_2(PEt_3)(P\{2,6\text{-}F_2C_6H_3\}_3)$], in which only coupling between one ^{31}P and one ^{19}F was observed at low temperature [*J*(PF) = 30 Hz] and a fluxional process was attributed to restricted rotation of the aryl groups. In comparison, a doublet and a septet are observed in the ^{19}F and ^{31}P NMR spectra respectively for free $P(2,6\text{-}F_2C_6H_3)_3$ [*J*(PF) = 39 Hz].[3] In the report by Saunders, no explanation was given for the lack of P-F coupling, but potentially the orbital overlap which facilitates the coupling mechanism is sensitive to slight changes in the bridging bond angles (i.e. the Karplus equation).[9] The reason why only

doublet multiplicity is observed in the ^{31}P signal of **2-F,F** at 223 K is potentially due to restricted aryl rotation making the fluorine atoms on the same aryl rings inequivalent but there is still overall C_{2V} symmetry in the complex, and the ^{31}P nucleus only couples to one ^{19}F out of the possible four.

Restricted aryl rotation would not account for the change in symmetry observed for the NBD fragment at different temperatures. Instead, we propose a low energy ring-flipping process between two C_2 states is occurring in **2-F,F** in solution which gives time-averaged C_{2V} symmetry at higher temperature (Scheme 3.3). This process retains C_2 or C_{2V} symmetry throughout, hence the preservation of a single ^{31}P signal at all temperatures. We suggest the C_2 geometry is similar to the solid-state structure of **2-^{i}Pr** (section 2.3.1), in which the oxygen sits closer to the RhP_2 plane than the envelope-like[5] C_1 structures of **2-H**, **2-Me** and **2-OMe**. The proposed fluxionality within **2-F,F** is different to that suggested for **2-H**, **2-Me** and **2-OMe** (section 2.3.2) which were observed as C_1 isomers at low temperatures. Restricted rotation of the partially fluorinated aryl groups is also occurring on the NMR timescale (Scheme 3.3). Ring-flipping processes are known in metal-Xantphos[10, 11] and metal-DPEphos complexes, as discussed in section 2.3.2.[1] This dynamic process in **2-F,F** tempers the through-space F···F interactions, unlike **6-F,F**, in which no backbone fluxionality was observed, which is discussed in section 3.6.

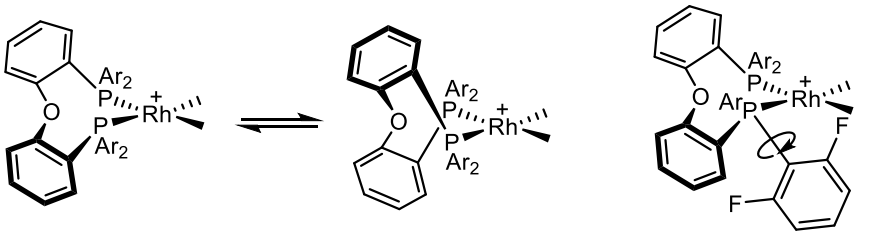

Scheme 3.3. Proposed fluxional processes occurring in **2-F,F** in solution.

Returning to the crystal structure of **2-F,F**, instead of *ortho*-aryl protons situated in the apical position to the rhodium, as seen in **2-R** in Chapter Two, two *ortho*-fluorine atoms are located *trans* to one another in similar positions (F1 and F6, Figure 3.5). The Rh···F distance of one of the contacts is similar to anagostic interactions in **2-H** with D(Rh···F1) = 2.876(2) Å, and the other is slightly longer; D(Rh···F6) = 3.147(2) Å. However, considering the covalent radius of F is 0.26 Å larger than H (0.57 and 0.31 Å respectively),[12] the F atoms are closer, relatively, to the rhodium. The angle between the P1–Rh–P_2

plane and the apical fluorine atoms (Φ) are 65.5° and 58.0°, which are very similar to the protons in **2-H** (Φ = 63.1° and 58.0°).

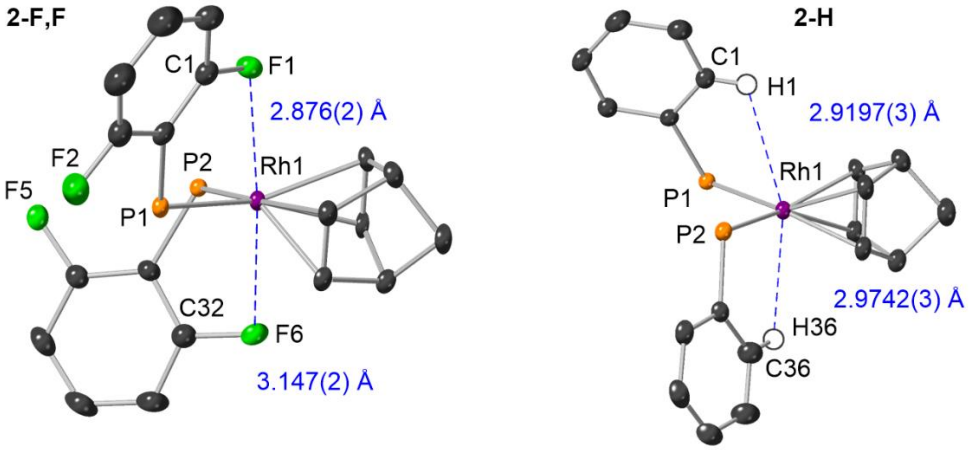

Figure 3.5. Truncated structures of **2-F,F** and **2-H** (section 2.3.1) highlighting the close Rh···F and Rh···H contacts. Ellipsoids shown at the 50% probability level. $[BAr^F{}_4]^-$ anion, hydrogen atoms and aryl groups not involved in metal contacts are removed for clarity.

Close metal fluorine interactions have been reported before by Togni and co-workers in [MCl(COD)diphenyl(5,6,7,8-tetrafluoronapthalen-1yl)] (M = Rh or Ir, COD = cyclooctadiene) for which one fluorine atom is situated 3.0997(8) and 3.074(1) Å from the Rh and Ir centres respectively (Figure 3.6). No *J*(RhF) was observed in Togni's rhodium complex, but it is interesting to note that the ^{19}F NMR signal corresponding to the fluorine atom in close contact with the rhodium is shifted downfield by ~20 ppm compared to the other signals.[13] This downfield shift is reminiscent of a M···H–C anagostic interaction.[14]

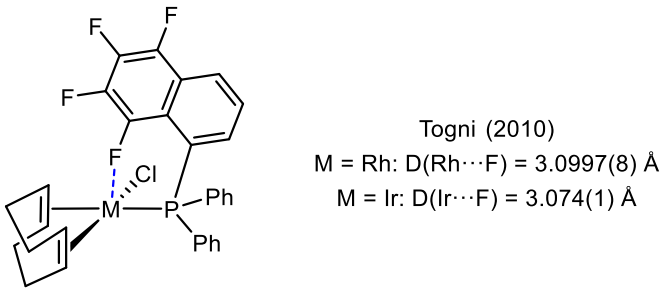

Figure 3.6. Diagram of the M···F interactions observed by Togni and co-workers.[13]

If we assume a time-averaged C_2 symmetry in solution at low temperature, then F1 and F6 are likely to be chemically equivalent. One of the ^{19}F signals in **2-F,F**, at δ 90.9 (integral 2F), is shifted downfield by 9.8 ppm compared to the free ligand, and is ~10 ppm more downfield than the other signals. No *J*(RhF) is observed in any of the signals. However, it would be incorrect to directly compare the anagostic interactions analysed in **2-R** and the metal-fluorine interactions in **2-F,F**. Firstly, the covalent radius of fluorine is 0.57 Å, much larger than that of hydrogen (0.31 Å).[15] Also, C–F bonds are much more polarised than C–H bonds, and therefore any bonding interaction may well be more electrostatic in nature.[12] Such metal-fluorine interactions have been described as metal-dipole interactions, which can also be angle dependent,[16] or defined as closed-shell interactions which are stronger than van der Waals forces but weaker than most ionic or covalent bonds.[17] Nevertheless, it is interesting that the fluorine atoms in **2-F,F** are positioned similarly to the protons in **2-H**. Computational calculations are required to ascertain the exact bonding of these metal-fluorine interactions and also ascertain whether changes in local magnetic fields, dependent on the topological placing of the F atoms, influences the ^{19}F chemical shift.

3.4 Hydrogenation of [Rh(*o*-F,F-DPEphos)(NBD)][BAr$^F_4$] in d_6-acetone

Schrock-Osborn catalysts are typically activated by hydrogenation of the diene fragment in a coordinating solvent.[18] **2-H** has previously been activated in this way in the present of *o*-xylene,[19] acetone,[6] and C_6H_5F[20], which resulted in the formation of Rh(κ^2-P,P-DPEphos)(η^6-*o*-xylene)][BAr$^F_4$] (**i-17**),[19] [Rh(κ^2-P,P-DPEphos)(η^1-O-acetone)$_2$][BAr$^F_4$] (**i-18**)[6] and [Rh(κ^2-P,P-DPEphos)(η^6-C_6H_5F)][BAr$^F_4$] (**i-19**)[20] respectively. Acetone was also employed in Chapter Two with the other mono-*ortho*-substituted DPEphos variants. The less bulky variants formed solvated complexes, e.g. [Rh(*o*-H,DPEphos)(acetone)$_2$][BAr$^F_4$] (**3-H**) and [Rh(*o*-OMe-DPEphos)(acetone)$_2$][BAr$^F_4$] (**3-OMe**), whereas, hydride complexes were formed with the more bulky ligands, such as [Rh(*o*-Me-DPEphos)(H)$_2$(acetone)][BAr$^F_4$] (**4-Me**), and C–H activation occurred in the bulkiest, *ortho*-isopropyl variant, forming {[Rh(*o*-^{i}Pr-DPEphos')(H)][BAr$^F_4$] (**4-^{i}Pr**).[1]

We now extend these studies to **2-F,F**. Application of a H_2 atmosphere (15 PSI gauge pressure) to a sample of **2-F,F** in d_6-acetone solvent resulted in an colour change from orange to red on the time of mixing, immediately indicative of a Rh(I) solvated complex rather than a Rh(III) dihydride, which are

typically pale yellow. The in-situ NMR data confirmed complete conversion of **2-F,F** to a new complex, which is assigned as [Rh(*o*-F,F-DPEphos)(d_6-acetone)$_2$][BAr$^F{}_4$] (**3-F,F**, Scheme 3.4). Attempts to isolate **3-F,F** resulted in decomposition of the complex and so it was subsequently characterised by in-situ NMR spectroscopy only (Figure 3.7).

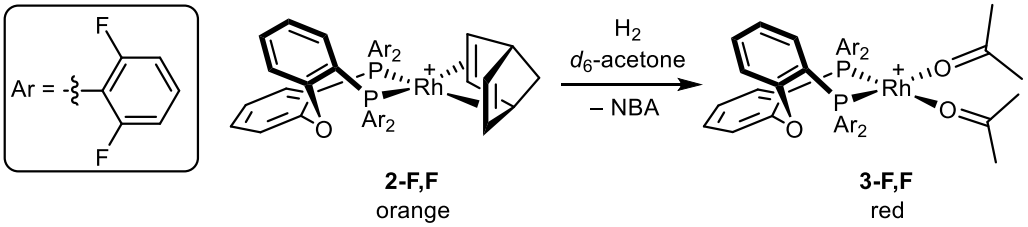

Scheme 3.4. Hydrogenation of **2-F,F** in d_6-acetone to form solvated complex **3-F,F**. [BAr$^F{}_4$]$^-$ anion omitted for clarity.

In the $^{31}P\{^1H\}$ NMR spectrum of **3-F,F** only one signal is observed, at δ 3.0, shifted downfield by 20.4 ppm compared to **2-F,F**. There is a similar change in shift between **2-H** (δ 17) and **3-H** (δ 41.8).[6] The ^{31}P signal of **3-F,F** contains doublet multiplicity with a very large *J*(RhP) of 222 Hz, which is suggestive of weakly bound acetone ligands at a Rh(I) centre. In comparison, the *J*(RhP) value observed for **3-H** is 209 Hz,[6] and 194-223 Hz for **3-Me** and **3-OMe**.[1] The lack of hydrides and the presence of free NBA observed in the ^1H NMR spectrum of **3-F,F** also suggest the formation of a solvated Rh(I) complex. In the $^{19}F\{^1H\}$ NMR spectrum of **3-F,F**, only one signal is observed, which is at δ –97.2, with an integral of 8F relative to the [BAr$^F{}_4$]$^-$ signal (Figure 3.7). This suggests rapid rotation of the 2-6-$F_2C_6H_4$ groups and time-averaged C_{2V} symmetry, consistent with the single ^{31}P NMR signal. It is interesting to note that there is no observable *J*(PF). This is similar to the ^{19}F NMR signal previously reported by Saunders and co-workers for [RhCl(CO){P(2,6-$F_2C_6H_4$)$_3$}$_2$], which was observed as a singlet at δ –96.8.[3] No *J*(PF) is observed in the ^{31}P NMR signal of **3-F,F** either. Rapid P–C rotation is reflected in the aromatic signals in the ^1H NMR spectrum of **3-F,F** (Figure 3.7), for which only six signals are observed in a 2:2:2:2:8:4 ratio, which are assigned as four backbone signals and *meta*-H and *para*-H on the fluorinated aromatics respectively. The NMR signals corresponding to **3-F,F** did not change after removal of the H_2 atmosphere.

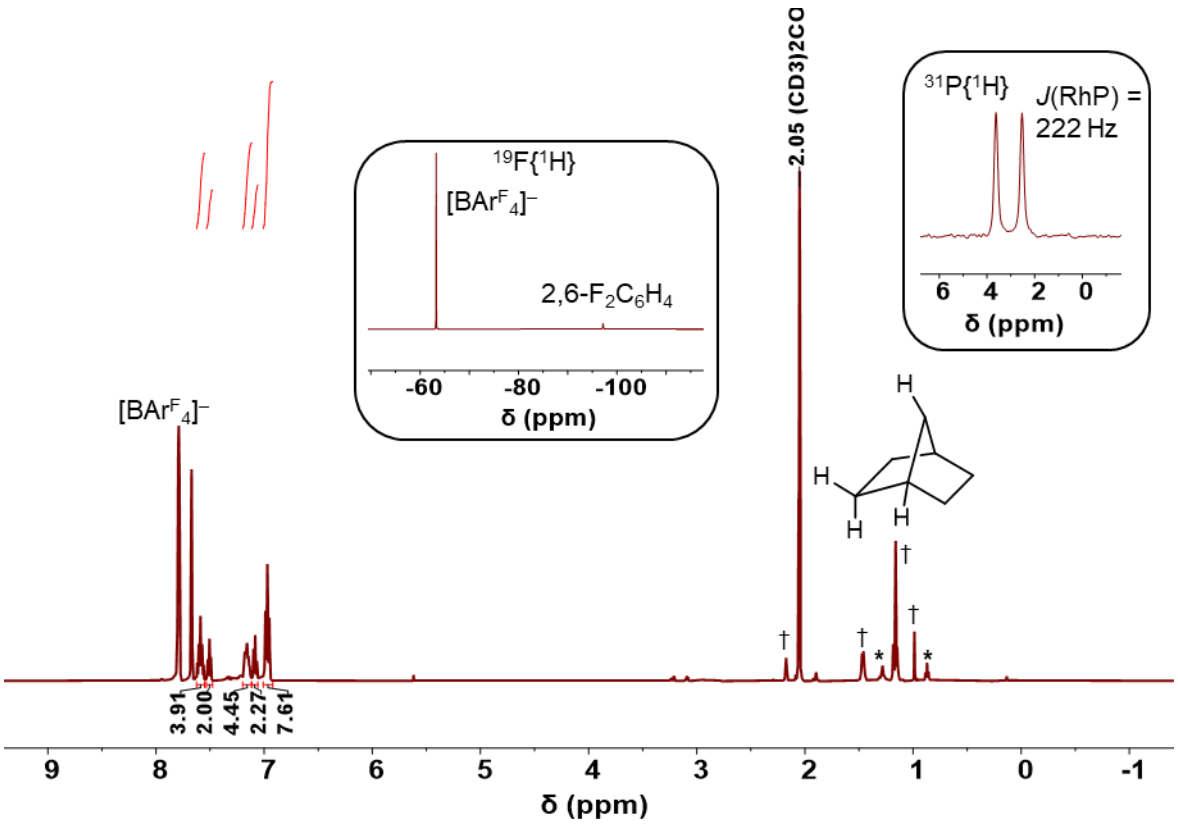

Figure 3.7. ^{1}H NMR spectrum of in-situ formed **3-F,F** (500 MHz, d_6-acetone, 298 K). Integrals relative to one of the *o*-F,F-DPEphos backbone signals. * Denotes pentane impurity and † denotes free NBA. The insets show the ^{19}F and ^{31}P signals (471 and 202 MHz respectively, acetone-D_6, 298 K).

Cooling a sample of **3-F,F** to 183 K did not result in any change in the ^{31}P signal in the ^{31}P{^{1}H} NMR spectrum, maintaining a doublet multiplicity with *J*(RhP) = 222 Hz at δ 3.0. The ^{19}F signals, however, changed from a broad singlet at δ –97.2 to six broad signals, two of which are twice the integral of the others (Figure 3.8). We suggest that there are eight ^{19}F environments, with two sets of two coincident signals. This shows that P–C rotation can be frozen out at low temperature on the NMR timescale to give distinct ^{19}F environments. Eight ^{19}F environments is indicative of a C_1 symmetry complex, however, only one ^{31}P signal is observed (i.e. C_2 symmetry), therefore, either the ^{31}P environments are coincident or there is a low energy dynamic process[10, 11] that makes the ^{31}P chemically equivalent at 183 K but the phosphine substituents are frozen out. No *J*(PF) is observed at 183 K. The aromatic signals are broad in the ^{1}H NMR spectrum of **3-F,F** at 183 K and not useful for structure elucidation.

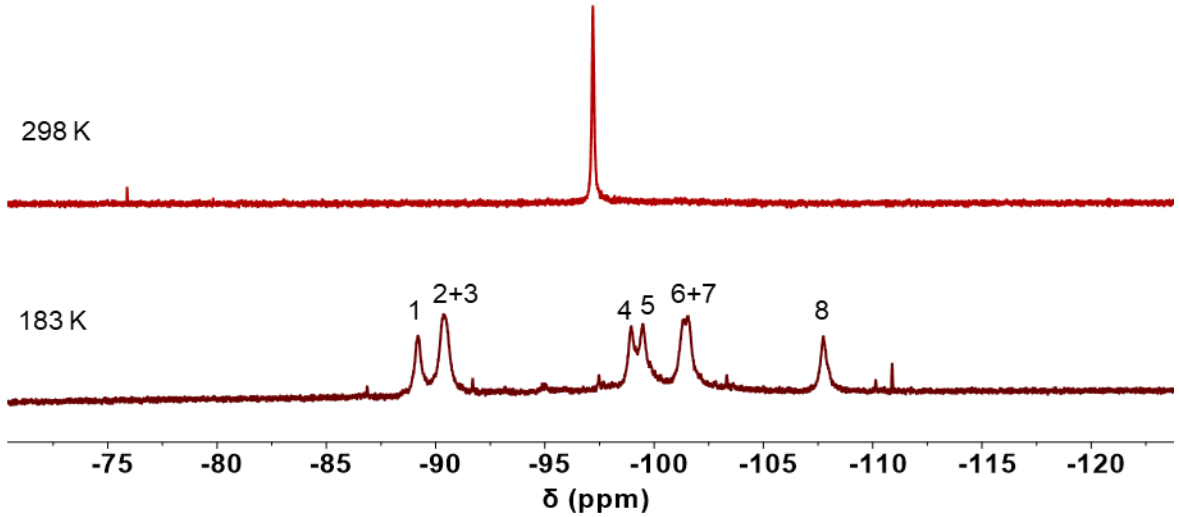

Figure 3.8. Selected region of the ^{19}F NMR spectrum of **3-F,F**, showing the 2,6-$F_2C_6H_3$ signals, at 298 K and 183 K (471 MHz, d_6-acetone).

3.5 Hydrogenation products in 1,2-$F_2C_6H_4$

In this next section, the hydrogenation products of **2-H**, **2-Me** and **2-F,F** in 1,2-$F_2C_6H_4$ solvent will be compared. 1,2-$F_2C_6H_4$ is known to be a weakly coordinating aryl ligand due to the reduced ability for π-donation and the partial positive charge,[21, 22] and the reactivity of **2-H** with H_2 has not been explored using this solvent. An atmosphere of 15 PSI H_2 was added to a sample of **2-H** in 1,2-$F_2C_6H_4$ which resulted in an immediate colour change from orange to dark red. Analysis by in-situ NMR spectroscopy revealed that **2-H** had completely reacted after 20 minutes and two new ^{31}P signals were observed at δ 42.9 and 36.2, as well as free NBA in the ^{1}H NMR spectrum. The new complex, **4-H**, was isolated as a purple solid in a good yield (80%) and characterised using NMR spectroscopy and ESI-MS (Scheme 3.5). Unfortunately, crystals suitable for diffraction could not be obtained.

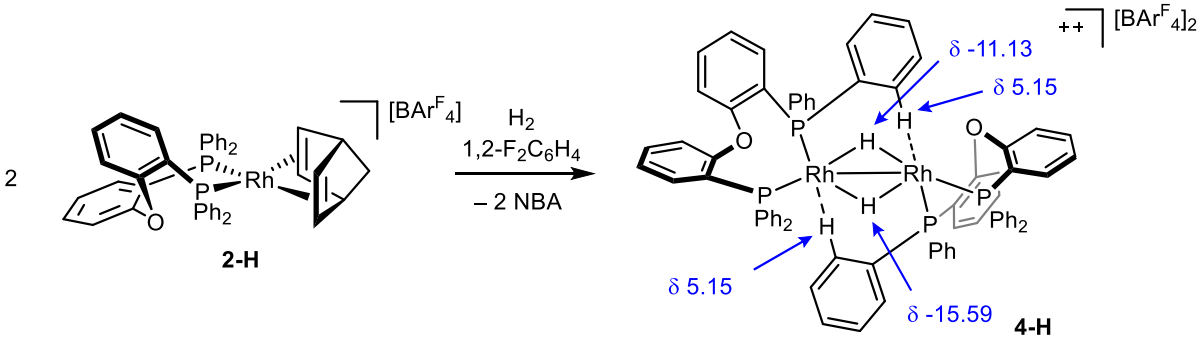

Scheme 3.5. Hydrogenation of **2-H** to form **4-H**.

In the $^{31}P\{^{1}H\}$ NMR spectrum of isolated **4-H** (CD_2Cl_2), two signals are observed; one as an apparent doublet of doublets at δ 43.3 with second order character[23] [*J*(RhP) = 174 Hz and *J*(PP) = 26 Hz] and the second at δ 36.5 observed as a complex second order multiplet (Figure 3.9). A ^{31}P NMR experiment, with no ^{1}H-decoupling, showed the signal at δ 43.3 as a broad doublet with *J*(RhP) = 174 Hz, and the signal at δ 36.5 as a broad doublet of doublets, with the latter comprising of *J*(RhP) = 154 Hz and a large *J*(PH) of 74 Hz. This is indicative of a *trans*-hydride arrangement. A similarly large *J*(PH) of 75 Hz has been reported for the two equivalent bridging hydrides, *trans* to PPh_3, in $[(PPh_3)_2RhH(\mu\text{-}H)_2(\mu\text{-}Cl)HRh(PPh_3)_2][CB_{11}H_{12}]$, for which the *trans*-hydride arrangement was confirmed by crystallography.[24]

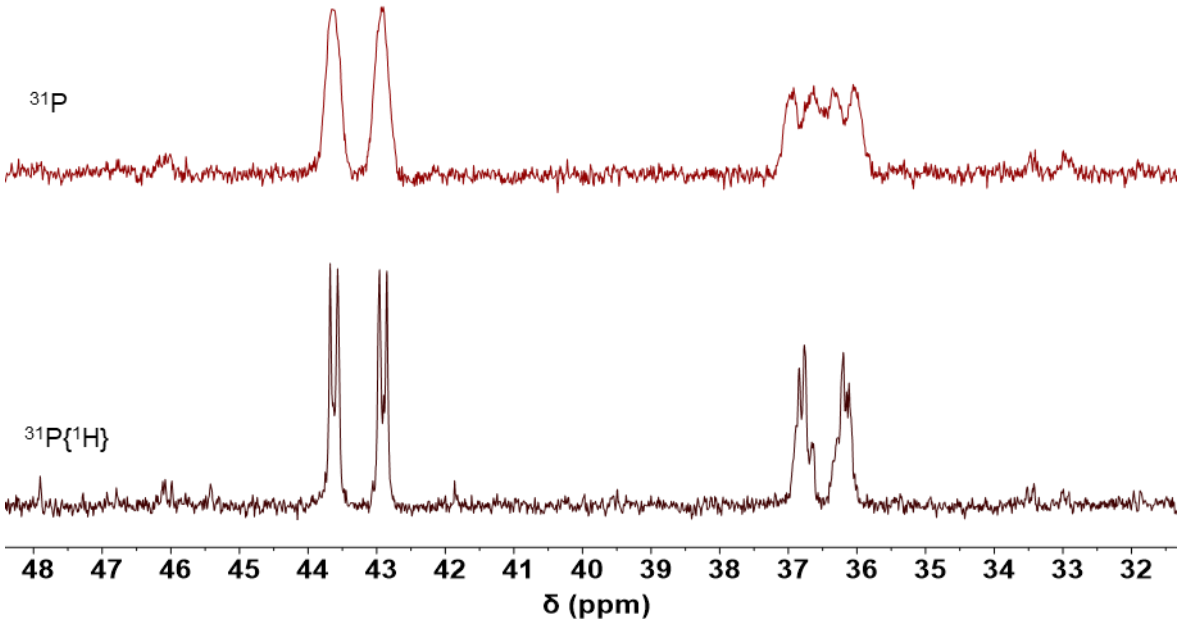

Figure 3.9. ^{31}P and $^{31}P\{^{1}H\}$ NMR spectra of **4-H**.

In the ^{1}H NMR spectrum of **4-H**, two hydride signals at δ –11.13 and –15.59 are both observed as complex multiplets, with the former containing the same large *J*(PH) of 74 Hz (Figure 3.10). The hydrides integrate to 1:1:2 relative to the $[BAr^F_4]^-$ anion, and the total aromatic protons sum up to 51H (theoretically 54H). These data imply the formation of a dicationic dimer with two inequivalent bridging hydrides, i.e. $[Rh(o\text{-H-DPEphos})(\mu\text{-}H)]_2[BAr^F_4]_2$.

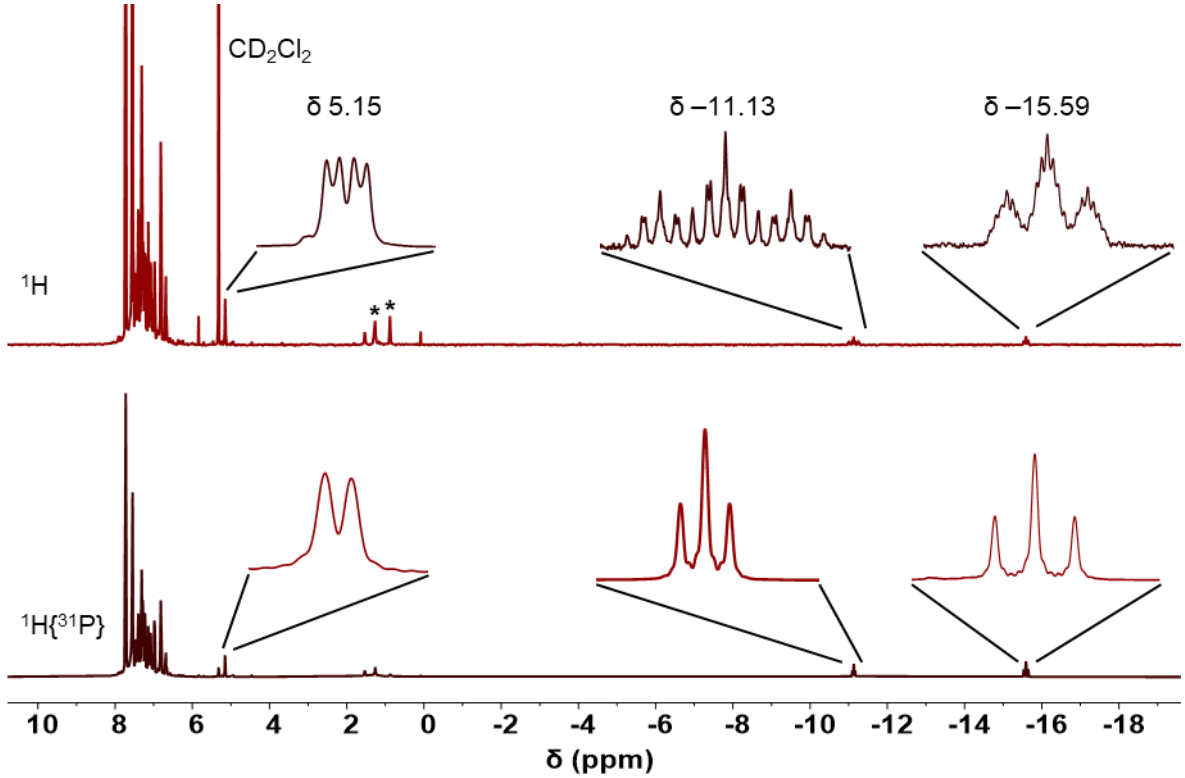

Figure 3.10. ^{1}H (top) and $^{1}H\{^{31}P\}$ (bottom) spectra of **4-H** (600 MHz, CD_2Cl_2, 298 K). The insets highlight the hydride signals and the agostic C–H. * Denotes pentane impurity.

Spin simulation studies replicated the experimental data best when the hydride corresponding to the signal at δ –11.13 couples to two of each of the following: Rh [*J*(RhH) = 20 Hz], *trans*-P [*J*(PH) = 74 Hz], *cis*-P [*J*(PH) = 17 Hz] and small *cis*-hydride/hydride coupling [*J*(HH) ≈ 2 Hz] (Figure 3.11). The coupling pattern of the signal at δ –15.59 is best simulated when coupling to two: Rh [*J*(RhH) = 34 Hz], *cis*-P [*J*(PH) = 9 Hz], *cis*-P [*J*(PH) = 5 Hz] and small *cis*-hydride/hydride coupling [*J*(HH) ≈ 2 Hz]. This is consistent with the $^{1}H\{^{31}P\}$ spectrum (Figure 3.10), that shows the hydride signals as triplets, each coupling to two equivalent Rh nuclei, with the hydride *trans* to the strongly coordinating phosphine exhibiting a smaller *J*(RhH) (20 Hz and 34 Hz respectively). This also coincides with the difference in chemical shift between the two hydrides, i.e. *trans* to a weakly donating ligand gives a more upfield chemical shift, as previously shown in $[Ru(IMe)_4(L)H][BAr^F{}_4]$ (IMe = 1,3-dimesitylimidazol-2-ylidene).[25]

Attempts to spin-simulate the $^{31}P\{^{1}H\}$ NMR spectrum matched less closely but give an acceptable fit (Figure 3.11). One theory is that improper ^{1}H-decoupling of the strong *trans*-hydride relationship influences the experimental coupling pattern, which cannot be replicated in the simulation. Nevertheless, the second order character of these signals, was only replicated when the two chemically

equivalent ^{31}P, *trans* to the hydride, couple to one another with *J*(PP) = 42 Hz. The other coupling constants were calculated as: *J*(*cis*-PP) = 29 Hz, *J*(proximal-RhP) = 150 and 172 Hz and *J*(distal-RhP) = ~4 Hz. The two ^{31}P signals were also shown to couple via a ^{31}P-COSY experiment.

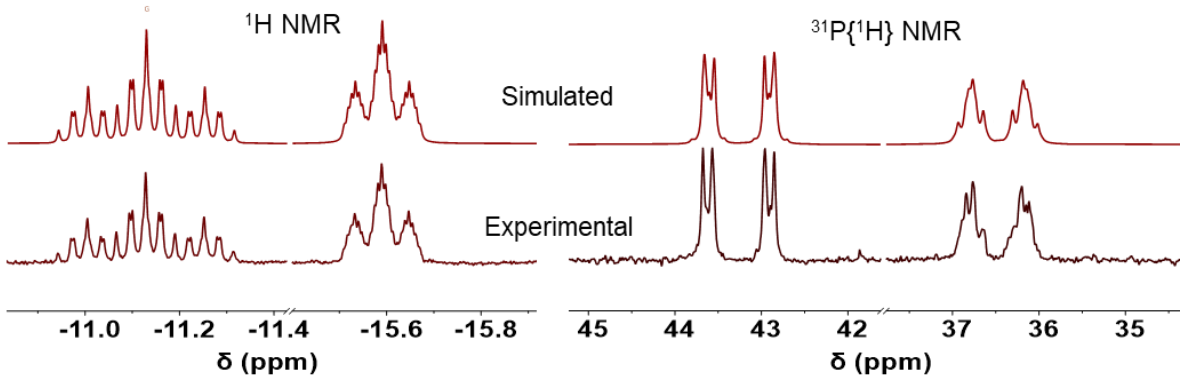

Figure 3.11. The experimental and spin-simulated AA'MM'NN'XX' coupling pattern in the hydride signals of **4-H** as well as the complex second order signals in the $^{31}P\{^{1}H\}$ NMR spectrum signals (600 and 243 MHz respectively, 298 K, CD_2Cl_2).

Another defining feature of the NMR spectra of **4-H** is displayed by an upfield shifted aromatic signal at δ 5.15, integral 2H, (Figure 3.10) which is observed as a doublet of doublets in the ^{1}H NMR spectrum [*J*(PH) = 4 Hz and *J*(HH) = 8 Hz]. This signal collapses to a doublet upon ^{31}P-decoupling and is assigned as an *ortho*-aryl proton, shifted 2.1 ppm compared to the equivalent signal in the free ligand. Upfield shifted signals are characteristic of M···H–E agostic bonds, as discussed in Chapter Two.[14, 26] A similarly upfield shifted signal was reported for $[Rh_2(\sigma,\mu\text{-CH-}\kappa^2\text{-P,P-}o\text{-H-DPEphos})_2(\sigma,\mu\text{–}(H_2B)_2NHMe)][Al(OC(CF_3)_3)_4]$ at δ 3.94 (integral 2H) and was assigned crystallographically to two equivalent agostic bonds between an *ortho*-aryl C–H and the distal rhodium, forming two bridging moieties (Figure 3.13).[27] Consequently, we propose two similar bridging agostic C–H bonds within **4-H** (Scheme 3.5).

Without a crystal structure, we turned to anaerobic ESI-MS for further support in our assignment.[28] When **4-H** was analysed by ESI-MS (positive mode), only mass values corresponding to $[Rh(o\text{-H-DPEphos})]^+$ (obs. 641.2 m/z, calc. 641.1 m/z) and $[Rh(o\text{-H-DPEphos})]_2^{2+}$ (obs. 641.2 m/z with 0.5 m/z spacings, calc. 641.1 m/z) were observed, even when a low capillary exit voltage was used (~90 V) (Figure 3.12). These cations are formed via H_2 loss and dimer fragmentation. When a sample of **2-H** was placed under an atmopshere of 15 PSI D_2, formation of $[Rh(o\text{-H-DPEphos})(\mu\text{-D})]_2[BAr^F{}_4]_2$ (***d*$_2$-4-H**) was confirmed by ^{2}H NMR and ^{31}P NMR spectroscopy. Deuterides observed at δ –10.95 and

–15.17 in the ^{2}H NMR spectrum of ***d*$_2$-4-H** closely resemble the hydrides in **4-H** (δ –11.13 and –15.59) and the ^{31}P signals in the ^{31}P{^{1}H} NMR spectrum of ***d*$_2$-4-H** at δ 43.3 and 36.5 are also very similar to **4-H**. Analysis of ***d*$_2$-4-H** by ESI-MS revealed mass values corresponding to [Rh(*o*-H-DPEphos)]$^{+}$ when the exit capillary voltage was set to 173 V. Using a lower exit voltage of 93 V produced mass values that correspond to [Rh(*o*-H-DPEphos)(μ-D)]$_2^{2+}$ (obs. 643.2 m/z with 0.5 spacings, calc. 643.1) and [Rh(*o*-H-DPEphos)]$_2^{2+}$ (obs. 641.2 m/z with 0.5 spacings, calc. 641.1) (Figure 3.12). This suggests that D loss is less facile than H under ESI-MS conditions, which has been observed before in radical fragmentation studies with ESI-MS.[29, 30] This is an example of a kinetic isotope effect (KIE), which can be extracted from mass spectrometry fragmentation.[31]

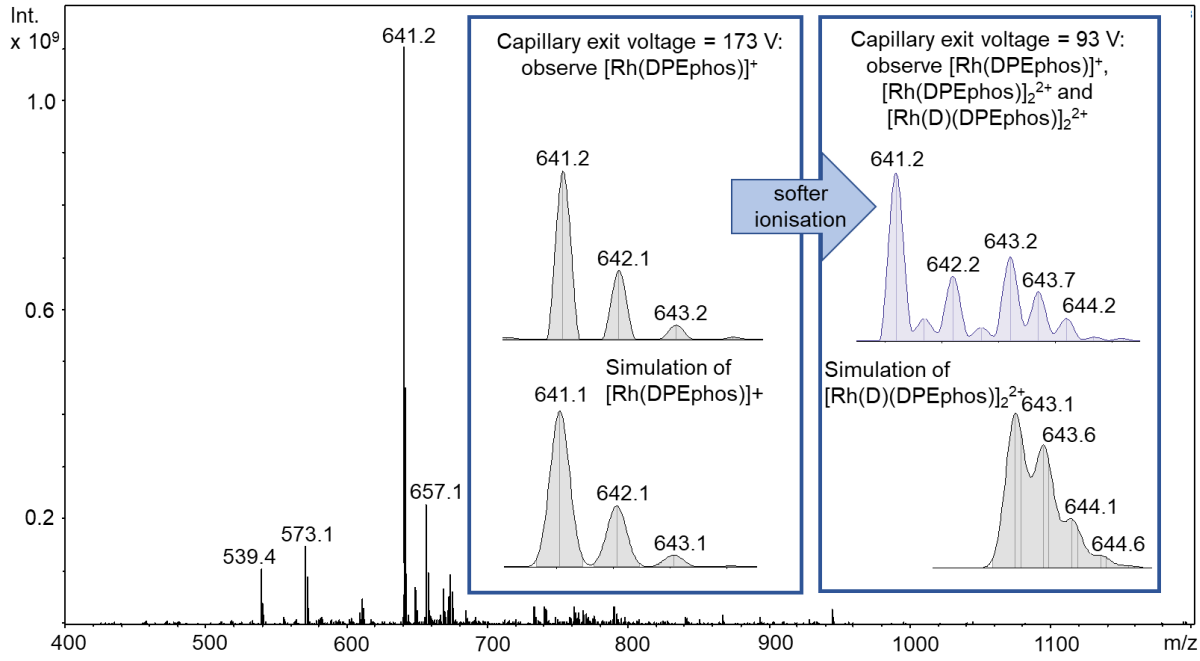

Figure 3.12. ESI mass spectrum of a sample of ***d*$_2$-4-H** (exit voltage = 173 V, 1,2-$F_2C_6H_4$). The insets show the molecular ions with the capillary exit voltage set at 173 V {corresponding to [Rh(DPEphos)]$^{+}$}, and at 93 V {corresponding to {[Rh(DPEphos)]$^{+}$, Rh(DPEphos)]$_2^{2+}$ and [RhD(DPEphos)]$_2^{2+}$}, along with a simulation of [Rh(DPEphos)]$^{+}$ and [RhD(DPEphos)]$_2^{2+}$ for comparison.

Without a solid-state structure, it is difficult to definitively ascertain whether the diphenyl ether backbone is coordinated via the oxygen, occupying a *fac*-κ^3-P,O,P geometry, or in *cis*-κ$_2$-P,P geometry. Electron counting with the oxygen bound gives 34 electrons, which then makes 36 with a Rh–Rh bond over two formally Rh(II) centres. A Rh(II)–Rh(II) bond was also proposed for [Rh_2(σ,μ-CH-κ^2-P,P-*o*-H-DPEphos)$_2$(σ,μ–$(H_2B)_2$NHMe)][Al(OC$(CF_3)_3)_4$], which was supported by the solid-state structure that showed a close Rh···Rh distrance of 2.6421(4) Å (Figure 3.13).[27] A Rh–Rh bond within **4-H** also

accounts for the overall diamagnetism observed in the NMR spectrocopy data. Similar bridging hydridic arrangements have previously been reported in Rh-DPEphos complexes, such as: $[Rh_2(o\text{-H-DPEphos})_2(\mu\text{–H})(\mu\text{-}(H_2B{=}NHMe)][BAr^F{}_4]$[20, 27] and $[Rh_2(H)(\mu\text{–H})_3(o\text{-H-DPEphos})_2]$.[20] A similar dicationic structure has been shown for $[Ir(\kappa^3\text{-P,O,P-Xantphos})(H)(\mu\text{-H})]_2[BAr^F{}_4]_2$ which contains two chemically equivalent bridging hydrides (δ –6.68, integral 2H) that was also characterised crystallographically.[32]

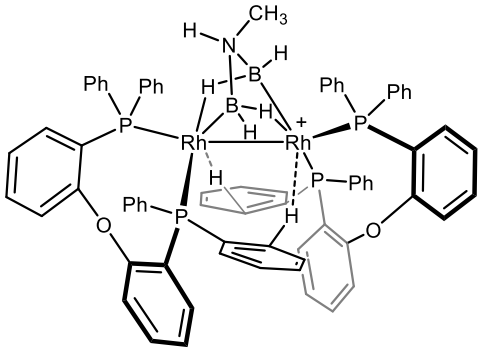

Figure 3.13. The cationic portion of $[Rh_2(\sigma,\mu\text{-CH-}\kappa^2\text{-P,P-o-H-DPEphos})_2(\sigma,\mu\text{–}(H_2B)_2NHMe)][Al(OC(CF_3)_3)_4]$, showing a similar Rh(II)-Rh(II) bond and bridging agostic C–H bond that is proposed in **4-H**.

The reactivity with H_2 was investigated with **2-F,F**, but a very different product is characterised by in-situ NMR. The addition of 15 PSI H_2 to a sample of **2-F,F** in $1,2\text{-}F_2C_6H_4$ was accompanied by a colour change from orange to light yellow and a quantitative conversion to a new complex, **4-F,F**, after 20 minutes (Scheme 3.6).

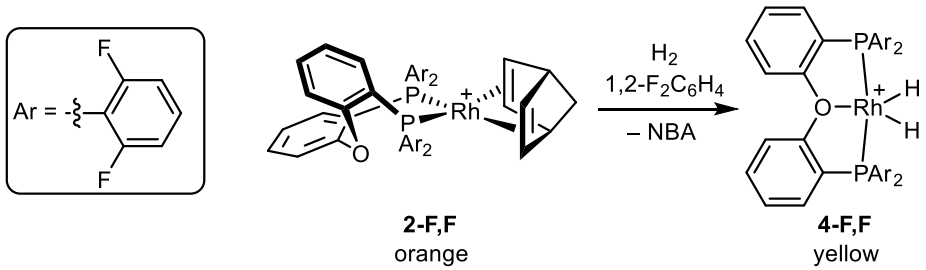

Scheme 3.6. Hydrogenation of **2-F,F** to form Rh(III) dihydride complex **4-F,F**. $[BAr^F{}_4]^-$ anions omitted for clarity.

A single ^{31}P environment at δ –6.7 is observed in the $^{31}P\{^1H\}$ NMR spectrum of **4-F,F** as a doublet, with a small *J*(RhP) of 130 Hz (Figure 3.14). A smaller *J*(RhP) value is indicative of a Rh(III) centre with a *trans*-P,P arrangement,[33] i.e. *mer*-κ^3-P,O,P, compared to the larger Rh(I)-P coupling in **2-F,F** of 162 Hz.

In the ^{1}H NMR spectrum of **4-F,F**, one hydride environment at δ –20.00 is observed as a doublet of triplets, coupling to two equivalent *cis*-P nuclei [*J*(PH) = 17 Hz] and one Rh [*J*(PH) = 34 Hz], which simplifies to a doublet upon ^{31}P-decoupling. The integral of this hydride signal is 2H compared to free NBA (Figure 3.14). The ^{19}F NMR spectrum also reflects this symmetry, as only one broad ^{19}F environment is observed at δ –100.9 (integral 8F) for the 2,6-$F_2C_6H_3$ groups and the BAr^F_4 signal is observed at δ –63.1 (integral 24F). One ^{19}F environment for the substituted aromatics suggests rapid rotation about the P–C bond, faster than the NMR timescale, as well as overall C_{2v} symmetry of the complex, which is consistent with the ^{31}P and ^{1}H NMR data. It is interesting to note that, like **3-F,F**, there is no observable P-F coupling. The aromatic signals are masked by the overwhelming 1,2-$F_2C_6H_4$ solvent signals. In light of all of this data, we asign **4-F,F** as a Rh(III) monomeric complex with a *mer*-κ^3-P,O,P-*o*-F,F-DPEphos arrangement and two equivalent hydrides: [Rh(*mer*-κ^3-P,O,P-*o*-F,F-DPEphos)$(H)_2$][BAr^F_4] (**4-F,F**) (Scheme 3.6). Removal of the H_2 atmosphere by successive freeze-pump-thaws resulted in decomposition of **4-F,F** and so it could not be isolated as a solid. Analysis of **4-F,F** by ESI-MS produced only mass values corresponding to [Rh(*o*-F,F-DPEphos)]$^+$ (m/z = 785.0, calc. 785.0), which is consistent with the decomposition of **4-F,F** upon removal of the H_2 atmosphere.

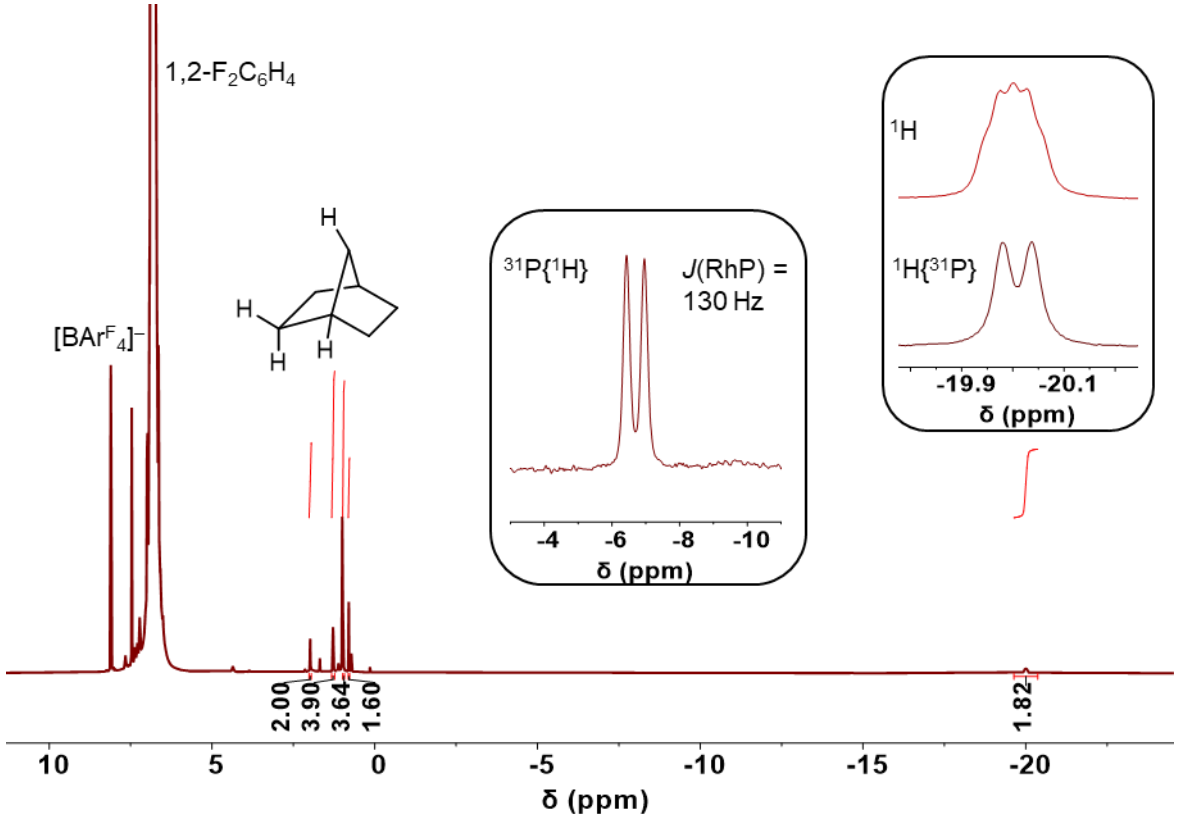

Figure 3.14. In-situ ^{1}H NMR spectrum of **4-F,F (**600 MHz, 1,2-$F_2C_6H_4$, 298 K). Integrals relative to the free NBA signals. The insets show the single ^{31}P signal in the $^{31}P\{^{1}H\}$ NMR spectrum and the hydride resonance in the ^{1}H NMR spectrum, with and without ^{31}P-decoupling (243 MHz and 600 Hz, 1,2-$F_2C_6H_4$, 298 K).

Similar Rh(III) dihydride complexes have been reported previously for POP ligands.[34] The hydride signal in [Rh(*mer*-κ^3-P,O,P-Xantphos-^{t}Bu)(H)$_2$][SbF_6] was reported at δ –21 with a doublet of triplet multiplicity [*J*(RhH) = 40 Hz and *J*(PH) = 11 Hz] and only one ^{31}P signal in the $^{31}P\{^{1}H\}$ NMR spectrum with doublet multiplicity of *J*(RhP) = 111 Hz, which is very similar to **4-F,F**.[35] [Rh(*mer*-κ^3-P,O,P-Xantphos-Ar)(H)$_2$][BAr^F_4] (Ar = 3,5-CF_3-C_6H_3) has also been shown to exist as the Rh(III) five-coordinate system in C_6H_5Cl solution but crystallised as a six-coordinated complex with an added η^1-Cl-C_6H_5Cl ligand.[34] We do not suspect any coordination of the weakly coordinating solvent 1,2-$F_2C_6H_4$[22] in **4-F,F** and therefore asign it as a coordinatively unsaturated five-coordinate species (Scheme 3.6). It is interesting to note that without the availability for *ortho*-CH agostic interactions, as assigned in **4-H**, we do not get the same dimeric complex forming. Although, the different hydrogenation product could also be a consequence of the larger steric bulk of the partially fluorinated aryl groups.[3]

As a comparison for the influence of *ortho*-fluorine substitution, the same reaction was conducted with the mono-*ortho*-substituted DPEphos ligand, *o*-Me-DPEphos (Scheme 3.7). This ligand contains an *ortho*-proton but is also bulkier than the parent *o*-H-DPEphos due to the methyl group.[1] When an atmosphere of 15 PSI H_2 (gauge pressure) was applied to a sample of **2-Me** in 1,2-$F_2C_6H_4$ solvent, the solution changed colour from orange to yellow within the time of mixing, similar to the formation of **4-F,F**. In-situ NMR spectroscopy showed that **2-Me** had quantitatively reacted to a new complex (**4-MeH**) after ten minutes. In the ^{1}H NMR spectrum of **4-MeH**, a hydride resonance was observed as a doublet of triplets [*J*(RhH) = 40 and *J*(PH) = 14 Hz] at δ –19.74 (Figure 3.15), which collapsed to a doublet upon ^{31}P-decoupling. This hydride signal integrates to 2H compared to the *o*-CH_3 signal and the *o*-$BAr^F{}_4$ signal, which is very similar to the hydride observed for **4-F,F**. Only one, broad signal corresponds to the CH_3 groups (δ 1.75) which suggests high time-averaged symmetry (Figure 3.15). In the ^{31}P{^{1}H} NMR spectrum of **4-MeH**, a single broad signal is observed at δ 27.1.

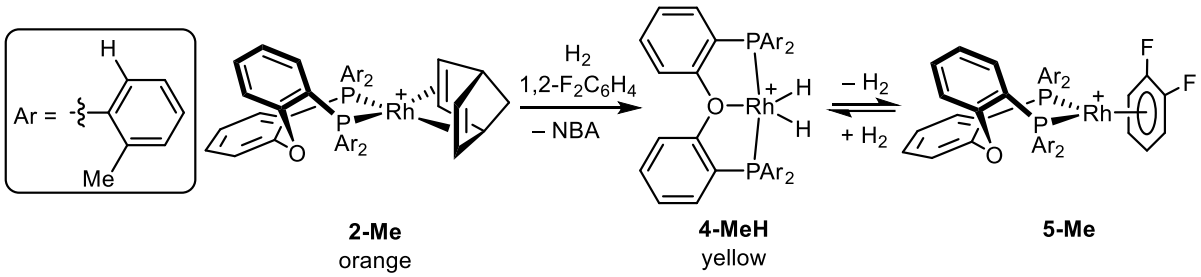

Scheme 3.7. Hydrogenation of **2-Me** in 1,2-$F_2C_6H_4$. $[BAr^F{}_4]^-$ anions omitted for clarity.

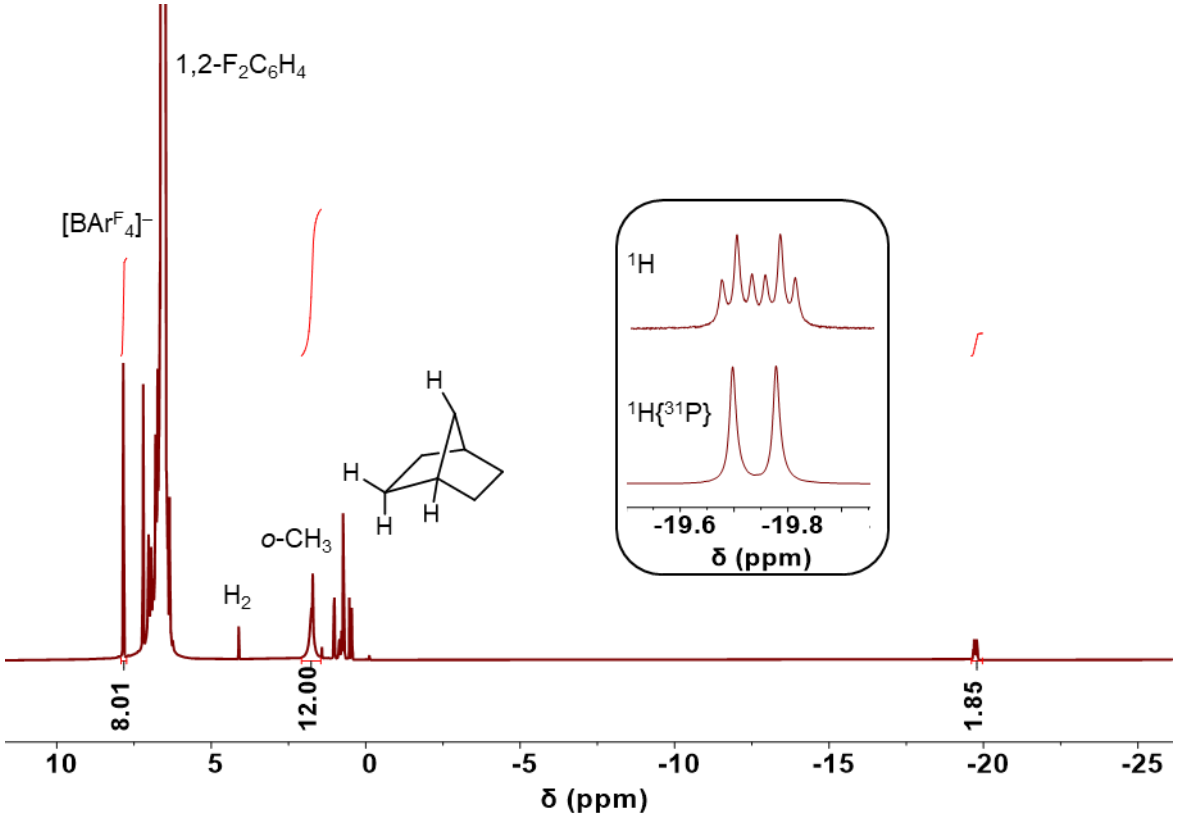

Figure 3.15. In-situ ^{1}H NMR spectrum of **4-MeH** (600 MHz, 1,2-$F_2C_6H_4$, 298 K). Integrals relative to the *ortho*-CH_3 signals. The inset shows the hydride resonance with and without ^{31}P-decoupling.

Interestingly, upon removal of the H_2 atmosphere in a sample of **4-MeH** by ten successive freeze-pump-thaws, a new complex is formed, **5-Me**, in a 1:2 ratio of **4-MeH**:**5-Me**. **5-Me** is defined by a doublet in the ^{31}P{^{1}H} NMR spectrum at δ 37.1 with a large *J*(RhP) of 207 Hz (Figure 3.16). This is similar to the ^{31}P signal in [Rh(*o*-H-DPEphos)(η^6-C_6H_5F)][BAr^F_4] (δ 31.8, *J*(RhP) = 220 Hz][20] and the characteristically large *J*(RhP) values observed in other *cis*-κ^2-diphosphine Rh(I) complexes with weakly bound η^6-1,2-$F_2C_6H_4$ ligands, such as: [Rh(^{i}Bu$_2$PCH$_2$CH$_2$P^{i}Bu$_2$)(η^6-1,2-$F_2C_6H_4$)][BAr^F_4] [*J*(RhP) = 204 Hz][36] and [Rh($Cy_2PCH_2CH_2PCy_2$)(η^6-1,2-$F_2C_6H_4$)][Al(OC(CF_3)$_3$)$_4$] (*J*(RhP) = 199 Hz).[21] An aryl signal at δ 6.13 is observed in the ^{1}H NMR as a broad singlet, which is shifted upfield compared to the free solvent and indicative of a coordinated η^6-1,2-$F_2C_6H_4$ ligand,[23, 37] which was not observed before degassing of the sample. A new methyl signal is also observed for **5-Me** at δ 1.65, in a 2:1 ratio with the methyl signal for **4-MeH**. The integral of the hydride signal also decreases by ~50% relative to the total methyl signals and the *o*-BAr^F_4 signal. Therefore, **5-Me** is assigned as [Rh(*o*-Me-DPEphos)(η^6-1,2-$F_2C_6H_4$)][BAr^F_4] (Scheme 3.7). Addition of H_2 back into the mixture of **4-MeH** and **5-Me** resulted in the quantitative formation of **4-MeH** (Figure 3.16), suggesting an equilibrium between **4-MeH** and **5-Me**, that favours **4-**

MeH when there is excess solvated H_2 but **5-Me** is also observed when the equilbrium is pushed in the other direction by removal of H_2.

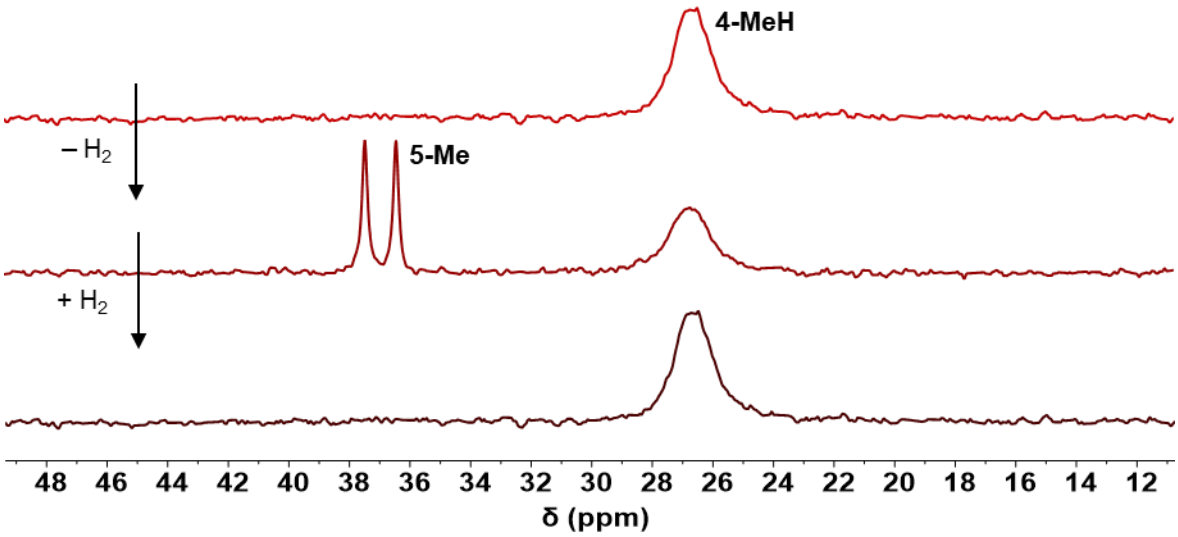

Figure 3.16. $^{31}P\{^1H\}$ NMR spectra of **4-MeH** (top), after degassing the same sample by ten successive freeze-pump-thaws (middle), and after addition of H_2 again (bottom) (202 MHz, 1,2-$F_2C_6H_4$, 298 K).

It has been suggested by Goldman that the weakly coordinating ether linkage encourages the oxidative addition of H_2 compared to PCP, PNP and PONOP ligands,[35] which typically form dihydrogen complexes.[38] Ligands with wider bite angles, such as Xantphos and DPEphos, have also been shown to favour Rh(III) complexes.[34, 39] Bercaw and co-workers deduced that whether a Rh(I) or a Rh(III) dihydride is formed is dependent on the bite angle of the P-P chelate, the cone angle and the donating ability of the phosphine substituents.[39] *Ortho*-fluorine substitution influences all of these variables by changing the electronic and steric properties of the phosphine.

3.6 Synthesis, characterisation and comparison of [Au_2Cl_2(*o*-R,R-DPEphos)]

Gold complexes of *ortho*-aryl substituted phosphines are known catalysts for some important reactions,[40] such as the hydrochlorination of alkynes.[41] The previously reported complex [Au_2Cl_2(*o*-H-H-DPEphos)] (**6-H**) has also been shown to be an effective σ and π bond activator in gold-catalysed synthesis of indoles.[42] Moreover, these complexes provide a means to investigate the rarer κ^1 binding mode of DPEphos ligands.[33, 43] To further explore the coordination chemistry of the novel *ortho*-fluorinated ligand, **1-F,F**, the corresponding [Au_2Cl_2(*o*-F-F-DPEphos)] complex, **6-F,F**, was synthesised.

6-F,F was prepared via the addition of two equivalents of [Au(THT)Cl] (THT = tetrahydrothiophene) to **1-F,F** in a CH_2Cl_2 solution (Scheme 3.8), in a similar manner as reported for **6-H**.[42] **6-F,F** was isolated as an analytically pure, white solid after recrystallisation from a pentane/CH_2Cl_2 solvent mixture in a modest yield (52%).

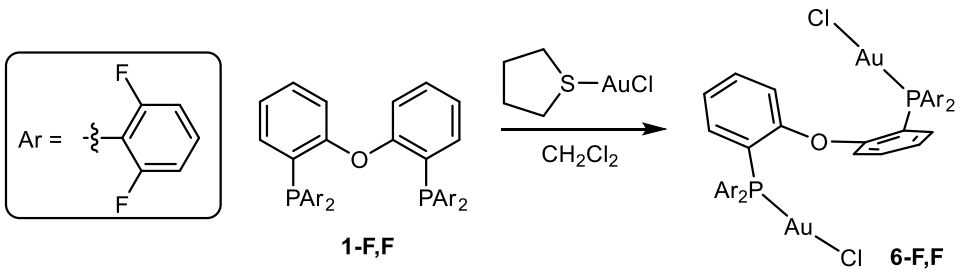

Scheme 3.8. Synthesis of [Au_2Cl_2(*o*-F,F-DPEphos)], **6-F,F**.

The solid-state structure of **6-F,F** revealed a single μ^2,κ^1,κ^1-*o*-F,F-DPEphos ligand bridging over two Au–Cl groups, both in a linear geometry [Cl–Au–P; 175.24(5)° and 177.09(6)°] (Figure 3.17). The Au–P bonds lengths are relatively uniform [2.225(1) and 2.276(1) Å] and standard for Au–P bonds.[44] The Au atoms are forced away from one another, in a *trans* arrangement [D(Au···Au) = 6.1792(6) Å], which is assisted by a twist in the diphenylether backbone by 73° (arene-arene plane angle). This would give rise to overall, non-crystallographic C_2 symmetry, if retained in solution. This *trans*-Au arrangement is in contrast to the reported solid-state structure of **6-H** (Figure 3.17) in which the diphenylether backbone of the parent *o*-H-DPEphos is twisted by 61° but the Au···Au distance is only 3.0116(4) Å.[42] This was assigned as an aurophilic interaction.[45] Aurophilic interactions have also been observed in [Au_2Br_2(*o*-H-DPEphos)]; D(Au···Au) = 2.976(1) Å, and [Au_2Br_2(Xantphos)]; D(Au···Au) = 2.9233(6) Å. A *trans*-Au arrangement, similar to **6-F,F**, has been reported for [Au_2Br_2(DBFphos)] [D(Au···Au) > 7.2 Å].[44] The fact that no aurophilic interactions are observed in **6-F,F** highlights the structural control *ortho*-fluorine substitution can provide.

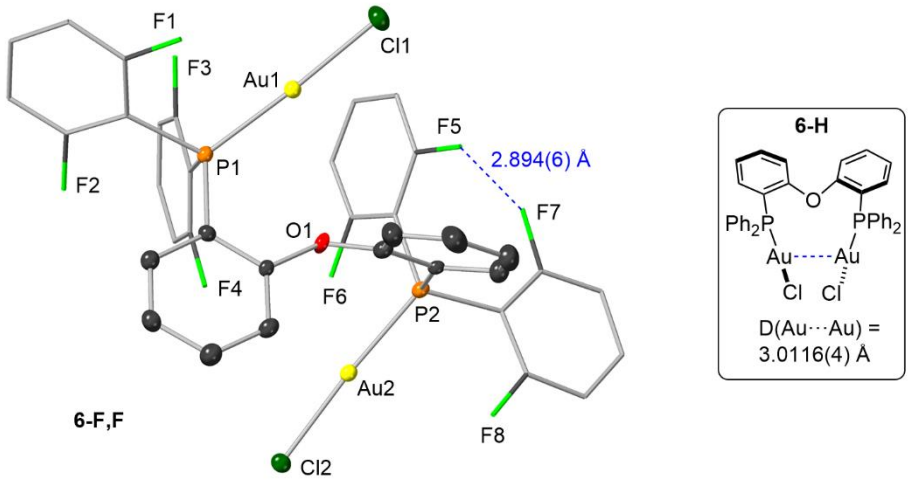

Figure 3.17. Crystallographically determined structure of **6-F,F**. Ellipsoids shown at the 50% probability level. Hydrogen atoms are omitted and the terminal aryl groups are modelled in stick form for clarity. Selected bond lengths (Å) and angles (°): P1–Au1, 2.225(1); Au1–Cl1, (2.276(1); P2–Au2, 2.230(1); Au2–Cl2, 2.278(1); Au1–Au2, 6.1792(6); Cl1–Au1–P1, 177.09(6); Cl2–Au2–P2, 175.24(5). A diagram of previously reported **6-H** is shown in the inset,[42] highlighting the aurophilic interaction in **6-H**, which is not present in **6-F,F**.

The non-crystallographic C_2 symmetry observed in the solid-state structure of **6-F,F** is carried forward into solution. A single ^{31}P environment is observed at δ –23.1, downfield shifted by 39.4 ppm compared to the free ligand, **1-F,F (**δ –62.5). This is notably upfield compared to **6-H** (δ 21.6).[42] The ^{31}P signal is observed as an apparent 1:2:3:2:1 quintet with *J*(PF) = 25 Hz, which is similar to **1-F,F**, albeit with a smaller coupling constant relative to the free ligand [**1-F,F**: *J*(PF) = 40 Hz]. The ^{19}F NMR spectrum of **6-F,F**, however, reveals some differences between the Au complex and the free ligand: two ^{19}F signals at δ –97.3 and –97.9, both with doublet of triplet multiplicity are observed at a similar shift to **1-F,F** (δ –100.7). The multiplicity comprises of coupling to one ^{31}P nucleus [*J*(PF) = 25 Hz] and two ^{19}F nuclei [*J*(FF) = 7 Hz], the latter determined by ^{19}F-COSY NMR spectroscopy (Figure 3.18).

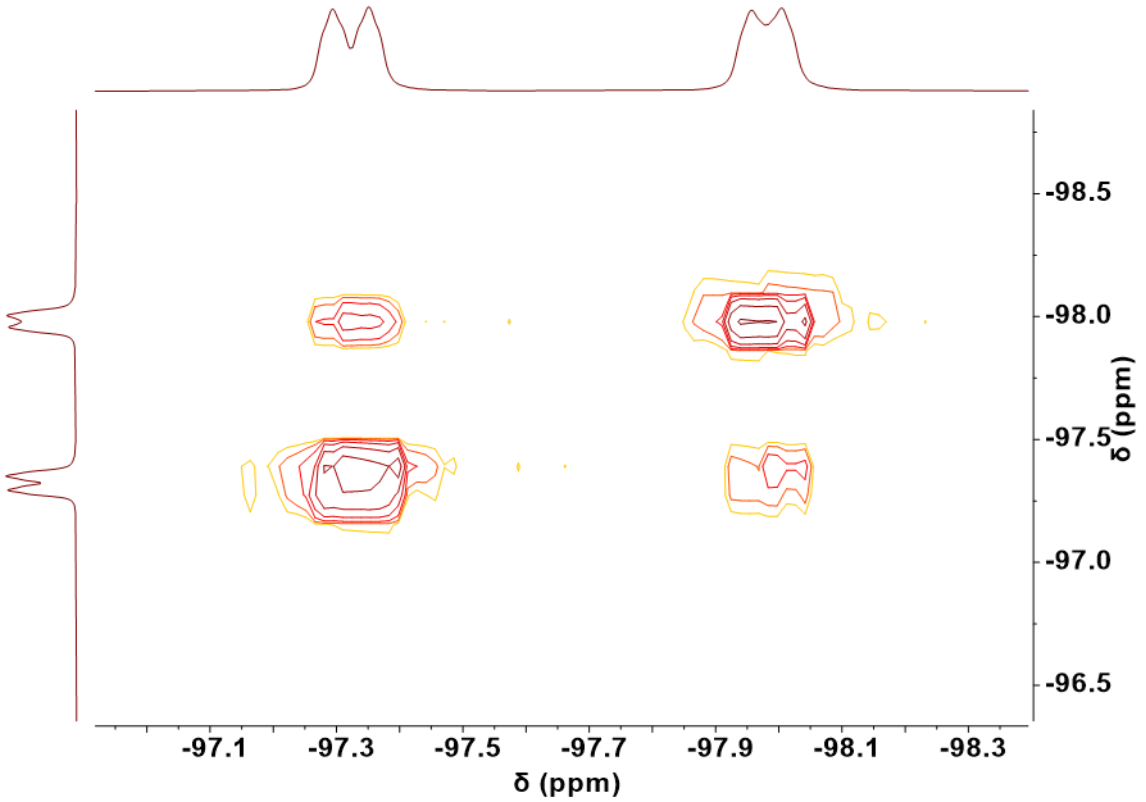

Figure 3.18. ^{19}F-COSY NMR spectrum of **6-F,F** showing the coupling between the two ^{19}F signals (CD_2Cl_2, 471 MHz, 295 K).

A total of eight aromatic environments in a 2:2:2:2:2:2:4:4 ratio were observed in the ^{1}H NMR spectrum. These are assigned as four backbone, two *para*-H and two *meta*-H environments respectively. This data suggests that there are two sets of distinct aryl groups, all rotating about the P–C bond faster than the NMR timescale at 295 K, which makes the *meta* protons on the same aryl group equivalent. C_2 rotation about the oxygen atom interchanges each aromatic with one equivalent. Consequently, free rotation of the aryl groups would result in the ^{19}F nuclei on the same ring being chemically equivalent and the observed ^{19}F-^{19}F coupling cannot be attributed to through bond F-F coupling. Therefore, we propose that through-space F-F interactions are occurring in **6-F,F**.[46, 47] The F···F distance dependence on the magnitude of through-space ^{19}F coupling constants has been computationally studied by Mallory and co-workers in 1,8-difluoronapthalene complexes. In Mallory's report, they predicted an F···F distance of 3.0 Å would give a *J*(FF) of roughly 7 Hz.[48] Returning to the solid-state structure of **6-F,F**, the closest F···F distance (F5 and F7) on adjacent aryl groups is 2.894(6) Å (Figure 3.17), therefore, an observed *J*(FF) value of 7 Hz is consistent with Mallory's analysis. Rapid P–C rotation in solution gives a time averaged signal, therefore, from the NMR data we can deduce that two chemically

equivalent ^{19}F nuclei on one aryl group are coupling through-space to two chemically equivalent ^{19}F nuclei on an adjacent aryl group. This would give the C_2 symmetry observed in solution and the doublet of triplet multplicity observed in the ^{19}F NMR spectrum.

There are no observable through-space *J*(FF) observed in **2-F,F**, despite the short F···F distances in the solid-state: D(F···F) = 2.820(2) Å between F2 and F3, and 2.859(2) Å between F5 and F6. Moreover, *J*(PF) of 25 Hz is observable in **6-F,F** and **1-F,F** (40 Hz), but is not observbed at all in the rhodium complexes **3-F,F** and **4-F,F**, and only coupling between one ^{19}F and ^{31}P was seen for **2-F,F** at 203 K. The exact reasons for this are not completely clear. Potentially, the through-bond orbital overlap is sensitive to the angles between the P and F atoms (i.e. the Karplus equation).[9] Considering the 2,6-$F_2C_6H_3$ groups were shown to rotate rapidly in both **6-F,F** and **2-F,F** they could be rotating at slightly different angles. The lone pair on P can overlap with the lone pairs on F, creating a through-space, or through-lone-pair interaction.[46] This interaction can dramatically increase the size of the *J*(PF) value. For example, the fluorine in the 8 position of Togni's fluorinated naphthyl phosphine complexes (Figure 3.6), exhibit *J*(PF) of over 200 Hz in the free ligand, despite the fact they are four bonds apart.[13] If we compare the average D(P···F) in the solid-state structure of **6-F,F** and **2-F,F** they are almost identical (both 3.05 Å) yet the *J*(PF) values vary between 40 Hz in **1-F,F**, 25 Hz in **6-F,F** and unobservable for **2-F,F**. In the free ligand, the P lone pair is available for through-space interactions, whereas they are involved in σ-donation to Rh in **2-F,F**. This does not explain the observed *J*(PF) for **6-F,F**, however, phosphine bonding to Rh d^8 is very different to bonding with more electron rich Au d^{10},[49] and Au d^{10} is known as being highly π-back-donating.[50] This could influence the occupied orbitals that are accessible for through-space coupling and subsequently alter the observed *J*(PF). Computational studies are required to ascertain the nature of the coupling constant and if they are dissipated in rhodium complexes of **1-F,F** because of through-space or through-bond effects.

The analogous complex was prepared with the *ortho*-methyl variant: [Au_2Cl_2(*o*-Me-DPEphos)], **6-Me** (Scheme 3.9). **6-Me** was isolated as a white solid and then purified by slow diffusion of pentane into a CH_2Cl_2 solution of **6-Me** to yield an analytically pure, white crystalline solid in a 59% yield. Very similar solid-state characteristics are observed between **6-Me** and **6-F,F**. A bridging *o*-Me-DPEphos ligand joining two linear Au-Cl fragments [P–Au–Cl = 174.7 and 175.7°] and a *trans*-Au arrangement [D(Au···Au) = 5.9627(4) Å] are observed (Figure 3.19). This gives the complex a non-crystallographic C_2 axis, as also observed in **6-F,F**.

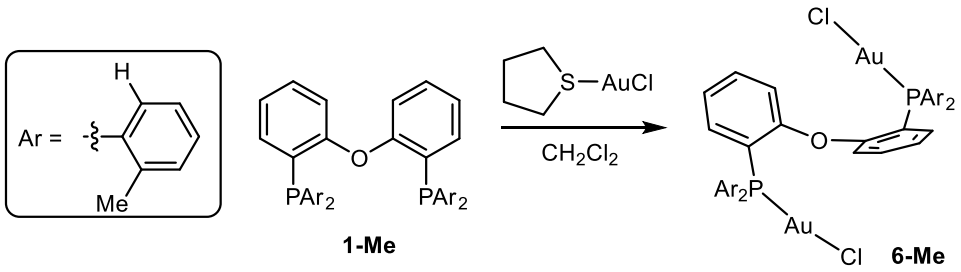

Scheme 3.9. Synthesis of [Au_2Cl_2(*o*-Me-DPEphos)], **6-Me.**

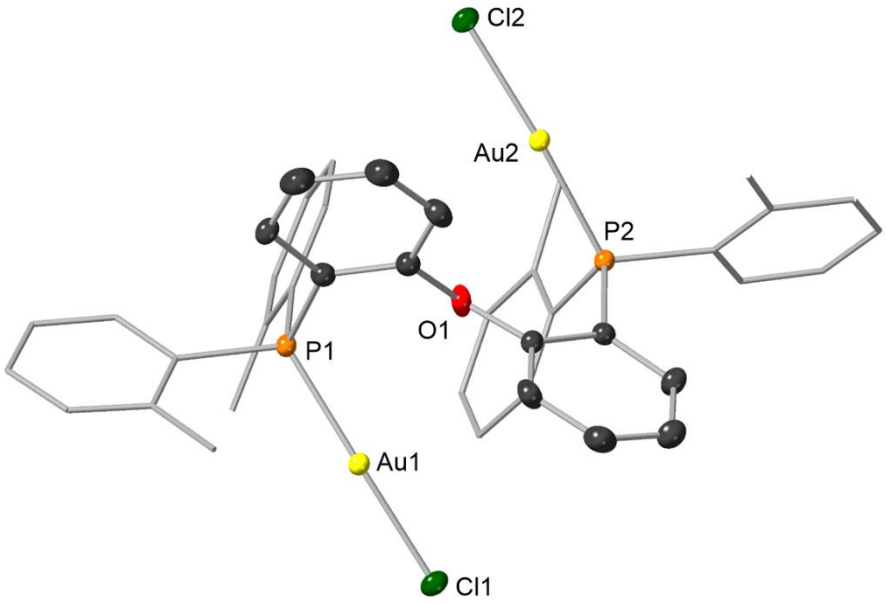

Figure 3.19. Crystallographically determined structure of **6-Me**. Hydrogen atoms and substituted aryl groups in stick form for clarity. Ellipsoids shown at the 50% probability level. Selected bond lengths (Å) and angles (°): P1-Au1, 2.2365(9); Au1-Cl1, (2.2917(10); P2-Au2, 2.2406(9); Au2-Cl2, 2.2864(10); Au1-Au2, 5.9627(4); Cl1-Au1-P1, 175.73(3); Cl2-Au2-P2, 174.72(3).

The solution-state NMR data of **6-Me** however, is less simple (Figure 3.20). Two signals are observed in the $^{31}P\{^{1}H\}$ NMR spectrum at 295 K as broad singlets, in a 0.15:1 ratio at δ 21.5 and 1.1 respectively. The major signal, at δ 1.0, is roughly 20 ppm more upfield than that reported for **6-H** (δ 21.6) but the minor signal is very similar.[42] In the ^{1}H NMR spectrum at 295 K, two broad methyl resonances at δ 2.83 and δ 2.36 are observed in a ~1:1 ratio (6H relative to the aromatic resonances), as well as broad aromatic signals. Upon cooling a sample of **6-Me** to 203 K in CD_2Cl_2, three sharp ^{31}P signals are observed in a 0.15:0.15:1 ratio. Warming to 318 K resulted in all of the signals coalescing, which is suggestive of a dynamic process that interconverts different isomers that are frozen out at lower temperatures, and become equivalent at higher temperature.[51] The ^{1}H NMR spectrum of **6-Me** at 203

K shows six methyl environments in a 0.15:0.15:0.15:0.15:1:1 ratio, which coalesce to two broad resonances at 318 K. Twelve major aromatic signals are also observed at 203 K, comprising of four backbone signals and two sets of four for the different aryl environments. The aromatic signals of the minor isomer cannot be distinguished. In light of this, we propose that two isomers of **6-Me** are observed in solution at low temperature. The major isomer adopts a geometry with C_2 symmetry, with a single ^{31}P and two methyl environments. This geometry is consistent with the solid-state structure and also the solution-state data of **6-F,F**. The minor isomer, which is present in roughly a sixth of the quantity of the major, exhibits C_1 symmetry, as shown by two ^{31}P and four methyl environments. The fluxional process is most likely a consequence of restricted rotation of the substituted aromatic groups,[51, 52] as seen in rhodium complexes of bulkier DPEphos ligands reported in Chapter Two, such as [Rh(*o*-Me-DPEphos)$(H)_2$(acetone)][BAr^F_4] (**4-Me**). The minor isomer is likely to be formed via locking of the substituted aryl groups in an asymmetric manner, potentially a different rotamer, as previously shown in the low temperature NMR of PO(*o*-Me-$C_6H_4)_3$,[53] although without a crystal structure we cannot be definitive.

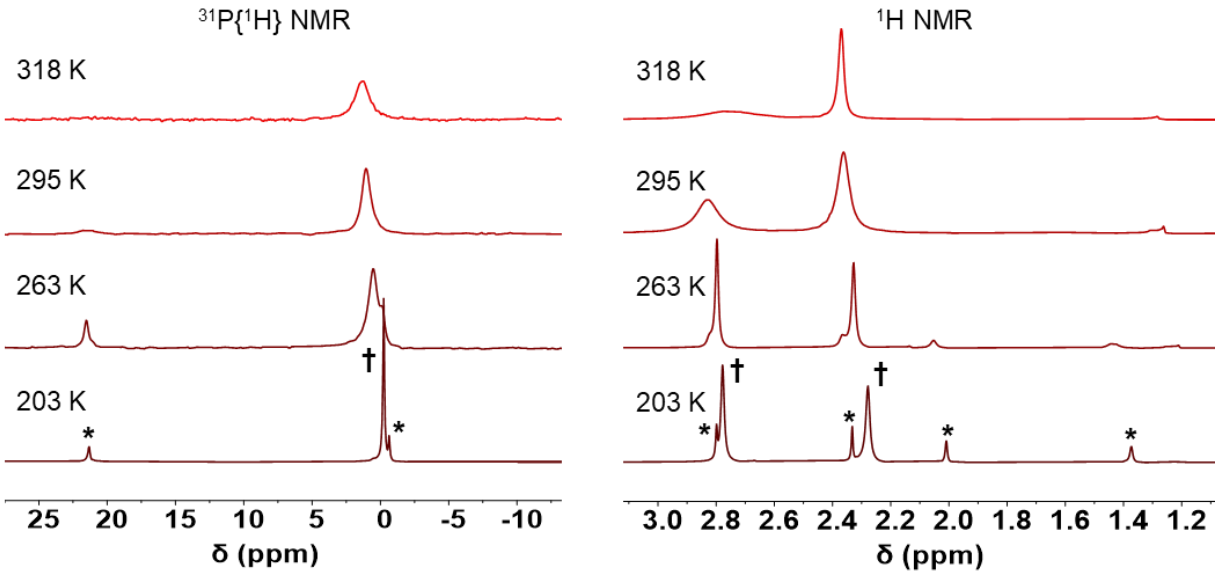

Figure 3.20. $^{31}P\{^1H\}$ NMR spectra (left) and the alkyl region of the ^1H NMR spectra (right) of **6-Me** at different temperatures (202 and 500 MHz respectively, CD_2Cl_2). * Denotes the minor, C_1 isomer and † denotes the major, C_2 isomer.

Interestingly, a downfield chemical shift is observed in the ^1H NMR spectrum of **6-Me** at 203 K at δ 8.52 with doublet of doublet multiplicity [*J*(PH) = 20 Hz and *J*(HH) = 8 Hz] (Figure 3.21). This is reminiscent of the *ortho*-aryl anagostic protons studied in great detail in Chapter Two.[1] The small integral of this

signal equates to 1:3 relative to one of the methyl signals in the minor isomer and therefore it is most likely one *ortho*-aryl proton on the minor isomer. We do not have any structural data of this isomer to refer to. Nevertheless, this appears to be a rare example of an anagostic interaction in a d^{10} compound,[54] which have been reported before in gold complexes,[55] such as gold-iron heterobimetallic complexes with bis(N-heterocyclicimine)silyliumylidene ligands.[56] The discovery of an anagostic interaction within **6-Me** highlights the surprising commonality of these interactions, particularly encouraged by *ortho*-aryl substituted phosphine ligands.

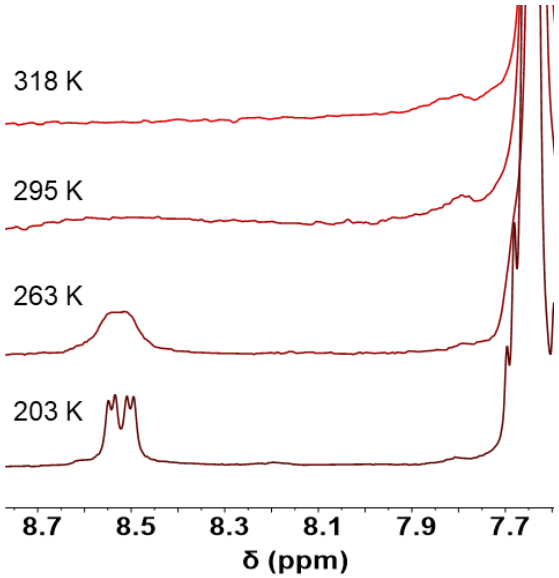

Figure 3.21. The downfield region of the ^{1}H NMR spectra of **6-Me** at different temperatures (500 MHz, CD_2Cl_2).

3.7 Conclusion

Within this Chapter, *ortho*-fluorine substitution in the common DPEphos ligand has been shown to influence the coordination chemistry within rhodium and gold complexes compared to the parent *o*-H-DPEphos. The hydrogenation of the NBD fragment in [Rh(*o*-F,F-DPEphos)(NBD)][BAr^F_4] (**2-F,F**) in d_6-acetone, led to the formation of a Rh(I) solvated complex; [Rh(*o*-F,F-DPEphos)(d_6-acetone)$_2$][BAr^F_4] (**3-F,F**), whereas the same methodology in 1,2-$F_2C_6H_4$, resulted in a Rh(III) dihydride; [Rh(*o*-F,F-DPEphos)$(H)_2$][BAr^F_4] (**4-F,F**). In comparison to the parent *o*-H-DPEphos, for which a solvated Rh(I) complex is formed in d_6-acetone and an unusual bonding arrangement in a rare dicationic dimer: [Rh(*o*-H-DPEphos)(μ-H)]$_2$[BAr^F_4]$_2$, is formed from the hydrogenation of **2-F,F** in 1,2-$F_2C_6H_4$. This complex

includes a *fac*-κ^3-P,O,P *o*-H-DPEphos ligand, two different bridging hydrides, two bridging CH agostic bonds and a Rh(II)-Rh(II) bond. This highlights the different coordination modes of DPEphos ligands, which can be controlled by *ortho*-fluorine substitution. Transitioning between these geometries can be vital for catalytic activity.[33, 57]

The novel rhodium complexes of *o*-F,F-DPEphos, **2-F,F**, **3-F,F** and **4-F,F** all show rapid rotation of the 2,6-fluorinated aryl groups at room temperature, despite the fact that the covalent radius of fluorine is 0.57 Å, compared to hydrogen, which is 0.31 Å.[15] The low temperature NMR data of **2-F,F**, however, did show restricted rotation about the P–C bond, which is not observed in the *o*-H-DPEphos equivalent, [Rh(*o*-H-DPEphos)(NBD)][BAr$^F{}_4$].[1] This shows the greater steric influence of *ortho*-fluorine substitution, as previously reported by Saunders and co-workers in *trans*-[PtCl$_2$(PEt$_3$){P(2,6-F$_2$C$_6$H$_3$)$_3$}].[3]

No *J*(PF) was observed in the NMR spectroscopy data of **2-F,F**, **3-F,F** and **4-F,F**, apart from one P-F interaction in [Rh(*o*-F,F-DPEphos)(NBD)][BAr$^F{}_4$] at 203 K, despite only a three bond separation. In contrast, in the ^{31}P{^{1}H} and ^{19}F NMR spectra of the bimetallic gold complex, [Au$_2$Cl$_2$(*o*-F,F-DPEphos)] and the free ligand, *J*(PF) was observed to be 25 Hz and 40 Hz respectively. The exact reasons for this are unclear, but most likely a complex interplay of through-bond[23] and through-space[46] variables account for the observed P-F interactions (or lack thereof).

We have also shown that the aurophilic interactions in bimetallic gold complexes, [Au$_2$Cl$_2$(*o*-R,R-DPEphos)], can be controlled by the different *ortho*-substituent. The *ortho*-fluorine and *ortho*-methyl DPEphos variants exhibited D(Au···Au) of over 5.9 Å in the solid-state, whereas the previously reported complex, [Au$_2$Cl$_2$(*o*-H-DPEphos)] contains an aurophilic interaction in the solid-state. [Au$_2$Cl$_2$(*o*-F,F-DPEphos)] also revealed some interesting through-space F-F coupling, which was not observed in the rhodium complexes, despite the close D(F···F) in the solid-state.

Further work on this project would include a computational analysis of the possible Rh···F–C interactions observed in **2-F,F** and compare these with the bonding characteristics of the Rh···H–C anagostic interactions discussed in Chapter Two. Moreover, ligands with one *ortho*-F and one *ortho*-R (R = H, Me, OMe and ^{i}Pr) could also be used for a systematic study of Rh···F–C interactions, in a similar manner to **2-R**, and the ^{19}F chemical shifts of the *ortho*-F could be experimentally determined and also calculated. Also, a comparison of *ortho*-fluorine and *ortho*-hydrogen substitution (i.e. **2-H** and **2-F,F**) in the catalysis of a simple reaction, such as hydroboration,[58] would be interesting.

3.8 References

[1] J. J. Race, A. L. Burnage, T. M. Boyd, A. Heyam, A. J. Martínez-Martínez, S. A. Macgregor, A. S. Weller, *Chem. Sci.,* **2021,** 12, 8832-8843.
[2] W. Chou, M. Pomerantz, *J. Org. Chem.,* **1991,** 56, 2762-2769.
[3] C. Corcoran, J. Fawcett, S. Friedrichs, J. H. Holloway, E. G. Hope, D. R. Russell, G. C. Saunders, A. M. Stuart, *J. Chem. Soc., Dalton Trans.,* **2000,** 161-172.
[4] S. A. Hauser, I. Prokes, A. B. Chaplin, *Chem. Commun.,* **2015,** 51, 4425-4428.
[5] A. G. Orpen, *Chem. Soc. Rev.,* **1993,** 22, 191-197.
[6] G. L. Moxham, H. Randell-Sly, S. K. Brayshaw, A. S. Weller, M. C. Willis, *Chem. Eur. J.,* **2008,** 14, 8383-97.
[7] J. S. Siegel, F. L. Anet, *J. Org. Chem.,* **1988,** 53, 2629-2630.
[8] M. J. Atherton, J. Fawcett, J. H. Holloway, E. G. Hope, D. R. Russell, G. C. Saunders, *J. Chem. Soc., Dalton Trans.,* **1997,** 2217-2220.
[9] J. Thomson, W. Keeney, M. C. Baird, W. F. Reynolds, *J. Organomet. Chem.,* **1972,** 40, 215-220.
[10] D. Pingen, T. Lebl, M. Lutz, G. S. Nichol, P. C. J. Kamer, D. Vogt, *Organometallics,* **2014,** 33, 2798-2805.
[11] W. Goertz, W. Keim, D. Vogt, U. Englert, M. D. K. Boele, L. A. Van Der Veen, P. C. J. Kamer, P. W. N. M. Van Leeuwen, *J. Chem. Soc., Dalton Trans.,* **1998,** 2981-2988.
[12] D. O'hagan, *Chem. Soc. Rev.,* **2008,** 37, 308-319.
[13] K. Stanek, B. Czarniecki, R. Aardoom, H. Rüegger, A. Togni, *Organometallics,* **2010,** 29, 2540-2546.
[14] M. Brookhart, L. H. Green Malcolm, G. Parkin, *PNAS,* **2007,** 104, 6908-6914.
[15] B. Cordero, V. Gómez, A. E. Platero-Prats, M. Revés, J. Echeverría, E. Cremades, F. Barragán, S. Alvarez, *Dalton Trans.,* **2008,** 2832-2838.
[16] H. Takemura, S. Nakashima, N. Kon, M. Yasutake, T. Shinmyozu, T. Inazu, *J. Am. Chem. Soc.,* **2001,** 123, 9293-9298.
[17] P. Pyykkö, *Chem. Rev.,* **1997,** 97, 597-636.
[18] J. R. Shapley, R. R. Schrock, J. A. Osborn, *J. Am. Chem. Soc.,* **1969,** 91, 2816-2817.
[19] J. F. Hooper, A. B. Chaplin, C. Gonzaíez-Rodríguez, A. L. Thompson, A. S. Weller, M. C. Willis, *J. Am. Chem.Soc,* **2012,** 134,
[20] D. E. Ryan, K. A. Andrea, J. J. Race, T. M. Boyd, G. C. Lloyd-Jones, A. S. Weller, *ACS Catal.,* **2020,** 10, 7443-7448.
[21] A. I. Mckay, J. Barwick-Silk, M. Savage, M. C. Willis, A. S. Weller, *Chem. Eur. J.,* **2020,** 26, 2883-2889.
[22] S. D. Pike, M. R. Crimmin, A. B. Chaplin, *Chem. Commun.,* **2017,** 53, 3615-3633.
[23] P. S. Pregosin, *NMR in Organometallic Chemistry* Wiley, Zurich, **2012**.
[24] A. Rifat, N. J. Patmore, M. F. Mahon, A. S. Weller, *Organometallics,* **2002,** 21, 2856-2865.
[25] L. J. L. Häller, E. Mas-Marzá, M. K. Cybulski, R. A. Sanguramath, S. A. Macgregor, M. F. Mahon, C. Raynaud, C. A. Russell, M. K. Whittlesey, *Dalton Trans.,* **2017,** 46, 2861-2873.
[26] J. E. Barquera-Lozada, A. Obenhuber, C. Hauf, W. Scherer, *J. Phys. Chem. A,* **2013,** 117, 4304-4315.
[27] G. M. Adams, D. E. Ryan, N. A. Beattie, A. I. Mckay, G. C. Lloyd-Jones, A. S. Weller, *ACS Catal.,* **2019,** 9, 3657-3666.
[28] A. T. Lubben, J. S. Mcindoe, A. S. Weller, *Organometallics,* **2008,** 27, 3303-3306.
[29] J. H. Bowie, *Environ. Health Perspect.,* **1980,** 36, 89-95.
[30] D. J. Underwood, J. H. Bowie, *J. Chem. Soc., Perkin Trans. 2,* **1977,** 1670-1674.
[31] P. J. Derrick, *Mass Spectrom. Rev.,* **1983,** 2, 285-298.
[32] A. J. Pontiggia, A. B. Chaplin, A. S. Weller, *J. Organomet. Chem.,* **2011,** 696, 2870-2876.
[33] G. M. Adams, A. S. Weller, *Coord. Chem. Rev.,* **2018,** 355, 150-172.
[34] P. Ren, S. D. Pike, I. Pernik, A. S. Weller, M. C. Willis, *Organometallics,* **2015,** 34, 711-723.
[35] M. C. Haibach, D. Y. Wang, T. J. Emge, K. Krogh-Jespersen, A. S. Goldman, *Chem. Sci.,* **2013,** 4, 3683-3692.
[36] S. D. Pike, A. L. Thompson, A. G. Algarra, D. C. Apperley, S. A. Macgregor, A. S. Weller, *Science,* **2012,** 337, 1648-1651.
[37] S. D. Pike, I. Pernik, R. Theron, J. S. Mcindoe, A. S. Weller, *J. Organomet. Chem.,* **2015,** 784, 75-83.
[38] M. Findlater, K. M. Schultz, W. H. Bernskoetter, A. Cartwright-Sykes, D. M. Heinekey, M. Brookhart, *Inorg. Chem.,* **2012,** 51, 4672-4678.
[39] A. D. Wilson, A. J. M. Miller, D. L. Dubois, J. A. Labinger, J. E. Bercaw, *Inorg. Chem.,* **2010,** 49, 3918-3926.
[40] D. Malhotra, M. S. Mashuta, G. B. Hammond, B. Xu, *Angew. Chem. Int. Ed.,* **2014,** 53, 4456-4459.
[41] R. Ebule, S. Liang, G. B. Hammond, B. Xu, *ACS Catal.,* **2017,** 7, 6798-6801.
[42] M. Lankelma, V. Vreeken, M. A. Siegler, J. I. Van Der Vlugt, *Inorganics,* **2019,** 7,
[43] R. Venkateswaran, M. S. Balakrishna, S. M. Mobin, H. M. Tuononen, *Inorg. Chem.,* **2007,** 46, 6535-6541.

[44] D. V. Partyka, J. B. Updegraff Iii, M. Zeller, A. D. Hunter, T. G. Gray, *Dalton Trans.,* **2010,** 39, 5388-5397.
[45] H. Schmidbaur, A. Schier, *Chem. Soc. Rev.,* **2012,** 41, 370-412.
[46] J.-C. Hierso, *Chem. Rev.,* **2014,** 114, 4838-4867.
[47] T. Tuttle, J. Gräfenstein, D. Cremer, *Chem. Phys. Lett.,* **2004,** 394, 5-13.
[48] F. B. Mallory, C. W. Mallory, K. E. Butler, M. B. Lewis, A. Q. Xia, E. D. Luzik, L. E. Fredenburgh, M. M. Ramanjulu, Q. N. Van, M. M. Francl, D. A. Freed, C. C. Wray, C. Hann, M. Nerz-Stormes, P. J. Carroll, L. E. Chirlian, *J. Am. Chem. Soc.,* **2000,** 122, 4108-4116.
[49] D. G. Evans, D. Michael, P. Mingos, *J. Organomet. Chem.,* **1982,** 232, 171-191.
[50] G. A. Bowmaker, H. Schmidbaur, S. Krüger, N. Rösch, *Inorg. Chem.,* **1997,** 36, 1754-1757.
[51] R. A. Baber, A. G. Orpen, P. G. Pringle, M. J. Wilkinson, R. L. Wingad, *Dalton Trans.,* **2005,** 659-667.
[52] A. G. Orpen, P. G. Pringle, M. B. Smith, K. Worboys, *J. Organomet. Chem.,* **1998,** 550, 255-266.
[53] J. a. S. Howell, M. G. Palin, P. C. Yates, P. Mcardle, D. Cunningham, Z. Goldschmidt, H. E. Gottlieb, D. Hezroni-Langerman, *J. Chem. Soc., Perkin Trans. 2,* **1992,** 1769-1775.
[54] G. Dos Passos Gomes, G. Xu, X. Zhu, L.-M. Chamoreau, Y. Zhang, O. Bistri-Aslanoff, S. Roland, I. V. Alabugin, M. Sollogoub, *Chem. Eur. J.,* **2021,** 27, 8127-8142.
[55] H. Schmidbaur, H. G. Raubenheimer, L. Dobrzańska, *Chem. Soc. Rev.,* **2014,** 43, 345-380.
[56] F. Hanusch, D. Munz, J. Sutter, K. Meyer, S. Inoue, *Angew. Chem. Int. Ed.,* **2021,** 60, 23274-23280.
[57] J. Barwick-Silk, S. Hardy, M. C. Willis, A. S. Weller, *J. Am. Chem. Soc.,* **2018,** 140, 7347-7357.
[58] M. Dietz, A. Johnson, A. Martínez-Martínez, A. S. Weller, *Inorg. Chim. Acta,* **2019,** 491, 9-13.

4 Chapter Four – Dehydropolymerisation of primary phosphine-boranes with a [Rh(dppe)]$^+$ catalyst

4.1 Preamble

The *ortho*-substituted DPEphos ligands described in Chapter Two and Three were clearly of interest with regard to their use in homogeneous catalysis. As described in the next few pages, initial scoping studies were unsuccessful but this led to the development of a simple and effective catalyst for the dehydropolymerisation of primary phosphine-boranes using the ligand dppe. The following paragraphs will summarise a series of investigations that led to the study that is discussed in Chapter Four.

The cationic system based upon [Rh(*o*-H-DPEphos)]$^+$, has been shown to be an effective catalyst in the dehydropolymerisation of $H_3B{\cdot}NMeH_2$ to form poly(methylaminoborane) of high molecular weight and with control of polymer chain length (Scheme 4.1).[1] The analogous *ortho*-aryl substituted DPEphos systems, [Rh(*o*-R-DPEphos)]$^+$, detailed in Chapter Two and Three, were tested as catalysts in the dehydropolymerisation of $H_3B{\cdot}NMeH_2$ (R = Me, OMe, ^{i}Pr or F,F). Unfortunately, using the hydrogenation products from [Rh(*o*-R-DPEphos)(NBD)][BAr$^F{}_4$] in THF, such as [Rh(*o*-Me-DPEphos)(H)$_2$(THF)][BAr$^F{}_4$] and [Rh(*o*-^{i}Pr-DPEphos')(H)][BAr$^F{}_4$], as precatalysts, gave polymer of wide polydispersity (Đ = 2.7) and low molecular weight (M_n = 12,000 g mol^{-1}), with a slower reaction rate and more complicated kinetic data. As this was not an improvement on the DPEphos system and provided no further mechanistic insight further studies were not pursued.

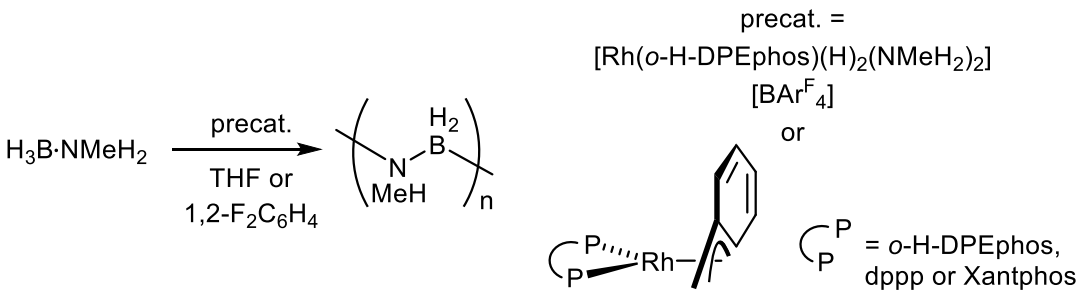

Scheme 4.1. Rhodium-diphosphine catalysed dehydropolymerisation of $H_3B{\cdot}NMeH_2$.

In 2020, it was reported by the Weller group that the neutral Rh-benzyl precatalysts, [Rh(diphosphine)(η^3-H$_2$CPh)] (diphosphine = DPEphos, Xantphos and dppp), are excellent catalysts for the dehydropolymerisation of amine-boranes (Scheme 4.1), providing key information on the catalyst

resting state, reliable kinetic data and polymer chain length control.[2] In light of this, an attempt to synthesise the *ortho*-aryl substituted analogues, [Rh(*o*-R-DPEphos)(η³-H₂CPh)], was conducted. However, these complexes could not be prepared, potentially due to the greater ligand bulk. Two synthetic routes were attempted: one via the addition of [Rh(*o*-R-DPEphos)(μ-Cl)]₂ to [Mg(H₂CPh)₂], or the other by addition of the *o*-R-DPEphos ligand to [Rh(COD)(η³-H₂CPh)], both of which resulted in a complex mixture of unknown, and as yet unidentified, products.

Inspired by the simple aryl substituted [Rh(diphosphine)(η³-H₂CPh)] complexes use in amine-borane dehydropolymerisation, we were interested to explore phosphine-borane dehydropolymerisation. Phosphine-borane dehydropolymerisation has been studied in great detail with rhodium-diphosphine systems (section 1.10).[3, 4] These studies have provided almost all of the mechanistic information published for this reaction[5-7] and much of this work has also been reported by the pioneer of this field, Ian Manners.[8, 9] Neutral benzyl catalysts, however, have not been studied. Subsequently, a range of simple [Rh(diphosphine)(η³-H₂CPh)] precatalysts were screened in the dehydropolymerisation of $H_3B{\cdot}PPhH_2$ using the same conditions as previously reported using [Cp*Rh(Me)(PMe₃)(CH₂Cl₂)][BAr$^F_4$] (**i-59**) as a precatalyst, i.e. 1 mol% catalyst, 1 M $H_3B{\cdot}PPhH_2$ in toluene at 100 °C for 19 hours[7] (diphosphine = DPEphos, Xantphos, dppf, dppp and dppe) (Scheme 4.2). Although all of the catalysts fully converted the monomer after 19 hours at 100 °C these were unselective, forming ill-defined oligomeric material, apart from [Rh(dppe)(η³-H₂CPh)] which gave the best selectivity to polymer.

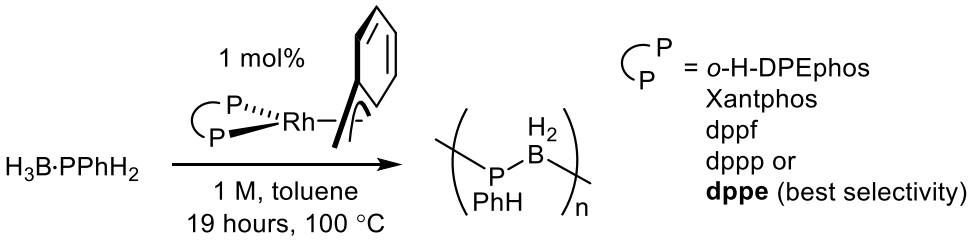

Scheme 4.2. Dehydropolymerisation of $H_3B{\cdot}PPhH_2$ using [Rh(diphosphine)(η³-H₂CPh)] precatalysts.

In-situ NMR spectroscopy studies of the dehydropolymerisation of $H_3B{\cdot}PPhH_2$ using [Rh(dppe)(η³-H₂CPh)] as a precatalyst under sealed conditions showed that the observed catalytic speciation was surprisingly cationic, in contrast with amine-borane dehydropolymerisation where a neutral Rh tetrahydride species was the observed resting state.[2] Hydride resonances at δ –1.8 and –14.3 in a 3:1

ratio in the in-situ NMR spectra resembled the hydride resonances reported for [RhH(dppp)(σ,η^2-$PPh_2BH_2PPh_2BH_3$)][BAr^F_4] (**i-56-Ph$_2$**) at δ –1.2 and –14.1 in the same ratio.[5] **i-56-Ph$_2$** was shown to be the catalyst resting state during the dehydrocoupling of $H_3B{\cdot}PPh_2H$. Subsequently, the simple cationic precatalyst, $[Rh(dppe)_2]Cl$, which had the added benefit of a very simple synthesis and is air and room temperature stable, unlike Rh(diphosphine)(η^3-H_2CPh), was used for all further investigations. Chapter Four thus describes an investigation into the dehydropolymerisation of primary phosphine-boranes using $[Rh(dppe)_2]Cl$ as a precatalyst.

Chapter Four begins with the synthesis and characterisation of polymeric $[H_2BPPhH]_n$ formed via the dehydropolymerisation of $H_3B{\cdot}PPhH_2$ using $[Rh(dppe)_2]Cl$ as a precatalyst. The mechanism of this reaction is probed using in-situ NMR spectroscopy, stoichiometric reactivity and polymer chain growth kinetics. A mechanism is proposed and then exploited to form previously unreported block copolymers of poly(phosphinoboranes), that are also shown to form self-assembled aggregates in solution.

4.2 Synthesis and characterisation of poly(phenylphosphinoborane)

The precatalyst $[Rh(dppe)_2]Cl$ (**4.1**) was prepared via the addition of excess dppe to [Rh(COD)(μ-Cl)]2 in THF solvent, as previously reported.[10] The resultant yellow solid was isolated as an analytically pure, air stable, yellow powder in good yield (75%). The resulting NMR spectroscopic data matched well with that previously reported.[11] Complex **4.1** was then tested in catalysis.

An NMR tube was charged with 1 mol% precatalyst **4.1**, $H_3B{\cdot}PPhH_2$ (1 M) in toluene solvent (0.2 cm^3) and heated at 100 °C for 19 hours in a sealed NMR tube (Scheme 4.3). After 19 hours, the NMR tube was cooled to room temperature and the catalytic mixture was analysed by in-situ NMR spectroscopy. In the $^{31}P\{^1H\}$ NMR spectrum (Figure 4.1), a signal relating to the borane adduct of dppe, $(H_3B)_2$dppe, is observed at δ 18.7, which matched with an independently synthesised sample of $(H_3B)_2$dppe formed via the addition of $H_3B{\cdot}SMe_2$ to dppe. A broad singlet at δ –48.9 is also observed, which matches with the previously reported ^{31}P signal for polymeric $[H_2BPPhH]_n$.[9] Smaller signals between δ –52 and –58 (~10%), which have previously been assigned as smaller cyclic species, such as $[H_2BPhH]_3$ and $[H_2BPhH]_4$,[8, 12] and free $PPhH_2$ at δ –122.6, are also observed.

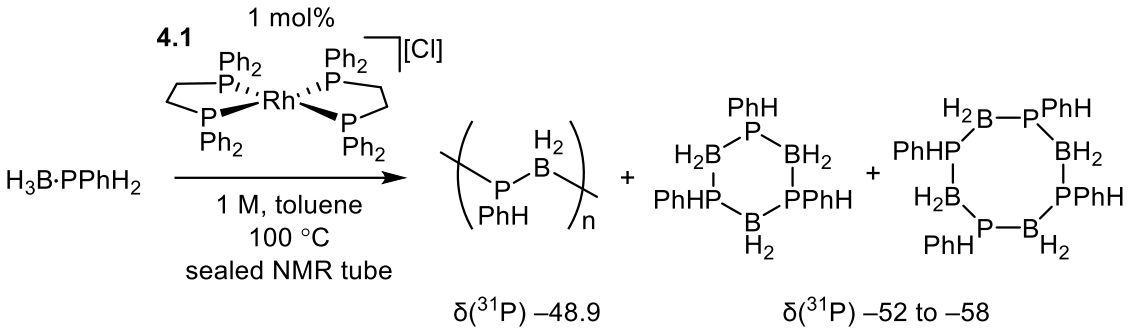

Scheme 4.3. Dehydropolymerisation of $H_3B{\cdot}PPhH_2$ using $[Rh(dppe)_2]Cl$ (**4.1**) as a precatalyst.

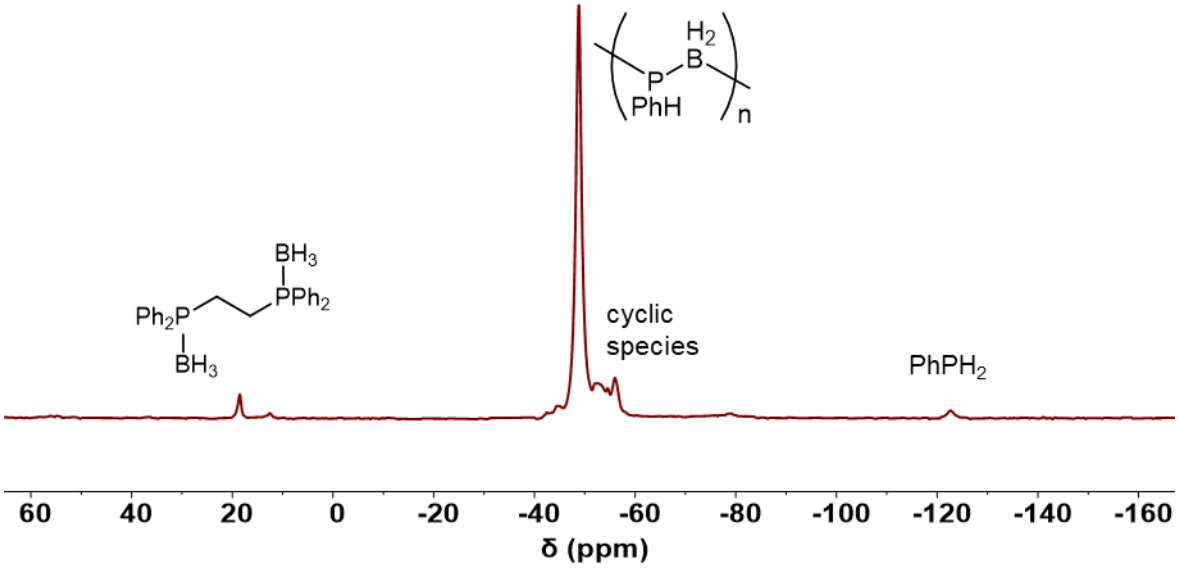

Figure 4.1. In-situ $^{31}P\{^1H\}$ NMR spectrum of the dehydropolymerisation of $H_3B{\cdot}PPhH_2$ using **4.1** as a precatalyst, reaction conditions: 1 M $H_3B{\cdot}PPhH_2$, toluene, 100 °C, 19 hours (202 MHz, toluene, 298 K).

The mixture was transferred to a vial via cannula and hexane was added, which immediately resulted in the precipitation of a white solid. The white material was isolated in good yield (84%) and characterised as polymeric $[H_2BPPhH]_n$, with NMR signals consistent with that previously reported by Manners using $[Rh(COD)(\mu\text{-}Cl)]_2$ as a precatalyst ($CDCl_3$, Figure 4.2).[9] A broad ^{31}P singlet observed in the $^{31}P\{^1H\}$ spectrum at δ –49.4, is similar to that observed in the in-situ mixture, which splits into a broad doublet in the ^{31}P NMR spectrum, with large ^1J(PH) of 355 Hz. In the ^1H NMR spectrum, broad signals relating to the phenyl group (δ 7.22-6.82, relative integral 5H), the PH signal, observed as a doublet at δ 4.18 [^1J(PH) = 355 Hz, integral 1H] that collapses to a singlet upon ^{31}P-decoupling, and a very broad BH_2 signal centred at δ 1.37 (integral 2H, FWHM = 251 Hz), which sharpens upon ^{11}B-decoupling.

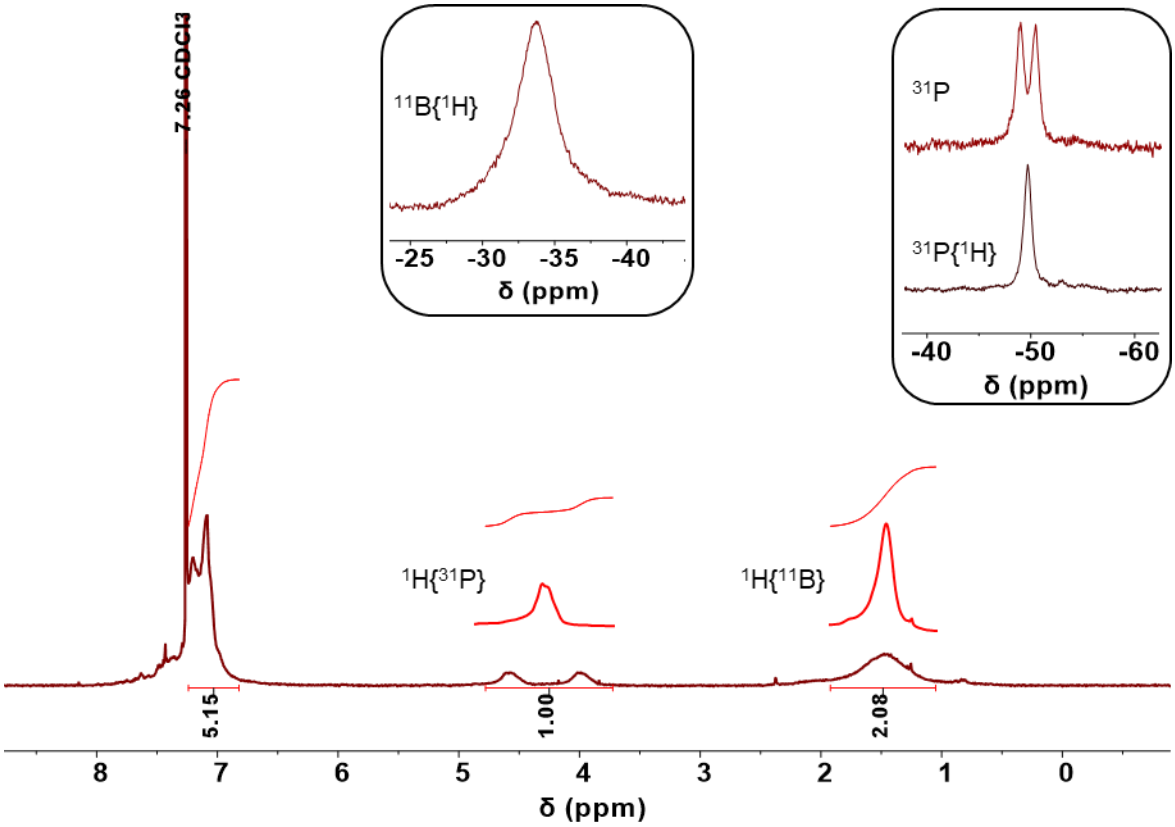

Figure 4.2. ^{1}H NMR spectrum of $[H_2BPPhH]_n$ from the dehydropolymerisation of $H_3B{\cdot}PPhH_2$ using **4.1** as a precatalyst. (600 MHz, $CDCl_3$, 298 K). The insets show the signals in the $^{11}B\{^{1}H\}$, ^{31}P and $^{31}P\{^{1}H\}$ NMR spectra (193 and 243 MHz respectively, $CDCl_3$, 298 K).

Analysis of the polymeric $[H_2BPPhH]_n$ by Gel Permeation Chromatography (GPC) confirmed that polymeric material had indeed been formed, with M_n of 36,000 g mol^{-1} and a polydispersity (Đ) of 1.4 (Figure 4.3). In comparison, $[H_2BPPhH]_n$ formed via the previously reported iron based catalyst, the current best in class of phosphine-borane dehydropolymerisation, $[Cp(CO)_2FeOTf]$ (**i-64**), gave polymer of M_n = 59,000 and Đ = 1.6 as measured by GPC analysis with conventional column calibration.[13] The polymer formed from the earlier reported Rh-based catalysts, such as $[Rh(COD)_2][OTf]$ could not be analysed by GPC analysis due to facile aggregation, which was confirmed via dynamic light-scattering (DLS) anaylsis,[14] but analysis via static light scattering analysis displayed a M_w of 20,000 g mol^{-1}.[8] In the GPC trace of $[H_2BPPhH]_n$ formed via $[Rh(dppe)_2]Cl$, a significant amount of lower molecular weight polymer with M_n of 2,000 g mol^{-1} (Đ = 1.4) is observed.

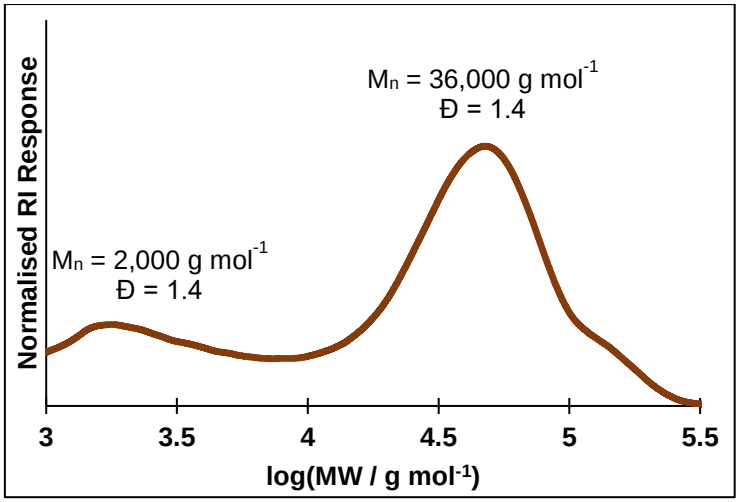

Figure 4.3. GPC trace of a sample of $[H_2BPPhH]_n$ formed from the dehydropolymerisation of $H_3B{\cdot}PPhH_2$ using **4.1** as a precatalyst, reaction conditions: 1 M $H_3B{\cdot}PPhH_2$, toluene, 100 °C, 19 hours.

Due to the high costs of the primary phosphine-borane monomers used in the dehydropolymerisation reactions conducted in this chapter, the reactions are done on a small scale (30-40 mg monomer) with between 0.2 and 0.5 ml of solvent. Therefore, all reactions are performed in high pressure NMR tubes. Whether the NMR tube was open to argon or sealed did not influence the reaction time or polymer molecular weight. Subsequently, sealed NMR tubes were used throughout for practicality. The build-up of H_2 never exceeded four bar at 100 °C and thus three bar at room temperature.

It is important to note that all of the GPC analyses reported in this Chapter are relative to a Conventional Column Calibration (CCC) using polystyrene samples of known molecular weight. This is not necessarily a reliable calibration for poly(phosphinoboranes) as they potentially exhibit different properties in solution due to the polarised P–B bonds and B–H and P–H bonds in the backbone. This results in different amounts of hydrogen-bonding interactions, and in turn, coiling and potentially interchain aggregation.[14, 15] For absolute molecular weight, a multi-angle light scattering (MALS) detector is used, but this does not register poly(phosphinoboranes) below M_n = 20,000 g mol^{-1}, therefore, a combination of MALS and CCC is thus used as appropriate. In order to do this a calibration between MALS and CCC is needed. A calibration graph has been compiled for samples of $[H_2BPPhH]_n$ produced during this project that both detectors can analyse (Figure 4.4). This shows that CCC overestimates the polymer molecular weight by three times at higher molecular weight and by a factor of nine at lower molecular by extrapolation of the graph under the conditions used (2 mg/cm^3 samples in 2 ml THF with 0.1 mol% NBu_4Br, three columns).

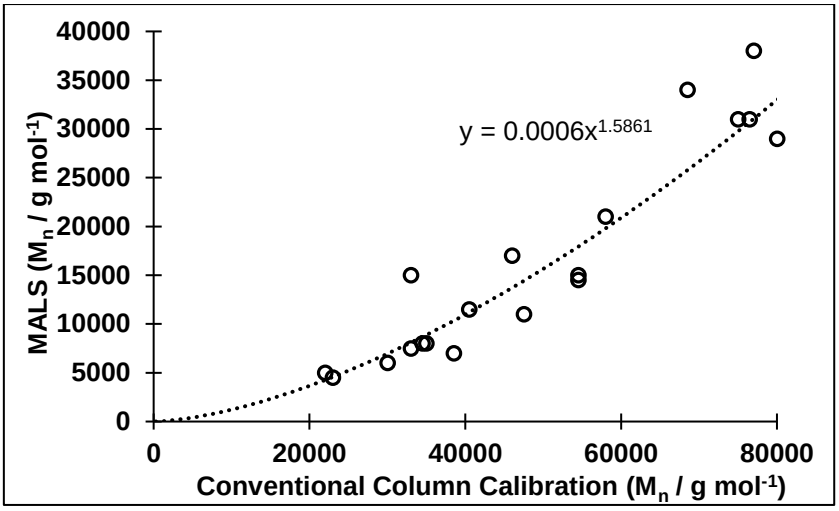

Figure 4.4. Calibration graph of the GPC analysis of samples of poly(phenylphosphinoborane) obtained during this project between a conventional column calibration detector and a multi-angle light scattering detector (MALS).

4.3 Catalyst optimisation

Screening of the anion, phosphine and catalyst loading in the dehydropolymerisation of $H_3B{\cdot}PPhH_2$ was carried out to optimise the reaction, for faster and cleaner conversion to $[H_2BPPhH]_n$ in an attempt to reduce both the cyclic species and lower M_n material.

4.3.1 Different anions and monomer concentration

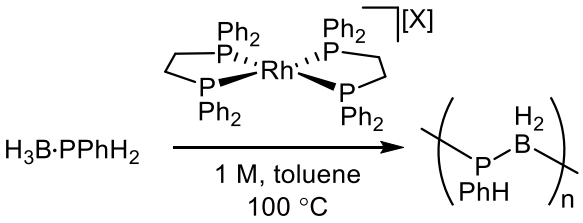

Scheme 4.4. Anion screen in $[Rh(dppe)_2][X]$ precatalysts. [X] = Cl^-, $[BF_4]^-$, $[BAr^F{}_4]^-$ and H^-.

In order to determine the influence of the anion on the dehydropolymerisation reaction, a range of $[Rh(dppe)_2][X]$ catalysts with different anions were tested in the dehydropolymerisation of $H_3B{\cdot}PPhH_2$, $[X]^-$ = Cl^-, $[BF_4]^-$ and $[BAr^F{}_4]^-$ (Scheme 4.4). These catalysts were formed via the addition of NaX to $[Rh(dppe)_2]Cl$ in 1,2-$F_2C_6H_4$, followed by filtration to remove NaCl and evaporation of the solvent in a

similar manner to that previously reported for $[Rh(dppe)_2][BF_4]$.[16] $[Rh(dppe)_2][X]$ were isolated as analytically pure, yellow solids. The neutral complex $RhH(dppe)_2$ was prepared according to a literature procedure[17] and was also tested in the dehydropolymerisation of $H_3B{\cdot}PPhH_2$. Catalytic mixtures of 1 mol% catalyst, 1 M $H_3B{\cdot}PPhH_2$ in toluene at 100 °C were left for 19 hours in a sealed NMR tube and the resultant polymers were isolated via precipitation into hexanes, and then analysed by GPC (Table 4.1). All of the catalysts formed polymeric $[H_2BPPhH]_n$ of reasonably similar molecular weight and polydispersity (28,000-38,000 g mol^{-1}, if discounting $[BAr^F_4]^-$ catalyst, and Đ = 1.4-1.8). The $[BAr^F_4]^-$ anion is observable in the refractive index trace in the GPC analysis and coincides with the polymer signal, leading to a distortion of the calculated polymer size.[2] In light of this, we decided to use the simplest catalyst, **4.1**, for further investigations as there is no significant anion effect.

As noted in section 4.2, a small amount of lower molecular weight polymer (M_n = 2,000 g mol^{-1}, Đ = 1.4) was formed alongside polymer of higher molecular weight. By increasing the monomer concentration from 1 M to 1.25 M the lower molecular weight polymer significantly decreased in intensity, giving a more monomodal molecular weight distribution, albeit with a slight sacrifice in polymer chain molecular weight of the higher molecular weight portion (36,000 to 26,500 g mol^{-1}, Figure 4.5). Subsequently, all further reactions were conducted at 1.25 M.

Table 4.1. Different precatalysts tested in the dehydropolymerisation of $H_3B{\cdot}PPhH_2$ (1 M, toluene, 100 °C, 19 hours). Molecular weight and polydispersity calculated by GPC analysis.

Catalyst	Cat. loading (mol%)	Starting monomer concentration (M)	M_n (g mol^{-1})	PDI (Đ)	Yield (%)
$[Rh(dppe)_2][BAr^F_4]$	1	1.0	13,500	1.8	82
$[Rh(dppe)_2][BF_4]$	1	1.0	38,500	1.4	75
$RhH(dppe)_2$	1	1.0	27,500	1.6	70
$[Rh(dppe)_2]Cl$ **(4.1)**	1	1.0	36,000[a]	1.4[a]	85
$[Rh(dppe)_2]Cl$ **(4.1)**	1	1.25	26,500	1.6	86

[a] Molecular weight and polydispersity of the higher molecular weight portion of the bimodal distribution.

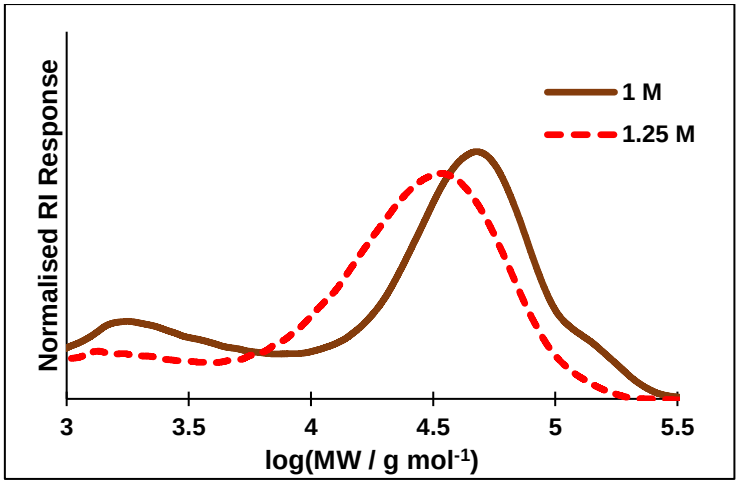

Figure 4.5. GPC trace of $[H_2BPPhH]_n$ from the dehydropolymerisation of $H_3B{\cdot}PPhH_2$ at 1 M and 1.25 M using 1 mol% **4.1** for 19 hours at 100 °C in toluene.

4.3.2 In-situ formation of precatalyst and a screen of different phosphine ligands

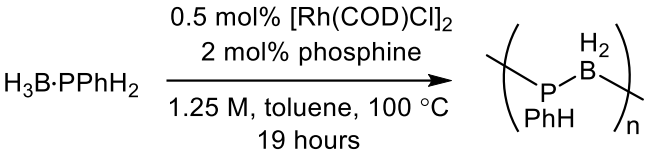

Scheme 4.5. In-situ prepared Rh–Phosphine catalysts for the dehydropolymerisation of $H_3B{\cdot}PPhH_2$ (1.25 M). The range of phosphines used are shown in Table 4.2.

To test the flexibility of this catalyst system further and make the phosphine screening easier, the in-situ formation of the precatalyst was investigated by adding a 2:1 ratio of dppe and $[Rh(COD)(\mu\text{-}Cl)]_2$ to the reaction mixture instead of preformed **4.1** (reaction conditions: 1.25 M $H_3B{\cdot}PPhH_2$, toluene, 100 °C, 19 hours) (Scheme 4.5). Polymer formation did occur, but a bimodal distribution was observed in the GPC trace. Potentially, two catalysts are at play; a $[Rh(dppe)]^+$ based catalyst, similar to that formed from **4.1**, and a catalyst from $[Rh(COD)(\mu\text{-}Cl)]_2$, as this precursor has also shown to be an effective catalyst for dehydropolymerisation of $H_3B{\cdot}PPhH_2$.[9] By using four equivalents of dppe, a monomodal distribution was obtained, giving polymer of high molecular weight (M_n = 44,500 g mol^{-1}) and a narrower dispersity (Đ = 1.5). Five other phosphines were then tested in a 4:1 ratio of phosphine:$[Rh(COD)(\mu\text{-}Cl)]_2$ (Scheme 4.5, Table 4.2). Polymeric $[H_2BPPhH]_n$ was formed in all cases (M_n = 28,000-45,000 g mol^{-1}) with reasonably narrow polydispersities (Đ = 1.5-1.9) (Table 4.2). This method highlights the ease for which phosphines can be tested in the rhodium-catalysed dehydropolymerisation of $H_3B{\cdot}PPhH_2$ and

the flexibility within this catalyst type. The fact that different polymer is formed with the different ligand implies the ligand is coordinating to the rhodium and in turn, influencing the catalytic activity. This also provides control over polymer molecular weight by addition of different ligands.

Larger diphosphine backbones, such as dppp and dppb, appear to produce polymer of lower molecular weight and wider dispersity. We are not sure of the reason behind this. ^{31}P signals corresponding to BH_3 adducts of free phosphine (δ 30-10), $PhPH_2$ and polymeric and cyclic species were observed in all cases in the in-situ $^{31}P\{^{1}H\}$ NMR spectrum.

The catalyst containing dppe produces polymer of the largest molecular weight and the lowest dispersity, and therefore the dppe ligand was used in all further investigations. The reason why polymer of higher molecular weight is observed via the in-situ formed catalyst is unclear, but could be due to a weighing issue of small amounts of $[Rh(COD)(\mu\text{-}Cl)]_2$, and therefore $[Rh(dppe)_2]Cl$ (**4.1**) was used as a preformed precatalyst for consistency.

Table 4.2. GPC analysis of the polymeric material formed in the dehydropolymerisation of $H_3B{\cdot}PPhH_2$ using different phosphines in an in-situ formed rhodium catalyst (1.25 M monomer, 0.5 mol% $[Rh(COD)Cl]_2$, 2 mol% phosphine, toluene, 100 °C for 19 hours).

Ligand	M_n (g mol^{-1})	PDI (Đ)	Modality	Yield (%)
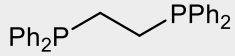	58,000[a]	1.8[a]	Bimodal[a]	76
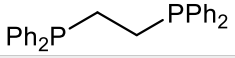	44,500	1.5	Monomodal	74
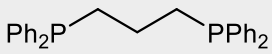	29,500	1.7	Monomodal	81
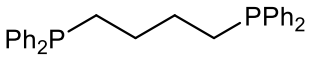	32,500	1.7	Monomodal	83
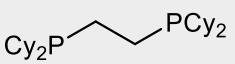	41,000	1.8	Monomodal	62
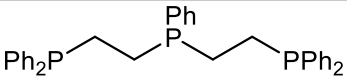	28,000	1.9	Monomodal	66

[a] 1 mol% of dppe used.

4.3.3 Catalyst loading variation

With a reliable and simple precatalyst in hand with $[Rh(dppe)_2]Cl$ (**4.1**), the effect of catalyst loading on the resultant polymer whilst keeping the other reaction conditions constant was investigated (Table 4.3). Polymer was formed with catalyst loadings down to 0.1 mol%, albeit with a much lower molecular weight

and wider polydispersity after 19 hours of reaction time at 100 °C as determined by GPC analysis of the isolated polymer (M_n = 7,500 g mol^{-1}, Đ = 2.2). Only 75% of $H_3B{\cdot}PPhH_2$ had reacted at 0.1 mol% catalyst loading as determined by integration of the ^{11}B NMR spectrum. At 0.5 mol% catalyst loading, 90% of the monomer had reacted after 19 hours and polymer of higher molecular weight was observed via GPC analysis, with a narrower polydispersity (M_n = 18,000 g mol^{-1}, Đ = 1.7). At 2 mol%, all of the monomer had reacted, and even longer polymer than at 1 mol% was observed (M_n = 33,000 g mol^{-1}, Đ = 1.5). Therefore, variation of the catalyst loading provides a method of control in the resultant poly(phenylphosphinoborane) molecular weight and polydispersity. The unreacted monomer can be removed by a hexane wash or even sublimation. Similar control via catalyst loading has been reported for the iron-based catalyst $[CpFe(CO)_2(OTf)]$.[13]

Table 4.3. GPC analysis of $[H_2BPPhH]_n$ formed via the dehydropolymerisation of $H_3B{\cdot}PPhH_2$ using **4.1** as a precatalyst with different loadings (1.25 M, toluene, 100 °C, 19 hours).

Cat. loading (mol%)	M_n (g mol^{-1})	PDI (Đ)	Conversion of $H_3B{\cdot}PPhH_2$ (%)	Yield (%)
0.1	7,500	2.2	75	51
0.5	18,000	1.7	90	60
1	26,500	1.6	100	85
2.0	33,000	1.5	100	82

4.4 Molecular weight of $[H_2BPPhH]_n$ versus conversion of $H_3B{\cdot}PPhH_2$ experiments

The observation of different degrees of polymerisation at 75%, 90% and 100% monomer conversion in the catalyst loading variation experiments described above, led to an investigation into the molecular weight change with differing conversion of $H_3B{\cdot}PPhH_2$. To do this, eight individual reactions were set up in sealed NMR tubes with the same reaction conditions, i.e. 1.25 M $H_3B{\cdot}PPhH_2$ in 0.2 ml toluene, with 1 mol% of catalyst **4.1** at 100 °C, with the only variable being time. After a set amount of time, the catalytic mixture was cooled to room temperature and analysed by ^{11}B NMR spectroscopy and the conversion of $H_3B{\cdot}PPhH_2$ was determined by the relative integral of the monomer signal. ^{11}B and ^{31}P signals relating to the previously reported linear dimer, $H_3B{\cdot}PPhHBH_2{\cdot}PPhH_2$ (**LD-Ph**) were observed,[7] alongside free monomer (if conversion < 100%) and polymeric $[H_2BPPhH]_n$ (Figure 4.6).[9] After 45 minutes of reaction time, the concentration of **LD-Ph** is at an observed maximum, at 30% of the mixture, which was subsequently consumed as the reaction was left for longer pointing to its role as an intermediate. **LD-Ph** was isolated from the catalytic mixture and its use as a precursor was studied (see

section 4.7). The in-situ observation of linear dimer has been reported previously in the dehydropolymerisation of $H_3B{\cdot}PPhH_2$ when $[Cp^*Rh(Me)(PMe_3)(CH_2Cl_2)][BAr^F{}_4]$ (**i-59**) was used a precatalyst, during which, **LD-Ph** was also produced and then completely consumed, as $H_3B{\cdot}PPhH_2$ was also consumed. [7]

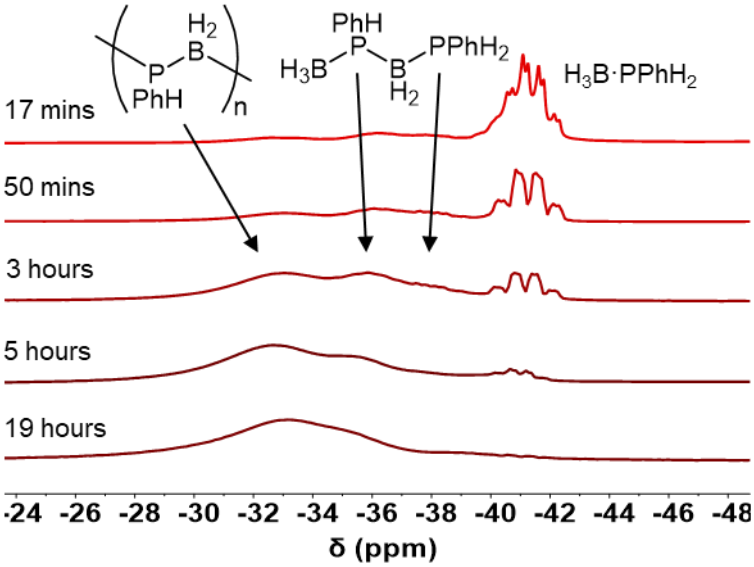

Figure 4.6. ^{11}B NMR spectra of the dehydropolymerisation of $H_3B{\cdot}PPhH_2$ with 1 mol% **4.1** in toluene (1.25 M) stopped after different periods of time at 100 °C (193 MHz, toluene, 298 K).

The resultant oligomeric/polymeric $[H_2BPPhH]_n$ samples from this course study were isolated via precipitation into hexanes and analysed by GPC. A resulting plot of conversion of $H_3B{\cdot}PPhH_2$ versus degree of polymerisation (as measured by M_n) is shown in Figure 4.7. The polymer molecular weight increases steadily but slowly from 0% conversion (t = 0) to 95% conversion (t = 5 hours), after which time the M_n of $[H_2BPPhH]_n$ was determined to be 7,500 g mol^{-1}. When the conversion of $H_3B{\cdot}PPhH_2$ reaches ~100% after 5 hours, M_n increases rapidly. At t = 19 hours the M_n is 32,000 g mol^{-1} but the reaction left for 5 days resulted in polymer of M_n = 77,000 g mol^{-1}. The polydispersity of the resultant polymer decreases steadily over the reaction course, from Đ = 3.0 at 20% conversion of **LD-Ph**, down to Đ = 1.7 at ~100% conversion. The observation of low molecular weight polymer up until higher conversion of monomer, when longer polymer chains are then formed, is characteristic of a step-growth like mechanism.[18] However, in classical step-growth polymerisation, monomer is fully consumed at early stages of the reaction, whereas in chain growth monomer decreases steadily, but high molecular weight polymer is observed almost instantaneously.[19] Step-growth polymerisations are often accompanied by the loss of a small molecule in the process of forming new bonds between two different

functional end groups of a monomer/oligomer/polymer chain. A widely used example of this is the polycondensation of acids and alcohols to form polyesters, with the concurrent loss of H_2O. The functionality can be within the same monomer [e.g. $HO(CH_2)_9COOH$] or two different monomers with different functional end groups [e.g. $HO(CH_2)_2OH$ and 1,4-(CO_2H)-C_6H_4].[20] In the case of phosphine-borane dehydropolymerisation, a bifunctional monomer is used, i.e. the BH_3 and PRH_2 moieties are within the same monomer unit, and the coupling process produces molecular H_2.[14] Rapid monomer conversion at the start of the reaction, and decreasing polydispersity over time, are both diagnostic of a step-growth mechanism,[21] but it is important to note that as monomer is still observed after 19 hours (1%) it is not a classical step-growth polymerisation.

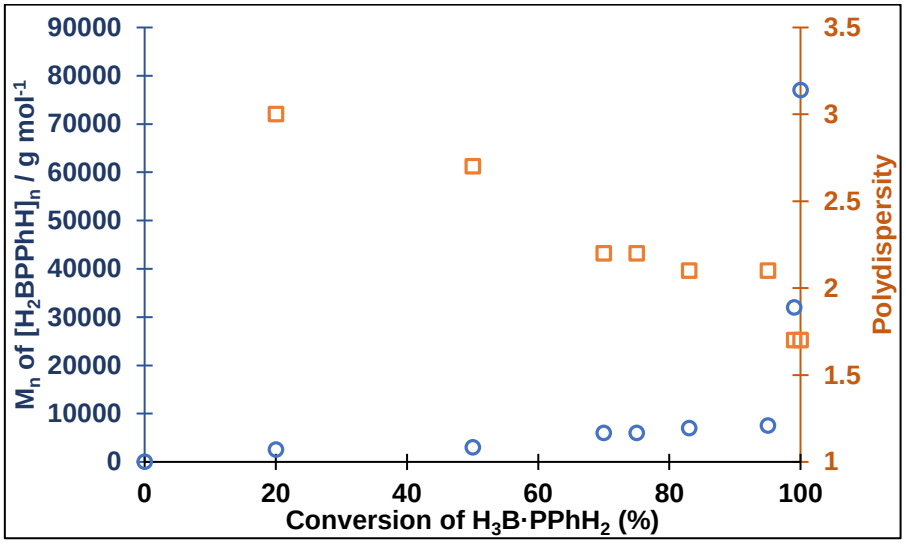

Figure 4.7. M_n (blue, left y-axis) and polydispersity (orange, right y-axis), as calculated by GPC analysis, against the consumption of $H_3B{\cdot}PPhH_2$ in the dehydropolymerisation of $H_3B{\cdot}PPhH_2$ to form $[H_2BPPhH_2]$ (1 mol% **4.1**, 1.25 M, toluene, 100 °C). The conversion is measured by ^{11}B NMR spectroscopy.

This molecular weight versus conversion experiment also highlights the control over molecular weight that is possible with this catalytic system. By simply leaving the catalytic reaction for different periods of time, polymer of a specific molecular weight can be formed, which is shown to be useful in later sections of this Chapter (*vide infra*).

4.5 Synthesis, characterisation and molecular weight vs conversion experiments of polymeric $[H_2BP(Ar')H]_n$ [Ar' = 3,5-$(CF_3)_2C_6H_3$]

To test the functional group tolerance of this catalytic system, the bis-*meta*-trifluoromethylated phosphine-borane variant $H_3B{\cdot}PAr'H_2$ [Ar' = 3,5-$(CF_3)_2C_6H_3$] was used as a monomer. $H_3B{\cdot}PAr'H_2$ was

prepared according to the literature procedure,[22] and added to precatalyst **4.1** (1 mol%) in toluene solvent (1.25 M) and heated to 100 °C in a sealed NMR tube, as for $H_3B{\cdot}PPhH_2$ (Scheme 4.6). After 19 hours at 100 °C, the reaction mixture was analysed by in-situ ^{11}B and $^{31}P\{^1H\}$ NMR spectroscopy. Similar to the experiments conducted with $H_3B{\cdot}PPhH_2$, signals corresponding to $(H_3B)_2$dppe, free $PArH_2$, polymeric $[H_2BPAr'H]_n$ and smaller cyclic species are observed in the $^{31}P\{^1H\}$ NMR spectrum [Ar = 3,5-$(CF_3)_2C_6H_3$].

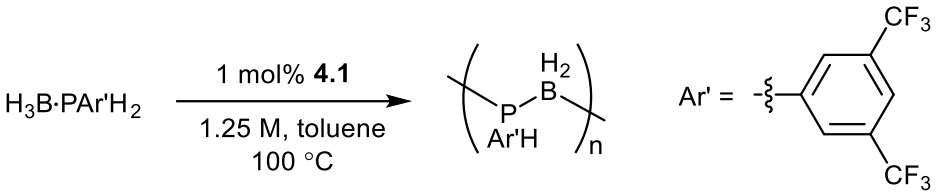

Scheme 4.6. Preparation of polymeric $[H_2BPArH]_n$ from the dehydropolymerisation of $H_3B{\cdot}PAr'H_2$ using **4.1** as a precatalyst [Ar' = 3,5-$(CF_3)_2C_6H_3$].

The resulting polymeric material $[H_2BPAr'H]_n$ was isolated by precipitation into hexanes, in a moderate yield (62%), and the resultant white solid was fully characterised by multinuclear NMR spectroscopy. The NMR signals matched those previously reported for polymer of M_n = 209,000 g mol^{-1} and Đ = 1.3 made from $[CpFe(CO)_2OTf]$.[22] $[H_2BPAr'H]_n$ is an excellent example of where different tactic environments within the polymer backbone chain give rise to three different ^{31}P chemical shifts (Figure 4.8). The ratio of the three peaks in the $^{31}P\{^1H\}$ NMR spectrum is 1:2:1. which is as predicted from the statistical distribution of the different tactic environments; mm:mr+rm:rr,[23] suggesting an overall atactic polymer has been formed.[24] This is the same ratio found for the $[H_2BPAr'H]_n$ formed via the iron-catalysed route (see section 1.10.3).[22] Interestingly, only one, broad ^{19}F resonance is observed for this polymer at δ –63.5 in the ^{19}F NMR spectrum, and only one broad P–H signal is observed in the ^1H NMR spectrum [δ 4.60, *J*(PH) = 365 Hz], showing that the different tactic environments are only observable in the ^{31}P NMR spectrum. Different tactic environments have also been observed in the ^{31}P NMR analysis of poly(methylenephosphines).[25]

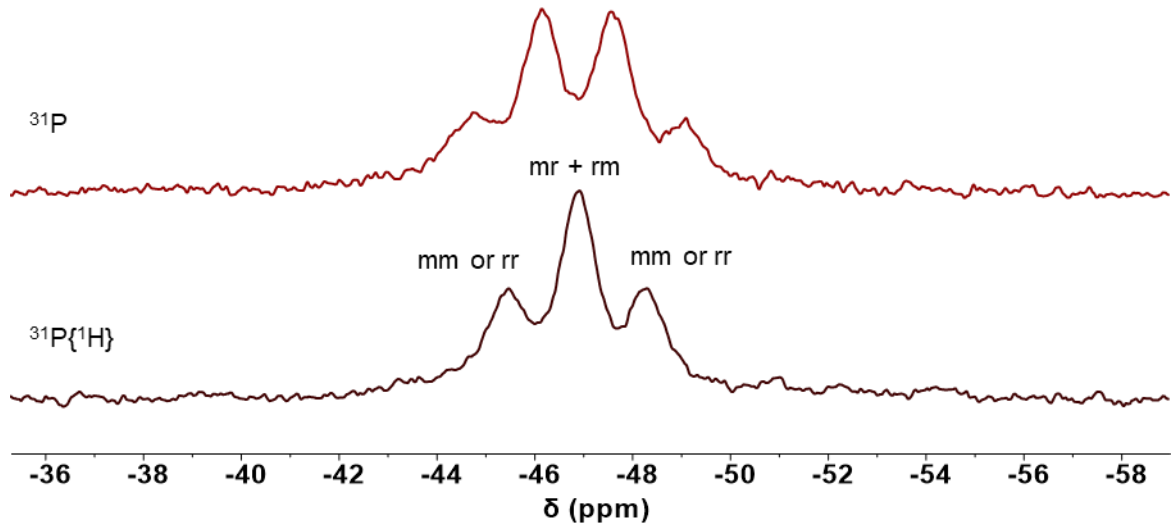

Figure 4.8. ^{31}P (top) and $^{31}P\{^{1}H\}$ (bottom) of isolated $[H_2BPAr'H]_n$ from the dehydropolymerisation of $H_3B{\cdot}PAr'H_2$ using **4.1** as a precatalyst.

After 19 hours of reaction time at 100 °C, isolated $[H_2BPAr'H]_n$ was determined to have an M_n of 127,500 g mol^{-1} and a polydispersity (Đ) of 1.2 by GPC analysis. By MALS the M_n = 38,000 g mol^{-1} and Đ = 1.2. This is roughly four times the size of the phenyl equivalent $[H_2BPPhH]_n$ under the same conditions and reaction time. A proposed explanation for the longer polymer is due to the electron-withdrawing feature of the *meta*-CF_3 groups which activates the P–H bond and in turn, increases the rate of dehydrocoupling and a longer polymer chain is formed during the same reaction time. This observation has been reported before for the dehydropolymerisation of $H_3B{\cdot}PArH_2$ (Ar = 4-$CF_3C_6H_4$), which underwent dehydropolymerisation to form $[H_2BPArH]_n$ at 60 °C using $[Rh(COD)(\mu\text{-}Cl)]_2$ under neat conditions, whereas $H_3B{\cdot}PPhH_2$ required 90-130 °C to form polymeric $[H_2BPPhH]_n$ using the same catalyst.[26] Moreover, in the dehydrocoupling of $H_3B{\cdot}PAr_2H$ [Ar = 3,5-$(CF_3)_2C_6H_3$ and 4-C_6H_4OMe] the monomer containing the more electron withdrawing monomer reacted to 90% conversion after one hour in the melt phase using a $[Rh(dppp)]^+$ catalyst, whereas the less activated electron-donating monomer was only 50% converted after one hour.[6]

A conversion versus M_n experiment was conducted with $H_3B{\cdot}PAr'H_2$ [Ar' = 3,5-$(CF_3)_2C_6H_3$] using reaction conditions of: 100 °C in toluene, 1.25 M monomer and 1 mol% precatalyst **4.1**. The M_n of the isolated polymers was compared to the conversion of $H_3B{\cdot}PAr'H_2$ (Figure 4.9). A very similar step-growth like trend is observed. Up until 100% conversion of the monomer, the polymer molecular weight increases steadily and after complete conversion the molecular weight continues to grow. One

noticeable difference, however, is the steeper increase in molecular weight up until 100% conversion of the monomer. We propose this is caused by the more activated monomer, with electron-withdrawing CF_3 substituents, reacting faster and so the degree of polymerisation is greater. For comparison, after 10 minutes using $H_3B{\cdot}PAr'H_2$ as the monomer, 30% is converted, whereas with $H_3B{\cdot}PPhH_2$, after 17 minutes only 20% of the monomer is converted. Complete conversion of monomer is observed for $H_3B{\cdot}PAr'H_2$ after just four hours, compared to 19 hours for $H_3B{\cdot}PPhH_2$.

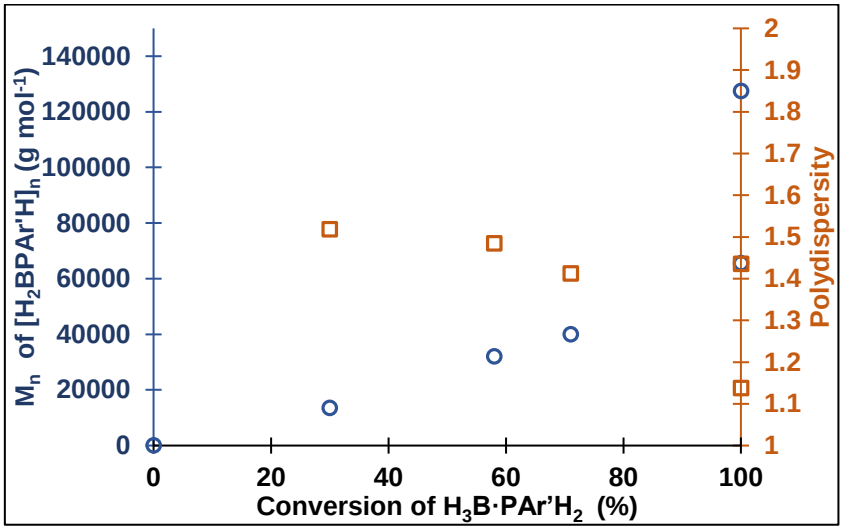

Figure 4.9. M_n (blue, left y-axis) and polydispersity (orange, right y-axis), as calculated by GPC analysis, against the consumption of $H_3B{\cdot}PAr'H_2$ in the dehydropolymerisation of $H_3B{\cdot}PAr'H_2$ to form polymeric $[H_2BPAr'H]_n$ (1 mol% **4.1**, 1.25 M, toluene, 100 °C). The conversion is measured by ^{11}B NMR spectroscopy.

During these experiments, a similar linear dimer intermediate to **LD-Ph**, $H_2B{\cdot}PAr'HBH_2{\cdot}PAr'H_2$ (**LD-*m*CF$_3$**) was observed in the in-situ ^{11}B NMR spectra for the *m*-CF_3 variant (Figure 4.10). This was assigned from two broad ^{11}B signals at δ –35.9 and –38.3, which are at a similar chemical shift to the previously reported phenyl version (δ –36.5 and –38.9).[7] Two broad ^{31}P signals are also observed at δ –51.0 to –53.8, which are similar to **LD-Ph** (δ –51.4 and –53.4, both broad). These observations suggest a similar mechanism is occurring for both aryl phosphine-boranes, as well as the formation and then consumption of the linear dimers, **LD-Ph** and **LD-*m*CF$_3$** during dehydropolymerisation.

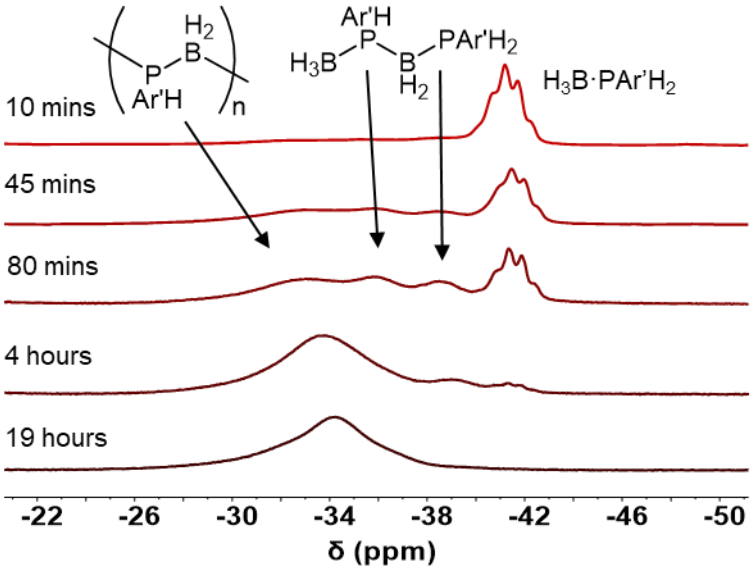

Figure 4.10. In-situ ^{11}B NMR spectra of the dehydropolymerisation of $H_3B{\cdot}PAr'H_2$ with 1 mol% **4.1** in toluene (1.25 M) stopped after different periods of time at 100 °C (193 MHz, toluene, 298 K).

4.6 In-situ ^{1}H NMR studies of the dehydropolymerisation of $H_3B{\cdot}PPhH_2$

With some insight from the in-situ ^{11}B NMR, this section details the in-situ ^{1}H NMR experiments of the dehydropolymerisation of $H_3B{\cdot}PPhH_2$ that are ran periodically over the course of the reaction (Figure 4.11). This provides more detail of monomer consumption, linear dimer formation and polymer production. A lower concentration of 0.25 M was used to increase the volume of solvent in the NMR tube so effective locking and shimming could be obtained without overcharging the NMR tube. A higher concentration of 3 mol% was also used so the reaction went to completion within a reasonable time frame (7 hours). The intensity of the signals relating to monomer $H_3B{\cdot}PPhH_2$ decreased rapidly at the start of the reaction and the PH_2 doublet signal corresponding to linear dimer **LD-Ph** at δ 5.12 [*J*(PH) = 399 Hz] is observable in the first spectrum collected. This signal assigned to the **LD-Ph** PH_2 matches with the previously reported characterisation of **LD-Ph**: doublet at δ 5.85 with *J*(PH) = 406 Hz, in CD_2Cl_2.[7] Over time, the polymer signals grow in intensity as **LD-Ph** and $H_3B{\cdot}PPhH_2$ diminish completely. This corroborates with the in-situ ^{11}B NMR spectra taken in the molecular weight vs conversion experiment that showed the formation and then consumption of **LD-Ph**. Dissolved H_2 (δ 4.48), free $PhPH_2$ (δ 3.78) and CH_2 in the dppe (δ 2.53) are also observed in the ^{1}H NMR spectrum of the catalytic mixture. Complete conversion of $H_3B{\cdot}PPhH_2$ is observed after 6.5 hours.

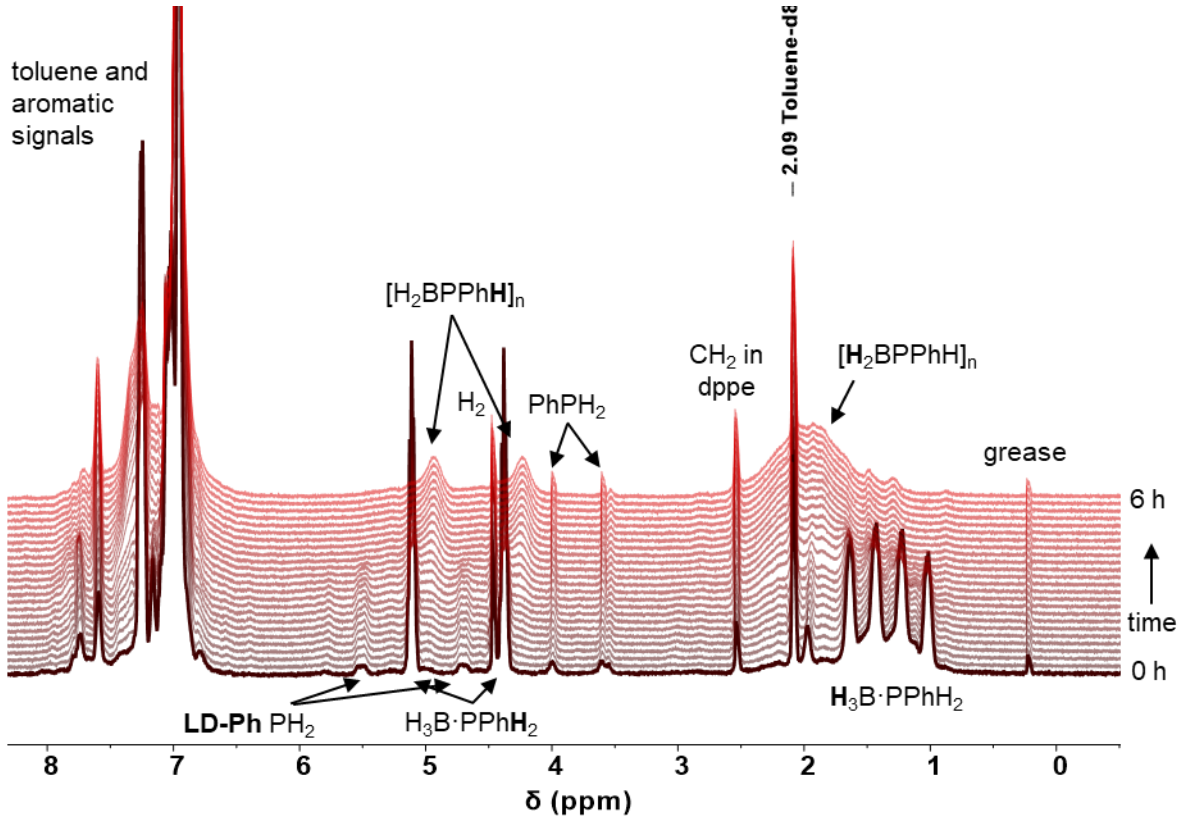

Figure 4.11. In-situ ^{1}H NMR of the dehydropolymerisation of $H_3B{\cdot}PPhH_2$, catalytic conditions: 3 mol% **4.1**, 0.25 M monomer in d_8-toluene, 373 K (500 MHz). Darker lines are earlier in the experiment and lighter red lines are at the end of the six-hour experiment.

The relative integrals of the P–H signals in $H_3B{\cdot}PPhH_2$ and $[H_2BPPhH]_n$**,** and the B–H signal of **LD-Ph** are plotted against time in Figure 4.12. The concentration of **LD-Ph** peaks at roughly 4000 seconds, after which it is consumed to completeness over the course of the reaction. Polymer formation and monomer consumption are faster at the start of the reaction and decrease in relative rate during the reaction. The formation of polymeric $[H_2BPPhH]_n$ and the formation and disappearance of **LD-Ph** do not fit simple integrated rate plots which is unsurprising considering the polymer peaks include trimer, tetramer, pentamer etc. which will all be produced at different rates. The consumption of $H_3B{\cdot}PPhH_2$ however, fits a first order decay with a k_{obs} of 3 ± 0.02 x 10^{-4} s^{-1} (Figure 4.12). The molecular weight from these catalytic conditions was calculated to be bimodal, with one component of M_n = 32,000 g mol^{-1} (Đ = 1.5) and the other M_n = 2,500 g mol^{-1} (Đ = 1.4), which is consistent with the earlier observation that a lower monomer concentration increases the proportion of lower molecular weight material formed.

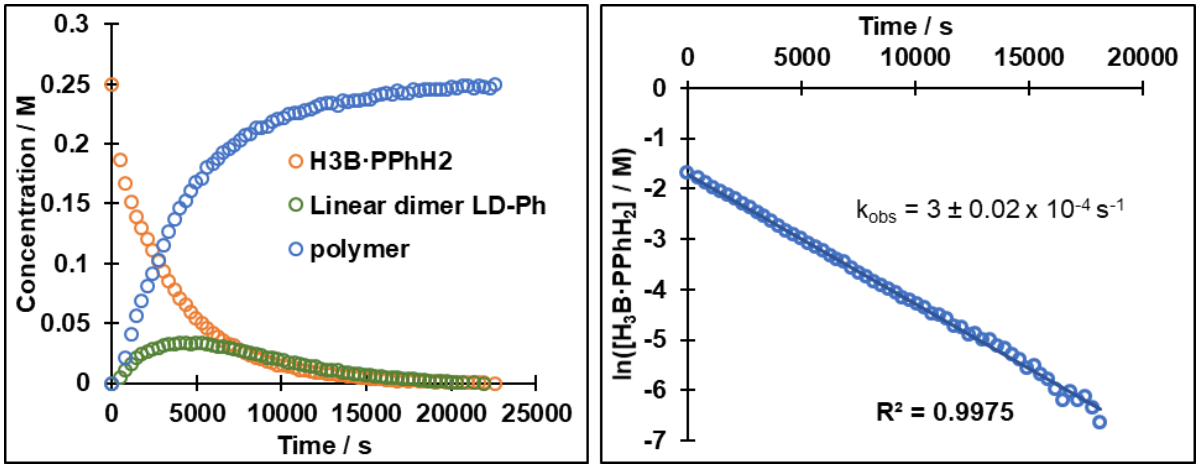

Figure 4.12. Left- relative integral plots of $H_3B{\cdot}PPhH_2$, $[H_2BPPhH]_n$ and **LD-Ph** over time during the dehydropolymerisation of $H_3B{\cdot}PPhH_2$ using **4.1** as a precatalyst. Integrals relative to the initial concentration of $H_3B{\cdot}PPhH_2$. Right- the first order integrated rate plot of $[H_3B{\cdot}PPhH_2]$.

4.6.1 Re-charging of $H_3B{\cdot}PPhH_2$ experiment

To ascertain whether the catalyst decomposes during the reaction a re-charge experiment was conducted. The in-situ ^1H NMR experiment was repeated using the same conditions (3 mol% **4.1**, 0.25 M in d_8-toluene, 100 °) but stopped after complete conversion of $H_3B{\cdot}PPhH_2$ was observed (4.5 hours) and then fresh $H_3B{\cdot}PPhH_2$ was added into the reaction mixture. The concentration of $H_3B{\cdot}PPhH_2$ was monitored by in-situ ^1H NMR during the entire experiment (Figure 4.13). The rate of consumption of $H_3B{\cdot}PPhH_2$ is twice as fast in the initial charge. A first order decay is observed for both charges with k_{obs} of $3 \pm 0.07 \times 10^{-4}$ s^{-1} and $1.5 \pm 0.07 \times 10^{-4}$ s^{-1} respectively. There is evidently a reasonable amount of active catalyst in the mixture. The fact that the rate slows could be due to some catalyst decomposition, or, due to a greater concentration of polymer in the second charge, i.e. product inhibition may occur. The final polymer was isolated and analysed by GPC, revealing M_n = 33,000 g mol^{-1}, and a reasonably narrow dispersity of Đ = 1.5. This polymer is too large and uniform to be obtained via uncatalyzed dehydropolymerisation,[8, 27] therefore, the rhodium species within the mixture at the end of catalysis can still catalyse the reaction.

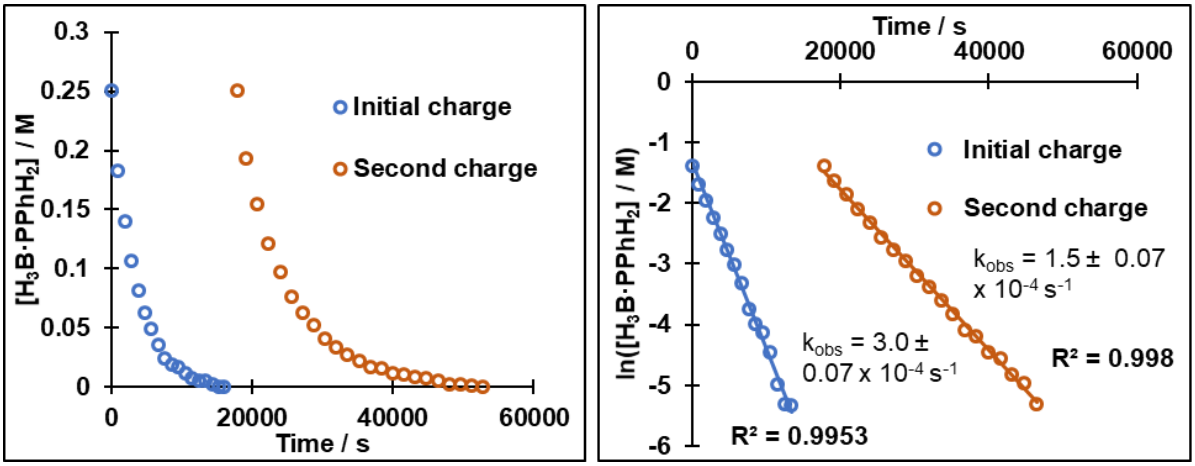

Figure 4.13. Left – concentration plot of $H_3B{\cdot}PPhH_2$ during the dehydropolymerisation of $H_3B{\cdot}PPhH_2$ using **4.1** as a precatalyst with a re-charge of the same amount of monomer after 4.5 hours (3 mol%, 0.25 M in d_8-toluene, 373 K). Right – First order integrated rate plot of the re-charge experiment. Concentrations determined from the signal integrals from the in-situ monitored ^{1}H NMR spectra and are relative to the initial monomer concentration.

Obtaining reliable and accurate kinetic data is difficult for this system for several reasons: 1) H_2 formation, which may affect the rate of reaction as H_2 could be involved in the rate limiting step[2] and is difficult to remove from a sealed NMR tube during in-situ analysis. 2) The concentration of free $PPhH_2$ in the catalytic mixture has also been shown to be influential in the Fe-based systems,[28] and this is difficult to control. 3) Uncatalyzed dehydropolymerisation is also occurring,[8, 27] albeit much slower than the catalysed route. Therefore, no further information could be extracted from the in-situ NMR data detailed so far in this chapter on the formation and consumption of linear dimer $H_2B{\cdot}PPhHBH_2{\cdot}PPhH_2$ (**LD-Ph**). In light of this, **LD-Ph** was prepared independently and applied in catalysis.

4.7 The synthesis of linear dimer $H_3B{\cdot}PPhHBH_2{\cdot}PPhH_2$ and its application in catalysis

To isolate **LD-Ph**, a dehydropolymerisation reaction of $H_3B{\cdot}PPhH_2$ using 1 mol% **4.1** as the precatalyst was stopped after 45 minutes at 100 °C. **LD-Ph** was isolated from the catalytic mixture via a hexane extraction, solvent evaporation and careful removal of residual monomer by sublimation. The sample of **LD-Ph** was inspected by NMR spectroscopy (d^8-toluene): two broad signals in the $^{31}P\{^1H\}$ NMR spectrum are observed at δ –53.2 and –54.5, and two complex multiplet in the ^{11}B NMR spectrum are observed at δ –36.1 and –34.5. In the ^{1}H NMR spectrum, the P–H signals are observed at δ 4.95 and 4.84 with J(PH) = 405 and 390 Hz respectively. This data is consistent with the previously reported

literature data[7] and in the assignment of **LD-Ph** in the in-situ ^{11}B and ^{1}H NMR experiments detailed above. A small proportion of residual $(H_3B)_2$dppe could not be removed from the linear dimer. Due to the relatively low proportion of **LD-Ph** in the catalytic mixture (~30% by in-situ ^{11}B NMR) only a small amount of **LD-Ph** could be isolated (20 mg, 17% yield).

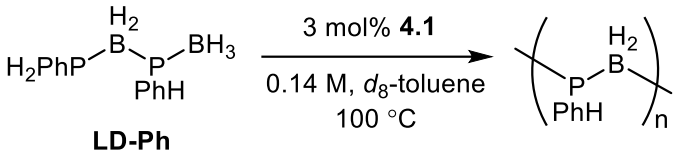

Scheme 4.7. Dehydropolymerisation of **LD-Ph** using **4.1** as a precatalyst.

To see if **LD-Ph** undergoes dehydropolymerisation to form polymeric $[H_2BPPhH]_n$, the isolated **LD-Ph** was added into an NMR tube with **4.1** (3 mol%) and d_8-toluene, and the mixture was heated to 100 °C in an NMR spectrometer and monitored by in-situ ^{1}H NMR spectroscopy for 14 hours (Scheme 4.7, Figure 4.14). As only a small amount of **LD-Ph** could be isolated a lower concentration of 0.14 M was used. It is evident from the in-situ ^{1}H NMR data that the P–H, B–H and aromatic signals corresponding to **LD-Ph** reduce over time as signals increase in intensity. Dissolved H_2 (δ 4.51), ethylene signals from dppe (δ 2.54), and free $PPhH_2$, [δ 3.82, d, J(PH) = 197 Hz] are also observed. Importantly, there is no $H_3B{\cdot}PPhH_2$ observed, so if **LD-Ph** is a precursor to free monomer then it is reacting onwards faster than can be detected by NMR spectroscopy. Free $PhPH_2$ is observed at the start of the reaction, but does not increase in intensity further into the reaction progress, suggesting there is some dissociation of the linear dimer at the start of the reaction which may be part of the catalyst activation, i.e. loss of one dppe ligand. This is supported by the observation of $(H_3B)_2$dppe in the ^{31}P{^{1}H} NMR spectrum taken at the end of catalysis. **LD-Ph** is completely consumed after 12 hours.

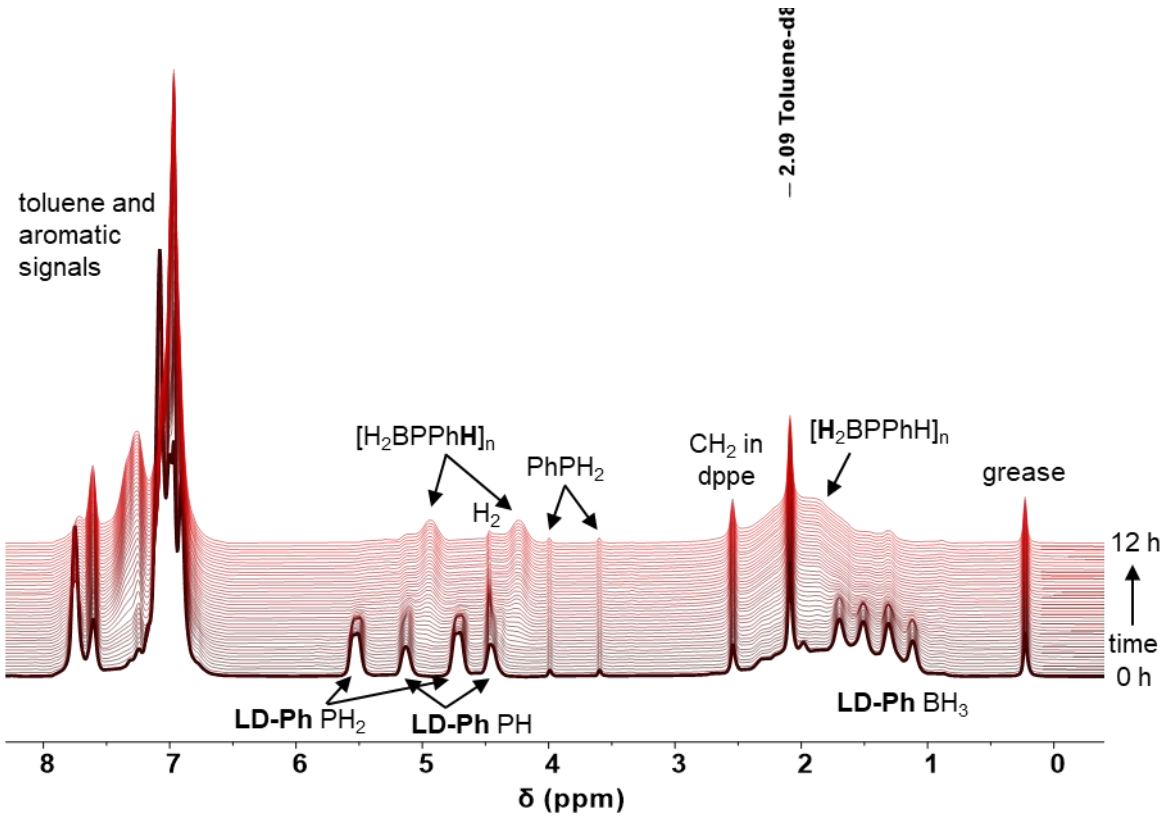

Figure 4.14. In-situ ^{1}H NMR spectra of the dehydropolymerisation of **LD-Ph**, catalytic conditions: 3 mol% **4.1**, 0.14 M **LD-Ph** in d_8-toluene, 373 K (500 MHz). Darker lines are earlier in the experiment and lighter red lines are at the end of the experiment.

At the end of the in-situ ^{1}H NMR monitoring experiment, the catalytic mixture was interrogated by ^{31}P{^{1}H} and ^{11}B NMR spectroscopy, confirming that all of the **LD-Ph** had reacted. Signals corresponding to polymeric $[H_2BPPhH]_n$, smaller cyclic phosphine-borane species,[8] $(H_3B)_2$dppe and free $PhPH_2$ are also observed in the ^{31}P{^{1}H} NMR spectrum. The resultant polymer, $[H_2BPPhH]_n$, was isolated and analysed via GPC. The GPC trace showed a bimodal distribution. The higher molecular weight portion was calculated to be of M_n = 61,000 g mol^{-1} with a polydispersity (Đ) of 1.3. The lower molecular weight fraction is M_n = 3,000 g mol^{-1} and Đ = 1.3 (Figure 4.15). Dehydropolymerisation of $H_3B{\cdot}PPhH_2$ was repeated at the lower concentration of 0.14 M at 3 mol% catalyst loading of **4.1**. Using these conditions, complete conversion of $H_3B{\cdot}PPhH_2$ was observed after 11 hours and the resultant polymer was also bimodal: M_n = 45,000 and 2,500 g mol^{-1} and Đ = 1.3 and 1.4 respectively. This is consistent with the earlier observation that a lower concentration of monomer gives a higher proportion of lower molecular weight polymer (section 4.3.1). In summary, **LD-Ph** undergoes dehydropolymerisation to polymeric

$[H_2BPPhH]_n$ of similar M_n and bimodality, and over a similar time to the dehydropolymerisation of $H_3B{\cdot}PPhH_2$.

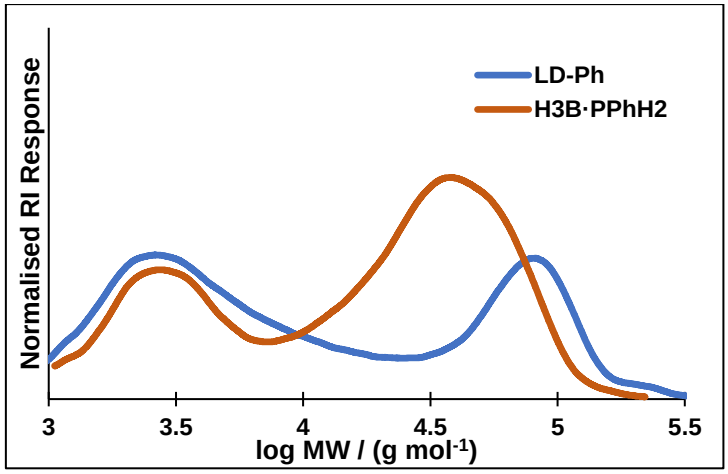

Figure 4.15. GPC trace of the poly(phosphinoboranes) formed from the dehydropolymerisation of $H_3B{\cdot}PPhH_2$ and **LD-Ph** respectively at 0.14 M, 100 °C.

4.8 Catalyst speciation: in-situ NMR spectroscopy and stoichiometric reactivity

4.8.1 In-situ NMR studies

Inspection of the hydride regions of the in-situ ^1H NMR data collected during the dehydropolymerisation of $H_3B{\cdot}PPhH_2$ (section 4.6) and **LD-Ph** (section 4.7) also allowed for insights into catalyst speciation. These revealed that similar hydride resonances are observed for both reactions. At the start of the dehydropolymerisation of $H_3B{\cdot}PPhH_2$, hydride signals at δ –1.90 and –14.45 in a 3:1 ratio are observed (Figure 4.16). Gradually, these signals decrease in intensity and new signals between δ –16.00 and –16.6 increase in intensity throughout the reaction. A very broad signal between δ –8.6 and –10.2 is also observed, which grows in intensity as the concentration of $H_3B{\cdot}PPhH_2$ and **LD-Ph** decreases.

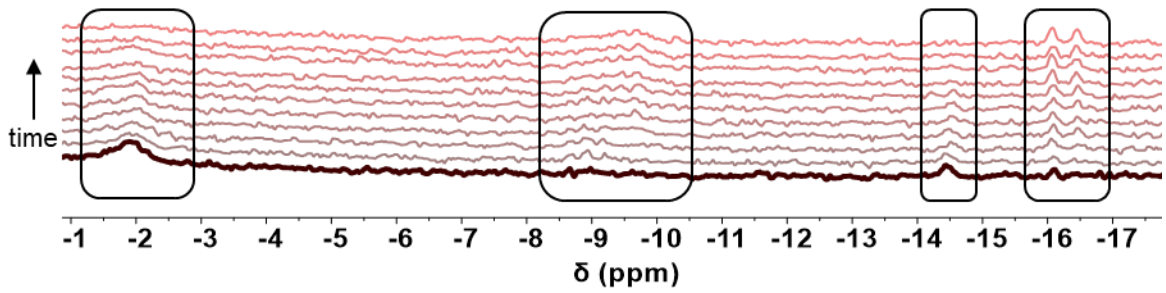

Figure 4.16. Hydride region of the in-situ ^{1}H NMR of the dehydropolymerisation of $H_3B{\cdot}PPhH_2$, catalytic conditions: 3 mol% **4.1**, 0.25 M $H_3B{\cdot}PPhH_2$ in d_8-toluene, 373 K (500 MHz). Darker lines are earlier in the experiment and lighter red lines are at the end of the experiment.

At the start of dehydropolymerisation of **LD-Ph**, two signals are observed in the hydride region, one as a broad singlet centred at δ –1.9 and the second, observed as a sharper singlet at δ –14.43, in a relative integral ratio of 3:1 (Figure 4.17), very similar to the dehydropolymerisation of $H_3B{\cdot}PPhH_2$ (Figure 4.16). As the catalysis progresses, these signals diminish, and new signals between –16.00 and –16.61 appear. The disappearance of these hydride signals coincides with the consumption of **LD-Ph**.

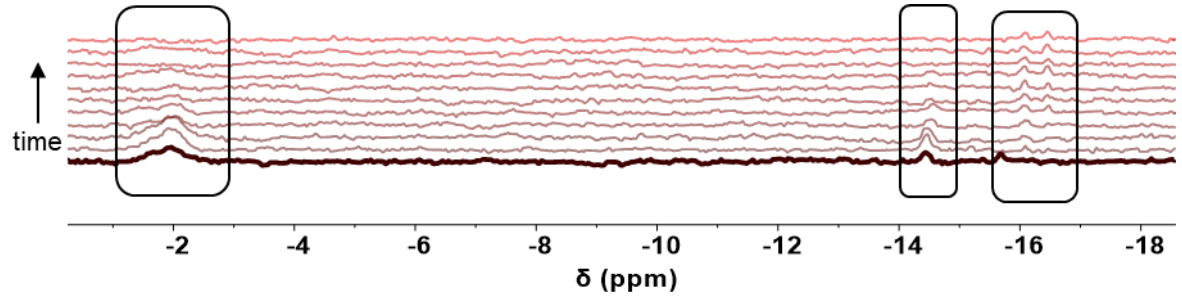

Figure 4.17. Hydride region of the in-situ ^{1}H NMR of the dehydropolymerisation of **LD-Ph**, catalytic conditions: 3 mol% **4.1**, 0.14 M **LD-Ph** in d_8-toluene, 373 K (500 MHz). Darker lines are earlier in the experiment and lighter red lines are at the end of the experiment.

The hydride signals observed at the start of these dehydropolymerisation reactions are similar to the hydride resonances reported for [RhH(dppp)(σ,η^{2}η^2-$PPh_2{\cdot}BH_2PPh_2{\cdot}BH_3$)][$BAr^F_4$] (**i-56-Ph$_2$**) by Huertos and Weller in 2013.[5] The rhodium hydride signal of **i-56-Ph$_2$** was reported as a broad singlet at δ –14.1 and the agostic BH_3 was observed at δ –1.19, integrating in a 1:3 ratio, that further suggests a rapid rotation of the BH_3 unit.[5] **i-56-Ph$_2$** was reported as the catalyst resting state during the [Rh(dppp)]$^+$ catalysed dehydrocoupling of $H_3B{\cdot}PPh_2H$ to form secondary linear dimer $H_3B{\cdot}PPh_2BH_2{\cdot}PPh_2H$ and could also be independently synthesised via the addition of $H_3B{\cdot}PPh_2BH_2{\cdot}PPh_2H$, to [Rh(dppp)(η^6-$C_6H_5F$)][$BAr^F_4$]. Are we observing a similar complex, namely [RhH(dppe)(σ,η^{2}η^2-

PPhH·BH_2PPhH·BH_3)][Cl] (**4.2**) as the catalyst resting state during the dehydropolymerisation of $H_3B{\cdot}PPhH_2$ using **4.1** as a precatalyst (Figure 4.18)?. An investigation utilising further in-situ catalyst speciation and stoichiometric reactivity was therefore conducted.

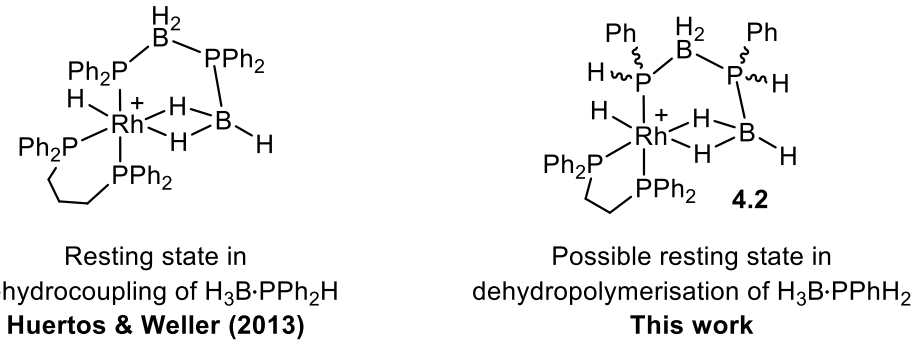

Figure 4.18. Proposed catalytic resting states.

In order to obtain more spectroscopic information on the proposed catalyst resting state (**4.2**) an NMR tube was charged with precatalyst **4.1**, 20 equivalents (5 mol%) of $H_3B{\cdot}PPh_2H$ and d_8-toluene (Scheme 4.8). The mixture was heated to 100 °C for 10 minutes before it was cooled to room temperature and analysed by NMR spectroscopy. Cooling the sample stops catalytic turnover, and thus the organometallic species can be interrogated via NMR spectroscopy, using multiple different nuclei, which was not accessible during the in-situ ^{1}H NMR experiments detailed above that were run under array conditions. A higher catalyst loading of 5 mol% also allows for clearer observation of the organometallic species present. After 10 minutes, 60% of $H_3B{\cdot}PPh_2H$ had reacted to form **LD-Ph** and $[H_2BPPhH]_n$ in a 1:1 ratio.

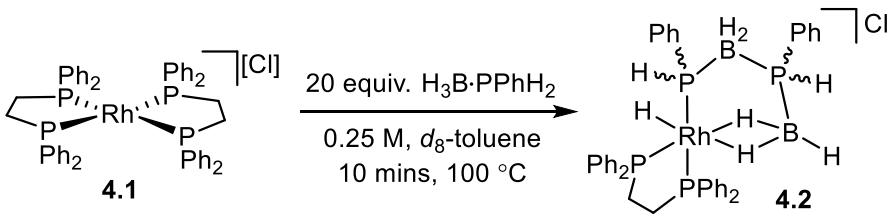

Scheme 4.8. 5 mol% speciation experiment.

In the hydride region of the resulting ^{1}H NMR spectrum, two hydride signals, at δ –1.9 and –14.2 are observed in a 3:1 ratio are similar to those observed in the in-situ ^{1}H NMR data detailed above (Figure 4.19). The resonance at δ –1.9 is broad and comprises of at least two overlapping signals. This has been observed in the analogous primary cyclohexyl linear dimer bound complex, [RhH(dppp)(σ,$\eta^2\eta^2$-

PCyH·BH_2PCyH·BH_3)][BAr^F_4] for which different BH_3 signals were attributed to different diastereomers due to the chiral P atoms in the linear dimer ligand (Scheme 4.8).[6] The signal at δ –1.9 sharpened upon ^{11}B-decoupling, whereas the more upfield signals did not change. Several other unknown signals are observed between δ –15 and –17 which could be catalyst decomposition products or different closely-related products.

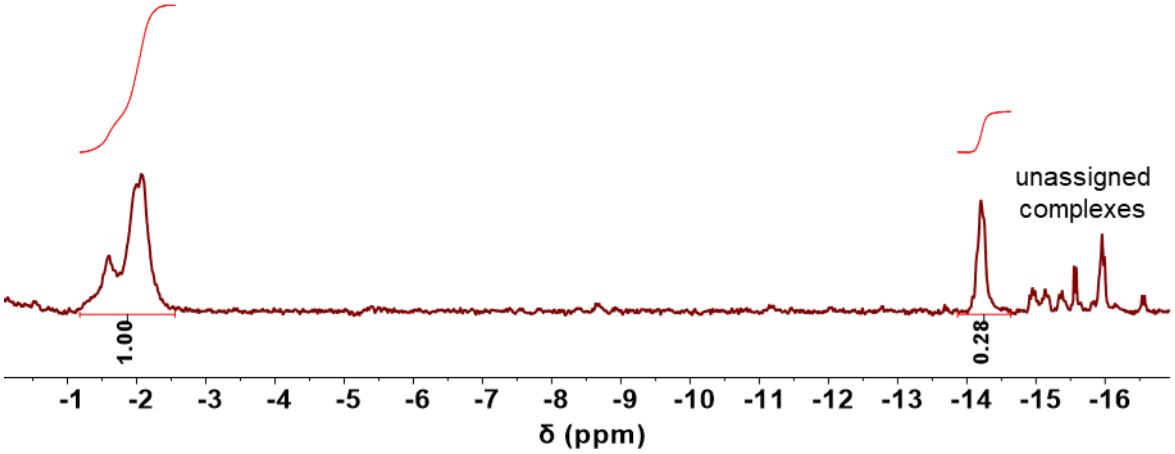

Figure 4.19. Hydride region of the ^{1}H NMR spectrum of the catalytic mixture of $H_3B{\cdot}PPhH_2$ with 5 mol% **4.1** in d_8-toluene (0.25 M) stopped after 10 minutes at 100 °C (500 MHz, d_8-toluene, 298 K).

In the ^{11}B NMR spectrum of this reaction, two broad ^{11}B signals at δ –3.1 and –16.6 are observed and assigned as the BH_3 and BH_2 groups in **4.2** respectively (Figure 4.20). These are reasonably similar to those reported for [RhH(dppp)(σ,$\eta^2\eta^2$-$PPh_2{\cdot}BH_2PPh_2{\cdot}BH_3$)][$BAr^F_4$] at δ 3.2 and –27.2.[5] Linear dimer and polymer are also observed.

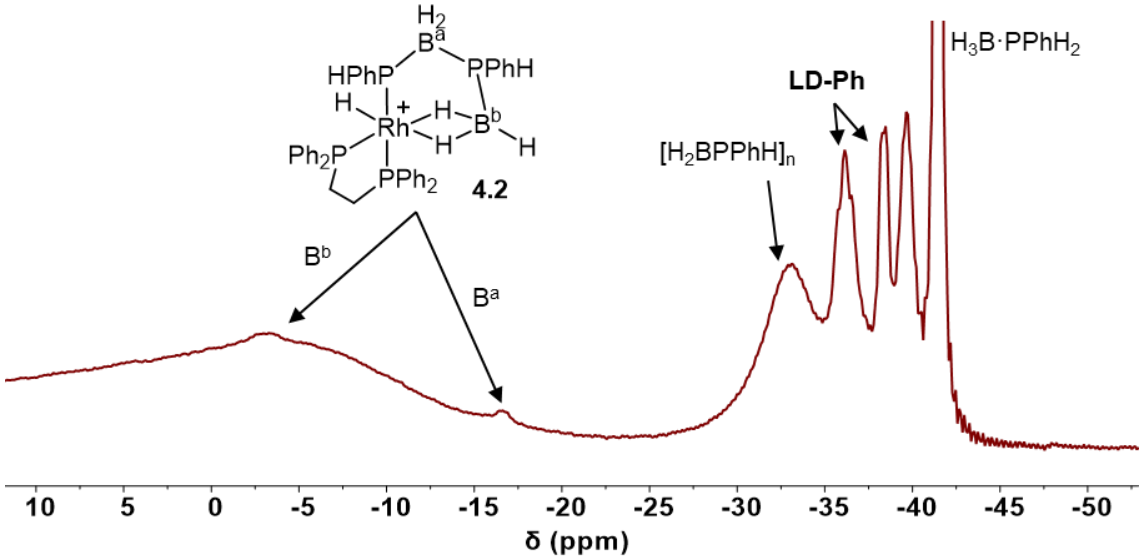

Figure 4.20. $^{11}B\{^{1}H\}$ NMR spectrum of the catalytic mixture of $H_3B{\cdot}PPhH_2$ with 5 mol% **4.1** in d_8-toluene (0.25 M) stopped after 10 minutes at 100 °C (160 MHz, d_8-toluene, 298 K).

In the $^{31}P\{^{1}H\}$ NMR spectrum, signals reflecting unreacted **4.1**, $(H_3B)_2$dppe (10% compared to the total P–B species), monomer $H_3B{\cdot}PPhH_2$, linear dimer **LD-Ph**, polymeric $[H_2BPPhH]_n$, and $PhPH_2$ are observed (Figure 4.21). Broad signals between δ 62-54 may correspond to the ^{31}P nuclei in the dppe fragment (P^a and P^b) and broad signals between δ –30 and –45 are tentatively assigned as the main group ligand (P^c and P^d) within **4.2**. However, these signals are broad and difficult to specifically assign and the ^{31}P NMR spectrum does not clearly show the catalyst speciation.

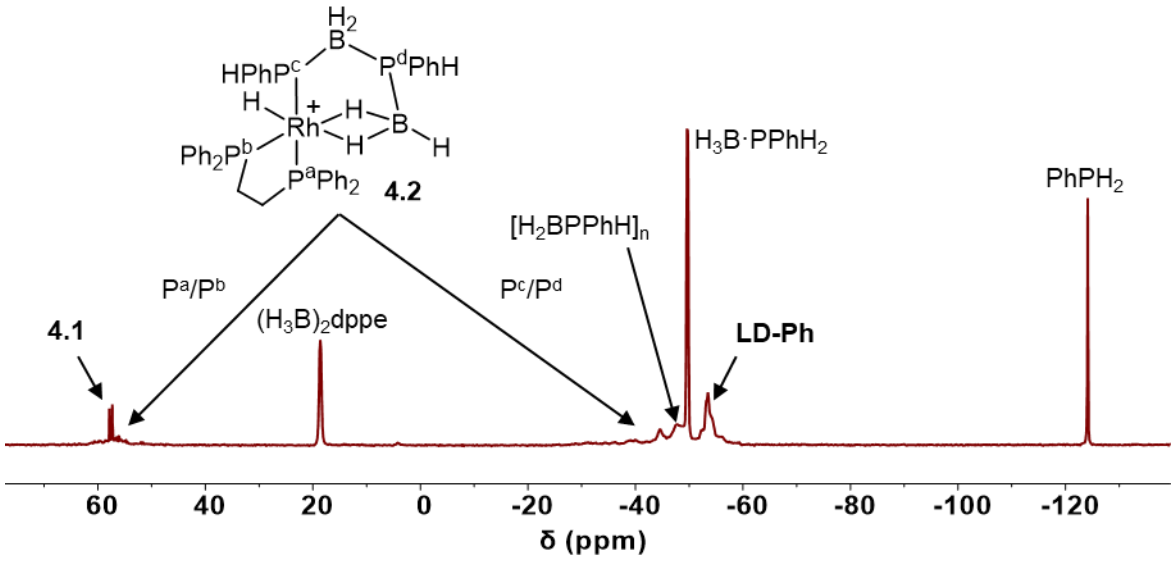

Figure 4.21. $^{31}P\{^{1}H\}$ NMR spectrum of the catalytic mixture of $H_3B{\cdot}PPhH_2$ with 5 mol% **4.1** in d_8-toluene (0.25 M) stopped after 10 minutes at 100 °C (202 MHz, d_8-toluene, 298 K).

In an attempt to gain some insight into the catalyst speciation at the end of catalysis the same reaction was repeated (5 mol% **4.1**, 20 equiv. of $H_3B{\cdot}PPhH_2$, 0.25 M d_8-toluene, 100 °C) but the reaction was left for 50 minutes, in which time 98% of $H_3B{\cdot}PPhH_2$ had reacted to give **LD-Ph** and $[H_2BPPhH]_n$. In the ^1H NMR spectrum of this catalytic mixture, a small amount of **4.2** is still observable, accompanied by a broad hydride signal centred at δ – 9.0, which dominates the hydride region. The other NMR data is very broad and not useful for structure elucidation. Instead, ESI-MS analysis using a HCTultra ETD II ESI-ion trap spectrometer in the positive mode interfaced into a glovebox was used to gain insight into this catalyst speciation. A molecular ion of 855.3 m/z is observed, which matches with a calculated formula of **4.2** + PC_6H_5 (calc. 855.2 m/z) with the same isotope pattern. The structure of this complex could not be unambiguously assigned but tandem MS/MS concentrated at 855 m/z led to fragmentation to a signal at 747.2 m/z, i.e. the linear dimer bound complex **4.2** (Figure 4.22). Therefore, the new complex is likely a product formed via insertion of $H_3B{\cdot}PPhH_2$ into **4.2** with concurrent loss of H_2, consistent with oligomeric species being formed, but the only species observed via MS has fragmented to lose BH_3. Linking this information back to the re-charge experiment (section 4.6.1), a first order decay of $H_3B{\cdot}PPhH_2$ was observed throughout both charges of monomer and the rate did not change considerably in the second charge suggesting the mechanism does not change. Therefore, it is likely the catalyst resting states at the beginning and at the end of catalysis are similar. ESI-MS of the catalytic mixture earlier in catalysis was unsuccessful.

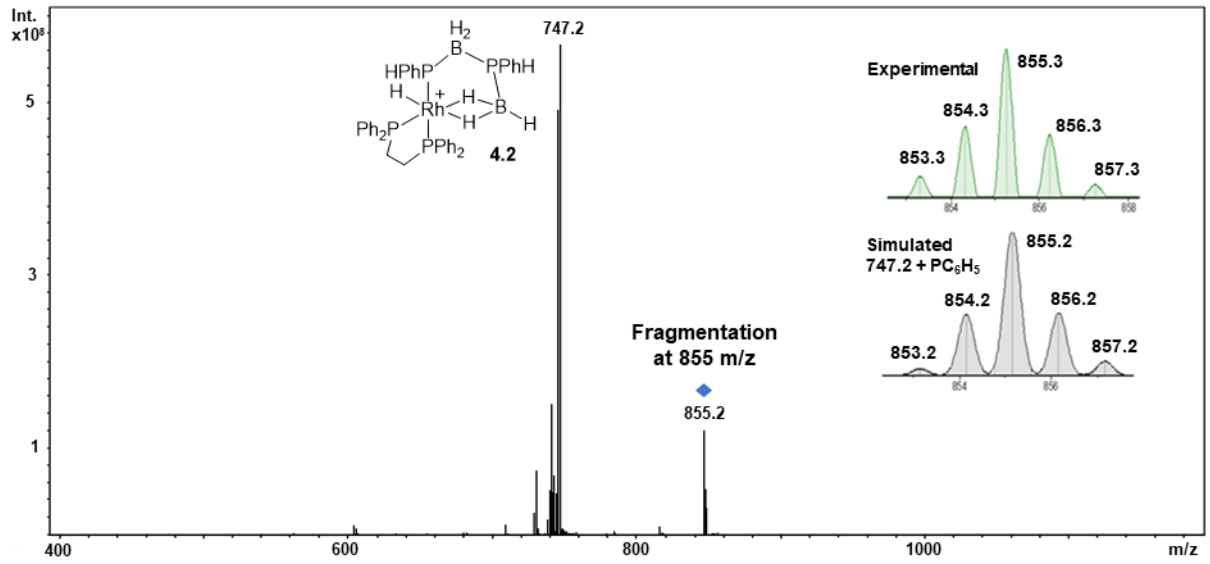

Figure 4.22. ESI-MS (ion trap, positive mode) tandem MS/MS spectrum with fragmentation centred at 855 m/z of the catalytic mixture of $H_3B{\cdot}PPhH_2$ with 5 mol% **4.1** in toluene (0.25 M) stopped after 50 minutes at 100 °C (diluted with 1,2-$F_2C_6H_4$). The inset shows the experimental isotope pattern of the signal at m/z 855.3 and the simulated isotope pattern of **4.2** + PC_6H_5.

4.8.2 Stoichiometric reactivity with the linear dimer $H_3B{\cdot}PPhHBH_2{\cdot}PPhH_2$

To support the assignment of a linear dimer bound resting state **4.2** during the dehydropolymerisation of $H_3BP{\cdot}PhH_2$, a series of stoichiometric reactions were conducted to independently synthesise **4.2** and characterise it in more detail.

LD-Ph and **4.1**, in a 3:1 molar ratio, were added to an NMR tube with d_8-toluene (Scheme 4.9). The mixture was heated to 100 °C for five minutes and analysed by NMR spectroscopy.

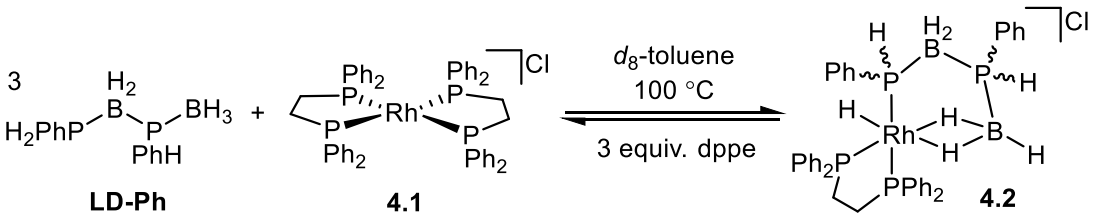

Scheme 4.9. Addition of linear dimer **LD-Ph** to **4.1**, forming the linear dimer bound complex, **4.2**. Addition of dppe to **4.2** reformed **4.1**.

Signals corresponding the agostic-BH_3 and Rh–H environments in **4.2** were observed at δ –1.9 and –14.2 respectively in a 3:1 ratio in the ^{1}H NMR spectrum. This matches the in-situ ^{1}H NMR data from the dehydropolymerisation of $H_3BP{\cdot}PhH_2$ and **Ph-LD**. Upon the application of ^{31}P-decoupling, two different

Rh–H signals are observed almost overlapping at δ –14.18 and –14.27, both with doublet multiplicity [*J*(RhH) = 21 Hz] (Figure 4.23). These are typical *J*(RhH) values for a Rh(III) hydride, such as [Rh(H)$_2$(κ^2-PCy$_2$biPh)][BAr$^F{}_4$] with *J*RhH) = 25 Hz (biPh = biphenyl).[29] Two signals are also observed for the agostic-BH_3 moiety, although the relative integrals do not match for the separate isomers, and therefore, there are likely more isomers within the broad resonance centred at δ –1.9. The different signals are assigned as diastereomers of **4.2** that arise due to the chiral P atoms, which was also observed for the primary linear dimer bound complex [RhH(dppp)(σ,η^{2}η^2-PCyH·BH$_2$PCyH·BH$_3$)][BAr$^F{}_4$] (**i-56-CyH**).[6] When ^{31}P-decoupling was applied to the ^{1}H NMR experiment, the signals sharpened most when the decoupler was centred at –22 ppm, and the doublet multiplicity of each signal was poorly resolved when centred at +50 ppm or –50 ppm, suggesting that the hydride couples to ^{31}P nuclei in both the dppe and the main group ligands. (H$_3$B)$_2$dppe was also observed at δ 18.0 in the ^{31}P{^{1}H} NMR spectrum. Three equivalents of dppe were added to the reaction mixture at room temperature, which resulted in little change in the hydride signals until the NMR tube was heated to 100 °C for five minutes and then quantitative conversion of linear dimer bound **4.2** to the original precatalyst **4.1** was observed in the ^{31}P{^{1}H} NMR spectrum [**4.1** is observed as a doublet at δ 57.7 with *J*(RhP) = 133Hz] and supported by the lack of hydride signals (Figure 4.23). This illustrates the reversibility of linear dimer coordination, which was also shown to be true for the related complexes [RhH(dppp)(σ,η^{2}η^2-PPh$_2$·BH$_2$PPh$_2$·BH$_3$)][BAr$^F{}_4$][5] (**i-56-Ph$_2$**) and [RhH(dppp)(σ,η^{2}η^2-PCyH·BH$_2$PCyH·BH$_3$)][BAr$^F{}_4$] (**i-56-CyH**)[6] which formed [Rh(dppp)(dppe)][BAr$^F{}_4$] upon addition of dppe. It also shows that, likely, the formation of (H$_3$B)$_2$dppe inhibits this deleterious equilibrium.

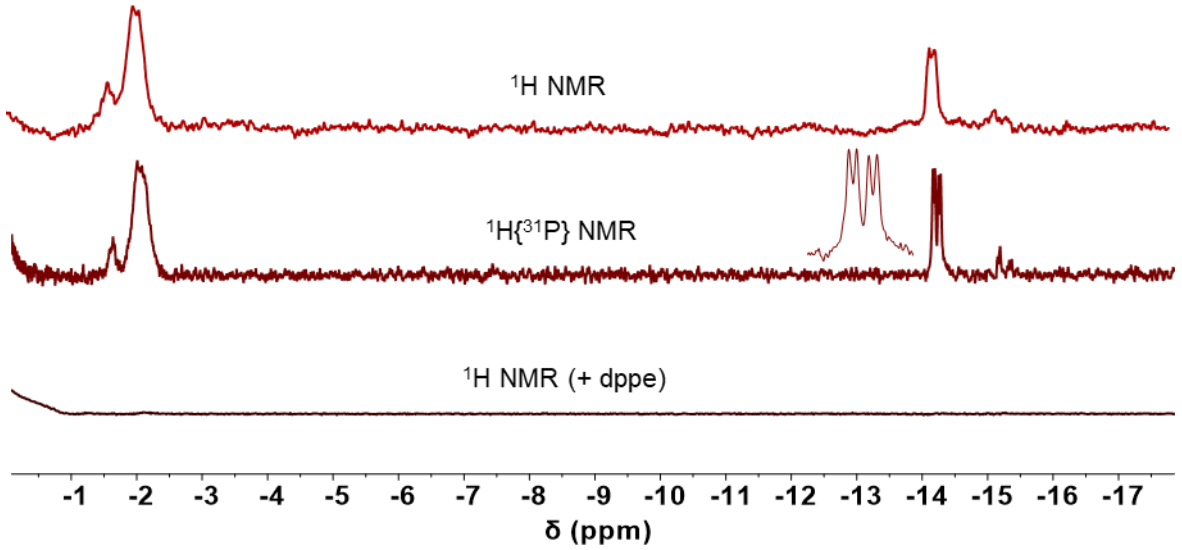

Figure 4.23. Hydride region of the ^{1}H NMR (top) and ^{1}H{^{31}P} centred at –22 ppm (middle) spectra of **4.2**, formed via the addition of **LD-Ph** to **4.1** in d_8-toluene. Addition of dppe results in the formation of **4.1** (bottom) (500 MHz, d_8-toluene, 298 K).

The ^{31}P signals of **4.2** are difficult to determine, however, upon addition of dppe to **4.2** the broad signals which were tentatively assigned as isomers of the dppe (δ 62-54) and bound linear dimer (δ –30 to –45) ligands, are no longer observed (Figure 4.24). Alongside the concurrent loss of the hydride signals, this is good evidence for the assignment of **4.2**. The relative integral of the **4.1** signal also increases.

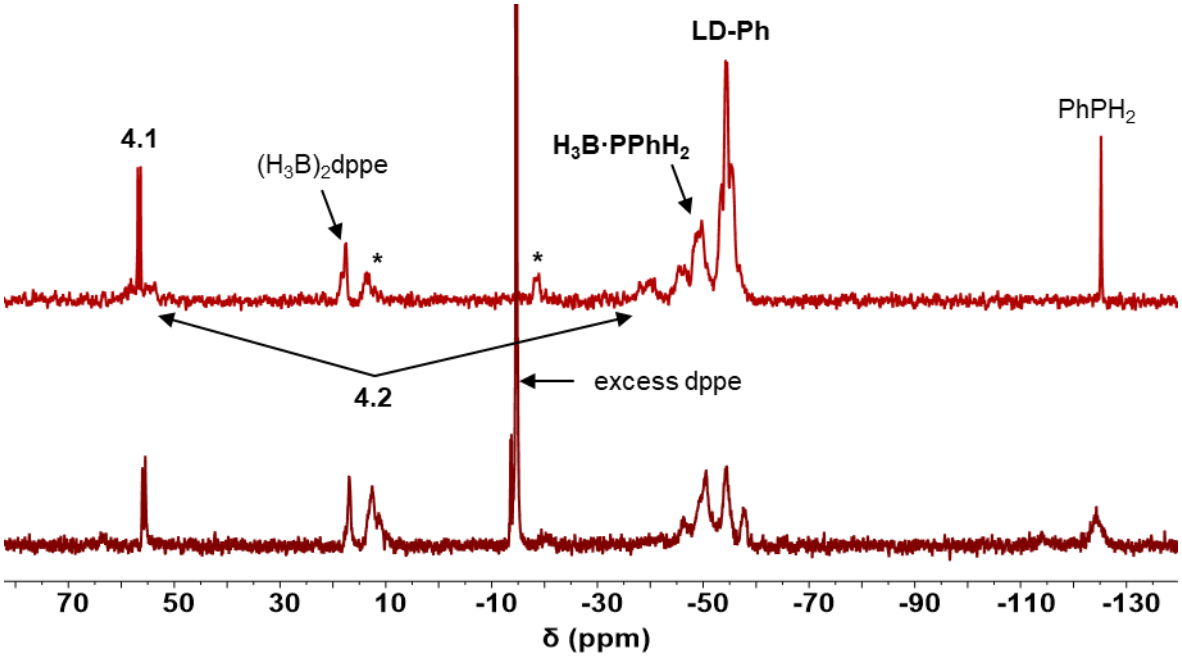

Figure 4.24. ^{31}P{^{1}H} NMR spectra of the reaction mixture of **4.1** and **LD-Ph** addition (top) and after addition of three equivalents of dppe (bottom) (243 MHz, d_8-toluene, 298 K). * Denotes unknown compound.

A more reactive rhodium precursor, namely [Rh(dppe)(η^6-C_6H_5F)][BAr^F_4] (**4.3**) was used next with the aim to obtain further evidence for the formation of **4.2.** The η^6-C_6H_5F ligand is labile,[30, 31] and is more readily displaced than the dppe ligand. **4.3** was prepared via a literature procedure.[32] Addition of two equivalents of **LD-Ph** to **4.3** in d_8-toluene at room temperature, resulted in the formation of the [BAr^F_4]$^-$ analogue of **4.2**, **4.2-[BAr^F_4]** (Scheme 4.10). In the ^{1}H NMR spectrum, two broad signals at δ –1.5 and –14.2 in 3:1 ratio are also observed (Figure 4.25). Several unknown hydride signals are also observed between δ –14.5 and –15.5 which were observed in the in-situ NMR experiments. Broad ^{31}P signals are observed between δ 61 to 53 and δ –35 to –42 in the ^{31}P{^{1}H} NMR spectrum (Figure 4.26), similar to previous observations for **4.2** but no more useful for structural elucidation. The broadness and complexity of the signals could be due to the different possible isomers. Signals relating to [H_2BPPhH]$_n$ are also observed and this may account for the hydride signals between δ –14.5 and –15.5. Some residual (H_3B)$_2$dppe is transferred with the **LD-Ph** as both are soluble in hexanes and therefore difficult to separate.

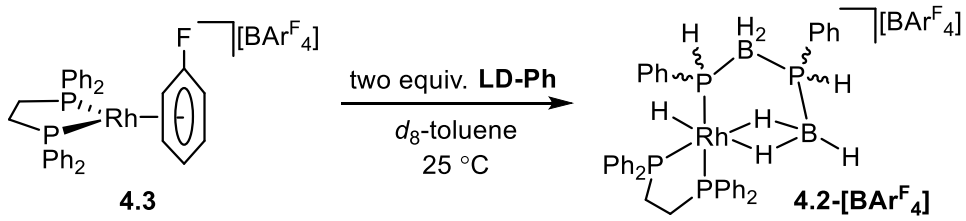

Scheme 4.10. Addition of linear dimer, **LD-Ph** to **4.3**.

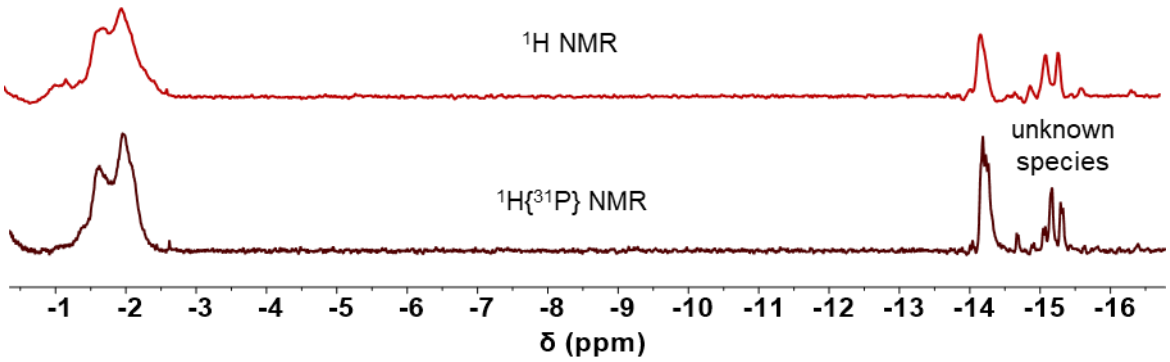

Figure 4.25. Hydride region of the ^{1}H NMR (top) and ^{1}H{^{31}P} centred at –22 ppm (bottom) spectra of **4.2**, formed via the addition of **LD-Ph** to **4.3** in d_8-toluene (500 MHz, d_8-toluene, 298 K).

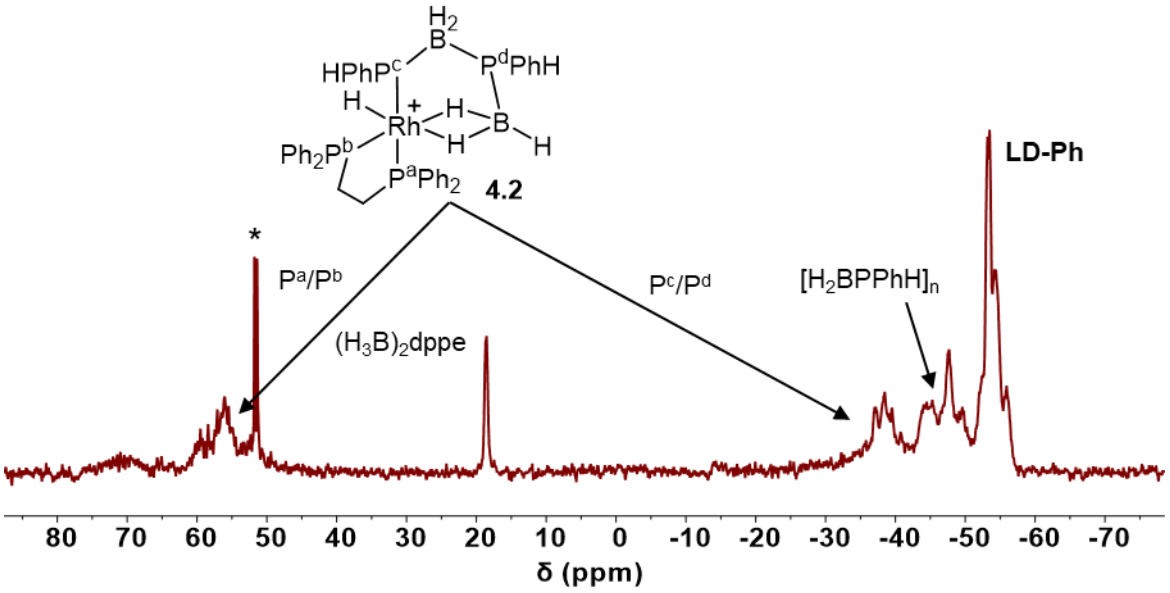

Figure 4.26. $^{31}P\{^{1}H\}$ NMR spectra of the reaction mixture of **4.3** and **LD-Ph** (243 MHz, d_8-toluene, 298 K). * Denotes unknown compound.

The sample of **4.2-[BAr$^{F}_{4}$]** was analysed by air sensitive ESI-mass spectrometry, using a bespoke glovebox[33] connected to a HCTultra ETD II ESI-ion trap spectrometer set in positive mode. The molecular ion is observed at 747.2 m/z, which matches well with that calculated for the cationic portion of **4.2** (calc. = 747.2 m/z) with the same isotopic pattern (4.27). A mass value corresponding to a small amount of residual $[Rh(dppe)_2]^+$ is also observed (899.2, calc. 899.2 m/z) which we propose is carried over from the starting material **4.3**. A signal at 855.2 m/z matches the observed species at the end of catalysis i.e. **4.2** + PC_6H_5, and the observation of this complex in this reaction suggests the two species are formed together, but no further information was obtained for this unknown complex.

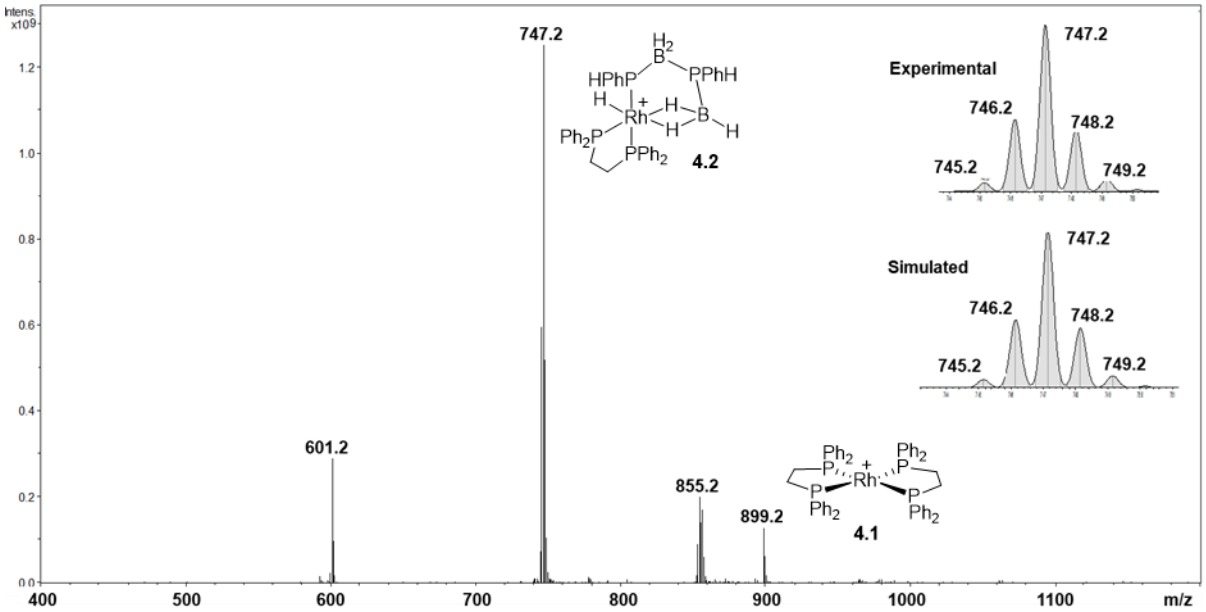

Figure 4.27. ESI mass spectrum using an ion trap detector (positive mode) of the reaction mixture of **4.3** and **LD-Ph** to form **4.2**. The inset shows the experimental and simulated isotope distribution of the cationic portion of **4.2**.

In an attempt to ascertain whether larger oligomeric chains can coordinate to the $[Rh(dppe)]^+$ scaffold, oligomeric $[H_2BPPhH]_n$ was prepared via the dehydropolymerisation of $H_3B{\cdot}PPhH_2$ using **4.1** as the precatalyst with a 45 minute reaction time. The molecular weight of the oligomeric material was measured as M_n of 7,000 g mol^{-1} (Đ = 2.4) by conventional column calibration. This equates to an approximate absolute molecular weight of 750 g mol^{-1} when calibrated with multi-angle light scattering data (Figure 4.4), which is an approximate degree of polymerisation of six repeat units. Without purifying, the reaction mixture, including both unreacted monomer $H_3B{\cdot}PPhH_2$ and dimer **LD-Ph**, was added to **4.3** in 1,2-$F_2C_6H_4$ solvent and analysed by NMR spectroscopy (Scheme 4.11).

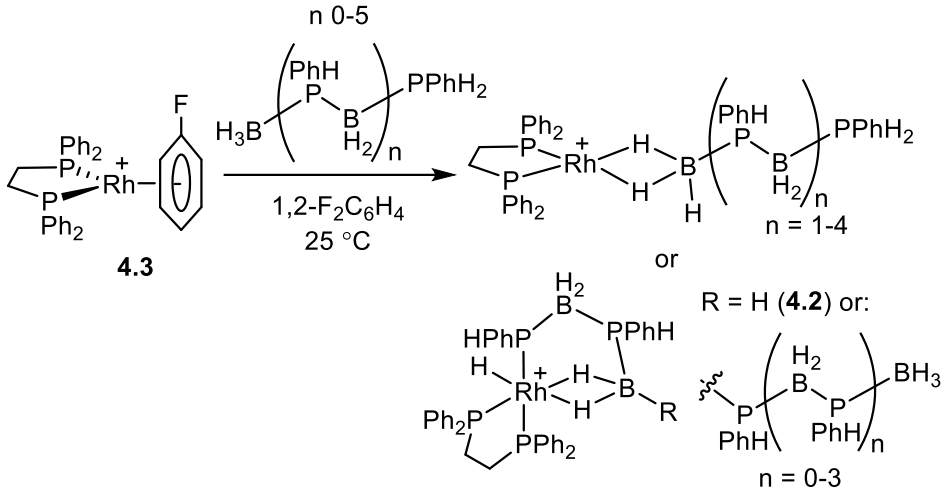

Scheme 4.11. Addition of oligomeric phosphinoborane to **4.7**. $[BAr^F_4]^-$ anions omitted for clarity.

In the ^{1}H NMR spectrum of the resulting reaction mixture, a broad hydride signal is observed at δ –1.9, consistent with the previously assigned B–H agostic BH_3 motif in complex **4.2** (Figure 4.25). Two broad Rh–H signals, more distinct than observed in the previous experiments (Figure 4.28), are observed at δ –13.82 and –14.34. ^{31}P-decoupling revealed doublet multiplicity, with *J*(RhH) = 18 Hz. The signal at δ –14.34 is similar to the Rh–H observed in the reaction of **4.3** and linear **Ph-LD** (δ –14.34) but the more downfield hydride at δ –13.82 has not been observed previously and could be an indication of a P–H activated β-B–H agostic complex of a larger oligomer. Application of ^{11}B-decoupling resulted in the separation of two major BH_3 environments, which integrate 3:1 with the two main Rh–H signals, and several minor BH_3 environments for which the Rh–H counterparts are too small to assign. This suggests there are two sets of Rh–H and BH_3 signals that could be different molecular weight oligomers bound, or isomers of **4.2**. A signal at δ –0.82 is also observed in the ^{1}H NMR spectrum, which is the region that sigma-borane complexes are observed, such as $[Rh(H)_2(P^tBu_2H)_2(\eta^2\eta^2\text{-}H_3B{\cdot}P^tBuH)][BAr^F_4]$ (δ –0.89),[3] and could be indicative of different bonding geometries of the oligomers. In the ^{31}P{^{1}H} NMR spectrum of the reaction mixture, broad signals in the region, δ 68-56 (dppe signals) and δ –30 to –45 (bound linear dimer) are similar to those previously assigned in **4.2**. This reaction mixture was analysed by air sensitive mass spectrometry using an HCTultra ETD II ESI-ion trap spectrometer in the positive mode (Figure 4.29). The molecular ion is observed at 747.3 m/z, corresponding to the cationic portion of **4.2** (calc. 747.2) and the isotope patterns match well. There are no complexes containing larger oligomers

observable via this method. A small amount of **4.1** that is carried over with the starting material **4.3** and the reoccurring signal at 855.2 m/z are also observed.

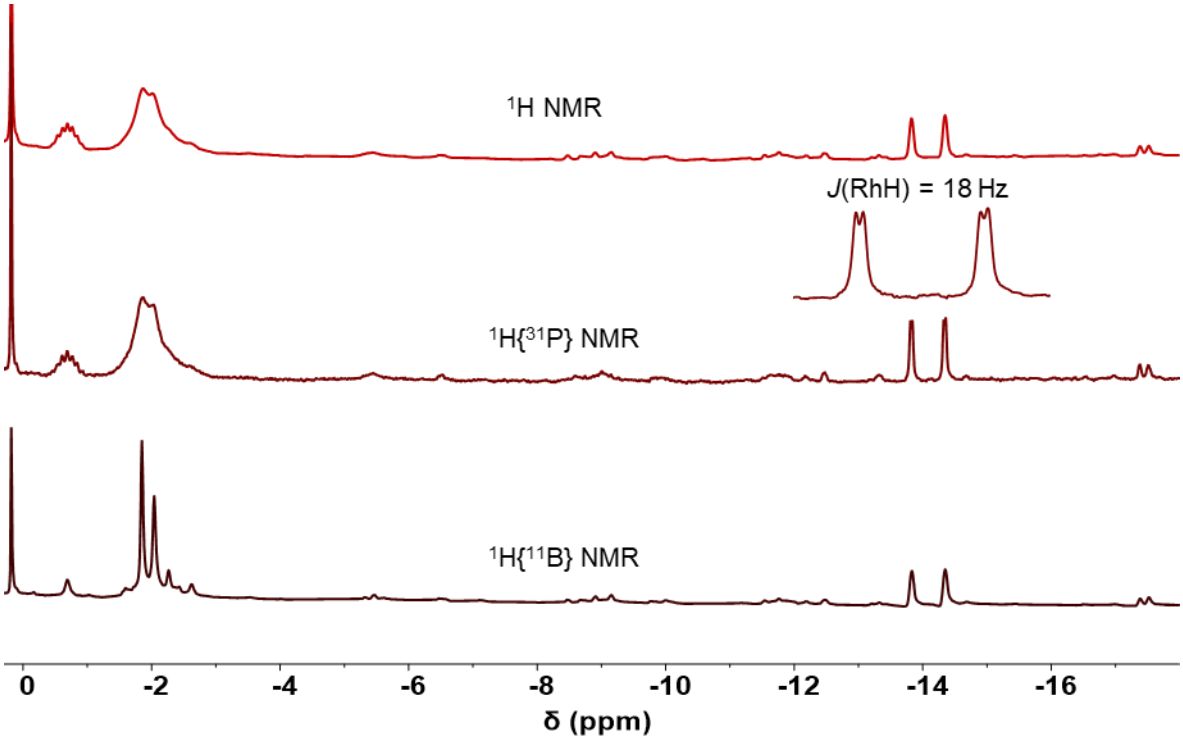

Figure 4.28. ^{1}H (top), ^{1}H{^{31}P} (middle) and ^{1}H{^{11}B} (bottom) NMR spectra of the reaction mixture of **4.3** with a mixture of $H_3B{\cdot}PPhH_2$, **LD-Ph** and oligomeric $[H_2BPPhH]_n$ in 1,2-$F_2C_6H_4$.

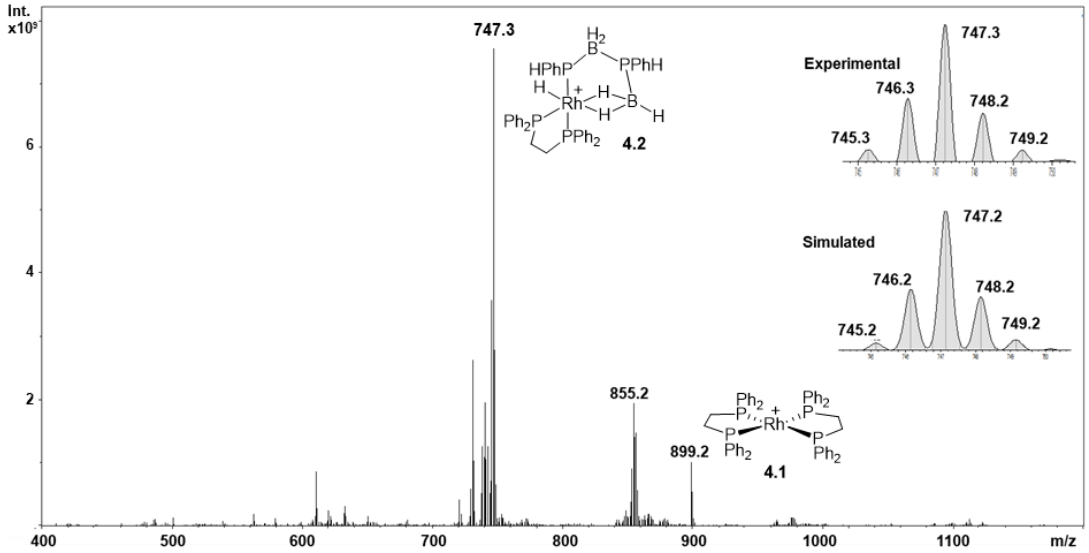

Figure 4.29. ESI mass spectrum using a HCTultra ETD II ESI-ion trap spectrometer in the positive mode, of the reaction mixture of **4.3** with a mixture of $H_3B{\cdot}PPhH_2$, **LD-Ph** and oligomeric $[H_2BPPhH]_n$ in 1,2-$F_2C_6H_4$.

The same reaction mixture was analysed via ESI-MS using a Waters Acquity Triple Quadrupole Detector equipped with Z-spray ionisation source in the laboratories of Professor J. S. McIndoe, University of Victoria, which is a softer ionisation method than the HCTultra ETD II ESI-ion trap spectrometer used so far in this chapter. Using a pressurised sample infusion technique,[34, 35] complexes with larger oligomers bound to $[Rh(dppe)]^+$ are observed, i.e. $[Rh(dppe)\{H_3B(PhHPBH_2)_nPPhH_2\}]^+$ (Figure 4.30). The m/z values of the dimer, trimer, tetramer and pentamer bound complexes matched well with the calculated values, and the isotope distributions are in good agreement. This is good evidence for the coordination of longer oligomers. While we cannot definitively assign the bonding mode of these ligands as the sigma-borane Rh(I) $\eta^2\eta^2$-H_3BR bound and Rh(III) P–H activated B–H agostic activated complexes have the same mass, it is likely that the stabilising chelating agostic make the Rh(III) geometry more stable. Also, within the Rh(III) agostic geometry, we do not know whether the agostic interaction is with a terminal BH_3 (like in **4.2**) or an internal BH_2. Related sigma-borane complexes include $[Rh(P^tBu_2H)_2(\eta^2\eta^2\text{-}H_3BP^tBu_2H)][BAr^F{}_4]$ and $[Rh(P^tBu_2H)_2(\eta^2\eta^2\text{-}H_3B{\cdot}P^tBu_2PBH_2{\cdot}P^tBu_2H)][BAr^F{}_4]$,[3] but the Rh(III) P–H activated mode is favoured in $[RhH(dppp)(\sigma,\eta^2\eta^2\text{-}PPh_2{\cdot}BH_2PPh_2{\cdot}BH_3)][BAr^F{}_4]$[5] and $[RhH(dppp)(\sigma,\eta^2\eta^2\text{-}PCyH{\cdot}BH_2PCyH{\cdot}BH_3)][BAr^F{}_4]$.[6] To date, there has not been any report of larger oligomers bound to the catalyst in the dehydropolymerisation of $H_3B{\cdot}PPhH_2$.

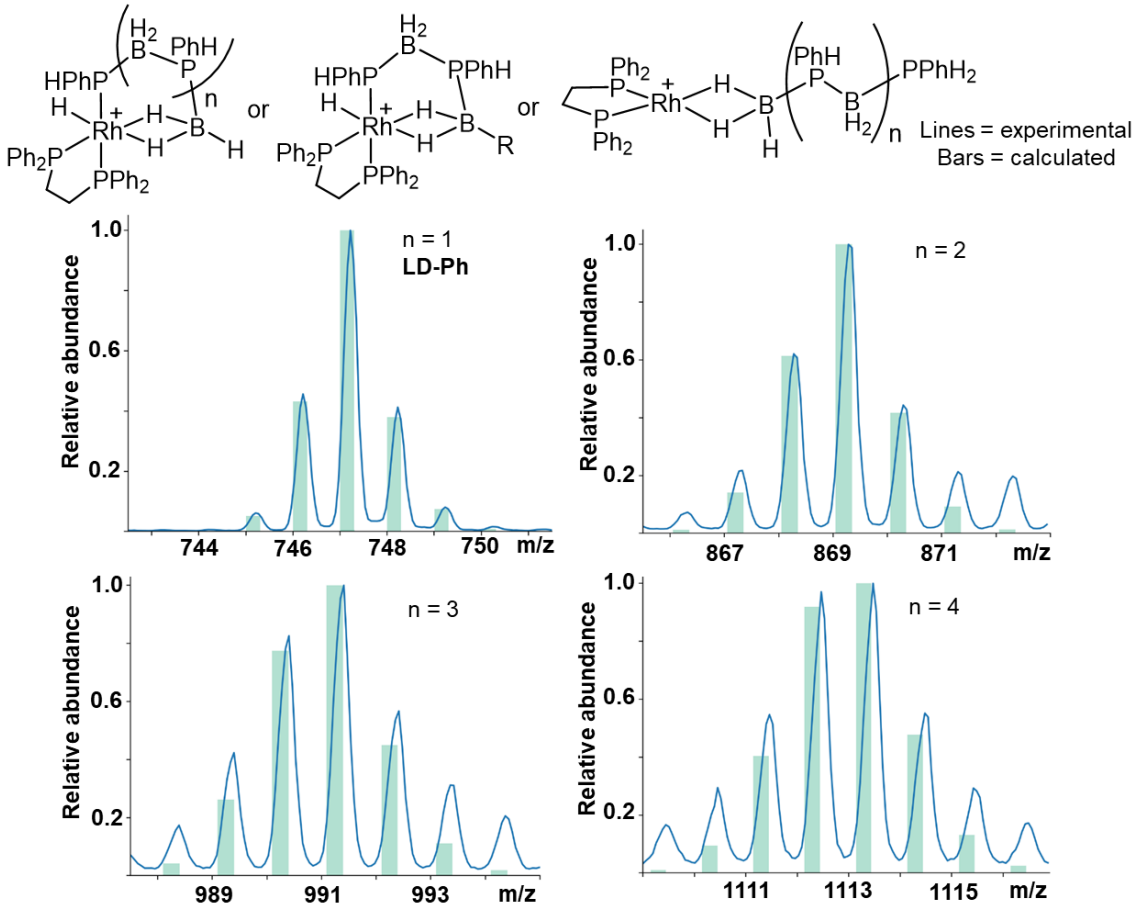

Figure 4.30. ESI mass spectrum using a Waters Acquity Triple Quadrupole Detector, of the reaction mixture of the reaction mixture of **4.3** with a mixture of $H_3B{\cdot}PPhH_2$, **LD-Ph** and oligomeric $[H_2BPPhH]_n$ in 1,2-$F_2C_6H_4$.

4.9 Proposed mechanism for primary phosphine-borane dehydropolymerisation

With some insight into the catalyst speciation in hand, a mechanism for the dehydropolymerisation of $H_3B{\cdot}PPhH_2$ is proposed (Scheme 4.12). This mechanism is based upon earlier studies by Huertos and Weller on the dehydrocoupling of $H_3B{\cdot}PPh_2H$,[3, 5, 6] and the dehydropolymerisation of $H_3B{\cdot}PPhH_2$ using $[RhCp^*Me(PMe_3)(CH_2Cl_2)][BAr^F{}_4]$ (**i-59**) as a precatalyst.[7] Overall, the $[Rh(dppe)]^+$ framework mediates a dehydrocoupling process between a terminal BH_3 group on a monomer/oligomer/polymer and a terminal $PPhH_2$ group on a different monomer/oligomer/polymer with the concurrent loss of H_2. Initially, dppe is irreversibly displaced by $H_3B{\cdot}PPhH_2$ to form a sigma-borane complex **4.4. 4.4** is not observed in the in-situ experiments, but $(H_3B)_2$dppe is, and similar sigma phosphine-borane complexes, such as $[Rh(P^tBu_2H)_2(\eta^2\eta^2\text{-}H_3B{\cdot}P^tBu_2H][BAr^F{}_4]$ (**i-38**)[3] and $[Rh(dppp)(\eta^2\eta^2\text{-}H_3B{\cdot}PAd_2H][BAr^F{}_4]$ (**i-39**)[5] are known.

Free dppe is trapped by a $BH_{3(s)}$ group to form $(H_3B)_2$dppe, as observed by $^{31}P\{^1H\}$ NMR and thus does not coordinate back onto the Rh. BH_3 is derived from dissociation of $H_3B{\cdot}PPhH_2$, which is consistent with the free PhH_2 observed in the in-situ ^1H NMR spectrum. P–B bond dissociation has been reported previously in the dehydrocoupling of $H_3B{\cdot}P^tBu_2H$[3] and the dehydrocoupling of $H_3B{\cdot}PPh_2H$[36] using rhodium catalysts.

Another molecule of $H_3B{\cdot}PPhH_2$ undergoes P–H activation at the terminal phosphorus, to form complex **4.5**, which contains a β-B–H agostic phosphido-borane and a η^1-$H_3B{\cdot}PPhH_2$ ligand. Analogous complexes with secondary phosphine-boranes have been isolated by Huertos, such as: $[RhH(dppp)(\sigma,\eta\text{-}PPh_2BH_3)(\eta^1\text{-}H_3B{\cdot}PPh_2H)][BAr^F{}_4]$.[5] Phosphido-boranes have also been show as key intermediates in the dehydropolymerisation of $H_3B{\cdot}PPhH_2$ using $[Cp^*Rh(Me)(PMe_3)(CH_2Cl_2)][BAr^F{}_4]$ (**i-59**).[37]

Subsequent B–H activation, most likely via a sigma-CAM type mechanism[38] to avoid a Rh(V) intermediate, produces a dihydrogen ligand. Dissociation of the B–H agostic group forms a five-coordinate Rh(III) complex (**4.6**). Reductive coupling from five-coordinate organometallic complexes is well known,[39, 40] and results, in this case, with the formation of a new P–B bond and contemporaneous loss of H_2. Dissolved H_2 is observed in the ^1H NMR spectrum (δ 4.48). The new, longer, phosphinoborane unit then binds to the Rh(I) centre via a sigma borane motif weakly by the terminal BH_3, or more likely in Rh(III) P–H activated form. The fact that hydride signals relating to a Rh(III) P–H activated complex are observed during catalysis and were supported by the independent synthesis of $[RhH(dpp)(\sigma,\eta^2\eta^2\text{-}PPhH{\cdot}BH_2PPhH{\cdot}BH_3)][Cl]$ (**4.2**) suggests that the equilibrium favours the Rh(III) complex and this is the catalyst resting state. This implies that the turnover limiting step is likely the step proceeding formation of the Rh(III) P–H activated complex that gets the catalyst back onto the cycle, i.e. **4.2** to **4.4**. This would be a fist order process in terms of $H_3B{\cdot}PPhH_2$, which was observed during the in-situ ^1H NMR studies and good evidence for an off-cycle equilibrium.

It is not only $H_3B{\cdot}PPhH_2$ that could displace the oligomer in complex **4.7**. Any monomer, oligomer or polymer could coordinate reversibly via a sigma borane complex with the terminal BH_3, and then undergo a dehydrocoupling process via the same mechanism, with any other monomer, oligomer or polymer. This is called a reversible chain transfer mechanism.[41] Sigma complexes have been

reported as key intermediates in the dehydropolymerisation of $H_3B{\cdot}NH_3$[42] and the dehydrocoupling of $H_3B{\cdot}NMeH_2$ using $\{Ir(PCy_3)_2(H)_2\}^+$ as a catalyst.[43]

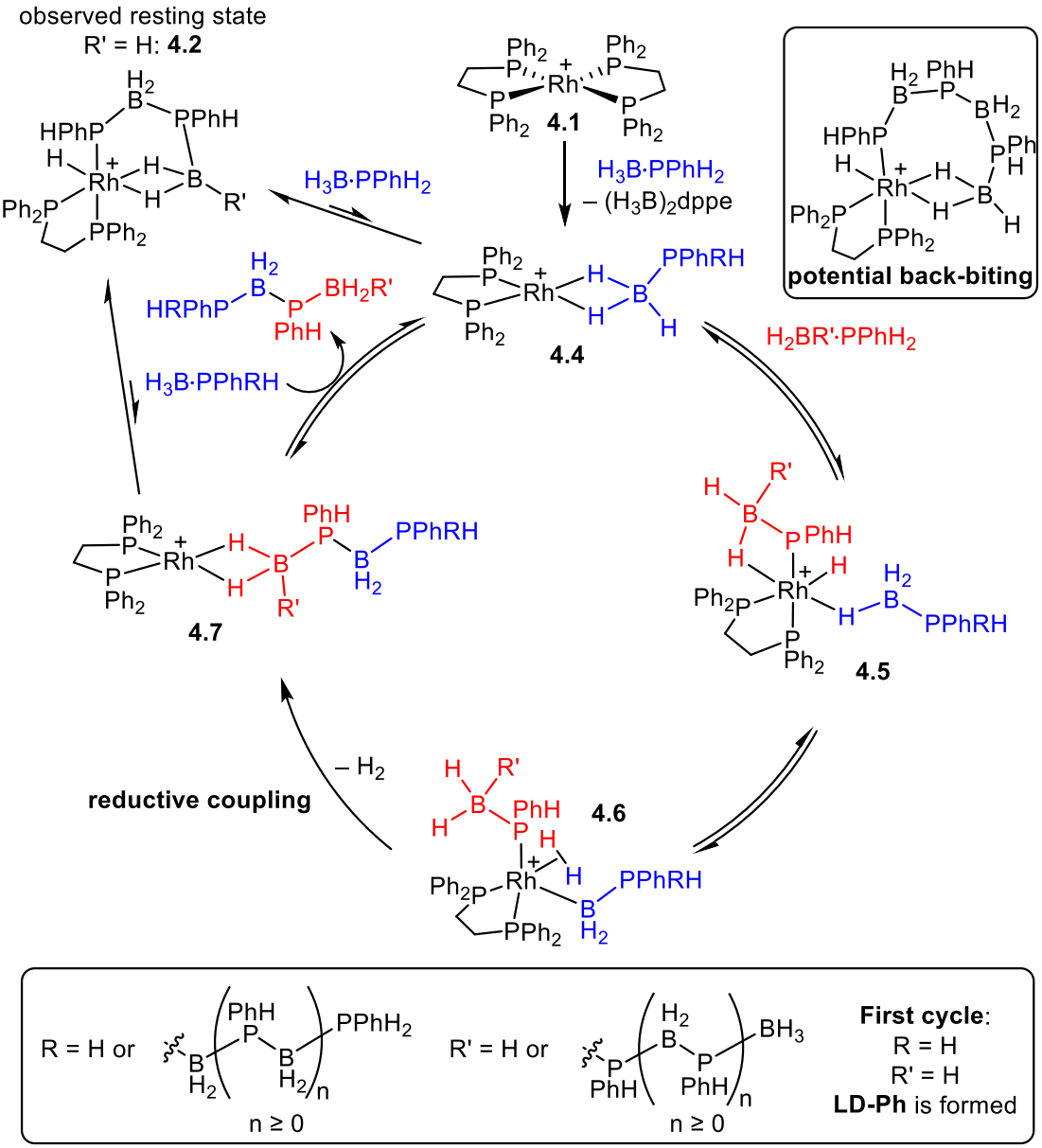

Scheme 4.12. Proposed mechanism for the $[Rh(dppe)]^+$ catalysed dehydropolymerisation of $H_3B{\cdot}PPhH_2$. Cl^- anions omitted for clarity.

Cyclic species, such as $[H_2BPPhH]_3$ and $[H_2BPPhH]_4$ can form via a back-biting reaction in this mechanism (see inset of Scheme 4.12). Cyclic species are commonly observed during the dehydropolymerisation primary phosphine-boranes,[8, 14] and six and eight-membered rings have been isolated for the secondary phosphine-boranes, such as: cyclic $[H_2BPArH]_3$ and $[H_2BPArH]_4$ (Ar = 4-CF_3-

C_6H_4).[44] The linear dimer, however, does not form the energetically unfavourable four-membered ring, and six and eight membered rings are likely to be the optimum size.

It is suggested that this mechanism is applicable to other phosphine-boranes, as similar polymer chain growth characteristics are observed with $H_3B{\cdot}PAr'H_2$ [Ar' = 3,5-$(CF_3)_2C_6H_3$]. Further evidence on alkyl-phosphine-borane dehydropolymerisation is provided in section 4.11. Several observations made thus far in this investigation support the proposed mechanism: 1) The proposed observed catalyst resting state, **4.2**, is the primary analogue to that reported by Huertos; [RhH(dppp)(σ,$\eta^2\eta^2$-$PPh_2{\cdot}BH_2PPh_2{\cdot}BH_3$)][$BAr^F_4$] during the dehydrocoupling of $H_3B{\cdot}PPhH_2$, for which the mechanism was studied in great detail and is very similar to that in Scheme 4.12.[5] 2) Linear dimer (**LD-Ph**) formation occurs at the early stages of the reaction, and is then consumed gradually, alongside monomer H_3BPPhH_2, which is consistent with monomer units coupling together to form dimer at the start of the reaction. Larger, more sterically encumbering phosphineboranes coordinate less favourably and subsequently longer chains are not observed earlier in the reaction by GPC analysis (see the molecular weight vs conversion experiment in section 4.4). Moreover, statistically there will also be a higher chance that a smaller phosphine-boranes such as monomer or dimer, which are in higher concentration at the start, will coordinate to the rhodium. 3) The step-growth trend in the molecular weight versus conversion investigations is consistent with this mechanism. Some of the defining features of step-growth polymerisation are the retention of the functional group at the chain terminus, and any size units can combine.[20] In a step-growth mechanism, a single reaction is responsible for all steps contributing to polymer formation (i.e. no initiation, propagation etc.).[45] 4) Faster monomer conversion at the start compared to later in the reaction, and a decreasing polydispersity with conversion, are also features of a step-growth mechanism.[21]

4.10 Experiments that support a reversible chain transfer mechanism

To support the proposed reversible chain transfer mechanism, that can in theory, dehydrocouple monomers, oligomers and polymers of varying size, three further experiments were conducted that combine $[H_2BPPhH]_n$ of varying size.

Oligomeric $[H_2BPPhH_2]_n$ was formed via the dehydropolymerisation of $H_3B{\cdot}PPhH_2$ with **4.1** and a 45-minute reaction time. The resultant polymer, of M_n = 6,000 g mol^{-1} and Đ = 2.8 (approximate

absolute M_n of 590 g mol^{-1} with a degree of polymerisation of five repeat units via calibration with MALS data, Figure 4.4), was isolated by precipitation into hexanes and then dissolved in toluene. To this mixture, precatalyst **4.1** was added (Scheme 4.13). The mixture was heated to 100 °C for 19 hours which resulted in the formation of polymer with substantially higher molecular weight and a narrower polydispersity, as determined by GPC analysis of the isolated polymer: M_n = 49,000 g mol^{-1} and Đ = 1.5 (Figure 4.31). By MALS direct detection, the M_n is calculated to be 16,500 g mol^{-1} (Đ = 1.4) which equates to a degree of polymerisation of 135. Free $PhPH_2$ (δ –123.8) and $(H_3B)_2$dppe (δ 18.7) are also observed in the $^{31}P\{^1H\}$ NMR spectrum, and H_2(dissolved) (δ 4.55) is observed in the ^1H NMR spectrum of the reaction mixture after 19 hours.

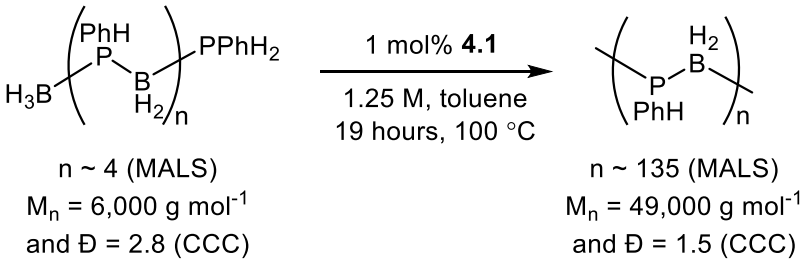

Scheme 4.13. Dehydropolymerisation of oligomeric $H_3B{\cdot}PPhH_2$, using **4.1** as a precatalyst.

The GPC trace (Scheme 4.13) shows that some shorter molecular weight material is still observed after the 19 hour reaction (Figure 4.31). This could be cyclic material[12] which cannot increase in weight as there are no terminal groups for dehydrocoupling.

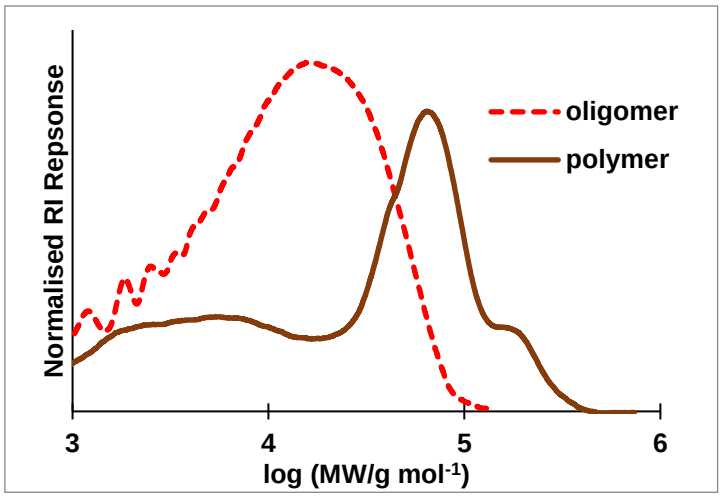

Figure 4.31. GPC analysis of the starting oligomeric $[H_2BPPhH]_n$ (n~5 by MALS) and polymeric $[H_2BPPhH]_n$ formed from the dehydrocoupling of the oligomer using **4.1** as a precatalyst.

In a second reaction, monomer $H_3B{\cdot}PPhH_2$ was added to polymeric $[H_2BPPhH]_n$ (15 mg, M_n = 54,500 g mol^{-1} and Đ = 1.5), using catalyst **4.1** (1 mol%) and toluene solvent (1.25 M relative to $H_3B{\cdot}PPhH_2$) in a sealed NMR tube. The reaction was heated to 100 °C and left for 44 hours as not all of the $H_3B{\cdot}PPhH_2$ had reacted after this time (Scheme 4.14).

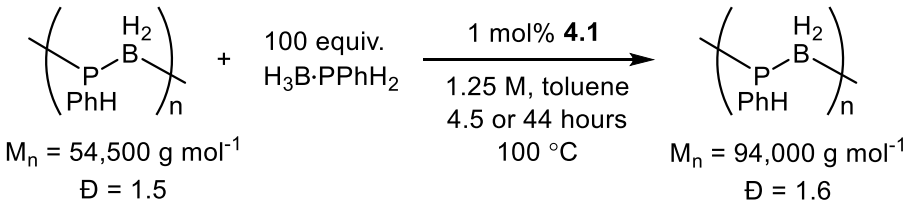

Scheme 4.14. Preparation of longer molecular weight $[H_2BPPhH]_n$ from the dehydropolymerisation of $H_3B{\cdot}PPhH_2$ and shorter $[H_2BPPhH]_n$.

The initial ratio of the ^{11}B and ^{31}P and signals are 2:1 monomer:polymer and the degree of polymerisation of the starting polymer is 160 (by MALS), therefore the molar ratio of monomer:polymer is roughly 320:1. The isolated polymer from the reaction left for 44 hours at 100 °C, was shown to be bimodal by GPC. The total molecular weight including both distributions measured as M_n = 94,000 g mol^{-1} and Đ = 1.6 (Figure 4.32), clearly much longer than the original polymer. The lower molecular weight component is measured as Mn = 81,000 g mol^{-1} and the higher molecular weight component measures as M_n of 240,000 g mol^{-1}. In comparison, the dehydropolymerisation of $H_3B{\cdot}PPhH_2$ under the same catalytic conditions produced polymer of M_n = 54,500 g mol^{-1} (Đ = 1.5). Therefore, the dehydrocoupling of monomer and polymer has occurred to ultimately form polymer of longer molecular weight than monomer alone.

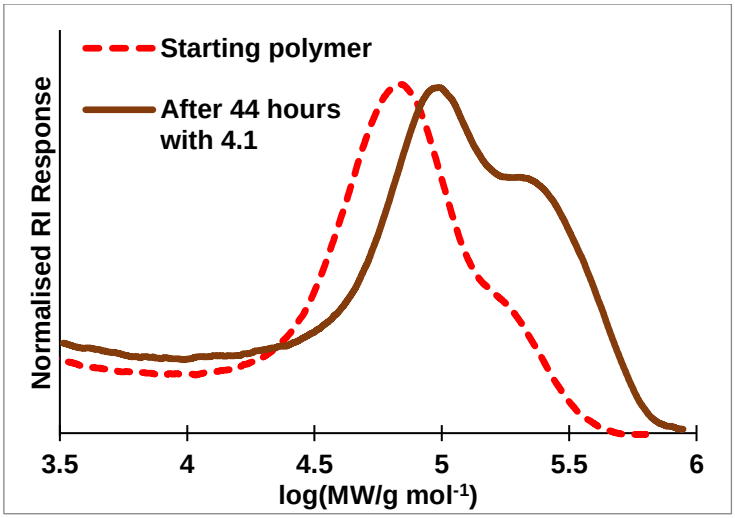

Figure 4.32. GPC analysis of the resultant polymer from the dehydropolymerisation of $H_3B{\cdot}PPhH_2$ and polymeric $[H_2BPPhH]_n$ using **4.1** as a precatalyst.

Finally, two samples of high molecular weight $[H_2BPPhH]_n$ of different molecular weights (M_n = 54,500 g mol^{-1}, Đ = 1.5 and M_n = 30,000 g mol^{-1}, Đ = 1.6) were combined in an NMR tube with **4.1** and toluene solvent and heated to 100 °C for 44 hours (Scheme 4.15).

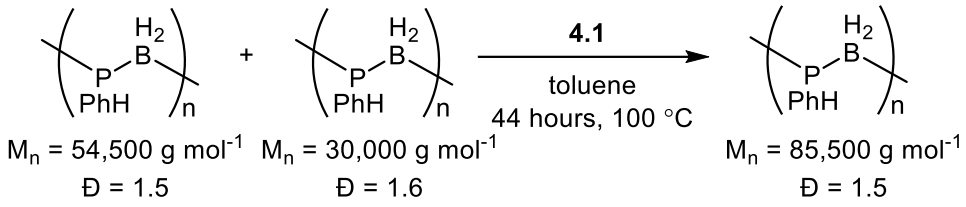

Scheme 4.15. Dehydrocoupling of polymeric $[H_2BPPhH]_n$ to form polymer of higher molecular weight.

The resultant polymer was measured to be of higher weight than the two original polymers, with the overall average of M_n = 85,500 g mol^{-1} and Đ = 1.5 (Figure 4.33). Once again, the final polymer has a bimodal distribution. The lower molecular weight portion is roughly M_n = 61,000 g mol^{-1} and Đ = 1.2, and the higher molecular weight polymer is M_n = 236,000 g mol^{-1} and Đ = 1.2. The smaller polymer of M_n = 61,000 g mol^{-1} could be the combination of two initial polymers, i.e. 30,000 + 30,000 g mol^{-1}, and the larger polymer is then the product of dehydrocoupling of higher molecular weight polymers, bearing in mind the distribution of the polymer chain sizes. The polymer chains are combining to form polymer of higher molecular weight at a much slower rate than smaller units (monomer/dimer) dehydrocouple under the same conditions. This is due to three reasons: 1) There is a smaller proportion of the polymer

chain end groups at higher molecular weight and therefore statistically less likely to coordinate to the rhodium.[24] 2) The polymer chains are bulkier than the smaller units, therefore, rhodium coordination and the dehydrocoupling process is likely to be a higher energy process. 3) There are less of the polymer chains relative to the catalyst concentration. This reaction was repeated without any catalyst and there was no evidence of polymer chains combining, and a bimodal distribution of the two original polymers was observed.

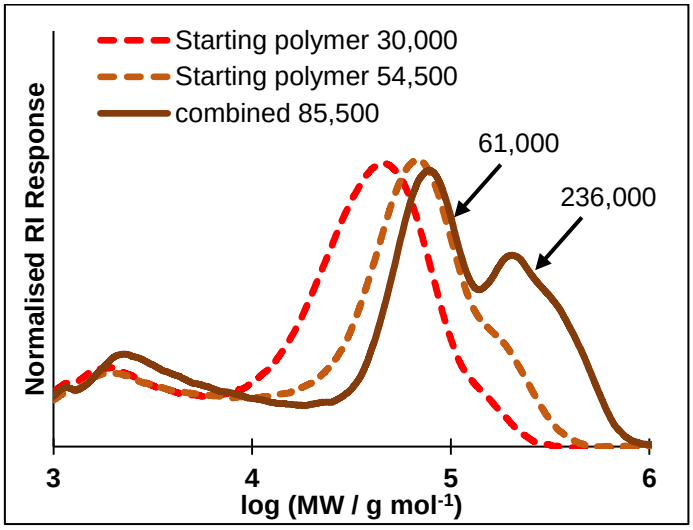

Figure 4.33. GPC analysis of the resultant polymer from the dehydrocoupling of polymeric $H_3B{\cdot}PPhH_2$ to form polymer of higher molecular weight using **4.1** as a precatalyst. Units of the quoted molecular weights are measured in g mol^{-1}.

Within these three experiments it has been shown that using **4.1** as a precatalyst in toluene solvent at 100 °C the dehydrocoupling of the following occurs: 1) short chain oligomers, 2) monomer and polymer, and 3) long chain polymers. This is good evidence for the reversible chain transfer mechanism proposed in section 4.9.

4.11 Dehydropolymerisation of $H_3B{\cdot}P^nHexH_2$

To assess the generality of the $[Rh(dppe)]^+$ dehydrocoupling system, a primary alkyl phosphine-borane, $H_3B{\cdot}P^nHexH_2$ was tested with the same catalytic conditions as the aryl phosphine-boranes detailed above (Scheme 4.16).

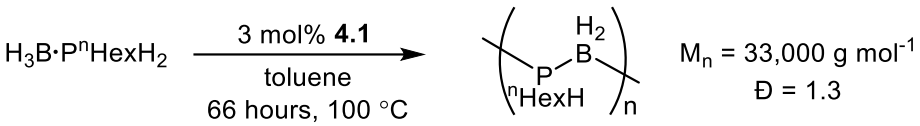

Scheme 4.16. Dehydropolymerisation of $H_3B{\cdot}P^nHexH_2$ using **4.1** as a precatalyst.

At 1 mol% catalyst loading of precatalyst **4.1** at 1.25 M $H_3B{\cdot}P^nHexH_2$ in toluene, unreacted monomer was still observed after 96 hours, alongside a complex array of cyclic, oligomeric and polymeric material by $^{31}P\{^1H\}$ NMR spectroscopy. In comparison to the dehydropolymerisation of $H_3B{\cdot}PPhH_2$ which was completed reacted after 19 hours under the same conditions and only 10% of the products were cyclics, $H_3B{\cdot}P^nHexH_2$ thus reacts much more slowly and less cleanly. Alkyl phosphine-boranes are known to dehydropolymerise more slowly than aryl equivalents due to the electron-donating effects of the alkyl group which deactivates the P–H bond in the alkyl derivatives.[6, 28] This is also consistent with the observation that the more electron-withdrawing monomer, $H_3B{\cdot}PAr'H_2$ [Ar' = 3,5-$(CF_3)_2C_6H_3$], reacted to completion after just four hours, faster than $H_3B{\cdot}PPhH_2$ (19 hours) and much faster than $H_3B{\cdot}P^nHexH_2$ (not finished after 96 hours). This is also reflected in other catalyst systems, such as $[Cp(CO)_2FeOTf]$, which required 100 hours at 100 °C for complete conversion of $H_3B{\cdot}P^nHexH_2$[28] but only 24 hours was needed for $H_3B{\cdot}PPhH_2$.[13] When an increased catalyst loading of 3 mol% **4.1** was used with $H_3B{\cdot}P^nHexH_2$, however, full conversion of $H_3B{\cdot}P^nHexH_2$ was observed after 66 hours at 100 °C, by $^{31}P\{^1H\}$ and ^{11}B NMR spectroscopy. In the in-situ $^{31}P\{^1H\}$ NMR spectrum after 66 hours, free P^nHexH_2 (δ –138.2), $(H_3B)_2$dppe (δ 18) and polymeric $[H_2BP^nHexH]_n$ are observed (Figure 4.34). As $[H_2BP^nHexH]_n$ is soluble in hexane, purification via precipitation into hexane was not possible, instead the polymer was partially purified by passage through Celite® and Fluorosil® plugs using CH_2Cl_2 as the eluent, although the $(H_3B)_2$dppe was not removed via this method. A moderate yield of 51% of the resulting impure polymeric $[H_2BP^nHexH]_n$ was obtained. A broad ^{11}B signal centred at δ –35 in the ^{11}B NMR spectrum and signals corresponding to P–H [doublet at δ 3.8, *J*(PH) = 335 Hz] and broad ^{n}hexyl and BH_2 moieties in the ^1H NMR spectrum match well with the reported literature values.[28, 46] Unlike the literature precedent, in which multiple tactic environments are observed for $[H_2BP^nHexH]_n$ in the $^{31}P\{^1H\}$ NMR spectrum, only one broad ^{31}P signal is observed in this instance, even with ^1H coupling. While this could indicate the selective formation of an isotactic polymer this is not definitive. Similar observations have been reported before in the synthesis of $[H_2BP^tBuH]_n$, for which three tactic environments were

observed via a non-catalytic Lewis base stabilised route,[23] but only one ^{31}P environment was observed when $[Cp(CO)_2Fe(OTf)]$ was used as a catalyst.[28]

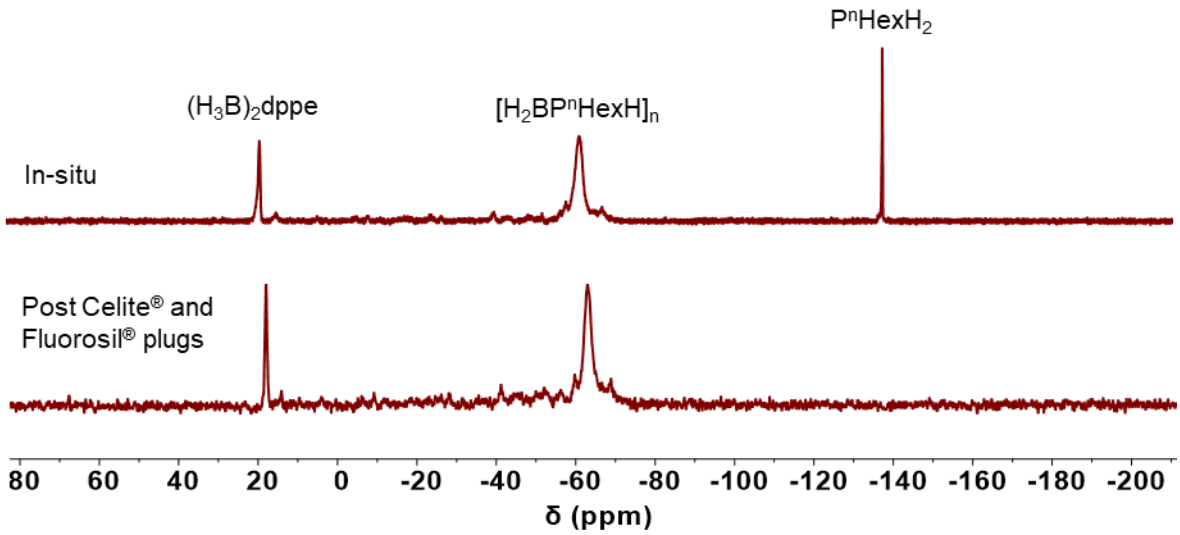

Figure 4.34. In-situ $^{31}P\{^1H\}$ NMR spectrum of the dehydropolymerisation of $H_3B{\cdot}P^nHexH_2$ after 66 hours at 100 °C with 3 mol% **4.1** (top, toluene) and the mixture post purification (bottom, $CDCl_3$) (243 MHz, 298 K).

GPC analysis confirmed that polymeric $[H_2BP^nHexH]_n$ had formed, with M_n of 33,000 g mol^{-1} and a polydispersity of 1.3 (Figure 4.35). This is slightly shorter than that reported for the Fe-catalyst, $[Cp(CO)_2FeOTf]$ which was M_n = 57,200 g mol^{-1} and Đ = 1.3,[28] but larger than when $[Rh(COD)(Cl)]_2$ was used: M_n = 8,800 g mol^{-1} and Đ = 2.2.[46] Similar to the synthesis of the phenyl equivalent $[H_2BPPhH]_n$, some lower molecular weight polymer is observed with M_n of 2,500 g mol^{-1} and Đ = 1.3, which could be cyclic species.[12]

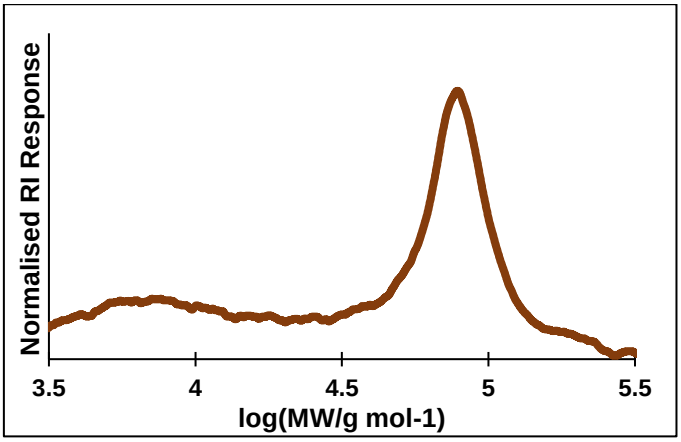

Figure 4.35. GPC trace of polymer $[H_2BP^nHexH]_n$.

4.12 Formation of block copolymer poly(phenylphosphinoborane)-*b*-poly(n-hexylphosphinoborane), BCP-Ph/^{n}Hex

4.12.1 Synthesis and characterisation

The reversible chain transfer mechanism proposed for the dehydropolymerisation of primary phosphine-boranes using a $[Rh(dppe)]^{+}$ catalyst allows for the coupling of different monomer/oligomer/polymer units as demonstrated in section 4.9. To further test and exploit this mechanism, the coupling of polymers with different R groups could be combined to form a copolymer. Copolymers exhibit different materials properties to the constituent homopolymers.[19, 20] An example of this on a global scale is that most polystyrene products are not made from pure homopolymer, as this is brittle and has low solvent resistance. Instead, 1,3-butadiene is copolymerised with styrene to form a copolymer with much higher elasticity.[18] Copolymers can be formed in a random arrangement of monomer units, i.e. a random copolymer, or they can be assembled into distinct blocks, i.e. an AB block copolymer (Figure 4.36). The notation for an AB block copolymer of blocks A and B is A_x-*b*-B_y, with the degree of polymerisation of each block as the subscripts x and y.

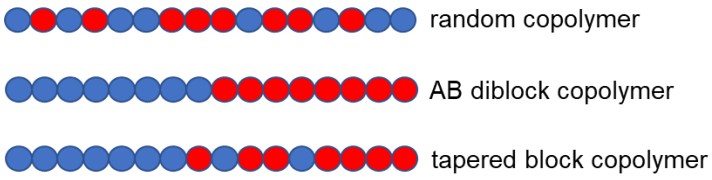

Figure 4.36. Examples of copolymer composition.

With three different primary phosphine-boranes that undergo dehydropolymerisation in hand: $H_3B{\cdot}PRH_2$, R = Ph, 3,5-$(CF_3)_2C_6H_3$ and ^{n}Hex, the formation of copolymer containing different R groups was investigated. More is known about the formation of poly(phenylphosphinoborane) from the studies in this chapter and it is also the easiest to prepare monomer. $[H_2BPPhH]_n$ and $[H_2BPAr'H]_n$ (Ar' = 3,5-$(CF_3)_2C_6H_3$) have very similar ^{1}H and ^{31}P chemical shifts, which would make determining the incorporation of both monomers into the polymer difficult (Table 4.4). Moreover, $[H_2BPPhH]_n$ and $[H_2BPAr'H]_n$ have similar solubilities as both are isolated by precipitation in hexane which is not useful for aggregation in solution[47] (*vide infra*). $[H_2BP^{n}HexH]_n$, however, exhibits ^{1}H signals in the alkyl region

of the ^{1}H NMR spectrum which will make assignment of a block copolymer easier via ^{1}H NMR experiments such as DOSY (Diffusion Ordered NMR Spectroscopy), and $[H_2BP^nHexH]_n$ is soluble in hexane, which will aid in copolymer purification. In light of this, the preparation and analysis of a block copolymer comprising phenyl and n-hexyl phosphinoboranes, namely, poly(phenylphosphinoborane)-*b*-poly(n-hexylphosphinoborane) **BCP-Ph/^{n}Hex** was explored.

Table 4.4. The different poly(phosphinoboranes) prepared in this Chapter and their NMR and solubility properties.

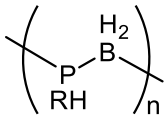	**Ph**	**3,5-$(CF_3)_2C_6H_3$**	**^{n}Hex**
δ(^{1}H) R	7.2-6.7	7.8-7.2	1.7-0.7
δ(^{31}P)	–49.5	–49.6	–63.2
Solubility in hexane	insoluble	insoluble	soluble

Firstly, the two different monomers, $H_3B{\cdot}PPhH_2$ and $H_3B{\cdot}P^nHexH_2$ were combined in a 1:1 ratio and 1 mol% **4.1** was added with toluene (1.25 M, Scheme 4.17). The reaction was monitored by in-situ $^{31}P\{^{1}H\}$ NMR (Figure 4.37). $H_3B{\cdot}P^nHexH_2$ reacts much slower than $H_3B{\cdot}PPhH_2$ as observed in the earlier experiments in the synthesis of the homopolymers $[H_2BPPhH]_n$ and $[H_2BP^nHexH]_n$. All of the $H_3B{\cdot}PPhH_2$, but only 50% of $H_3B{\cdot}P^nHexH_2$ had reacted after 18 hours at 100 °C. An ill-defined mixture of cyclic and polymeric species were produced via this method which could not be separated.

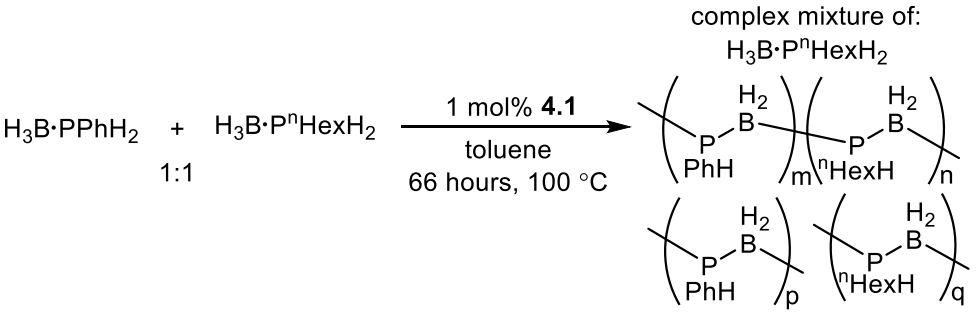

Scheme 4.17. Attempted synthesis of copolymer poly{phenyl(phosphinoborane)-*co*-n-hexyl(phosphinoborane)}, **BCP-Ph/^{n}Hex**.

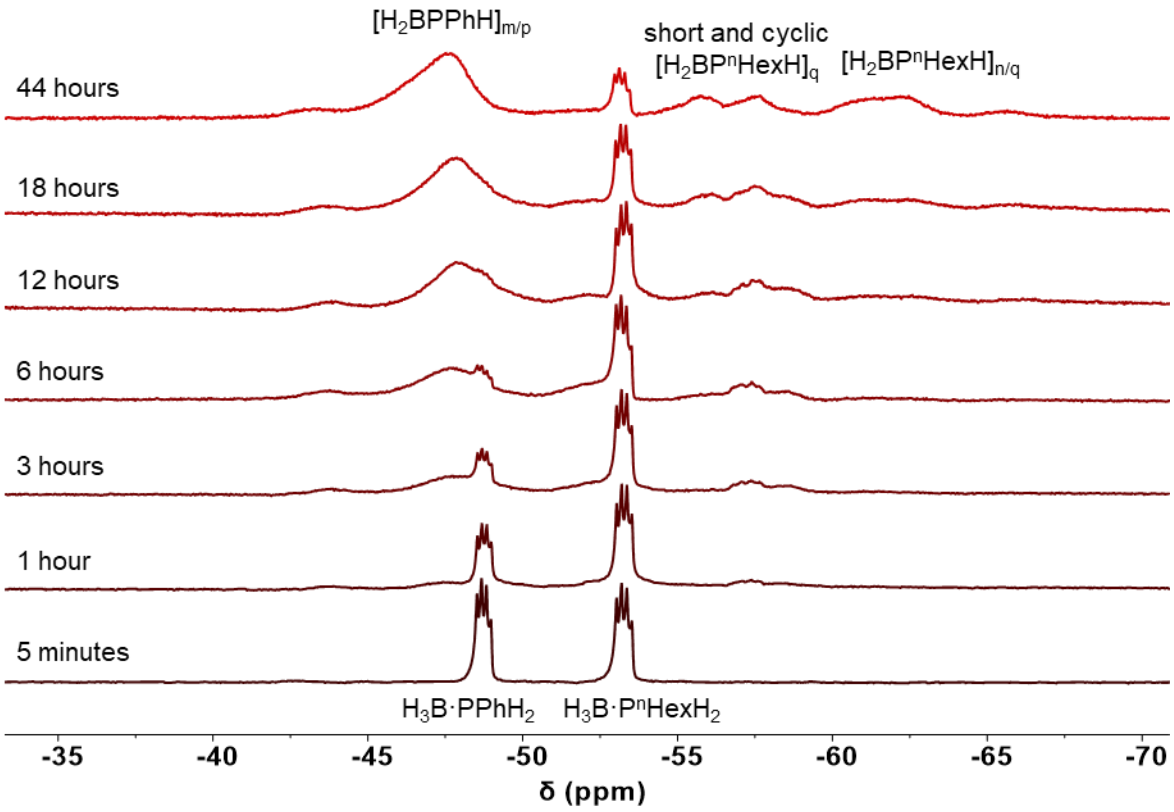

Figure 4.37. In-situ $^{31}P\{^{1}H\}$ NMR of the copolymerisation attempt of $H_3B{\cdot}PPhH_2$ and $H_3B{\cdot}P^nHexH_2$ in a 1:1 mixture with 1 mol% **4.1** (202 MHz, d_8-toluene, 373 K).

A purer copolymer was isolated via the addition of $H_3B{\cdot}P^nHexH_2$ (1.25 M) to preformed polymeric $[H_2BPPhH]_n$ (M_n = 26,500 g mol^{-1}, Đ = 1.5) and **4.1** in toluene solvent (Scheme 4.18). A higher catalyst loading of 3 mol% was used and a reaction time of 66 hour as we have previously shown this led to complete conversion of $H_3B{\cdot}P^nHexH_2$ in the formation of homopolymer $[H_2BP^nHexH]_n$.

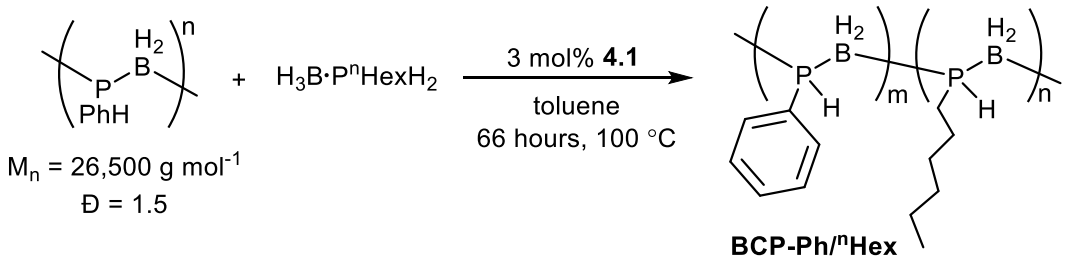

Scheme 4.18. Synthesis of copolymer **BCP-Ph/^{n}Hex** via the dehydrocoupling of $[H_2BPPhH]_n$ and $H_3B{\cdot}P^nHexH_2$ using **4.1** as a precatalyst.

After 66 hours at 100 °C, the mixture was analysed by in-situ NMR spectroscopy. Signals corresponding to $[H_2BPPhH]_m$ and $[H_2BP^nHexH]_n$ are both observed, alongside unreacted $H_3B{\cdot}P^nHexH_2$ and a mixture of oligomeric and short chain cyclic species.[12] Utilising the solubility differences of $[H_2BPPhH]_m$

(insoluble in hexane) and n-hexyl phosphinoboranes (all hexane soluble), the species containing only n-hexyl groups were extracted with hexane. Interestingly, in the hexane insoluble mixture, signals corresponding to polymeric $[H_2BP^nHexH]_n$ are still observed at δ –63 in the ^{31}P NMR spectrum. This is an initial indication that there is some phenyl(phosphinoborane) component in the n-hexyl polymer, i.e. a copolymer: poly{phenyl(phosphinoborane)-*co*-n-hexyl(phosphinoborane)} (**BCP-Ph/^{n}Hex**). Three overlapping but distinct ^{31}P signals are observed at δ –62.0, –63.4 and –64.6 in the ^{31}P NMR spectrum and assigned as the different tactic environments for the $[H_2BP^nHexH]_n$ component of the copolymer, and are very similar to those reported in the literature for the homopolymer $[H_2BP^nHexH]_n$ (Figure 4.38).[28, 46] A ^{31}P signal corresponding to $[H_2BPPhH]_n$ is also observed at δ –49.5 as a doublet, with a large ^1J(PH) of 350 Hz but no indication of multiple tactic environments. The ratio of these two signals is 3:1 Ph:^{n}Hex. A third signal at δ –54 is observed, with a broad apparent triplet line shape ^1J(PH) ~ 380 Hz, which simplifies to a broad singlet upon ^1H-decouplng. This signal integrates to 0.3 relative to $[H_2BP^nHexH]_n$. Upon closer inspection of the $^{31}P\{^1H\}$ NMR spectrum, a signal of similar intensity to the signal at δ –54 is observed slightly downfield of the $[H_2BPPhH]_m$ signal, at δ –48, which was not observed in the starting $[H_2BPPhH]_n$. These two smaller signals, at δ –48 and δ –54 could potentially be connecting units of phenylphosphinoborane and n-hexylphosphinoborane, as these will have a slightly different chemical shift. However, they could also reflect hexane insoluble cyclic species that cannot be removed from the polymer via washing in hexane. $(H_3B)_2$dppe is also removed via the hexane wash.

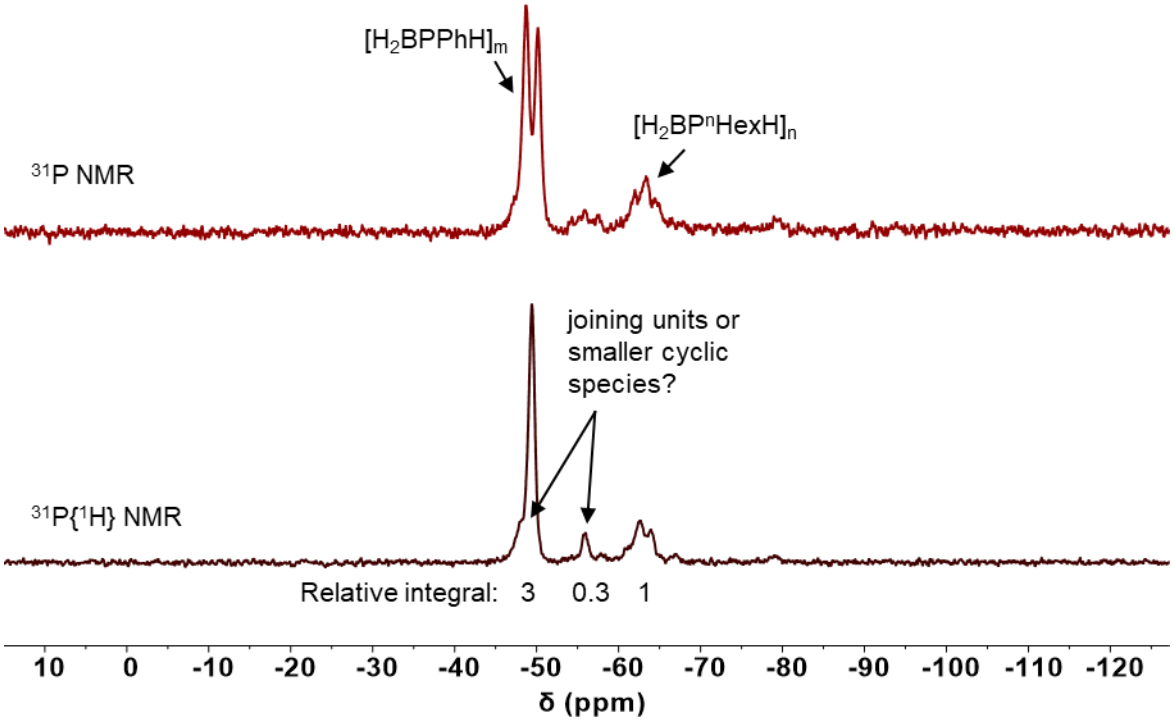

Figure 4.38. ^{31}P (top) and $^{31}P\{^{1}H\}$ (bottom) NMR spectra of **BCP-Ph/^{n}Hex** (243 MHz, $CDCl_3$, 298 K).

In the ^{1}H NMR spectrum of **BCP-Ph/^{n}Hex**, aromatic and P–H signals which match well with those for $[H_2BPPhH]_n$ are observed (Figure 4.39). For the n-hexyl component {i.e. $[H_2BP^{n}HexH]_n$}, CH_3 (δ 0.87) and CH_2 (δ 1.28 and 1.55) environments are observed, which overlap with the broad BH_2 signal. Only half of the P–H signal for $[H_2BP^{n}HexH]_n$ can be seen at δ 3.4, as the other half is coincident with the phenyl P–H signal, but the chemical shift of the observable peak matches well with the literature (the two peaks of the doublet are reported at δ 4.21 and 3.37)[28]. Application of ^{31}P-decoupling simplifies the P–H resonances to singlets and ^{11}B-decoupling results in sharpening of the BH_2 signals (Figure 4.39). The relative integral of the P–H signals is 3:1 again Ph:^{n}Hex consistent with the relative integrals in the ^{31}P NMR spectrum. The only observable ^{11}B signals are broad and overlapping and are centred at δ –35.1, which is the region for four coordinate ^{11}B in poly(phosphinoboranes).[9, 28]

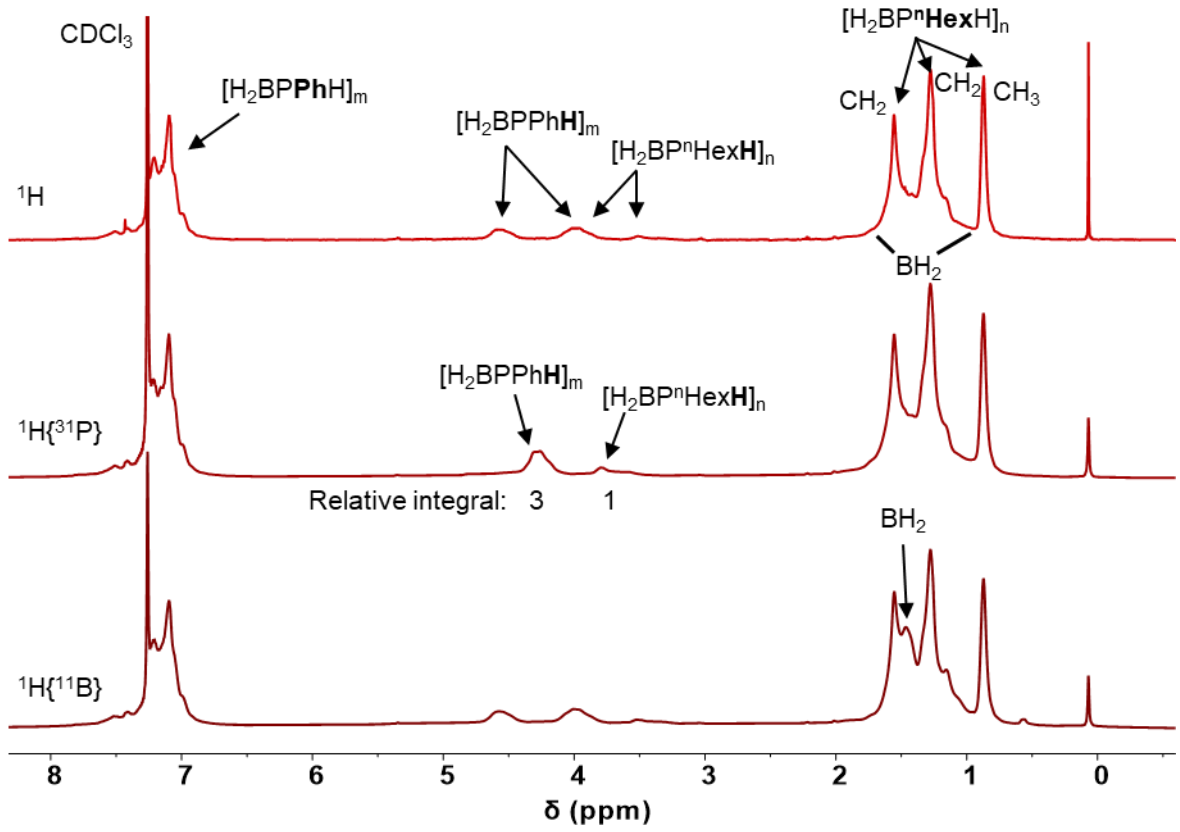

Figure 4.39. ^{1}H (top), $^{1}H\{^{31}P\}$ (middle) and $^{1}H\{^{11}B\}$ (bottom) NMR spectra of **BCP-Ph/^{n}Hex** (600 MHz, $CDCl_3$, 298 K).

Analysis of **BCP-Ph/^{n}Hex** by GPC revealed an increase in molecular weight from the initial polymer $[H_2BPPhH]_n$ (M_n = 26,500 g mol^{-1}, Đ = 1.5) to give a new material of M_n = 45,000 g mol^{-1}, with a narrower polydispersity of 1.3 (Figure 4.40). A small amount of lower molecular weight species with M_n = 3,000 and Đ = 1.7 is also observed in the GPC, which are likely to be cyclic species.[12] GPC analysis of a sample of using a MALS detector, which gives absolute molecular weight, gave an M_n value of 8,000 g mol^{-1} with a polydispersity of 1.1. Considering the block ratio of 3:1 Ph:^{n}Hex determined by NMR spectroscopy, this equates to an average polymer composition of $[H_2BPPhH]_{48}$-*b*-$[H_2BP^{n}HexH]_{16}$ for **BCP-Ph/^{n}Hex**. More evidence for a block copolymer is provided by dynamic light-scattering (DLS) and transmission electron microscopy (TEM) discussed later.

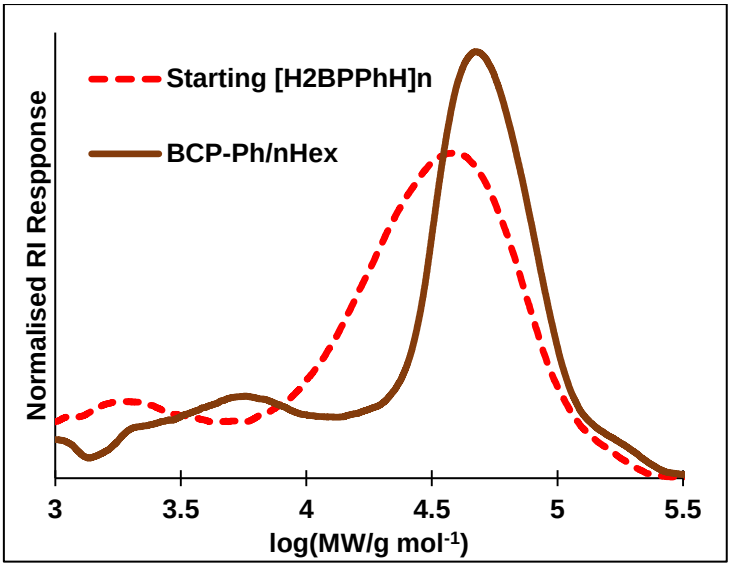

Figure 4.40. GPC trace of **BCP-Ph/^{n}Hex** (orange) and the starting polymer $[H_2BPPhH]_n$ the copolymer was formed from (brown).

The observation of both $[H_2BPPhH]_m$ and $[H_2BP^{n}HexH]_n$ within the sample of **BCP-Ph/^{n}Hex** after a hexane wash is good evidence that a copolymer has formed. However, 1D NMR alone does not confirm that both components are within the same polymer chain, and therefore ^{1}H DOSY NMR experiments were employed. Figure 4.41 shows the ^{1}H DOSY NMR spectrum of a sample of **BCP-Ph/^{n}Hex**. It is evident that the all of phenyl, P–H, BH_2 and n-hexyl signals diffuse at the same rate, at 2.00 ± 0.2 x 10^{-10} m^2/s. The $CDCl_3$ solvent signal diffuses much faster, and so does a signal at δ 1.58, which coincides with a CH_2 within $[H_2BP^{n}HexH]_n$. Moreover, there is also some stretching of the CH_3 signal (0.87) and it is therefore likely that there is some smaller cyclic species, which diffuse faster than the polymer, within the copolymer mixture and the unassigned ^{31}P signal could relate to these species. The fact that all of the $[H_2BPPhH]_m$ appears to be diffusing at the same rate is good evidence that there is no long chain $[H_2BPPhH]_n$ homopolymer present in the mixture.

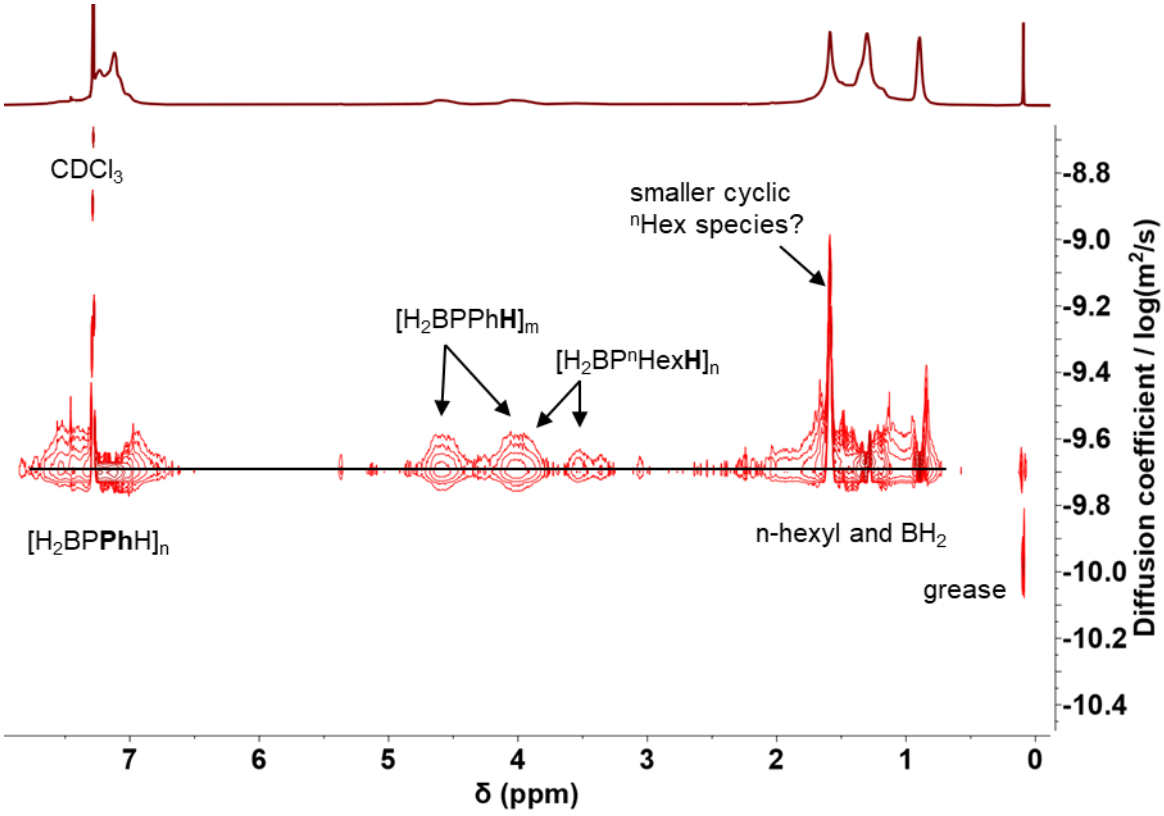

Figure 4.41. ^{1}H DOSY NMR of **BCP-Ph/^{n}Hex** (600 MHz, $CDCl_3$, 298 K).

For comparison with the copolymer sample of **BCP-Ph/^{n}Hex** (Figure 4.41), a sample containing a mixture of the two homopolymers, $[H_2BPPhH]_n$ and $[H_2BP^{n}HexH]_n$, was also analysed by ^{1}H DOSY NMR (Figure 4.42). Homopolymer samples of similar molecular weight to the copolymer {$[H_2BPPhH]_n$: M_n = 44,000 g mol^{-1}, Đ = 1.5, and $[H_2BP^{n}HexH]_n$: M_n = 33,000 g mol^{-1}, Đ = 1.3} were used for the closest comparison (**BCP-Ph/^{n}Hex**: M_n = 45,000 g mol^{-1}, Đ = 1.3). The phenyl and P–H signals of homopolmer $[H_2BPPhH]_n$ diffuse at 1.26 ± 0.3 x 10^{-10} m^2/s whereas the n-hexyl and P–H signals of homopolymer $[H_2BP^{n}HexH]_n$ diffuse at 3.16 ± 0.3 x 10^{-10} m^2/s. Interestingly, the diffusion rate of the copolymer **BCP-Ph/^{n}Hex** is roughly in the middle of the two homopolymers (2.00 ± 0.2 x 10^{-10} m^2/s). This is excellent evidence that $[H_2BPPhH]_m$ and $[H_2BP^{n}HexH]_n$ components are within the same copolymer. Quantitative ^{1}H DOSY NMR was conducted by Dr Alex Heyam at the University of York, on the same sample of **BCP-Ph/^{n}Hex**, and a hydrodynamic radius of less than 1 nm was calculated. This indicates a singular polymer chain, with no major aggregation or entangling of multiplet homopolymers.[48]

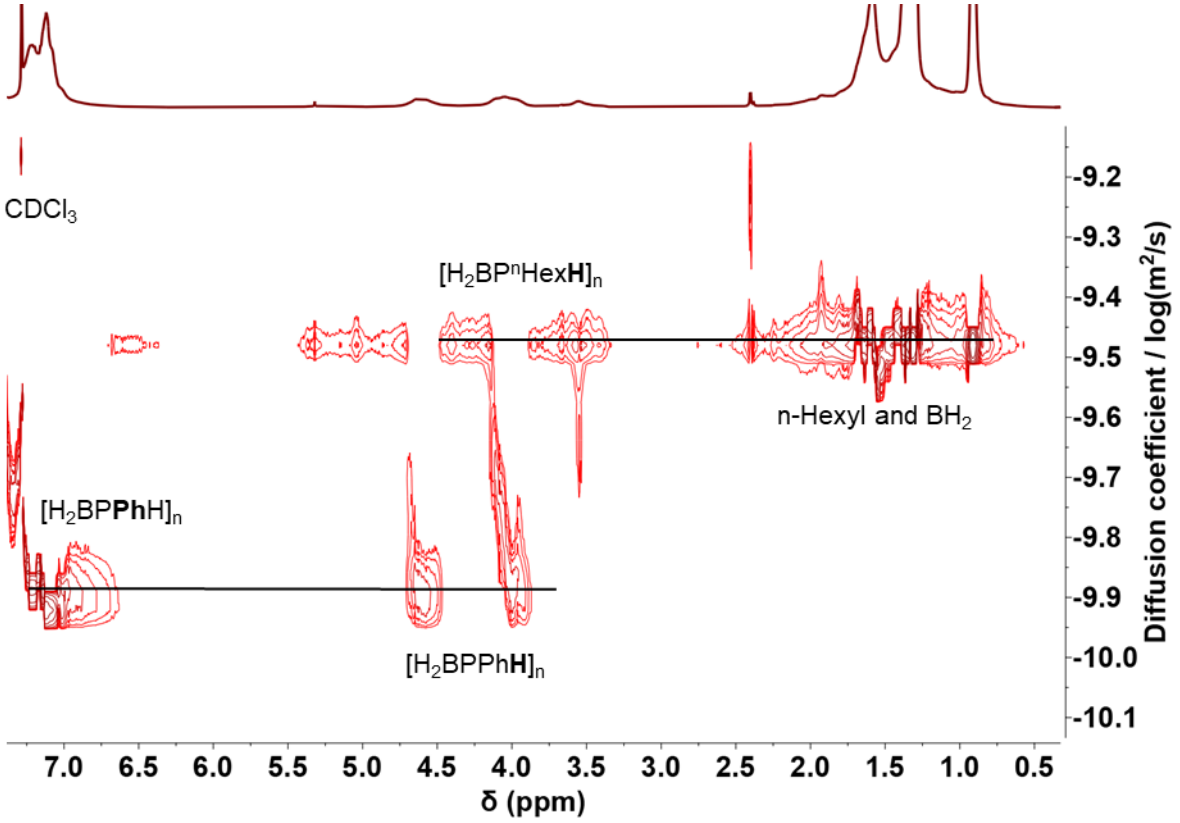

Figure 4.42. ^{1}H DOSY NMR of a mixture of $[H_2BPPhH]_n$ (M_n = 44,000 g mol^{-1}, Đ = 1.5) and $[H_2BPPhH]_n$ **(**M_n = 33,000 g mol^{-1}, Đ = 1.3) (600 MHz, $CDCl_3$, 298 K).

BCP-Ph/^{n}Hex was also analysed via ESI-MS in a 1 mg/ml THF solution (Figure 4.43). The repeating unit of 130.1 m/z is observed, which corresponds with the mass value of a $H_2BP^{n}HexH$ unit (calc. 130.1 m/z). Up to eight repeat units are observed, and two sets of repeat units start from 1225.6 and 1419.6 m/z. No mass differences corresponding to H_2BPPhH are seen in the spectrum (122.1 m/z). The mass values of m/z = 1225.6 and 1419.6 do not match those for any combination of pure n-hexyl oligomer {$[H_2BP^{n}HexH]_n$} and instead the closest mass value calculated was 1222.5 m/z, which corresponds to $[H_3BPPhH(H_2BPPhH)_8H_2BPPhH_3]^+$. The difference between 1225.6 and 1419.6 equates to H_2BPPhH + THF (194 m/z) and therefore, the second, smaller set of repeat units is likely representative of a THF adduct of the other. Therefore, it appears as if the only polymer that was detectable in this experiment was an AB diblock copolymer (Figure 4.36), namely, $[H_2BPPhH]_{10/11}$-*b*- $[H_2BP^{n}HexH]_{0\text{-}8}$. However, care must be taken to not over interpret this data, as it is not representative of the whole sample and only reflects what reaches the detector. Different concentrations and solution mixtures were tested but they did not provide any further information. More in depth studies using matrix-assisted laser/desorption

ionization tandem spectrometry (MALDI) are required to elude further information on the block sizes and polymer composition.[49]

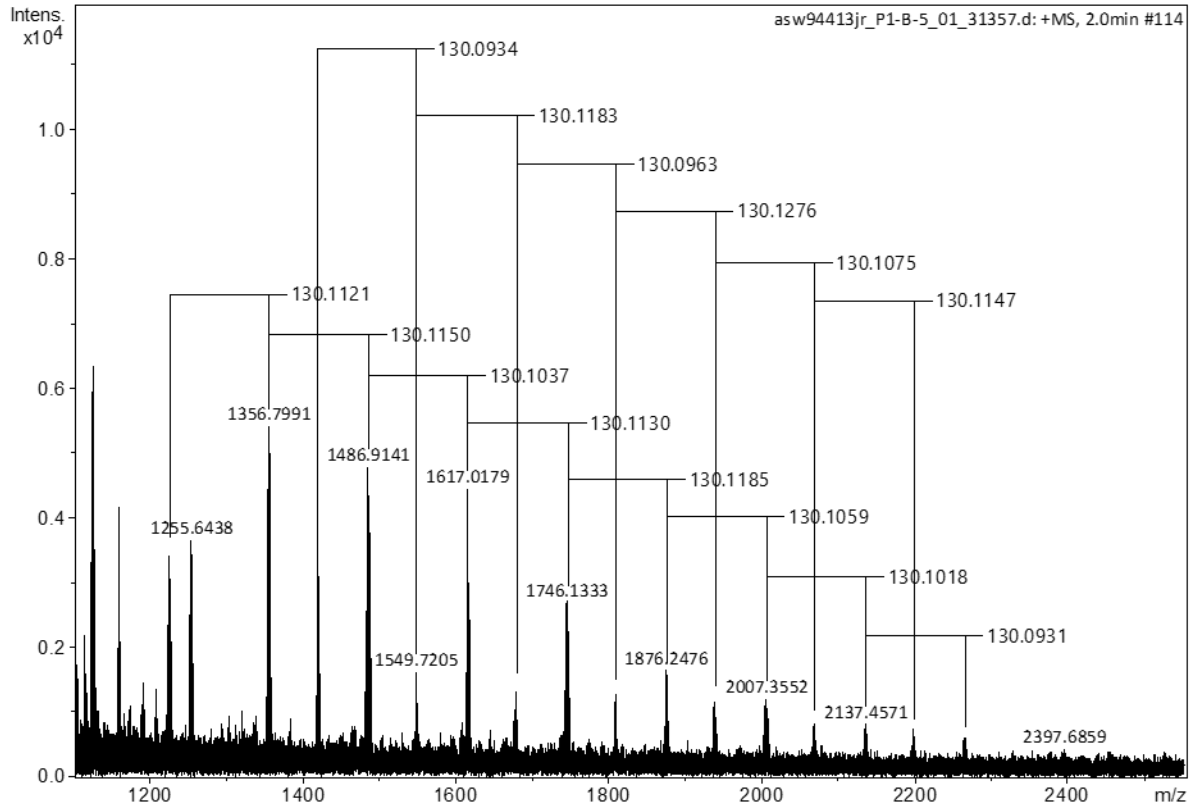

Figure 4.43. ESI mass spectrum of **BCP-Ph/^{n}Hex** in positive mode (1 mg/ml THF).

Copolymers of poly(phospinoboranes) have not been reported before, but there are examples of the formation of random copolymers of poly(aminoboranes), such as [MeNH-BH_2]$_n$-*r*-[NH_2-BH_2]$_m$, using IrH_2POCOP as a precatalyst [POCOP = κ^3-1,3-(OP^tBu_2)$_2C_6H_3$)].[50] These were formed via the copolymerisation of the two monomers, $H_3B{\cdot}NMeH_2$ and $H_3B{\cdot}NH_3$, which gave little control over copolymer arrangement. Other similar copolymers, such as poly(phosphazene) block copolymers [i.e. (R_2P=N)-*b*-(R'_2P=N)] have been prepared via the living cationic polymerisation of phosphoranimines such as $R_2ClP{=}NSiMe_3$.[51] Also, polystyrene-*b*-poly(methylenephosphine) block copolymers have been prepared via living anionic polymerisation.[52] Block copolymers can be formed via a wide range of methods, such as ionic, ring-opening, living and metal mediated chain end controlled polymerisations,[53] but a general method is the addition of catalyst (or initiator) and monomer B to a preformed polymer A, in a similar manner to that used here for the synthesis of **BCP-Ph/^{n}Hex**.

Relating back to the reversible chain transfer mechanism proposed in section 4.9, we suggest that at the start of the reaction in which **BCP-Ph/^{n}Hex** is formed, when there is a high concentration of $H_3B{\cdot}P^{n}HexH_2$, there is predominantly only dehydrocoupling of $H_3B{\cdot}P^{n}HexH_2$ to form short chained oligomers. We have already shown that the combination of larger polymers is very slow (section 4.10) and therefore the formation of longer chain of $[H_2BPPhH]_n$ is unlikely to occur at high concentrations of $H_3B{\cdot}P^{n}HexH_2$. When the concentration of $H_3B{\cdot}P^{n}HexH_2$ is lower, and shorter chain oligomers/polymers of $[H_2BP^{n}HexH]_n$ are present in the mixture, the likelihood of an end group of $[H_2BPPhH]_n$ coordinating to the $[Rh(dppe)]^+$ catalyst increases. This can occur due to the reversible chain transfer feature of the mechanism, i.e. a coordinated phosphinoborane can be displaced by any other. Subsequently, a dehydrocoupling process occurs between one end group of the polymeric $H_3B{\cdot}PPhH_2$ and a shorter chain oligomer/polymer of $H_3B{\cdot}P^{n}HexH_2$ to form a block copolymer **BCP-Ph/^{n}Hex** (Scheme 4.19). As the dehydrocoupling of n-hexylphosphineboranes is much slower, long chain polymers of $[H_2BP^{n}HexH]_n$ do not form before coupling to $[H_2BPPhH]_n$, and therefore the n-hexyl block is shorter than the phenyl block. Shorter oligomers could still dehydrocouple with the n-hexyl polymer end group, increasing the block ratio in favour of n-hexyl but once the longer copolymer is formed, the chances of coordinating to the Rh are even smaller.

As we have already shown that P–H activation is faster at the terminal $PPhH_2$ group compared to $P^{n}HexH_2$, a single $H_3BP^{n}HexH_2$ monomer could dehydrocouple with the polymer $[H_2BPPhH]_n$ end group and then a growing chain of n-hexyl monomers could dehydrocouple off the end. This would result in the same block copolymer **BCP-Ph/^{n}Hex**.

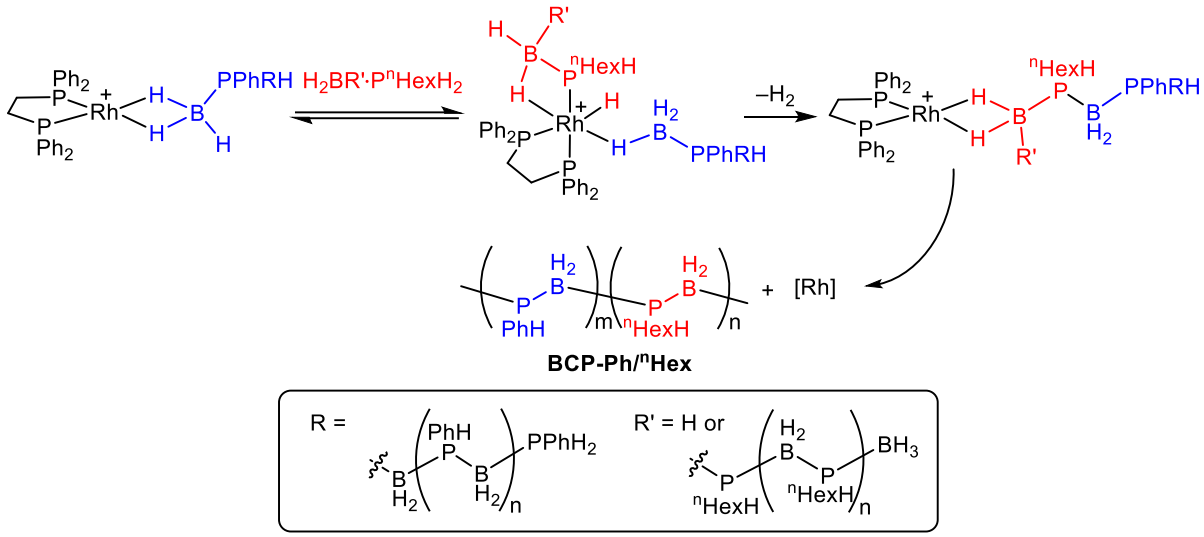

Scheme 4.19. Proposed rhodium-mediated dehydrocoupling process based upon a reversible chain transfer mechanism that allows for the formation of block-copolymer **BCP-Ph/^{n}Hex**.

Due to the inherent bifunctionality of phosphine-borane terminal groups, the dehydrocoupling process could occur on either end of the polymer to from an BAB triblock copolymer.[54] Moreover, dehydrocoupling could occur between two long chains of $[H_2BPPhH]_n$ but as shown in section 4.10, this a slow process that is unlikely to occur before n-hexyl dehydrocoupling (it took 44 hours to combine polymers of M_n = 54,500 g mol^{-1} and 30,000 g mol^{-1} to get polymer of M_n of 85,500 g mol^{-1}).

Synthesis of block copolymers via reversible-addition fragmentation chain transfer (RAFT) polymerisation is a very common radical polymerisation process,[55] but reversible chain transfer is less common. The mechanism proposed in this system is similar to an immortal polymerisation.[56] The defining characteristics of an immortal polymerisation are the absence of a chain transfer or termination step or that these steps are reversible, and the catalyst acts like a chain transfer agent to form bonds between monomers/oligomers and polymers.[57, 58] The reversible chain transfer mechanism proposed in section 4.9 and the observations made so far in this study resemble these characteristics. Assuming the polymer end groups remain active, and not capped by an unreactive end group, the dehydrocoupling process can occur indefinitely. In reality, however, slow catalyst decomposition occurs, as seen in the re-charge experiment (section 4.6.1) and catalytic efficiency decreases over time. Also, the coordination of long chain polymer becomes less probable as they increase in size. In the previously reported dehydropolymerisation of $H_3B{\cdot}PPhH_2$ using an Fe based catalyst, $[Cp(CO)_2FeOTf]$, polymer molecular weight is controlled by the addition of $PhPH_2$, which was shown by ESI-MS to cap the end of the

polymer.[28] This would decrease the concentration of terminal BH_3 groups and thus reduce the extent of polymerisation. It would be interesting to repeat this experiment with the $[Rh(dppe)]^+$ system to see if the same observations support the reversible chain transfer mechanism.

Immortal polymerisations also result in the formation of narrow dispersity polymer ($Đ < 1.1$) of high molecular weight as the chains keep combining until theoretically only one long polymer is formed. In reality this does not occur, and instead the polydispersity narrows during the reaction period until the catalyst decomposes or statistically the combination of long chain polymer becomes almost impossible. In the molecular weight versus conversion experiment in section 4.4, a narrowing of the dispersity was observed.

Immortal polymerisations are most commonly found in metal-catalysed lactide and lactone ring-opening polymerisations,[56, 59, 60] but have never been described for main-group polymers.

4.12.2 Aggregation in solution

AB block copolymers (Figure 4.44A) comprising of blocks of different solvent affinities can form aggregates in solution. The blocks with a lower affinity for a particular solvent congregate to minimise solvent interactions, resulting in the lowering of the free energy of the system. This is called the micelle core. The more readily solvated blocks form an outer shell, termed a corona (Figure 4.44B). Aggregation of copolymers in solution has been extensively studied since the 1990's,[61, 62] but never with poly(phosphinoboranes). The block copolymers made as part of this work offers the opportunity to preform well-defined aggregates of these relatively unexplored polymers in solution. There are a wide range of possible aggregate size and morphologies, such as: spheres, rods and lamellas, and which one forms is dependent on the solvent, copolymer concentration and polymer make-up (e.g. block sizes, block ratio, polymer chain composition).[47, 63] The possible uses of polymer aggregates include drug delivery systems,[64] functional nanomaterials and lithography.[65]

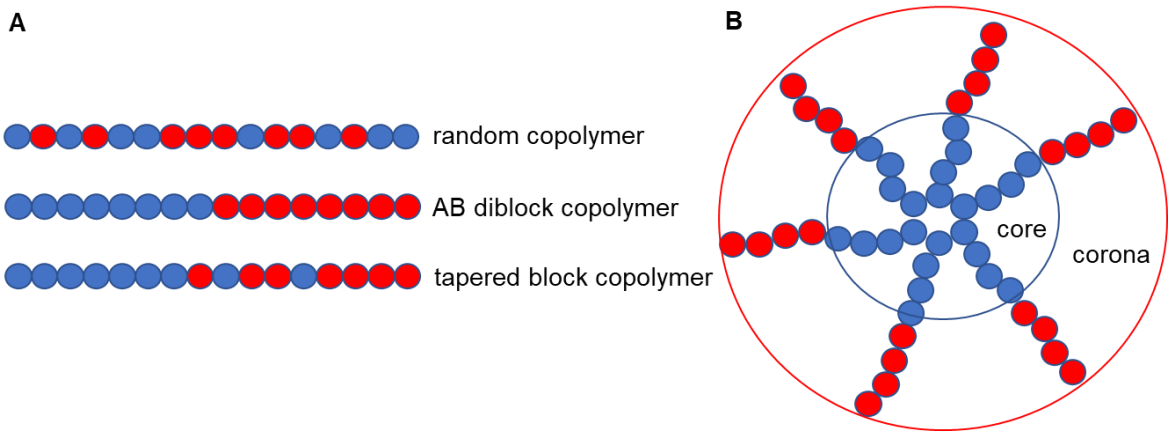

Figure 4.44. **A**) Examples of copolymer composition. **B**) Aggregation of AB diblock copolymers in solution to form a spherical micelle like aggregate.

Formation of aggregates in solution gives a good indication of the formation of an AB block copolymer. Random copolymers and taper block copolymers also aggregate but these are rarely used due to their inherently ill-defined properties and broader polydiserpsity.[66] One method of testing for aggregation is via dynamic light scattering (DLS) analysis.[48, 67] The apparent hydrodynamic radius $R_{H,app}$ measured by DLS is an estimate of the size of a particle in comparison to the diameter of a sphere that has the same translational diffusion coefficient.[68] While the value itself is not reliable in an absolute sense, comparing the relative size of particles in solution is useful. The number distribution is a plot of the particle sizes by abundancy, with the most abundant particles size giving the highest intensity. All DLS data was collected by Dr Charlotte Ellis at the University of Victoria, Canada, in the Manners Group. Figure 4.45 shows the number distribution DLS analysis of homopolymer $[H_2BPPhH]_n$ (M_n = 26,500, Đ = 1.5), **BCP-Ph/^{n}Hex** (M_n = 45,000, Đ = 1.3) and homopolymer $[H_2BP^nHexH]_n$ (M_n = 33,000, Đ = 1.3) in THF (2.5 ml) at 25 °C. It is evident that the particle size of **BCP-Ph/^{n}Hex** is in between that of the two homopolymers with the $R_{H,app}$ calculated as 6 ± 2, 106 ± 28 and 1037 ± 28 nm respectively. This DLS data shows that $[H_2BP^nHexH]_n$ forms relatively large aggregates in solution, whereas polymeric $[H_2BPPhH]_n$ is likely in a chain like form as it is only a few nm in diameter.[48] **BCP-Ph/^{n}Hex**, however, is in the middle of the two and smaller aggregates are observed. This is interesting as both n-hexyl and phenyl groups are soluble in THF and thus aggregates were not expected for any of the polymers. Nevertheless, comparing these three samples shows that $[H_2BP^nHexH]_n$ aggregates in THF at 2.5 mg/ml, $[H_2BPPhH]$ does not, and **BCP-Ph/^{n}Hex** contains both of these components and aggregates to a lesser extent. This is good evidence for copolymer formation.

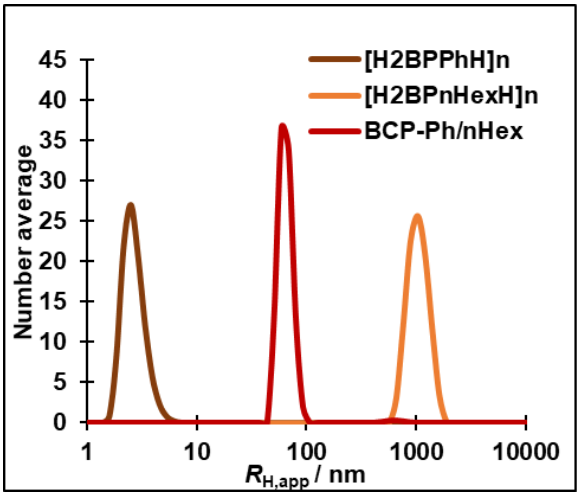

	M_n (g mol^{-1})	Đ	$R_{H,app}$ (nm)
$[H_2BPPhH]_n$	26,500	1.5	6 ± 2
$[H_2BP^nHexH]_n$	33,000	1.3	1037 ± 28
BCP-Ph/^{n}Hex	45,000	1.3	106 ± 28

Figure 4.45. Left - representative number average DLS data for samples of homopolymers $[H_2BPPhH]_n$ and $[H_2BP^nHexH]_n$ and copolymer **BCP-Ph/^{n}Hex** in THF (2.5 mg/ml). Right – summary table of the polymer molecular weights, Đ and hydrodynamic radii.

It is proposed that the $[H_2BP^nHexH]$ component of **BCP-Ph/^{n}Hex** is forming the core of the aggregate (Figure 4.46) as homopolymer $[H_2BP^nHexH]$ was shown to aggregate in THF, and therefore $[H_2BPPhH]$ must form the corona. To test this theory, the solution was changed from pure THF to 25:75 hexane:THF and the sample of **BCP-Ph/^{n}Hex** was reanalysed by DLS (Figure 4.46). This reduction in solvent polarity led to an increase in the particle size from $R_{H,app}$ = 106 ± 28 nm to $R_{H,app}$ = 1505 ± 208 nm, which suggests an aggregation of smaller aggregates.[69] This is consistent with $[H_2BPPhH]_m$ being the corona section of the smaller aggregate, as $[H_2BPPhH]$ is not soluble in hexane and therefore this block now has a lower affinity with the solution and the smaller aggregates congregate to minimise corona/solvent interactions. The concentration of the sample is very influential on aggregation.[70] Further DLS studies are currently underway that analyse **BCP-Ph/^{n}Hex** in different concentrations and with a broader range of solvent polarities to support the formation of a block copolymer and also exploit this control to form nanoparticles of a specific size.

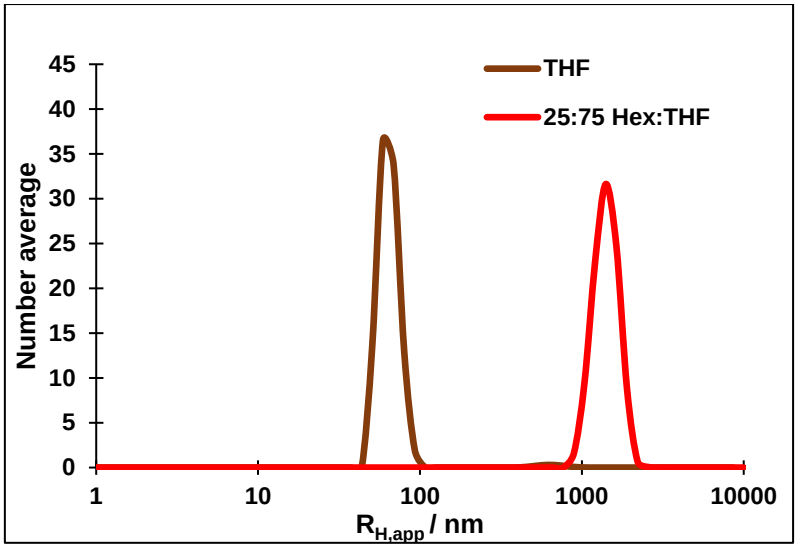

Figure 4.46. Representative number average DLS data for samples of **BCP-Ph/^{n}Hex** in THF and 25:75 hexane:THF (2.5 mg/ml).

Analysis of **BCP-Ph/^{n}Hex** by transmission electron microscopy (TEM) was also conducted by Dr Charlotte Ellis at the University of Victoria. A sample was prepared by drop-casting a 1 mg/ml THF solution of **BCP-Ph/^{n}Hex** onto a carbon coated grid. Figure 4.47 shows a representative image of this sample. It is evident that there are many small, circular or spherical aggregates on the grid which is an indication of a spherical micelle or vesicle when in solution.[47] The particles range in size from 13 nm to 2 nm with a number average length of 7 ± 2 nm (as measured by ImageJ software). These are clearly much smaller in size than those determined by DLS. However, in TEM analysis often only the core section of the aggregate is observed as the electron density, which is imaged via TEM, is too diffuse in the more disperse and less concentrated corona.[47] The hydrodynamic radius, as determined by DLS in THF was 106 ± 28 nm. Using this data and assuming a perfect spherical aggregate has formed with a diameter equalling two end-to-end chains of **BCP-Ph/^{n}Hex** and a block ratio of 3:1 Ph:^{n}Hex, the central ^{n}Hex core would equate to 25 nm, which is much closer to 7 nm. However, DLS only provides an estimate of the hydrodynamic radius and there could also be solvent swelling of the core in the THF solution.[71] In light of this, it is likely that the TEM images are capturing spherical micelles formed from the aggregation of an AB block copolymer **BCP-Ph/^{n}Hex**.

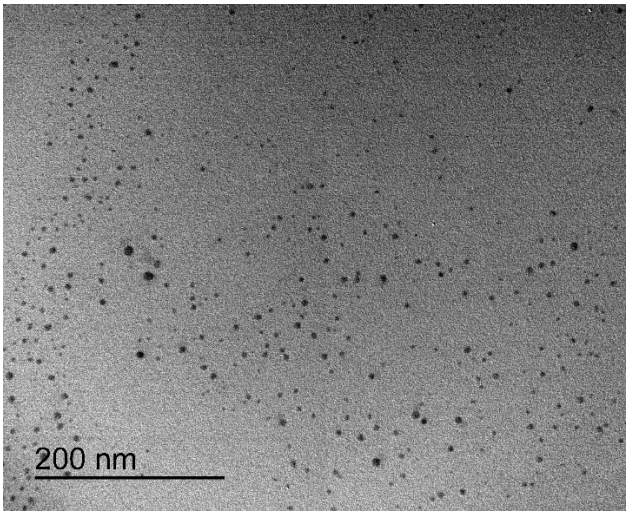

Figure 4.47. A representative TEM image of a sample of **BCP-Ph/^{n}Hex** from a 1 mg/ml THF solution. Scale bar = 200 nm.

There are three main factors that influence the morphology of the aggregate: the degree of stretching of the core-forming blocks, the interfacial tension between the micelle core and the solvent outside the core, and the repulsive interactions among corona-forming chains. This can give rise to a complex array of different morphologies.[47] The TEM images of **BCP-Ph/^{n}Hex** suggests that spherical aggregates have formed. There are no reported aggregates of polymers similar to **BCP-Ph/^{n}Hex** but spherical micelles obtained from a hexane/THF solution of polystyrene$_{170}$-*b*-polyisoprene$_{140}$ were measured to be 25 nm in diameter by TEM imaging.[71] Polystyrene$_{180}$-*b*-poly(acrylic acid)$_{18}$ was also shown to form sphere aggregates in DMF, dioxane and THF, with an average diameter of 27 nm by TEM imaging.[72]

In collaboration with the Manners group at the University of Victoria, further studies of the self-assembled aggregates of **BCP-Ph/^{n}Hex** are currently underway. By altering the block ratio and solvent system we hope to control the size of the aggregates. The materials properties of these novel copolymers are also under investigation.

4.13 Conclusion

Within this chapter, the very simple precatalyst, [Rh(dppe)$_2$]Cl has been used to catalytically dehydropolymerise primary phosphine-boranes $H_3B{\cdot}PRH_2$ to form poly(phosphinoboranes) of high molecular weight. When R = Ph, 19 hours and 1 mol% catalyst loading was required. The more activated monomer,[6, 28] when R = 3,5-$(CF_3)_2C_6H_3$, required only four hours for complete conversion,

whereas when R = n-hexyl, a reaction time of 66 hours and 3 mol% catalyst loading was needed (Table 4.5). The polymers were formed with good purity and in moderate to good yields (51-84%). The largest polymer was formed with the most activated monomer.

Table 4.5. Dehydropolymerisation of primary phosphine-boranes using $[Rh(dppe)_2]Cl$.

Monomer	Time for 100% conv.	M_n (g mol^{-1}) (Đ)
$H_3B{\cdot}PPhH_2$	19 hours	32,000 (1.7)
$H_3B{\cdot}P(3,5\text{-}(CF_3)_2C_6H_3)H_2$	4 hours	127,500 (1.3)[b]
$H_3B{\cdot}P^nHexH_2$	66 hours[a]	33,000 (1.3)

[a] 3 mol% catalytic loading. [b] 19 hours reaction time for this molecular weight polymer.

The mechanism of the dehydropolymerisation of $H_3B{\cdot}PPhH_2$ was studied via a molecular weight vs conversion experiment, which revealed a step-growth like polymerisation.[18, 19] This was also observed when the more activated monomer $H_3B{\cdot}P\{3,5\text{-}(CF_3)_2C_6H_3\}H_2$ was used. Observations made via in-situ NMR spectroscopy revealed that one of the dppe ligands is displaced from the $[Rh(dppe)_2]Cl$ precatalyst and a linear dimer bound Rh(III) P–H activated complex is observed as the catalyst resting state at the start of catalysis. This is similar to the observed off-cycle resting state in the $[Rh(dppp)]^+$ catalysed dehydrocoupling of H_3BPPh_2H.[5] Stoichiometric addition of free linear dimer to $[Rh(dppe)_2]Cl$ and $[Rh(dppe)(\eta^6\text{-}C_6H_5F)][BAr^F{}_4]$ confirmed the formation of a linear dimer bound complex.[6]

In light of these observations, a reversible chain transfer mechanism was proposed that facilitates a sequential dehydrocoupling process between a terminal BH_3 and a terminal $PhPH_2$ of any combination of monomer, oligomer or polymer. This was substantiated by the dehydrocoupling of polymer and oligomer chains to form longer polymers without any monomer present.

The $[Rh(dppe)]^+$ catalyst also facilitated the combination of phosphine-boranes with different substituents on the phosphorus, resulting in the formation of an AB block copolymer of poly(phenylphosphinoborane)-*b*-poly(n-hexylphoshinoborane) in a block ratio of 3:1 Ph:^{n}Hex and a degree of polymerisation of 48:16. The formation of a copolymer was supported by multinuclear NMR spectroscopy and ^{1}H DOSY NMR experiments. Due to the different solubilities of the phenyl and n-hexyl blocks, aggregation was observed in solution with some preliminary evidence for the formation of spherical micelles by DLS and TEM analysis. Further work is currently underway to control the size and morphology of the aggregates.[47] This is the first example of block copolymers of poly(phosphinoboranes) and potentially provides an opportunity to preform nanoparticles of specific size and utilise the properties of poly(phosphinoboranes), such as fire-retardancy,[73] on the nanoscale.

There is a huge range of possible combinations of substituents that could be used in block copolymers of poly(phosphinoboranes). The different block solubilities of n-hexyl and phenyl groups in in **BCP-Ph/^{n}Hex** aided in self-assembly but this could have also been conducted with other groups, such as isopropyl and 3,5-$(CF_3)_2C_6H_3$ groups. This could give rise to different aggregate morphologies. There is also great scope within the study of the application of poly(phosphinoboranes).[4] For this, polymer synthesis on a larger scale with accurate control of polymer molecular weight is needed. A challenge for synthetic chemists is also the avoidance of the harsh conditions needed to form poly(phosphinoboranes) (e.g. 100 °C in toluene at 1.25 M of $H_3B{\cdot}PRH_2$). If the turnover limiting step is, as we suggest, the reductive elimination of the P–H bond to reform a Rh(I) complex (**4.2** to **4.4** in Scheme 4.12) then perhaps a ligand that might encourage this step, such as the more electron withdrawing $(C_6F_5)_2PCH_2CH_2P(C_6F_5)_2$, could lower the energetic barrier for catalytic turnover and milder conditions may be required.

4.14 References

[1] G. M. Adams, D. E. Ryan, N. A. Beattie, A. I. Mckay, G. C. Lloyd-Jones, A. S. Weller, *ACS Catal.,* **2019,** 9, 3657-3666.
[2] D. E. Ryan, K. A. Andrea, J. J. Race, T. M. Boyd, G. C. Lloyd-Jones, A. S. Weller, *ACS Catal.,* **2020,** 10, 7443-7448.
[3] M. A. Huertos, A. S. Weller, *Chem. Commun.,* **2012,** 48, 7185-7187.
[4] A. Staubitz, A. P. M. Robertson, M. E. Sloan, I. Manners, *Chem. Rev.,* **2010,** 110, 4023-4078.
[5] M. A. Huertos, A. S. Weller, *Chem. Sci.,* **2013,** 4, 1881-1888.
[6] T. N. Hooper, M. A. Huertos, T. Jurca, S. D. Pike, A. S. Weller, I. Manners, *Inorg. Chem.,* **2014,** 53, 3716-3729.
[7] T. N. Hooper, A. S. Weller, N. A. Beattie, S. A. Macgregor, *Chem. Sci.,* **2016,** 7, 2414-2426.
[8] H. Dorn, R. A. Singh, J. A. Massey, J. M. Nelson, C. A. Jaska, A. J. Lough, I. Manners, *J. Am. Chem. Soc.,* **2000,** 122, 6669-6678.
[9] H. Dorn, R. A. Singh, J. A. Massey, A. J. Lough, I. Manners, *Angew. Chem. Int. Ed.,* **1999,** 38, 3321-3323.
[10] J. Chatt, B. L. Shaw, *Journal of the Chemical Society A: Inorganic, Physical, Theoretical,* **1966,** 1437-1442.
[11] A. Mannu, G. Vlahopoulou, C. Kubis, H.-J. Drexler, *J. Organomet. Chem.,* **2019,** 885, 59-64.
[12] N. L. Oldroyd, S. S. Chitnis, V. T. Annibale, M. I. Arz, H. A. Sparkes, I. Manners, *Nature Communications,* **2019,** 10, 1370.
[13] A. Schäfer, T. Jurca, J. Turner, J. R. Vance, K. Lee, V. A. Du, M. F. Haddow, G. R. Whittell, I. Manners, *Angew. Chem. Int. Ed.,* **2015,** 54, 4836-4841.
[14] H. Dorn, J. M. Rodezno, B. Brunnhöfer, E. Rivard, J. A. Massey, I. Manners, *Macromolecules,* **2003,** 36, 291-297.
[15] A. R. Mcwilliams, H. Dorn, I. Manners, New Inorganic Polymers Containing Phosphorus. In *New Aspects in Phosphorus Chemistry I*, Majoral, J.-P., Ed. Springer Berlin Heidelberg: Berlin, Heidelberg, **2002**; pp 141-167.
[16] B. R. James, D. Mahajan, *Can. J. Chem.,* **1979,** 57, 180-187.
[17] E. a. K. Spearing-Ewyn, N. A. Beattie, A. L. Colebatch, A. J. Martinez-Martinez, A. Docker, T. M. Boyd, G. Baillie, R. Reed, S. A. Macgregor, A. S. Weller, *Dalton Trans.,* **2019,** 48, 14724-14736.
[18] G. Odian, *Principles of Polymerization*. Fourth ed., John Wiley & Sons, New Jersey, **2004**.
[19] H.-G. Elias, *An Introduction to Polymer Science*. VCH Publishers, New York, **1997**.
[20] P. J. Flory, *Principles of Polymer Chemistry*. Cornell University Press, London, **1986**.

[21] T. Jurca, T. Dellermann, N. E. Stubbs, D. A. Resendiz-Lara, G. R. Whittell, I. Manners, *Chem. Sci.,* **2018,** 9, 3360-3366.
[22] J. R. Turner, D. A. Resendiz-Lara, T. Jurca, A. Schäfer, J. R. Vance, L. Beckett, G. R. Whittell, R. A. Musgrave, H. A. Sparkes, I. Manners, *Macromol. Chem. Phys.,* **2017,** 218, 1700120.
[23] C. Marquardt, T. Jurca, K.-C. Schwan, A. Stauber, A. V. Virovets, G. R. Whittell, I. Manners, M. Scheer, *Angew. Chem. Int. Ed.,* **2015,** 54, 13782-13786.
[24] C. E. Carraher, *Introduction to Polymer Chemistry* Fourth ed., CRC Press, Florida, **2017**.
[25] C.-W. Tsang, M. Yam, D. P. Gates, *J. Am. Chem. Soc.,* **2003,** 125, 1480-1481.
[26] T. J. Clark, J. M. Rodezno, S. B. Clendenning, S. Aouba, P. M. Brodersen, A. J. Lough, H. E. Ruda, I. Manners, *Chem. Eur. J.,* **2005,** 11, 4526-4534.
[27] F. Schön, L. M. Sigmund, F. Schneider, D. Hartmann, M. A. Wiebe, I. Manners, L. Greb, *Angew. Chem. Int. Ed.,* **2022,** 61, e202202176.
[28] D. A. Resendiz-Lara, V. T. Annibale, A. W. Knights, S. S. Chitnis, I. Manners, *Macromolecules,* **2021,** 54, 71-82.
[29] A. R. O'connor, W. Kaminsky, D. M. Heinekey, K. I. Goldberg, *Organometallics,* **2011,** 30, 2105-2116.
[30] S. D. Pike, M. R. Crimmin, A. B. Chaplin, *Chem. Commun.,* **2017,** 53, 3615-3633.
[31] A. I. Mckay, J. Barwick-Silk, M. Savage, M. C. Willis, A. S. Weller, *Chem. Eur. J.,* **2020,** 26, 2883-2889.
[32] R. Dallanegra, A. P. M. Robertson, A. B. Chaplin, I. Manners, A. S. Weller, *Chem. Commun.,* **2011,** 47, 3763-3765.
[33] A. T. Lubben, J. S. Mcindoe, A. S. Weller, *Organometallics,* **2008,** 27, 3303-3306.
[34] K. L. Vikse, M. P. Woods, J. S. Mcindoe, *Organometallics,* **2010,** 29, 6615-6618.
[35] G. T. Thomas, L. Macgillivray, N. L. Dean, R. L. Stoddard, L. P. E. Yunker, J. S. Mcindoe, *Int. J. Mass spectrom.,* **2019,** 441, 14-18.
[36] M. E. Sloan, T. J. Clark, I. Manners, *Inorg. Chem.,* **2009,** 48, 2429-2435.
[37] T. N. Hooper, A. S. Weller, N. A. Beattie, S. A. Macgregor, *Chem. Sci.,* **2016,** 7, 2414-2426.
[38] R. N. Perutz, S. Sabo-Etienne, *Angew. Chem. Int. Ed.,* **2007,** 46, 2578-2592.
[39] A. T. Luedtke, K. I. Goldberg, *Inorg. Chem.,* **2007,** 46, 8496-8498.
[40] M. P. Lanci, M. S. Remy, D. B. Lao, M. S. Sanford, J. M. Mayer, *Organometallics,* **2011,** 30, 3704-3707.
[41] A. L. Colebatch, A. S. Weller, *Chem. Eur. J. ,* **2019,** 25, 1379-1390.
[42] A. Kumar, H. C. Johnson, T. N. Hooper, A. S. Weller, A. G. Algarra, S. A. Macgregor, *Chem. Sci.,* **2014,** 5, 2546-2553.
[43] H. C. Johnson, A. P. M. Robertson, A. B. Chaplin, L. J. Sewell, A. L. Thompson, M. F. Haddow, I. Manners, A. S. Weller, *J. Am. Chem. Soc.,* **2011,** 133, 11076-11079.
[44] T. J. Clark, J. M. Rodezno, S. B. Clendenning, S. Aouba, P. M. Brodersen, A. J. Lough, H. E. Ruda, I. Manners, *Chem. Eur. J. ,* **2005,** 11, 4526-4534.
[45] M. P. Stevens, *Polymer Chemistry. An Introduction*. Third ed., Oxford University Press, New York, **1999**.
[46] H. Cavaye, F. Clegg, P. J. Gould, M. K. Ladyman, T. Temple, E. Dossi, *Macromolecules,* **2017,** 50, 9239-9248.
[47] Y. Mai, A. Eisenberg, *Chem. Soc. Rev.,* **2012,** 41, 5969-5985.
[48] K. Stubenrauch, C. Moitzi, G. Fritz, O. Glatter, G. Trimmel, F. Stelzer, *Macromolecules,* **2006,** 39, 5865-5874.
[49] A. C. Crecelius, C. R. Becer, K. Knop, U. S. Schubert, *J. Polym. Sci., Part A: Polym. Chem.,* **2010,** 48, 4375-4384.
[50] A. Staubitz, M. E. Sloan, A. P. M. Robertson, A. Friedrich, S. Schneider, P. J. Gates, J. Schmedt Auf Der Günne, I. Manners, *J. Am. Chem. Soc.,* **2010,** 132, 13332-13345.
[51] H. R. Allcock, S. D. Reeves, J. M. Nelson, C. A. Crane, I. Manners, *Macromolecules,* **1997,** 30, 2213-2215.
[52] K. J. T. Noonan, D. P. Gates, *Angew. Chem. Int. Ed.,* **2006,** 45, 7271-7274.
[53] M. Hillmyer, *Curr. Opin. Solid State Mater. Sci.,* **1999,** 4, 559-564.
[54] J. M. Widin, A. K. Schmitt, A. L. Schmitt, K. Im, M. K. Mahanthappa, *J. Am. Chem. Soc.,* **2012,** 134, 3834-3844.
[55] D. J. Keddie, *Chem. Soc. Rev.,* **2014,** 43, 496-505.
[56] S. Asano, T. Aida, S. Inoue, *J. Chem. Soc., Chem. Commun.,* **1985,** 1148-1149.
[57] S. Inoue, *J. Polym. Sci., Part A: Polym. Chem.,* **2000,** 38, 2861-2871.
[58] S. M. Guillaume, J.-F. Carpentier, *Catal. Sci. Technol.,* **2012,** 2, 898-906.
[59] B.-T. Ko, C.-C. Lin, *Macromolecules,* **1999,** 32, 8296-8300.
[60] S. Inoue, *J. Macromol. Sci. A,* **1988,** 25, 571-582.
[61] L. Zhang, A. Eisenberg, *Science,* **1995,** 268, 1728-1731.
[62] J. C. M. Van Hest, D. a. P. Delnoye, M. W. P. L. Baars, M. H. P. Van Genderen, E. W. Meijer, *Science,* **1995,** 268, 1592-1595.
[63] S. B. Darling, *Prog. Polym. Sci.,* **2007,** 32, 1152-1204.
[64] Q. Zhang, N. Re Ko, J. Kwon Oh, *Chem. Commun.,* **2012,** 48, 7542-7552.
[65] J. K. Kim, S. Y. Yang, Y. Lee, Y. Kim, *Prog. Polym. Sci.,* **2010,** 35, 1325-1349.

[66] L. Li, K. Raghupathi, C. Song, P. Prasad, S. Thayumanavan, *Chem. Commun.,* **2014,** 50, 13417-13432.
[67] S. Okabe, K.-I. Seno, S. Kanaoka, S. Aoshima, M. Shibayama, *Macromolecules,* **2006,** 39, 1592-1597.
[68] J. Stetefeld, S. A. Mckenna, T. R. Patel, *Biophys. Rev.,* **2016,** 8, 409-427.
[69] B. Chu, T. Liu, C. Wu, Z. Zhou, V. Mark Nace, *Macromol.,* **1997,** 118, 221-227.
[70] P. Stepanek, T. P. Lodge, *Macromolecules,* **1996,** 29, 1244-1251.
[71] H. Zhao, Q. Chen, L. Hong, L. Zhao, J. Wang, C. Wu, *Macromol. Chem. Phys.,* **2011,** 212, 663-672.
[72] N. S. Cameron, M. K. Corbierre, A. Eisenberg, *Can. J. Chem.,* **1999,** 77, 1311-1326.
[73] A. W. Knights, M. A. Nascimento, I. Manners, *Polymer,* **2022,** 247, 124795.

5 Chapter Five – Experimental data

5.1 General methods

All experiments were performed under an atmosphere of argon, using standard Schlenk techniques on a dual vacuum/inlet manifold unless specified. Glassware was dried in an oven at 140 °C overnight or flame dried under vacuum prior to use. Pentane, hexane, THF, diethyl ether and CH_2Cl_2 were dried using an MBraun SPS-800 solvent purification system and degassed by three freeze-pump-thaw cycles. 1,2-$F_2C_6H_4$ was stirred over Al_2O_3 for two hours and then CaH_2 overnight before vacuum transfer and subsequent degassing by three freeze-pump-thaw cycles. CD_2Cl_2 and d_8-toluene were dried overnight with CaH_2 and d_6-acetone with K_2CO_3 before vacuum transfer and subsequent degassing by three freeze-pump-thaw cycles and stored over 3 Å molecular sieves. *O*-xylene was stored over 3 Å molecular sieves**.**

The following chemicals were prepared via literature procedures: $[RhCl(NBD)]_2$ and $[Rh(NBD)_2][Bar^F{}_4]$,[1] $[Rh(COD)Cl]_2$,[2] $RhH(dppe)_2$,[3] $H_3B{\cdot}PPhH_2$,[4] $H_3B{\cdot}PCyH_2$,[5] $H_3B{\cdot}P^iPrH_2$[6] and $H_3B{\cdot}PH_2$3,5-$(CF_3)_2C_6H_3$.[7] $[Rh(dppe)_2]Cl$ (dppe = 1,2-bis(diphenylphosphino)ethane) was prepared via addition of dppe to $[Rh(COD)Cl]_2$ in THF (THF = tetrahydrofuran and COD = cyclooctadiene). $[Rh(dppe)_2][X]$ (X = $[BF_4]^-$ and $[BAr^F{}_4]^-$ were prepared by the addition of NaX to $[Rh(dppe)_2]Cl$ in THF. $H_3B{\cdot}P^nHexH_2$ was prepared via the Grignard reagent, ^{n}HexMgBr, a modification from the literature method.[8] All other reagents were purchased from commercial vendors and used as received.

NMR data was collected on either a Bruker 400 MHz, Venus400, a Bruker Ascend 400 MHz, Bruker 500 MHz AVC, Bruker 500 MHz AVIIIHD or Bruker 600 MHz AVIIIHD widebore spectrometer. Residual protio solvent resonances were used as a reference for ^{1}H NMR spectra. $^{31}P\{^1H\}$ NMR spectra were referenced externally to 85 % H_3PO_4. All chemical shifts (δ) are quoted in ppm and coupling constants in Hz.

ESI-MS conducted in Chapter Two was carried out using a Bruker MicroTOF instrument directly connected to a modified Innovative Technology glovebox[9] unless otherwise specified. Typical acquisition parameters were used (sample flow rate 4 μL min^{-1}, nebulizer gas pressure: 0.4 bar, drying gas: argon at 333 K flowing at 4 L min^{-1}, capillary voltage: 4.5 kV, exit voltage: 60 V). The spectrometer was calibrated using a mixture of tetraalkyl ammonium bromides $[N(C_nH_{2n+1})_4]Br$ (n = 2-8, 12, 16 and

18). Samples were diluted to a concentration of 1 x 10^{-6} M in the specified solvent before sampling by ESI-MS. In Chapter Three and Four, aerobic ESI-MS conducted in Chapter Three and Four was carried out using a Bruker compact® time of flight mass spectrometer by Mr. Karl Heaton at the University of York for compounds. Air sensitive mass spectrometry in Chapter Three and Four was conducted using a bespoke N_2 filled glovebox connected to a HCTultra ETD II ESI-ion trap spectrometer.[9]

In the laboratory of Professor Scott McIndoe (University of Victoria, Canada), anaerobic ESI-MS using Waters Acquity Triple Quadrupole Detector equipped with a Z-Spray electrospray ionization source and pressurised sample infusion (PSI) was used to study the oligomer bound species in Chapter Four. A PSI flask[10] was equipped with 20 ml of 1,2-$F_2C_6H_4$ and [Rh(dppe)(η^6-C_6H_5F)][BAr^F_4] (3 mg, 2 µM) and was stirred at 100°C. A mixture of short chain polymer [H_2BPPhH]$_n$ (M_n = 7,000 g mol-1, PDI = 2.4, 2 mg) formed by a one hour reaction time using the general procedure was dissolved in 1 ml of 1,2-$F_2C_6H_4$ and added to the [Rh(dppe)(η^6-C_6H_5F)][BAr^F_4] solution. A pressure of 6 psi was applied to the flask to initiate pressurized sample infusion[11] into the mass spectrometer. The capillary voltage was held at 3.0 kV, cone voltage at 14.0 V, and extraction cone at 4.0 V. The MS cone voltage was optimized to eliminate in-source fragmentation of the catalyst. The desolvation gas flow rate was 200 l/hr, cone gas flow rate 200 l/hr, source temperature 105 °C and desolvation temperature 200 °C. The RF lens was set to an optimal voltage of 0.2 V, and the ion energy was maintained at 0.6. Isotope patterns were obtained by narrowing the *m/z* range and increasing both the LM resolution and the HM resolution to 17.0.

Elemental analyses were conducted by Mr Stephan Boyer at London Metropolitan University or Dr Graeme McAllister at the University of York.

Dynamic light scattering (DLS) was conducted using a Malvern Panalytical Zetasizer Ultra/Pro instrument equipped with a laser with a wavelength of 633 nm and a detector oriented at 173º to the incident radiation.

^{1}H DOSY spectra were collected by Dr Alex Heyam (University of York, UK) on a Bruker 600 MHz AVIIIHD spectrometer equipped with a room temperature 5 mm BBO probe. The dstebpgp3s pulse sequence was used to compensate for convection within the sample. For all experiments, the number of scans per increment was 16, the delay between scans was 10 s, and the temperature was 298 K. The diffusion delay d20 and gradient pulse length p30 were optimised to give a roughly 95 % drop in

polymer signal between the highest and lowest gradient strengths: this gave d20 = 200 ms and p30 = 1.2 ms (except for the sample of $[H_2BP^nHexH]_n$, where d20 = 150ms and p30 = 1 ms). For **BCP-Ph/^{n}Hex**, 16 linearly spaced increments were collected between 5% and 95% gradient strength; for all other samples, only 8 linearly spaced increments were collected. The gradient strength was calibrated using a sample of 1% H_2O in D_2O, which is known to have a diffusion coefficient of 1.872×10^{-9} m^2 s^{-1}. DOSY spectra were processed in Mestrenova using a Bayesian method with one repetition.

Transmission electron microscopy (TEM) was conducted by Dr Charlotte Ellis (University of Victoria, Canada) using copper grids (500 mesh) purchased from Ted Pella, Inc. and carbon films were prepared by using a Leica EM ACE600 instrument. Carbon films were deposited onto the copper grids by flotation on water and allowed to dry over 24 hours. Samples for electron microscopy were prepared by drop-casting 8 µL of **BCP-Ph/^{n}Hex** in a THF solution onto a carbon-coated copper grid followed by solvent evaporation. TEM images were obtained using a JEOL JEM 1011 operating at 80 kV, equipped with a Gatan Orius SC1000 CCD camera.

5.2 Synthesis of new complexes

5.2.1 Chapter Two

o-^{i}Pr-DPEphos **1-^{i}Pr**

The synthesis of **1-^{i}Pr** followed literature procedures to form the 2,2'-$(PCl_2)_2(C_6H_4)_2O$.[12, 13] In a separate flask Li[2-^{i}Pr-C_6H_4] (1.2 equiv.) was prepared at –78 °C from the addition of N,N,N',N'-tetramethylenediamine (0.46 ml, 3.1 mmol) to ^{n}BuLi (2.5 M in hexanes, 1.04 ml, 2.6 mmol) then dropwise addition of 1-bromo-2-isopropylbenzene (0.39 ml, 2.6 mmol) and the mixture was left to stir at –78 °C for 1 hour. Dropwise addition of this aryl lithium solution to the 2,2'-$(PCl_2)Ph_2O$ (200 mg, 0.54 mmol) in THF (5 ml) also kept at –78 °C formed a clear orange solution after 1 hour of stirring at –78 °C. Methanol (0.5 ml) was added at –78 °C and the mixture was warmed to room temperature (ligand is air stable). Saturated $[NH_4]Cl$ solution (10 ml) was added and the mixture was separated, and the organic phase extracted with pentane (3 x 10 ml). The organic phases were collated and the solvent removed *in vacuo* to yield the crude product as a pale-yellow solid which was recrystallised in hot pentane to yield pure **1-^{i}Pr** as a white solid (115 mg, 0.17 mmol, 30% yield).

$^{31}P\{^{1}H\}$ NMR (162 MHz, $CDCl_3$): δ –37.6 ppm (s).

^{1}H NMR (400 MHz, $CDCl_3$, 298 K): δ 7.27 (m, 8H, Ar), 7.04 (m, 6H, Ar), 6.88 (m, 6H, Ar), 6.73 (ddd, *J* = 2, 4 and 8 Hz, 2H, Ar), 6.36 (dd, *J* = 4 and 8 Hz, 2H, Ar), 3.63 (septet, *J*(HH) = 7 Hz, 4H, C*H*CH_3), 1.06 (d, *J*(HH) = 7 Hz, 24H, CHC*H*$_3$).

$^{13}C\{^{1}H\}$ NMR (126 MHz, $CDCl_3$, 298 K): δ 159.4 (d, *J*(PC) = 19 Hz, Ar), 153.4 (d, *J*(PC) = 28 Hz, Ar), 134.4 (s, Ar), 134.4 (s, Ar), 134.3 (s, Ar), 134.1 (s, Ar),129.8 (s, Ar), 128.9 (s, Ar), 125.7 (s, Ar), 125.1 (d, J_{PC} = 5 Hz, Ar), 123.2 (s, Ar), 118.0 (s, Ar), 31.1 (d, *J*(PC) = 27 Hz, CH) and 23.9 (d, *J*(PC) = 10 Hz, CH_3).

EI-MS (acetonitrile): *m/z* $[M]^+$ 706.4 (calc. 706.35) with the correct isotope pattern.

Multiple samples were submitted for elemental analysis, but no results were within 0.4% of the theoretical percentage mass by weight for carbon or hydrogen. Persistent pentane may be the cause of the inconsistent elemental analysis.

[Rh(*o*-R-DPEphos)(NBD)][BAr^F_4] (R = H, Me or OMe) **2-H**, **2-Me** and **2-OMe**

Ligand **1-H**, **1-Me** or **1-OMe** (200 mg) in 1,2-$F_2C_6H_4$ (2 ml) was added dropwise to $[RhCl(NBD)]_2$ (0.5 equiv.) and left to stir at room temperature for one hour. This solution was then added dropwise to Na[BAr^F_4] (1 equiv.) in 1,2-difluorobenzene (2 ml) and stirred at room temperature for one hour which resulted in formation of a precipitate (NaCl). The solution was filtered, and the precipitate was washed with 1,2-difluorobenzene then the solvent removed *in vacuo* leaving an oily residue. The residue was washed with pentane (3 x 5 ml) and the resulting orange solid was dried under Schlenk line vacuum (< 1 x 10^{-1} mbar) overnight to leave a dry solid (all orange crystalline solids) that were stored in an argon glovebox.

2-H (85% yield): NMR data at 298 K as previously reported.[14]

$^{31}P\{^{1}H\}$ NMR (202 MHz, $CDCl_2F$, 140 K): δ 21.5 (br d, *J*(RhP) = 154 Hz) and 13.8 (br d, *J*(RhP) = 154 Hz).

^{1}H NMR (500 MHz, $CDCl_2F$, 140 K) selected data: δ 8.32 (br s, *ortho*-CH).

2-Me (75% yield):

$^{31}P\{^{1}H\}$ NMR (162 MHz, acetone-D_6, 298 K): δ 17.6 (br s), 8.5 (d, 154 Hz), 2.8 ppm (br s).

$^{31}P\{^{1}H\}$ NMR (162 MHz, acetone-D_6, 183 K): δ 18.0 (dd, *J*(RhP) = 161 Hz, *J*(PP) = 28 ppm) and 1.82 (dd, *J*(RhP) = 152 Hz, *J*(PP) = 28 ppm).

^{1}H NMR (400 MHz, acetone-D_6, 298 K): δ 7.78 (s, 8H, *o*-C*H* BAr^{F}_4), 7.66 (s, 4H, *p*-CH BAr^{F}_4), 7.62-7.26 ppm (br m, 14H Ar), 7.25-7.02 (br s, 5H, Ar), 6.91 (m, 4H, Ar), 6.75 (br s, 1H, Ar), 4.11-3.31 (br s, 6H, sp^3-C*H* NBD (2H), sp^2-C*H* NBD (4H)), 2.23-1.51 (br s, 12H, CH_3), 1.38 (br s, sp^3-CH_2 NBD).

^{1}H NMR (400 MHz, acetone-D_6, 183 K): δ 10.27 (dd, *J*(PH) = 17 Hz, *J*(HH) = 7 Hz, 1H, *ortho*-H on substituted phenyl), 7.89 (s, 8H, *o*-CH BAr^{F}_4), 7.77 (s, 4H, *p*-CH BAr^{F}_4), 7.72-7.20 (m, 14H, Ar), 7.06 (m, 3H, Ar), 6.88 (m, 3H, Ar), 6.79 (dd, *J*(HH) = 8 Hz, *J*(PH) = 8 Hz, 1H, Ar), 6.68 (t, *J*(HH) = 7 Hz, 1H, Ar), 6.16 (dd, *J*(HH) = 8 Hz, *J*(PH) = 12 Hz, 1H, Ar), 5.34 (s, 1H, sp^2-C*H* NBD), 4.05 (s, 1H, sp^3-C*H* NBD), 3.85 (s, 1H, sp^2-C*H* NBD), 3.71 (s, 1H, sp^3-C*H* NBD), 3.68 (s, 3H, CH_3), 3.43 (m, 2H, sp^2-C*H* NBD), 1.92 (br s, CH_3), 1.58 (s, CH_3) and 1.27 (m, CH_2 NBD).

^{1}H NMR (500 MHz, CD_2Cl_2, 203 K) selected data: δ 9.97 (dd, 1H, *J*(PH) = 17 Hz, *J*(HH) = 8 Hz, *ortho*-H on substituted phenyl), 3.56 (s, 3H, CH_3).

ESI-MS (1,2-difluorobenzene): *m/z* $[M]^+$ 789.20 (Calc. 789.19) with the correct isotope pattern.

Elemental analysis found (calc. for $C_{79}H_{56}BF_{24}OP_2Rh$): C 57.52 (57.40) H 3.53 (3.42).

2-OMe (78 % yield).

$^{31}P\{^{1}H\}$ NMR (202 MHz, acetone-D_6, 298 K): δ 7.3 ppm (br s).

$^{31}P\{^{1}H\}$ NMR (202 MHz, acetone-D_6, 183 K) major isomer: δ 13.9 (dd, *J*(PP) = 27 Hz, *J*(RhP) = 164 Hz) and -0.6 (dd, *J*(PP) = 27 Hz, *J*(RhP) = 156 Hz), **minor isomer:** 11.2 (dd, *J*(PP) = 28 Hz, *J*(RhP) = 162 Hz) and -2.7 (dd, *J*(PP) = 28 Hz, *J*(RhP) = 158 Hz).

^{1}H NMR (500 MHz, acetone-D_6, 298 K: δ 7.79 (s, 8H, *o*-C*H* BAr^{F}_4), 7.67 (s, 4H, *p*-CH BAr^{F}_4), 7.53 (br s, 4H, Ar), 7.38-7.12 (m, 6H, Ar), 7.10-6.55 (m, 14H, Ar), 4.46-3.10 [broad overlapping signals, sp^2-C*H* NBD (4H), sp^3-C*H* NBD (2H) and OCH_3 (12H)] and 1.31 (s, 2H, CH_2 NBD).

^{1}H NMR (500 MHz, acetone-D_6, 183 K) major isomer: δ 9.53 (dd, *J*(PH) = 16 Hz, *J*(HH) = 7 Hz, 1H, *ortho*-H on substituted phenyl), 7.88 (s, 8H, *o*-C*H* BAr^{F}_4), 7.77 (s, 4H, *p*-CH BAr^{F}_4), 7.69-6.65 (complex multiplet, 21H, Ar), 6.57 (t, *J*(HH) = 7 Hz, 1H, Ar), 6.17 (t, *J*(HH) = 9 Hz, 1H, Ar), 4.24 (s, 3H, OCH_3), 4.20 (s, 1H, sp^2-C*H* NBD), 4.05 (s, 1H, sp^2-C*H* NBD), 3.82 (s, 3H, OCH_3), 3.81 (s, 1H, sp^2-C*H* NBD), 3.64 (s, 3H, OCH_3), 3.63 (br s, 2H, sp^2-C*H* and sp^3-C*H* NBD), 3.37 (s, 1H, sp^3-C*H* NBD), 3.26 (s, 3H,

OCH_3) and 1.24 (s, 2H, CH_2), **selected data minor isomer**: δ 9.37 (dd, *J*(PH) = 16 Hz, *J*(HH) = 7 Hz, 1H, *ortho*-H).

^{1}H NMR (500 MHz, CD_2Cl_2, 203 K) selected data major isomer: δ 9.19 (dd, 1H, *J*(PH) = 17 Hz, *J*(HH) = 7 Hz, *ortho*-H on substituted phenyl), **selected data minor isomer**: δ 9.32 (dd, *J*(PH) = 17 Hz, *J*(HH) = 7 Hz, 1H, *ortho*-H).

ESI-MS (1,2-difluorobenzene): *m/z* $[M]^+$ 853.18 (Calc. 853.17) with the correct isotope pattern.

Multiple samples were submitted for elemental analysis, but no results were within 0.4% of the theoretical percentage mass for carbon or hydrogen. Persistent pentane after recrystallisation may be the cause of the inconsistent elemental analysis.

[Rh(*o*-^{i}Pr-DPEphos)(NBD)][BAr^F_4] **2-^{i}Pr**

Ligand **1-^{i}Pr** (151 mg, 0.21 mmol) in 1,2-difluorobenzene (2 ml) was added dropwise to [Rh(NBD)$_2$][Bar^F_4] (246 mg, 0.21 mmol) to form a dark red solution. The solvent was removed *in vacuo* to leave a purple residue that was dissolved in DCM (2 ml) and added dropwise to a stirring flash of pentane (20 ml) that produced an orange precipitate. The solid was filtered and washed with pentane (3 x 5 ml) and then dried under Schlenk line vacuum (< 1 x 10^{-1} mbar) overnight to leave an orange solid (241 mg, 0.14 mmol, 65% yield).

^{31}P{^{1}H} NMR (202 MHz, acetone-D_6, 298 K): δ 20.8 (d, *J*(RhP) = 153 Hz).

^{1}H NMR (500 MHz, acetone-D_6, 298 K): δ 9.34 (dd, 2H, *J*(PH) = 17 Hz, *J*(HH) = 7 Hz, *ortho*-H on substituted phenyl), 7.96 (m, 2H, Ar), 7.79 (s, 8H, *o*-C*H* BAr^F_4), 7.71 (m, 4H, Ar), 7.67 (s, 4H, *p*-CH BAr^F_4), 7.56-7.30 (m, 10H, Ar), 7.17 (m, 4H, Ar), 6.80 (br s, 2H, Ar) 4.44 (s, 2H, sp^2 C*H*-NBD), 3.74 (s, 2H, sp^2 C*H*-NBD), 3.33 (m, 4H, sp^3 C*H*-NBD and methine C*H*), 2.91 (sept, 2H, *J*(HH) = 6 Hz, methine C*H*), 2.00 (d, 6H *J*(HH) = 6 Hz, CH_3), 1.51 (d, 6H, *J*(HH) = 6 Hz, CH_3), 1.27 (s, 2H, CH_2 NBD) 1.05 (d, 6H, *J*(HH) = 6 Hz, CH_3), 0.21 (d, 6H, *J*(HH) = 6 Hz, CH_3).

^{1}H NMR (500 MHz, CD_2Cl_2, 203 K) selected data: δ 9.14 (dd, 2H, *J*(PH) = 18 Hz, *J*(HH) = 8 Hz, *ortho*-H on substituted phenyl).

ESI-MS (1,2-difluorobenzene): *m/z* $[M]^+$ 901.32 (Calc. 901.3169) with the correct isotope pattern.

Elemental analysis found (calc. for $C_{87}H_{72}BF_{24}OP_2Rh$): C 59.06 (59.20) H 3.98 (4.11).

[Rh(*o*-Me-DPEphos)$(H)_2$(acetone)][BAr^F_4] **4-Me** and [Rh(*o*-Me-DPEphos)$(acetone)_2$][BAr^F_4] **3-Me**

A sample of **2-Me** (~20 mg) was dissolved in 0.5 ml acetone-D_6 in a high-pressure J. Youngs NMR tube and degassed by three successive freeze-pump thaws. The NMR tube was then put under an atmosphere of 2 bar H_2, shaken, then left for 30 minutes. The solution turned from orange to yellow (**4-Me**). The sample was then degassed again by five successive freeze-pump-thaws and put under an atmosphere of argon, resulting in a colour change to red (**3-Me**). Persistent vacuum on removal of solvent resulted in decomposition of **3-Me**.

4-Me:

$^{31}P\{^1H\}$ NMR (202 MHz, acetone-D_6, 298 K): δ 26.0 (br s).

$^{31}P\{^1H\}$ NMR (202 MHz, acetone-D_6, 183 K): δ 43.1 (dd, *J*(RhP) = 121 Hz, *J*(PP) = 343 Hz) and 23.3 (dd, *J*(RhP) = 114 Hz, *J*(PP) = 343 Hz).

^1H NMR (500 MHz, acetone-D_6, 298 K): δ 7.97 (br d, 2H, *J* = H, Ar), 7.85-7.72 (overlapping signals, 10 H, *o*-C*H* BAr^F_4 and Ar), 7.67 (s, 4H, *p*-CH BAr^F_4), 7.62-7.18 (br multiplet, 20 H, Ar), 2.50-2.10 (br multiplet, 12H, CH_3), –19.51 (br s, 2H, Rh–H).

^1H NMR (500 MHz, acetone-D_6, 183 K) major isomer: δ 8.28 (multiplet, 2H, Ar), 7.98-7.81 (overlapping signals, 10 H, *o*-C*H* BAr^F_4 and Ar), 7.77 (s, 4H, *p*-CH BAr^F_4), 7.69 (multiplet, 2H, Ar), 7.62-7.18 (br multiplet, 16 H, Ar), 2.55 (s, 3H, CH_3), 2.36 (s, 3H, CH_3), 2.08 (s, 3H, CH_3), 1.87 (s, 3H, CH_3), –18.36 (dddd, 1H, *J*(RhH) = 24 Hz, *J*(*cis*-PH) = 12 Hz, *J*(*cis*-PH) = 12 Hz, *J*(*cis*-HH) = 8 Hz, Rh–H) and –20.32 (dddd, 1H, *J*(RhH) = 30 Hz, *J*(*cis*-PH) = 12 Hz, *J*(*cis*-PH) = 12 Hz, *J*(*cis*-HH) = 8 Hz, Rh–H)).

^1H NMR (500 MHz, acetone-D_6, 183 K) major isomer, selected data: δ –18.34 (dd, 1H, *J*(RhH) = 24 Hz and $J_{H(cis)H}$ = 8 Hz, Rh–H) and –20.31 (dd, 1H, *J*(RhH) = 30 Hz and *J*(*cis*-HH)= 8 Hz, Rh–H).

^1H NMR (500 MHz, acetone-D_6, 183 K) minor isomer, selected data: δ 4.18 (s, 3H, CH_3), 3.81 (s, 3H, CH_3), 3.68 (s, 3H, CH_3), 2.47 (s, 3H, CH_3), –18.02 (br s, 1H, *J*(RhH) = 24 Hz, *J*(*cis*-PH) = 12 Hz, *J*(*cis*-PH) = 12 Hz, *J*(*cis*-HH) = 8 Hz, Rh–H) and –19.97 (dddd, 1H, *J*(RhH) = 30 Hz, *J*(*cis*-PH) = 12 Hz, *J*(*cis*-PH) = 12 Hz, *J*(*cis*-HH) = 8 Hz, Rh–H)).

3-Me:

$^{31}P\{^{1}H\}$ NMR (202 MHz, acetone-D_6, 298 K): δ 39.6 (br d, *J*(RhP) = 194 Hz) and 29.0 (br d, *J*(RhP) = 199 Hz).

^{1}H NMR (500 MHz, acetone-D_6, 298 K): δ 10.73 (br s, 1H, Ar), 7.96 (m, 1H, Ar), 7.79 (8H, *o*-C*H* BAr^{F}_4), 7.67 (s, 4H, *p*-CH BAr^{F}_4), 7.63-5.75 (complex m, 22H, Ar), 3.53 (br s, 3H, Ar-CH_3), 2.67 (br multiplet, 6H, Ar-CH_3), 2.35 (br s, 3H, Ar-CH_3).

[Rh(*o*-OMe-DPEphos)$(H)_2$(acetone)][BAr^{F}_4] **3-OMe**:

A sample of **2-OMe** (~20 mg) was dissolved in 0.5 ml acetone-D_6 in a high-pressure J. Youngs NMR tube and degassed by three successive freeze-pump thaws. The NMR tube was then put under an atmosphere of 2 bar H_2, shaken, then left for 30 minutes. The solution turned from orange to red (**3-OMe**). The sample did not change after five successive freeze-pump-thaws. Persistent vacuum on removal of solvent resulted in decomposition of **3-OMe**.

$^{31}P\{^{1}H\}$ NMR (162 MHz, acetone-D_6, 298 K): δ 44.7 (dd, *J*(RhP) = 168 Hz and *J*(PP) = 27 Hz), 36.6 (br multiplet) and 31.6 (br multiplet).

^{31}P $\{^{1}H\}$ NMR (162 MHz, acetone-D_6, 193 K): δ 44.3 (complex multiplet), 37.5 (dd, *J*(RhP) = 223 Hz and *J*(PP) = 58 Hz), 36.2 (d, *J*(RhP) = 213 Hz), 33.2 (dd, *J*(RhP) = 220 Hz and *J*(PP) = 58 Hz), 30.3 (dd, *J*(RhP) = 205 Hz and *J*(PP) = 58 Hz), 29.4 (dd, *J*(RhP) = 210 Hz and *J*(PP) = 58 Hz) and 19.7 (complex multiplet).

^{1}H NMR (400 MHz, acetone-D_6, 298 K): δ 8.09 (complex multiplet, 2H, Ar), 7.79 (8H, *o*-C*H* BAr^{F}_4), 7.67 (s, 4H, *p*-CH BAr^{F}_4), 7.64-6.26 (complex m, 22H, Ar), 3.69 (complex multiplet, 12H, OCH_3).

^{1}H NMR (400 MHz, acetone-D_6, 193 K) selected data: δ 9.16 (dd, 1H, anagostic Ar-*H*).

[Rh(*o*-^{i}Pr-DPEphos')(H)][BAr^{F}_4] **4-^{i}Pr**:

A sample of **2-^{i}Pr** (~20 mg) was dissolved in 0.5 ml acetone-D_6 in a high-pressure J. Youngs NMR tube and degassed by three successive freeze-pump thaws. The NMR tube was then put under an atmosphere of 2 bar H_2, shaken, then left for 30 minutes. The solution turned from orange to yellow (**4-**

Pr). The sample did not change after five successive freeze-pump-thaws. Persistent vacuum on removal of solvent resulted in decomposition of **4-^{i}Pr**.

^{31}P{^{1}H} NMR (162 MHz, acetone-D$_6$, 298 K): δ 20.8 (br s).

^{31}P{^{1}H} NMR (162 MHz, acetone-D$_6$, 183 K): δ 39.7 (dd, *J*(RhP) = 121 Hz and *J*(PP) = 357 Hz, isomer **a**), 26.1 (complex multiplet that contains the second ^{31}P environment for the three major isomers), 14.0 (dd, *J*(RhP) = 119 Hz and *J*(PP) = 359 Hz, isomer **b**) and 5.6 (dd, *J*(RhP) = 112 Hz and *J*(PP) = 362 Hz, isomer **c**).

^{1}H NMR (400 MHz, acetone-D$_6$, 298 K): δ 7.99 (multiplet, 2H, Ar), 7.79 (8H, *o*-CH BAr$^{F}_4$), 7.67 (s, 4H, *p*-CH BAr$^{F}_4$), 7.64-6.44 (complex m, 22H, Ar), 3.37 (br s, 4H, methine C*H*), 1.51-0.38 (br s, 24H, CH_3) and –19.81 (dvt, *J*(RhH) = 29 Hz and *J*(PH) = 15 Hz).

^{1}H NMR (400 MHz, acetone-D$_6$, 183 K): δ 8.27 (multiplet, 1H, Ar), 8.04 (multiplet, 1H, Ar), 7.89 (8H, *o*-CH BAr$^{F}_4$), 7.77 (s, 4H, *p*-CH BAr$^{F}_4$), 7.74-6.18 (complex m, 22H, Ar), 3.37 (br s, 4H, methine C*H*), 1.51-0.38 (br s, 24H, CH_3). There are six signal that could be methine CH signals, all broad singlets at 4.80, 3.65, 3.34, 3.21, 3.10, 2.72 ppm. There are many signals (> 10) in the alkyl region (2-38-0.08 ppm) that overlap with other signals so they cannot be fully assigned but most likely the *iso*-propyl CH_3 groups. Multiple hydride resonances are observed overlapping from –19.40 to –19.95 ppm that integrate to one proton overall.

[Rh(*o*-^{i}Pr-DPEphos)(CO)][BAr$^{F}_4$] **5-^{i}Pr**:

A sample of **2-^{i}Pr** (20 mg, 0.008 mmol) in 1,2-difluorobenzene (0.5 ml) was put under an atmosphere of 2 bar H_2 and left for 30 minutes. The H_2 was removed via three freeze-pump-thaws and the sample was put under an atmosphere of 2 Bar CO resulting in an immediate colour change from yellow to orange. The CO was removed via three times freeze-pump-thaws and the sample refilled with argon. The solution was transferred to a small J. Youngs flask then layered with pentane and kept at -20 ºC yielding orange crystals suitable for single crystal x-ray crystallography after two days that were separated via filtration and dried under Schlenk line vacuum (< 1 x 10^{-1} mbar) overnight (9 mg, 0.005 mmol, 63%).

$^{31}P\{^{1}H\}$ NMR (162 MHz, acetone-D_6, 298 K): δ 19.9 (d, *J*(RhP) = 123 Hz).

^{1}H NMR (500 MHz, acetone-D_6, 298 K): δ 7.97-7.55 (complex m, 25H, *o*-C*H* BAr^F_4 (8H), *p*-CH BAr^F_4 (4H) and Ar (13H)), 7.53-7.21 (m, 10H, Ar), 7.02 (br s, 1H, Ar), 4.74 (br s, 2H, methine C*H*) 3.10 (br s, 2H, methine C*H*), 1.49 (br s, 6H, CH_3), 1.17 (br s, 12H, CH_3), 0.40 (br s, 6H CH_3).

^{1}H NMR (500 MHz, acetone-D_6, 183 K): selected data δ 1.41 (d, *J*(HH) = 4 Hz, 6H, CH_3), 1.19 (d, *J*(HH) = 4 Hz, 6H, CH_3), 1.00 (d, *J*(HH) = 4 Hz, 6H, CH_3), 0.14 (d, *J*(HH) = 5 Hz, 6H, CH_3).

ESI-MS (1,2-difluorobenzene): *m/z* $[M]^+$ 837.249 (Calc. 837.250) with the correct isotope pattern.

Elemental analysis found (calc. for $C_{87}H_{72}BF_{24}OP_2Rh$): C 56.73 (57.19) H 3.73 (3.79).

IR (CO stretch): 2023 cm^{-1}

[Rh(*o*-^{i}Pr-DPEphos)(η^{2}η^2-$H_3B{\cdot}NMe_3$)][BAr^F_4] **6-^{i}Pr** and [Rh(κ^2-P,P-(*o*-^{i}Pr-DPEphos'')-η^2-BH_2NMe_3)][BAr^F_4] **7-^{i}Pr**

A sample of **2-^{i}Pr** (30 mg, 0.017 mmol) in 1,2-difluorobenzene was put under an atmosphere of 2 bar H_2 and rotated for 30 minutes. The sample was degassed by three successive freeze-pump-thaws and the sample put under an atmosphere of argon. $H_3B{\cdot}NMe_3$ (37 mg, 0.051 mmol, 3 equiv.) in 1,2-difluorobenzene (0.5 ml) was added to the yellow solution which formed a blue solution (**6-^{i}Pr**). 3,3-dimethylbutene (11 µl, 0.085 mmol, 5 equiv.) was then added and the solution was left for seven days with occasional shaking. The solvent was mostly removed *in vacuo* and then pentane was added to crash out a green precipitate. The solid was isolated by filtration and dried under Schlenk line vacuum (<1 x 10^{-1} mbar) to yield a green solid (27.1 mg, 0.015 mmol, 88% yield). Crystals suitable for x-ray diffraction were obtained by dissolving in minimal 1,2-$F_2C_6H_4$ and layering with pentane.

6-^{i}Pr:

$^{31}P\{^{1}H\}$ NMR (202 MHz, CD_2Cl_2, 298 K): δ 31.4 (d, *J*(RhP) = 209 Hz) and 19.4 (d, *J*(RhP) = 176 Hz).

^{1}H NMR (500 MHz, 1,2-$F_2C_6H_4$, 298 K) selected data: δ 8.06 (s, 8H, *o*-CH BAr^F_4), 7.47 (s, 4H, *p*-CH BAr^F_4), 2.54 (s, 9H, $N(CH_3)_3$), –2.80 (br s , 3H, BH_3).

$^{1}H\{^{11}B\}$ NMR (500 MHz, 1,2-$F_2C_6H_{42}$, 298 K) selected data: δ –2.80 (br s, 3H, BH_3).

$^{11}B\{^{1}H\}$ NMR (128 MHz, 1,2-F2C_6H_4, 298 K): δ 21.4 (br s, *B*H_3) and –6.4 (s, BAr^F_4).

7-^{i}Pr:

^{31}P{^{1}H} NMR (202 MHz, CD_2Cl_2, 298 K): δ 29.5 (dd, *J*(RhP) = 187 Hz and *J*(PP) = 31 Hz) and 8.5 (dd, *J*(RhP) = 165 Hz and *J*(PP) = 31 Hz).

^{1}H NMR (600 MHz, CD_2Cl_2, 298 K): δ 7.93 (dd, *J* = 7 Hz and 14 Hz, 1H, Ar) 7.72 (s, 8H, *o*-CH $BAr^F{}_4$), 7.56 (s, 4H, *p*-CH $BAr^F{}_4$), 7.60-6.94 (complex m, 16H Ar), 6.82 (m, 2H, Ar), 6.65 (m, 3H, Ar), 6.46 (dd, *J* = 8 and 11 Hz, 1H, Ar), 6.36 (dd, *J* = 8 and 11 Hz, 1H, Ar), 4.92 (m, 1H, anagostic methine C*H*), 4.75 (m, 1H, anagostic methine C*H*), 3.86 (s, 1H, C=C-*H*), 2.48 (s, 9H, N(CH_3)$_3$), 2.32 (m, 1H, methine C*H*), 1.72 (s, 3H, C=C-CH_3), 1.24 (d, *J*(HH) = 6 Hz, 3H, CH_3), 1.09 (d, *J*(HH) = 6 Hz, 3H, CH_3), 0.83 (d, *J*(HH) = 7 Hz, 3H, CH_3) 0.81 (d, *J*(HH) = 7 Hz, 3H, CH_3), 0.76 (d, *J*(HH) = 6 Hz, 3H, CH_3), 0.30 (d, *J*(HH) = 7 Hz, 3H, CH_3) and –7.54 (br s, 1H, agostic B-*H*). Second B*H* signal was not observable without ^{11}B decoupling due to the quadrupolar nature of the bonded B atom.

^{1}H{^{11}B} NMR (600 MHz, CD_2Cl_2, 298 K) selected data: δ 3.86 (s, 1H, C=C-*H*), 1.89 (br d, ^{2}J(HH) = 14 Hz, 1H, B*H*) and –7.54 (ddd, *J*(PB-*trans*) = 52 Hz, ^{2}J(HH) = 14 Hz, *J*(RhH) = 14 Hz, 1H, agostic B-*H*).

^{11}B NMR (128 MHz, CD_2Cl_2, 298 K): δ –6.3 to –14.1 (br s, *B*H_2) and –9.1 (s, $BAr^F{}_4$).

ESI-MS (1,2-difluorobenzene): *m/z* $[M]^+$ 878.33 (Calc. 878.33) with the correct isotope pattern.

Multiple samples were submitted for elemental analysis, but no results were within 0.4% of the theoretical percentage mass for carbon, hydrogen, or nitrogen. Persistent pentane after recrystallisation may be the cause of inconsistent elemental analysis.

5.2.2 Chapter Three

o-F,F-DPEphos **1-F,F**

Synthesis of 2,2'-$(PCl_2)_2(C_6H_4)_2O$ was done in accordance with literature procedures.[12, 13] In a separate J. Young's ampoule, N,N,N',N'-tetramethylenediamine (0.42 ml, 2.8 mmol, 4.3 equiv.) was added dropwise to ^{n}BuLi (1.07 ml, 2.4 M solution in hexanes, 2.6 mmol, 4 equiv.) at 0 °C. The mixture was cooled to –78 °C and THF (2 ml) and 2,6-difluorobromobenzene (0.29 ml, 2.6 mmol, 4 equivalents) were added dropwise and the mixture was left to stir for 1 hour at –78 °C. The previously prepared 2,2'-$(PCl_2)_2Ph_2O$ (200 mg, 0.54 mmol, 1 equiv.) in 4 ml of THF was cooled to –78 °C and the aryl lithium was added dropwise, keeping both solutions at –78 °C. The resulting orange mixture was allowed to

warm to room temperature, then stirred for 30 minutes and checked by ^{19}F and ^{31}P NMR spectroscopy for completion. The mixture was then cooled to 0 °C, quenched with methanol (1 ml) and saturated ammonium chloride solution (10 ml). The now air stable product was extracted with ethyl acetate (3 x 10 ml), dried over Na_2SO_4, filtered, and washed with cold pentane yielding the product as a white solid. Recrystallisation with pentane and CH_2Cl_2 yielded **1-F,F** as a white microcrystalline solid (109 mg, 30%).

$^{31}P\{^1H\}$ NMR (202 MHz, CD_2Cl_2, 295 K): δ –62.5 (quint, J_{FP} = 40 Hz).

^{19}F NMR (471 MHz, CD_2Cl_2, 295 K): δ –100.7 (d, J_{PF} = 40 Hz).

^1H NMR (500 MHz, CD_2Cl_2, 295 K): δ 7.33 (tt, *J* = 8 Hz and 6 Hz, 4H, *para*-H on substituted aryl), 7.26 (m, *J* = 8 and 2 Hz, 2H, backbone-Ar), 7.06 (dd, *J* = 7 and *J*(PH) = 4 Hz, 2H, backbone-Ar), 7.00 (dd, *J* = 8 and 7 Hz, 2H, backbone-Ar), 6.82 (dt, *J* = 8 and 2 Hz, 8H, *meta*-H on substituted phenyl), 6.74 (dd, *J*(HH) = 8 and *J*(PH) = 5 Hz, 2H, backbone-Ar).

$^{13}C\{^1H\}$ NMR (126 MHz, CD_2Cl_2, 295 K): δ 165.6 – 163.6 (dt, J_{CF} = 250 and J_{CP} = 9 Hz, Ar), 158.9 (s, Ar), 158.5 (s, Ar), 132.2 (s, Ar), 132.0 (t, *J* = 11 Hz), 130.4 (d, *J* = 1 Hz Ar), 123.5 (s, Ar), 117.4 (s, Ar), 111.6 (d, *J* = 5 Hz, Ar), 111.4 (dd, *J* = 5 Hz, *J* = 1 Hz, Ar).

ESI-MS (CH_2Cl_2): *m/z* $[M+H]^+$ 683.0942 (calc. 683.0934) with the correct isotope pattern.

Elemental analysis found (calc. for $C_{36}H_{20}F_8OP_2$): C 63.38 (63.35) H 3.19 (2.95).

[Rh(*o*-F,F-DPEphos)(NBD)][BAr^F_4] **2-F,F**

1,2-$F_2C_6H_4$ (10 ml) was added to [$Rh(NBD)_2$][BAr^F_4] (63 mg, 0.055 mmol, 1 equiv.)[15, 16] and **1-F,F** (38 mg, 0.055 mmol, 1 equiv.) in a J. Young's Ampoule to form an orange solution. The mixture was stirred for two hours at room temperature. The solvent was removed *in vacuo* to leave a purple oil which was triturated with pentane to give a red solid. The solid was filtered and washed with further pentane (3 x 5 ml) and dried under Schlenk line vacuum (< 1 x 10^{-1} mbar) overnight, leaving **2-F,F** as an orange microcrystalline powder (73 mg, 77%,).

$^{31}P\{^1H\}$ NMR (202 MHz, CD_2Cl_2, 295 K): δ –17.4 (d, *J*(RhP) = 163 Hz).

$^{31}P\{^1H\}$ NMR (202 MHz, CD_2Cl_2, 223 K): δ –17.1 (dd, *J*(RhP) = 163 Hz and *J*(PF) = 38 Hz).

^{19}F NMR (471 MHz, CD_2Cl_2, 295 K): δ –90.9 (br s, 2F), –97.8 (br s, 4F), –102.4 (br s, 2F).

^{19}F NMR (471 MHz, CD_2Cl_2, 183 K) selected data: δ –90.8 (s, 2F), –97.9 (s, 2F), –98.1 (d, *J*(PF) = 38 Hz, 2F), –103.5 (s, 2F).

^{19}F NMR (471 MHz, CD_2Cl_2, 318 K) selected data: δ –98.1 (br s, 8F).

^{1}H NMR (500 MHz, CD_2Cl_2, 295 K): δ 7.72 (s, 8H, *o*-CH, $BAr^F{}_4$), 7.55 (s, 4H, *p*-CH, $BAr^F{}_4$), 7.51 (br m, 4H, Ar), 7.40 (m, *J* = 9 Hz and 2 Hz, 4H, Ar), 7.13 – 6.83 (complex multiplet, 12H, Ar), 4.16 (s, 4H, sp^2-C*H* NBD), 3.80 (s, 2H, sp^3-C*H* NBD), 1.44 (s, 2H, CH_2 NBD). ^{1}H NMR (500 MHz, CD_2Cl_2, 318 K) selected data: δ 7.73 (s, 8H, *o*-CH, $BAr^F{}_4$), 7.55 (s, 4H, *p*-CH, $BAr^F{}_4$), 4.18 (s, 4H, sp^2-C*H* NBD), 3.81 (s, 2H, sp^3-C*H* NBD), 1.45 (s, 2H, CH_2 NBD).

^{1}H NMR (500 MHz, CD_2Cl_2, 183 K): δ 7.72 (s, 8H, *o*-CH, $BAr^F{}_4$), 7.57 (m, 4H, Ar), 7.51 (s, 4H, *p*-CH, $BAr^F{}_4$), 7.37 (m, 4H, Ar), 7.11 (t, *J* = 9 Hz, 2H, Ar), 7.07 – 6.93 (br m, 8H, Ar), 6.49 (t, *J* = 9 Hz, 2H, Ar), 4.23 (s, 2H, sp^2-C*H* NBD), 3.87 (s, 2H, sp^2-C*H* NBD), 3.74 (s, 2H, sp^3-C*H* NBD), 1.35 (s, 2H, CH_2 NBD).

^{19}F NMR (471 MHz, CD_2Cl_2, 295 K): δ –62.9 (s, 24F, $BAr^F{}_4$), –88.9 to –92.5 (br s, 2F), –95.2 to –100.2 (br s, 4F), –100.6 to –104.5 (br s, 2F).

ESI-MS (1,2-$F_2C_6H_4$): *m/z* $[M]^+$ 877.0557 (calc. 877.0543) with correct isotope pattern.

Elemental analysis found (calc. for $C_{75}H_{40}BF_{32}OP_2Rh$): C 51.74 (51.75) H 2.40 (2.32).

[Rh(*o*-F,F-DPEphos)(acetone)$_2$][$BAr^F{}_4$] **3-F,F**

A sample of [Rh(*o*-F,F-DPEphos)(NBD)][$BAr^F{}_4$] **2-F,F** (40 mg, 0.023 mmol) was dissolved in acetone-D_6 (0.5 ml) in a high pressure J. Youngs NMR tube. The atmosphere was removed by three successive freeze-pump-thaws and the NMR tube was placed under an atmosphere of 15 PSI H_2 and successively rotated for ten minutes which formed a deep red solution. **3-F,F** was characterised in-situ by multinuclear NMR spectroscopy (consistent application of vacuum for solvent removal resulted in the decomposition of **3-F,F**).

^{31}P{^{1}H} NMR (202 MHz, acetone-D_6, 298 K): δ 3.0 (d, *J*(RhP) = 222 Hz).

^{19}F NMR (471 MHz, acetone-D_6, 298 K): –63.3 (s, 24F, $Ar^F{}_4$), –97.2 (s, 8F, 2,6-$F_2C_6H_3$).

^{1}H NMR (500 MHz, acetone-D_6, 298 K) selected data: δ 7.79 (s, 8H, *ortho*-H $BAr^F{}_4$), 7.67 (s, 4H, *para*-H $BAr^F{}_4$), 7.59 (m, 4H, *p*-H), 7.51 (dd, *J*(HH) = 7 Hz, 2H, backbone-H), 7.16 (m, 4H, 2 x backbone-H), 7.08 (t, J(HH) = 8 Hz, 2H, backbone-H), 6.97 (dd, *J* = 9 Hz, 8H, *m*-H).

[Rh(*o*-H-DPEphos)(μ-H)][BAr^F_4] **4-H**

A sample of [Rh(*o*-H,H-DPEphos)(NBD)][BAr^F_4] **2-H** (40 mg, 0.025 mmol) was dissolved in 1-2-$F_2C_6H_4$ (0.5 ml) in a high pressure J. Youngs NMR tube. The atmosphere was removed by three successive freeze-pump-thaws and the NMR tube was placed under an atmosphere of 15 PSI H_2 and successively rotated for ten minutes which formed a dark red solution. The 1-2-$F_2C_6H_4$ solution was transferred to a Youngs Flask equipped with a stirrer bar. Pentane (5 ml) was added to the solution with vigorous stirring and a purple solid precipitated. The solvent was removed by filter cannular and the purple solid was washed with pentane twice more (5 ml) before drying under Schlenk line vacuum (< 1 x 10^{-1} mbar) for two hours (30 mg, 0.010 mmol, 80%).

$^{31}P\{^1H\}$ NMR (243 MHz, CD_2Cl_2, 298 K): δ 43.3 (dd, *J*(RhP) = 174 Hz and *J*(PP) = 26 Hz), 36.5 (complex 2nd order multiplet).

^{31}P NMR (243 MHz, CD_2Cl_2, 298 K): δ 43.3 (br d, *J*(RhP) = 174 Hz), 36.5 (br dd, *J*(RhP) = 154 Hz, *J*(PH) = 74 Hz).

^1H NMR (600 MHz, CD_2Cl_2, 298 K): δ 7.23 (s, 16H, *ortho*-H BAr^F_4), 7.60-7.50 (m, 6H, Ar), 7.55 (s, 8H, *para*-H BAr^F_4), 7.47 (m, 3H, Ar) 7.48 7.44-7.37 (m, 6H, Ar), 7.34-7.20 (m, 14H, Ar), 7.14 (dd, *J* = 6 Hz, 3H, Ar), 7.12-7.04 (m, 5H, Ar), 6.97 (dd, *J* = 8 and 12 Hz, 4H, Ar), 6.84-6.78 (m, 6H, Ar), 6.68 (dd, *J* = 7 Hz, 2H, Ar), 5.15 (dd, *J*(PH) = 4 and *J*(HH) 8 Hz, 2H, CH *σ*-agostic), –11.13 (complex multiplet, $J(PH)_{(trans)}$ = 74 Hz, $J(PH)_{(cis)}$ = 17 Hz, *J*(RhH) = 20 Hz, 1H, bridging hydride *trans* to ^{31}P) and –15.59 (complex multiplet, *J*(RhH) = 34 Hz, $J(PH)_{(cis)}$ = 5 Hz, $J(PH)_{(cis)}$ = 9 Hz, 1H, bridging hydride *trans* to CH σ-agostic).

$^1H\{^{31}P\}$ NMR (600 MHz, CD_2Cl_2, 298 K) selected data: δ –11.13 (apparent triplet, *J*(RhH) = 20 Hz, 1H, bridging hydride *trans* to ^{31}P), –15.59 (apparent triplet, *J*(RhH) = 34 Hz, 1H, bridging hydride *trans* to CH *σ*-agostic).

[Rh(*o*-F,F-DPEphos)$(H)_2$][BAr^F_4] **4-F,F**

A sample of [Rh(*o*-F,F-DPEphos)(NBD)][BAr^F_4] **3-F,F** (40 mg, 0.023 mmol) was dissolved in 1-2-$F_2C_6H_4$ (0.5 ml) in a high pressure J. Youngs NMR tube. The atmosphere was removed by three successive

freeze-pump-thaws and the NMR tube was placed under an atmosphere of 15 PSI H_2 and successively rotated for ten minutes which formed a yellow solution. **4-F,F** was characterised in-situ by multinuclear NMR spectroscopy (removal of the hydrogen atmosphere resulted in decomposition).

$^{31}P\{^1H\}$ NMR (243 MHz, 1,2-$F_2C_6H_4$, 298 K): δ –6.7 (d, *J*(RhP) = 130 Hz).

^{19}F NMR (565 MHz, 1,2-$F_2C_6H_4$, 298 K): –63.1 (s, 24F, $Ar^F{}_4$), –100.9 (s, 8F, 2,6-$F_2C_6H_3$).

^1H NMR (600 MHz, 1,2-$F_2C_6H_4$, 298 K) selected data: δ 8.11 (s, 8H, *ortho*-H $BAr^F{}_4$), 7.47 (s, 4H, *para*-H $BAr^F{}_4$) –20.0 (dt, *J*(PH) = 17 Hz, *J*(RhH) = 34 Hz, 2H, Rh–H).

$^1H\{^{31}P\}$ NMR (600 MHz, 1,2-$F_2C_6H_4$, 298 K) selected data: δ –20.00 (d, *J*(RhH) = 34 Hz).

[Rh(*o*-Me-DPEphos)$(H)_2$][$BAr^F{}_4$] **4-MeH** and [Rh(*o*-Me-DPEphos)(η^6-1,2-$F_2C_6H_4$)][$BAr^F{}_4$] **5-Me**

A sample of [Rh(*o*-Me-DPEphos)(NBD)][$BAr^F{}_4$] (40 mg, 0.023 mmol) was dissolved in 1-2-$F_2C_6H_4$ (0.5 ml) in a high pressure J. Youngs NMR tube. The atmosphere was removed by three successive freeze-pump-thaws and the NMR tube was placed under an atmosphere of 15 PSI H_2 and successively rotated for ten minutes which formed a yellow solution. [Rh(*mer*-κ^3-*o*-Me-DPEphos)$(H)_2$][$BAr^F{}_4$], **4-MeH**, was characterised in-situ by multinuclear NMR spectroscopy. Removal of the hydrogen atmosphere by ten successive freeze-pump-thaws resulted in a colour change from yellow to red and the concurrent formation of a complex that is tentatively assigned as the solvated complex [Rh(*o*-Me-DPEphos)(η^6-1,2-$F_2C_6H_4$)][$BAr^F{}_4$], **5-Me**, in 1:2 ratio of **4-MeH**:**5-Me**.

4-MeH:

$^{31}P\{^1H\}$ NMR (243 MHz, 1,2-$F_2C_6H_4$, 298 K): δ 27.1 (br s).

^1H NMR (600 MHz, 1,2-$F_2C_6H_4$, 298 K) selected data: δ 7.85 (s, 8H, *ortho*-H $BAr^F{}_4$), 7.20 (s, 4H, *para*-H $BAr^F{}_4$), 1.75 (br s, 12H, *o*-CH_3), –19.74 (dt, *J*(PH) = 14 Hz, *J*(RhH) = 40 Hz, 2H, Rh–H).

$^1H\{^{31}P\}$ NMR (600 MHz, 1,2-$F_2C_6H_4$, 298 K) selected data: δ –19.74 (d, *J*(RhH) = 40 Hz).

5-Me:

$^{31}P\{^1H\}$ NMR (243 MHz, 1,2-$F_2C_6H_4$, 298 K): δ 37.1 (d, *J*(RhP) = 207 Hz).

^{1}H NMR (600 MHz, 1,2-$F_2C_6H_4$, 298 K) selected data: δ 7.84 (s, *ortho*-H BAr^F_4), 7.20 (s, *para*-H BAr^F_4), 6.13 (br s, η^6-1,2-$F_2C_6H_4$), 1.65 (br s, *o*-CH_3).

[Au_2Cl_2(*o*-F,F-DPEphos)] **6-F,F**

A solution of **1-F,F** (100 mg, 1.05 equiv.) in CH_2Cl_2 (2 ml) was added dropwise to a CH_2Cl_2 (2 ml) solution of [Au(THT)Cl] (293 mg, 2 equiv.),[17] and left to stir for one hour, leaving a colourless solution. The solvent was mostly removed *in vacuo* before pentane (10 ml) was added, precipitating out a white solid. The precipitate was the filtered and washed with further pentane (4 x 5 ml) and dried under Schlenk line vacuum overnight ($< 1 \times 10^{-1}$ mbar) leaving a white powder that was transferred into an argon glovebox for storage. Colorless crystals suitable for x-ray diffraction were obtained by slow diffusion of pentane into a CH_2Cl_2 solution of **6-F,F**. (26 mg, 52%).

^{31}P{^{1}H} NMR (202 MHz, CD_2Cl_2, 295 K): δ –23.1 (quint, J_{FP} = 25 Hz).

^{19}F NMR (471 MHz, CD_2Cl_2, 295 K): δ –97.3 (dt, J_{PF} = 25 Hz and *J*(FF) = 7 Hz), –97.9 (dt, J_{PF} = 25 Hz and *J*(FF) = 7 Hz).

^{1}H NMR (500 MHz, CD_2Cl_2, 295 K): δ 7.60 (m, 2H, Ar), 7.56 (dd, *J* = 7 Hz, 2H, Ar), 7.44 (m, 2H, Ar), 7.27 (dd, *J* = 7 Hz, 2H, Ar), 7.22 (m, 2H, Ar), 7.06-6.99 (m, 6H {2+4 coincidence}, Ar), 6.82 (ddd, *J* = 9 and 4 Hz, 4H, Ar).

ESI-MS (CH_2Cl_2): *m/z* $[M\text{-}Cl]^+$ 1110.9852 (calc. 1110.9881) with correct the isotope pattern.

Multiple samples were submitted for elemental analysis, but no results were within 0.4% of the theoretical percentage mass by weight for carbon or hydrogen. Persistent pentane may be the cause of the inconsistent elemental analysis.

[Au_2Cl_2(*o*-Me-DPEphos)] **6-Me**

A solution of *o*-Me-DPephos (100 mg, 1.05 equiv.) in CH_2Cl_2 (2 ml) was added dropwise to a CH_2Cl_2 (2 ml) solution of [Au(THT)Cl] (336 mg, 2 equiv.),[17] and left to stir for one hour, leaving a colourless solution. The solvent was mostly removed *in vacuo* before pentane (10 ml) was added, precipitating out a white solid. The precipitate was the filtered and washed with further pentane (4 x 5 ml) and dried under Schlenk line vacuum overnight ($< 1 \times 10^{-1}$ mbar) leaving a white powder that was transferred into

an argon glovebox for storage. Colorless crystals suitable for x-ray diffraction were obtained by slow diffusion of pentane into a CH_2Cl_2 solution of **6-Me** (96.1 mg, 59%).

$^{31}P\{^1H\}$ NMR (243 MHz, CD_2Cl_2, 298 K): major isomer: δ 1.1 (s), minor isomer: δ 21.6 (s).

$^{31}P\{^1H\}$ NMR (202 MHz, CD_2Cl_2, 183 K): major isomer: δ -0.4 (s), minor isomer: δ 21.2 (s), -0.8 (s).

^1H NMR (600 MHz, CD_2Cl_2, 298 K) major isomer: δ 7.63 (t, *J* = 8 Hz, 2H, Ar), 7.47 (t, *J* = 8 Hz, 2H, Ar), 7.41 – 7.06 (br m, 12H, Ar), 6.98 (br m, 4H, Ar), 6.72 (br m, 4H, Ar), 2.83 (br s, 6H, C*H*$_3$), 2.36 (br s, 6H, C*H*$_3$).

^1H NMR (500 MHz, CD_2Cl_2, 183 K) major isomer: δ 7.64 (dd, *J*(HH) = 8 Hz, *J*(HH) = 8 Hz, 2H, Ar), 7.44 (dd, *J*(HH) = 8 Hz, *J*(HH) = 7 Hz, 2H, Ar), 7.35 (dd, *J*(HH) = 7 Hz, *J*(HH) = 6 Hz, 2H, Ar), 7.28 (br s, 4H, Ar), 7.21 (dd, *J*(HH) = 7 Hz, *J*(HH) = 6 Hz, 2H, Ar), 7.15 (dd, *J*(HH) = 8 Hz, *J*(HH) = 8 Hz, 2H, Ar), 7.08 (*J*(HH) = 8 Hz, *J*(HH) = 7 Hz, 2H, Ar), 6.96 (br m, 2H, Ar), 6.74 (br m, 2H, Ar), 6.58 (m, 2H, Ar), 6.50 (m, 2H, Ar), 2.75 (s, 6H, C*H*$_3$), 2.24 (s, 6H, C*H*$_3$), minor isomer: selected data 8.52 (dd, *J*(PH) = 20 Hz, *J*(HH) = 8 Hz, 2H, *ortho*-H on substituted phenyl), 2.77 (s, 3H, C*H*$_3$), 2.29 (s, 3H, C*H*$_3$), 1.96 (s, 3H, C*H*$_3$), 1.32 (s, 3H, C*H*$_3$)

ESI-MS (CH_2Cl_2): *m/z* $[M\text{-}Cl]^+$ 1023.1278 (calc. 1023.1261) with the correct isotope pattern.

Elemental analysis found (calc. for $C_{40}H_{36}Au_2Cl_2OP_2$): C 45.34 (45.34) H 3.20 (3.42).

5.3 Procedures used in Chapter Four

General procedure for preparation of $[H_2BPPhH]_n$ and $[H_2BPAr'H]_n$

Toluene (0.2 ml) was added to a high pressure NMR tube containing $[Rh(dppe)_2]Cl$ (2.3 mg, 0.025 mmol) and either $H_3B{\cdot}PPhH_2$ or $H_3B{\cdot}PAr'H_2$ [0.25 mmol, 1.25 M, Ar' = 3,5-$(CF_3)_2C_6H_3$] and the NMR tube was sonicated for five minutes before being heated to 100 °C with aid of an oil bath and left at this temperature, without stirring, for the specified time, depending on the desired molecular weight. **Important – the NMR tube is kept sealed during the reaction and with 33 mg $H_3B{\cdot}PPhH_2$ (0.25 mmol) the pressure is 3.9 Bar at 100 °C from H_2 evolution**. **Be careful if scaling up**. The reaction mixture was removed from the oil bath and allowed to cool to room temperature. The mixture was then analysed by ^{31}P and ^{11}B NMR spectroscopy to determine the conversion of monomer. The solution was

transferred by cannula to a vial and then hexane was added with vigorous stirring, resulting in the formation of a white precipitate. The polymer was allowed to settle, the solvent was removed and the white solid was dried under Schlenk line vacuum (< 1 x 10^{-1} mbar) for at least two hours before GPC analysis was conducted to determine the molecular weight of the polymer. Depending on the reaction time, different molecular weight polymer was formed, after 19 hours polymer of M_n = 32,000 g mol^{-1} (Đ = 1.7) and 127,500 (Đ = 1.2) for Ar = Ph and 3,5-$(CF_3)_2C_6H_3$ respectively (see section 4.4). The signals in the ^{31}P, ^{1}H and ^{11}B NMR spectra closely replicated the literature data.[7,18]

General Procedure for Preparation of $[H_2BP^nHexH]_n$

Toluene (0.2 ml) was added to a high pressure NMR tube containing $[Rh(dppe)_2]Cl$ (2.3 mg, 0.016 mmol) and $H_3B{\cdot}P^nHexH_2$ (1.6 mmol). The NMR tube was sonicated for five minutes before being heated to 100 °C with aid of an oil bath and left at this temperature, without stirring, for the specified time. The reaction mixture was removed from the oil bath and allowed to cool to room temperature. The mixture was then analysed by ^{31}P and ^{11}B NMR spectroscopy. Signals corresponding to P^nHexH_2, dppe-$(BH_3)_2$, $[H_2BP^nHexH]_n$ and cyclic $[H_2BP^nHexH]_n$ are observed. The solution was filtered through separate Florosil® and Celite® plugs using dichloromethane as the eluent. The solvent mixture was evaporated to dryness and the resultant colourless oil was dried under Schlenk line vacuum (< 1 x 10^{-1} mbar) for at least two hours. GPC analysis revealed the formation of polymer with M_n of 33,000 and Đ = 1.3. Signals in the ^{31}P, ^{1}H and ^{11}B NMR spectra replicated those reported in the literature.[6] Purifying with Florosil® and Celite® plugs removed the remaining $H_3B{\cdot}P^nHexH_2$, free P^nHexPH_2 and some potentially cyclic species,[6] however, the purifying process was not particularly successful and signals corresponding unknown species are persistent in the ^{31}P, ^{11}B and ^{1}H NMR spectra. A lower molecular weight component of the mixture is observable in the GPC trace which could reflect these species.

Isolation of linear dimer $H_3B{\cdot}PPhHBH_2{\cdot}PPhH2$ **LD-Ph**

In a method similar to that previously reported with $[RhCp^*Me(PMe_3)CH_2Cl_2)][BAr^F{}_4]$[19] toluene (1.3 ml) was added to a flask containing $[Rh(dppe)_2]Cl$ (15 mg, 0.016 mmol) and $H_3B{\cdot}PPhH_2$ (200 mg, 1.6 mmol). The flask was sonicated for five minutes before being heated to 100 °C with aid of an oil bath and left

at this temperature, without stirring, for 1.5 hours. The mixture was cooled to room temperature and the solvent was then removed *in vacuo*, resulting in a colourless residue. Hexane (5 ml) was added to the residue before sonication and then solvent was removed *in vacuo* to remove all of the toluene. Hexane (10 ml) was added to the residue and the flask was sonicated for 10 minutes. The solvent mixture was removed by cannula transfer into a separate flask and the colourless solids were washed with hexane (10 ml) two further times and the hexane fractions were combined. The solvent was removed *in vacuo* to leave a combination of $H_3B{\cdot}PPhH_2$ and $PhPH_2BH_2PhPHBH_3$ as an oily residue. $PhPH_2{\cdot}BH_3$ was removed by careful sublimation with a cold finger at –78 °C (50 °C, 5 x 10^{-2} mbar, 15 minutes) and the linear dimer was then diluted in toluene to form a stock solution. A small amount of $H_3BP(Ph)_2CH_2CH_2P(Ph)_2BH_3$ was also still present. The ^{31}P, ^{1}H and ^{11}B NMR spectroscopic signals were in good agreement with those previously reported.[19]

In-situ formation of [RhH(dppe)(σ,η²η²-PPhH·BH_2PPhH·BH_3)][Cl] **4.2**

Through a number of stoichiometric experiments, detailed in section 4.8, the linear dimer bound complex, [Rh(dppe)H(σ,η²η²-PPhH·BH_2PPhH·BH_3)]Cl (**4.2**) is assigned in-situ with the following data which matches with the in-situ catalyst speciation observations.

$^{31}P\{^{1}H\}$ NMR (202 MHz, toluene-D_8, 298 K): δ 55-60 [br multiplet, *P*$Ph_2CH_2CH_2$*P*Ph_2], –40 to –50 [br multiplet, Rh(σ,η²η²-H_3B-*P*PhHBH_2*P*PhHBH_3)].

^{1}H NMR (500 MHz, toluene-D_8, 298 K) selected data: δ 2.09 (s, 4H, $PPh_2CH_2CH_2PPh_2$), –1.9 (br m, 3H, Rh–H_3B), –14.2 (br s, 1H, Rh–H).

$^{11}B\{^{1}H\}$ NMR (160 MHz, toluene-D_8, 298 K) selected data: δ –16.7 (br s, BH_2) and –3.2 (br s, BH_3).

ESI-MS (1,2-$F_2C_6H_4$): *m/z* $[M]^+$ 747.2 (Calc. 747.2) with the correct isotope pattern.

Formation of $[H_2BPPhH]_m$-*b*-$[H_2BP^nHexH]_n$ **BCP-Ph/^{n}Hex**

A copolymer of poly(phenylphosphinoborane) and poly(n-hexylphosphinoborane) was produced via the addition of $H_3BP^nHexH_2$ to preformed and isolated $[H_2BPPhH]_n$, which was formed via the general procedure (above) and a reaction time of 19 hours. $H_3BP^nHexH_2$ (33 mg, 0.25 mmol, 1.25 M),

$[Rh(dppe)_2]Cl$ (2.3 mg, 0.00245 mmol, 1 mol%), $[H_2BPPhH]_n$ (10 mg, M_n = 26,500 g mol^{-1}, Đ = 1.5) and toluene (0.2 ml) were added to a high pressure NMR tube. The NMR tube was sonicated for five minutes before being heated to 100 °C in an oil bath and maintained at this temperature for 66 hours. The reaction mixture was analysed by NMR spectroscopy, which revealed that not all of the $H_3BP^nHexH_2$ had reacted. Signals corresponding to cyclic species of the ^{n}Hex variant, $[H_2BP^nHexH]_n$,[6, 8] and $[H_2BPPhH]_m$ are also observed. The reaction mixture was transferred via cannula to a vial, to which was added hexane (10 ml) and the mixture stirred vigorously for two hours. The solvent was removed and the colourless residue was washed with further hexane (2 x 10 ml). The resultant colourless residue was dried under Schlenk line vacuum (< 1 x 10^{-1} mbar) for two hours. The polymer was characterised via multinuclear NMR spectroscopy, GPC and ESI-MS.

^{31}P NMR (243 MHz, $CDCl_3$, 298 K): –49.4 (br d, J_{PH} = 358 Hz, $[H_2BPPhH]_m$), –63.4 (br m, $[H_2BP^nHexH]_n$).

^{31}P{^{1}H} NMR (243 MHz, CD_2Cl_2, 298 K): δ –49.4 (br s, $[H_2BPPhH]_m$), –63.4 (br m, $[H_2BP^nHexH]_n$).

^{11}B NMR (193 MHz, CD_2Cl_2, 298 K): δ –35.5 (br m).

^{1}H NMR (600 MHz, CD_2Cl_2, 298 K): δ 7.68-6.69 (br m, 5H, $[H_2BPPhH]_m$), 4.27 (br d, J_{PH} = 358 Hz, 1H, $[H_2BPPhH]_m$), 3.66 (br d, J_{PH} = ~340 Hz, 0.3H, $[H_2BP^nHexH]_n$), 1.87-0.69 (br m, 11H,). This latter signal comprises the BH_2 signals of both polymer blocks, the n-hexyl CH_2 signals (δ 1.56 and 1.28) and the CH_3 signal (δ 0.87).

5.4 References

[1] E. W. Abel, M. A. Bennett, G. Wilkinson, *J. Chem. Soc.,* **1959,** 3178-3182.
[2] G. Giordano, R. H. Crabtree, R. M. Heintz, D. Forster, D. E. Morris, *Inorg. Synth.,* **1990,** 88-90.
[3] E. a. K. Spearing-Ewyn, N. A. Beattie, A. L. Colebatch, A. J. Martinez-Martinez, A. Docker, T. M. Boyd, G. Baillie, R. Reed, S. A. Macgregor, A. S. Weller, *Dalton Trans.,* **2019,** 48, 14724-14736.
[4] K. Bourumeau, A.-C. Gaumont, J.-M. Denis, *J. Organomet. Chem.,* **1997,** 529, 205-213.
[5] B. Mohr, D. M. Lynn, R. H. Grubbs, *Organometallics,* **1996,** 15, 4317-4325.
[6] D. A. Resendiz-Lara, V. T. Annibale, A. W. Knights, S. S. Chitnis, I. Manners, *Macromolecules,* **2021,** 54, 71-82.
[7] J. R. Turner, D. A. Resendiz-Lara, T. Jurca, A. Schäfer, J. R. Vance, L. Beckett, G. R. Whittell, R. A. Musgrave, H. A. Sparkes, I. Manners, *Macromol. Chem. Phys.,* **2017,** 218, 1700120.
[8] H. Cavaye, F. Clegg, P. J. Gould, M. K. Ladyman, T. Temple, E. Dossi, *Macromolecules,* **2017,** 50, 9239-9248.
[9] A. T. Lubben, J. S. Mcindoe, A. S. Weller, *Organometallics,* **2008,** 27, 3303-3306.
[10] G. T. Thomas, L. Macgillivray, N. L. Dean, R. L. Stoddard, L. P. E. Yunker, J. S. Mcindoe, *Int. J. Mass spectrom.,* **2019,** 441, 14-18.
[11] K. L. Vikse, M. P. Woods, J. S. Mcindoe, *Organometallics,* **2010,** 29, 6615-6618.

[12] Y. Zhu, V. H. Rawal, *J. Am. Chem. Soc.,* **2012,** 134, 111-114.
[13] J. Wang, G. Meng, K. Xie, L. Li, H. Sun, Z. Huang, *ACS Catal.,* **2017,** 7, 7421-7430.
[14] G. L. Moxham, H. E. Randell-Sly, S. K. Brayshaw, R. L. Woodward, A. S. Weller, M. C. Willis, *Angew. Chem. Int. Ed.,* **2006,** 45, 7618-7622.
[15] S. K. Furfari, B. E. Tegner, A. L. Burnage, L. R. Doyle, A. J. Bukvic, S. A. Macgregor, A. S. Weller, *Chem. Eur. J.,* **2021,** 27, 3177-3183.
[16] B. Guzel, M. A. Omary, J. P. Fackler, A. Akgerman, *Inorganica Chim. Acta,* **2001,** 325, 45-50.
[17] K. T. Chan, G. S. M. Tong, W.-P. To, C. Yang, L. Du, D. L. Phillips, C.-M. Che, *Chem. Sci.,* **2017,** 8, 2352-2364.
[18] H. Dorn, R. A. Singh, J. A. Massey, A. J. Lough, I. Manners, *Angew. Chem. Int. Ed.,* **1999,** 38, 3321-3323.
[19] T. N. Hooper, A. S. Weller, N. A. Beattie, S. A. Macgregor, *Chem. Sci.,* **2016,** 7, 2414-2426.